Microfluidic Nanoparticle Synthesis via Continuous-Wave Laser Heating

MOHAMMAD LAHEJI

Thesis submitted to the University of Nottingham for the degree of Doctor of Philosophy

March 2021

Abstract

Microfluidic nanoparticle synthesis has attracted significant attention in recent years, with several advantages over conventional batch synthesis: smaller concentration and temperature gradients, well-controlled and rapidly changeable reaction conditions, and easier scalability. Laser synthesis is a route that offers rapid formation of nanoparticles. Most works in the literature focus on laser ablation in liquids or thermal decomposition of gaseous precursors, but relatively little work has been reported on the decomposition of liquid precursors, most of which have no flow control. The possibility of combining these two synthesis methods is investigated in this thesis. This work presents a novel approach for nanocrystal synthesis within microfluidic chips, wherein thermal decomposition of metal organic precursors was achieved by localised laser heating using a continuous wave laser to produce iron oxide and cadmium selenide particles. As only the precursor solution was being heated, the chips could be made using inexpensive, commercially obtained acrylic.

Laser synthesis of iron oxide nanoparticles carried out in microwells with no flow resulted in polydisperse particles between ~5-500 nm in size, and in many cases had extremely low yields. To overcome these issues, a microfluidic chip was designed with a vertical flow section where the laser was aimed. The greater control over the residence period offered by this design resulted in major improvements in the yield and size distribution. When synthesising iron oxide nanoparticles, the best results were particles with an average size of 84.7 nm and a standard deviation of 46.8 nm (55.3%).

The highly localised heating makes temperature measurement difficult. Hence a basic fluid flow and heat transfer simulation was conducted to gain a better understanding of the temperature distribution within the chip, which illustrated the limitations of the chip design and provided valuable insight for future work. The model was also used to determine suitable parameters for the microfluidic synthesis of cadmium selenide nanocrystals. Quantum dot samples with peak emission wavelengths between 457-500 nm were also synthesised in the chip, with the best result emitting at 500 nm with a FWHM of 39 nm. CdSe clusters and quantum dots could be differentiated by analysing the PL and PLE spectra of the samples.

The work presented in this thesis illustrates some of the possibilities of laser heating for nanoparticle synthesis, in combination with microfluidic chips for controlled irradiation of the reaction mixture. The experimental setup is easy to implement using inexpensive tools and materials.

Keywords: iron oxide, cadmium selenide, nanoparticles, quantum dots, thermal decomposition, synthesis, microfluidic, laser

Acknowledgements

First of all, I would like to thank my supervisors, Dr Lau Pei Li, Dr Chin Jit Kai and Prof. Ian Harrison, who have all helped in their own way, whether it be through guidance, motivation, ideas, editing, funding, or otherwise. I would also like to thank Dr Michelle Tan for her continued support throughout the years.

I would also like to thank the staff at the electronics fabrication lab, Hashimi, Irwan, and Saiful, for their help with the PCB fabrication and their patience with my endless requests for experimentation. Thanks to the staff at the mechanical workshop, for training and allowing the use of the machining tools for device fabrication.

Special thanks to Filzah and Kharani at the SEM lab, whose imaging skills helped shape the direction of this work. Thanks to Faizal and Andrew who helped me get started in the wet chemistry labs, Fatihah and Fareez for their help with the analysis, and Shabuddin, Asyraf, and Shahril for their help in the lab. Thanks to Afini, Siak Chung, and the staff at the FoS labs for training and the use of their instruments.

I would also like to thank the Graduate School for their help with professional development, the Postgraduate Student Association for looking out for the welfare of postgrad students, and both for their enjoyable events throughout the years. Thanks to all my office mates who made the place a second home.

Finally, I would like to thank my parents and family for their unending love and support.

List of Abbreviations and Nomenclature

FeOl	Iron oleate
FeOOH	Iron oxide-hydroxide
OA	Oleic Acid
NaOl	Sodium Oleate
ODE	Octadecene
HEX	Hexane
ACE	Acetone
V_{rc}	Volume of the reaction chamber
t_r	Average residence period of the fluid under the laser
Q	Volumetric flow rate of the fluid
(P)LAL	(Pulsed) Laser Ablation in Liquid
LRL	Laser Reaction in Liquid
PL	Photoluminescence
PLE	Photoluminescence Excitation
PL365	Photoluminescence spectrum, excited at 365 nm
EX400	Excitation spectrum, measured at an (example) emission wavelength of 400 nm
FWHM	Full Width at Half Maximum, a measure of the sharpness of a peak
MSC	Magic-Size Clusters
CdOA	Cadmium oleate
Nuclei	A seed which can potentially grow into larger nanocrystals
Monomer	A species that acts as building blocks for colloidal nanocrystal growth.

Table of Contents

Abstract ii

Acknowledgements iii

List of Abbreviations and Nomenclature iv

Table of Contents v

List of Figures xi

List of Tables xxii

1 Introduction 1

1.1 Background 1

1.2 Aims and objectives 2

1.3 Thesis structure 3

2 Literature review 5

2.1 Thermal decomposition synthesis of iron oxide nanoparticles 5

2.1.1 Nanoparticle growth mechanism 5

2.1.2 Comparison of iron source 7

2.1.3 Synthesis 8

2.1.4 Iron oleate synthesis 10

2.1.5 Effect of experimental parameters on particle morphology 11

2.2 Thermal decomposition synthesis of cadmium selenide quantum dots 13

2.2.1 Clusters 14

2.2.2 Purification 15

2.3 Microfluidic synthesis 16

2.3.1 Microfluidic device fabrication 16

2.3.2 Coprecipitation 17

2.3.3 Thermal Decomposition 18

2.4 Laser synthesis 22

2.4.1 Laser synthesis in solid media 22

2.4.2 Laser synthesis in aerosol streams 22

2.4.3 Laser synthesis in liquid media 23
2.4.4 Energy absorbed by the solution 26
3 Batch synthesis of iron oxide nanoparticles 27
3.1 Experimental setup 27
3.2 Precursor synthesis 28
3.2.1 FeOOH Synthesis 29
3.2.2 FeOl Synthesis 29
3.3 Nanoparticle synthesis 32
3.3.1 Reaction mixtures 32
3.3.2 Heating conditions 33
3.3.3 Purification 33
3.4 Results 34
3.4.1 FeOOH in octadecene 34
3.4.2 FeOOH in olive oil 35
3.4.3 FeOl in octadecene 37
3.4.4 FeOl in olive oil 39
3.4.5 Choice of iron source for microfluidic synthesis 41
3.5 Summary 42
4 Design and fabrication of continuous flow microfluidic chips 44
4.1 Thermal bonding Jig 44
4.1.1 Thermal bonding parameters 47
4.2 Straight channel chip 47
4.3 Vertical flow chip 49
4.3.1 Solvent vapour bonding 53
4.4 Summary 54
5 Preliminary microfluidic synthesis of iron oxide nanoparticles 56
5.1 Experimental Setup 56
5.1.1 Optical assembly 58

5.1.2 Structural fabrication 59
5.1.3 Control electronics 60
5.1.4 Beam characterisation 62
5.2 Solution preparation 65
5.3 Stationary synthesis 66
5.3.1 Aluminium well 66
5.3.2 Well array 69
5.3.3 Long-necked wells 70
5.4 Straight channel continuous flow device 74
5.4.1 Synthesis 74
5.4.2 Results and discussion 75
5.5 Summary 76
6 Microfluidic synthesis of iron oxide nanoparticles in vertical flow chips 77
6.1 Flow rate and residence times 77
6.2 Methodology 77
6.2.1 Purification 80
6.3 Synthesis 82
6.3.1 Preliminary tests 82
6.3.2 Final batch 86
6.3.3 Reactor damage 88
6.3.4 Temperature measurement 91
6.4 Results 92
6.4.1 UV-VIS 94
6.4.2 XRD 95
6.4.3 FTIR 98
6.4.4 SEM/STEM 106
6.5 Discussion 123
6.6 Summary 125

7 Simulation of fluid flow and heat transfer in microfluidic synthesis 127
7.1 Model setup 127
7.1.1 Parameters 128
7.1.2 Functions 129
7.1.3 Geometry 130
7.1.4 Materials 134
7.1.5 Laminar Flow (spf) 135
7.1.6 Heat Transfer in Fluids (ht) 137
7.1.7 Solid Mechanics (solid) 141
7.1.8 Multiphysics couplings 141
7.1.9 Mesh 142
7.2 Studies 145
7.2.1 Study 1: LF, Stationary 145
7.2.2 Study 2: LF, HT, and SM, Stationary 145
7.2.3 Study 3: LF and HT, Transient Study 145
7.3 Results 146
7.3.1 Study 1: LF Stationary 146
7.3.2 Study 2: LF, HT, and SM Stationary 148
7.3.3 Study 3: LF and HT Time-dependent 163
7.4 Discussion 164
7.4.1 Limitations of the model 164
7.4.2 Fluid flow 164
7.4.3 Solution temperature 165
7.4.4 Surface temperature rise 170
7.4.5 Reactor temperature and stress 171
7.5 Summary 172
8 Microfluidic synthesis of CdSe quantum dots by laser heating 174
8.1 Methods and materials 174

8.1.1 Fabrication 174
8.1.2 Changes to the experimental setup 175
8.2 Experiments 178
8.2.1 Precursor synthesis 178
8.2.2 Quantum dot synthesis 179
8.3 Characterisation 180
8.4 Results 181
8.4.1 FTIR 184
8.4.2 UV-VIS 185
8.4.3 Photoluminescence 186
8.5 Discussion 199
8.5.1 Batch synthesis 199
8.5.2 Cluster formation in reaction mixtures at low temperatures 200
8.5.3 Microfluidic synthesis 200
8.5.4 Size selective precipitation 202
8.5.5 Effects of atmospheric oxygen and filtration on cadmium oleate synthesis 202
8.6 Conclusion 203
9 Conclusions 205
9.1 Future work 207
9.1.1 Droplet-based or segmented flow 207
9.1.2 Alternate materials 208
9.1.3 Changes to the laser used 208
9.1.4 Post-synthesis addition of surfactants 208
9.1.5 Changes to the setup 209
9.1.6 Other improvements 209
10 References 210
11 Appendix 223
11.1 FTIR analysis of iron oleate and iron oxides 223

11.1.1 Iron oleate 223
11.1.2 Iron oxides 224
11.2 FTIR analysis of solvents 229
11.3 SEM and STEM images of nanoparticles produced by microfluidic synthesis 232
11.4 Material properties used for the simulation 239
11.5 UV-VIS spectra of solvents 242
11.6 Photoluminescence spectra of solvents 243
11.7 PL/PLE spectra of purified quantum dot samples 244
11.7.1 Samples made using Mix342 244
11.7.2 Samples made using Mix431 249
11.7.3 Samples made using Mix571 256

List of Figures

Figure 2.1: A basic LaMer diagram, outlining the nucleation and growth stages of the particle growth process. The y axis shows the concentration of monomers as it changes with time. 6
Figure 2.4: Aging temperature vs average particle size reported by various authors. The chosen data represents spherical nanoparticles produced by the thermal decomposition of iron oleate in the presence of oleic acid with the solution under constant stirring. 12
Figure 3.1: Diagram showing the experimental setup used for batch synthesis of iron oxide nanoparticles. 28
Figure 3.2: FTIR spectrum of the synthesised FeOOH powder 29
Figure 3.3: The synthesised FeOl after the final drying step. 30
Figure 3.4: FTIR spectrum of the synthesised FeOl. 31
Figure 3.5: TGA/DTG curves for the synthesised FeOl. (Range: 30 – 550 °C, Rate: 2 °C/min, Atmosphere: N_2, 5 mL/min) 32
Figure 3.6: DSC curve for the synthesised FeOl and its first differential. (Range: 30 – 550 °C, Rate: 2 °C/min, Atmosphere: N_2, 5 mL/min) 32
Figure 3.7: (top) SEM and (bottom) STEM imaging of iron oxide nanoparticles from run 1: FeOOH and oleic acid in octadecene. 35
Figure 3.8: (top) SEM and (bottom) STEM imaging of iron oxide nanoparticle products from run 2: FeOOH in olive oil. 36
Figure 3.9: FTIR spectrum of the iron oxide nanoparticles synthesised from run 2 (FeOOH in olive oil). 37
Figure 3.10: (top) SEM and (bottom) STEM imaging of iron oxide nanoparticles from run 3: FeOl and oleic acid in octadecene. 38
Figure 3.11: FTIR spectrum of the iron oxide nanoparticles synthesised from run 3 (FeOl in octadecene). 39
Figure 3.12: (top) SEM and (bottom) STEM imaging of iron oxide nanoparticles from run 4: FeOl in olive oil. 40
Figure 3.13: Difference between the reaction products obtained from run 3 (left) and run 4 (right) using FeOl as the iron source. Significant sedimentation (circled in red) can be seen in the olive oil based synthesis product in the vial on the right. This was not observed in run 2 (FeOOH in olive oil). 41
Figure 4.1: Design of the platens used for cutting, milling, and drilling. **Green**: Chip dimensions used as a guideline. **Yellow**: 3mm alignment holes. **Red**: 5mm/M3 clamping holes. 44

Figure 4.2: (top) Illustration and (bottom) photographs of the platens in use. 46
Figure 4.3: Design of the straight channel layers. The four holes on the corners of each layer are the alignment holes, and the two holes on the top layer are the inlet and outlet holes. All dimensions are in mm. 48
Figure 4.4: A straight channel chip being leak tested using dyed water. The overall dimensions of the chip are 75 mm * 25 mm. The channel has a width of ~500 µm. 49
Figure 4.5: Illustration of the vertical flow chip with the focused laser beam. Inset: Close-up of the reaction chamber with arrows indicating the direction of fluid flow. 50
Figure 4.6: The three layers of the chip, showing the steps of fabrication. In the top layer, the hole on the left is the inlet, and the hole on the right is the outlet. 51
Figure 4.7: Illustration of the channel fabrication using an acrylic scoring tool. 51
Figure 4.8: The bonded chip, showing the plugging of the inlet and outlet holes. 52
Figure 4.9: Leak testing of a vertical flow chip using dyed water. 53
Figure 4.10: Close-up of the reaction chamber showing the vertical flow region. 53
Figure 4.11: Solvent induced clouding observed in solvent bonded sample. 54
Figure 5.1: Illustration of the flow synthesis experimental setup used for microfluidic nanoparticle synthesis 56
Figure 5.2: The experimental setup used continuous flow synthesis run of iron oxide nanoparticles. 57
Figure 5.3: The optical assembly including the laser module, objective lens, and structural parts. The dotted lines show a cross-section of the internal structure of the assembly. This picture shows an earlier, smaller version of the heatsink. 59
Figure 5.4: Fabricated structural parts. The mounting holes at the bottom attach the mounting plate to the stage base. 60
Figure 5.5: Illustration of the various electronics components of the setup. The thickness of the connecting arrows is indicative of the amount of current/energy being transferred. 62
Figure 5.6: Diagram of the setup to find the height of the focal point and focal diameter for microfluidic synthesis 63
Figure 5.7: Illustration of the razor blade in the centre of the stage. As the stage moves, the laser spot is slowly uncovered. Inset: As the spot diameter changes with height, the time the blade takes to uncover the spot also changes. 64
Figure 5.8: Intensity scans between 2.25 and 2.45 mm. The left most column shows the height of the scan ($h_{platform}$). To its right is the calculated beam radius at that height. 65
Figure 5.9: Illustration of the aluminium well synthesis setup. 66

Figure 5.10: (Left) Photograph of the aluminium well with the reaction solution. (Right) Magnetic precipitates seen in the vial after purification. 67
Figure 5.11: Nanoparticles produced in the aluminium well. Smaller spherical particles can be seen, but most of the larger ones are pyramidal/bipyramidal. 68
Figure 5.12: Design of the acrylic well array. All dimensions are in mm. 69
Figure 5.13: (Left) Acrylic well array as fabricated. (Right) Well array filled and sealed. 70
Figure 5.14: (Top) Design of the long necked well (units: mm). (Bottom) Fabricated and filled wells. 71
Figure 5.15: Laser sweep pattern across the 3mm well. 72
Figure 5.16: (left) Magnetic material seen in sample 2 and (right) sample 3 synthesised in the individual long necked wells. Synthesis parameters for these sample are presented in Table 5.3. 73
Figure 5.17: Particles seen in sample 4 synthesised in the long neck well. Particles are agglomerated and difficult to differentiate. Synthesis parameters for this sample are presented in Table 5.3..... 74
Figure 5.18: Particles seen in sample 7 synthesised in the long neck well. Particles are agglomerated but can be differentiated. The average size of the particles is in the 10 nm range. Synthesis parameters for this sample are presented in Table 5.3. 74
Figure 6.1: Typical flow synthesis process for 100 µL runs in the vertical flow chips. 79
Figure 6.2: The vertical flow chip setup after a synthesis run (the laser power is set to minimum while taking this photograph). Inset: A close-up of the reaction chamber. The inlet, reaction chamber, and outlet channels can be clearly seen. The image at the bottom is the reflection of the channel from the bottom surface of the chip. 80
Figure 6.3: (A) The four preliminary samples (from Table 6.1) after synthesis. Each vial has ~100 uL of the heated solution. The samples were purified twice and allowed to settle beside a magnet. (C) Front view of the precipitates after 1 hour. (B) Side view of the precipitates after 18 hours. (D) Front view of the precipitates after 18 hours of settling. 83
Figure 6.4: (A and B) Two sites chosen for EDX analysis in sample 3. (C and D) Particles seen in sample 4. Sample 3 shows few individual particles. While spherical particles can be seen in sample 4, they are still agglomerated and coated in a thick layer of FeOl and/or oleic acid. 84
Figure 6.5: Low magnification SEM view of the iron oxide nanoparticles in sample 4, produced by microfluidic laser synthesis. 85
Figure 6.6: EDX elemental mapping of the region seen in Figure 6.5, showing nanoparticles from sample 4, produced by microfluidic synthesis. Iron (Fe) and oxygen (O) can be seen on the particles, while most of the carbon (C) counts come from the carbon tape that the sample was deposited on. 86

Figure 6.7: (Left) Close-up of chip 1's reaction chamber after it was blocked. (Right) Outlines showing the location of the inlet channel, reaction chamber, and outlet channel. 89
Figure 6.8: Close up of chip 2's reaction zone (left) before O8-1, and (right) after O8-1. The laser beam is pointed at the centre of the circular region, the top window of the reaction zone. 89
Figure 6.9: Close up of chip 3's reaction zone (left) after O8-2 and O8-3, and (right) after O8-2, O8-3, N8-1, N8-2, and N8-3 90
Figure 6.10: Side view of chip 3's reaction zone after sample N8-3. Fracturing can be seen in both the top and middle layers. 90
Figure 6.11: Measured surface temperature increase at four different flow rates for the O solution. O8-A and O6-A measurements are averages of 3 runs. 92
Figure 6.12: Left to right: Samples B2-3, O6-3, O8-3, N8-3 settled after 3 rounds of purification. 93
Figure 6.13: Left to right: Samples B2-3, O6-3, O8-3, N8-3 after 2 rounds of purification. In this picture, the samples were precipitated beside a magnet. 93
Figure 6.14: Increase in absorbance at 400 nm with increasing residence period using the B, O, and N solutions (average of all 3 repetitions). 95
Figure 6.15: XRD measurements of some of the O and N samples 96
Figure 6.16: XRD spectra of specially made samples (flow rate of 24 µL/min, laser power 250 mW) from the B and N solutions, **after** heating at 350 °C for 10 hours. 97
Figure 6.17: (top) Peaks detected in sample iron oxide B, and (bottom) Magnetite peaks from the HighScore database 97
Figure 6.18: (top) Peaks detected in sample iron oxide N, and (bottom) Hematite peaks from the HighScore database. 98
Figure 6.19: FTIR spectrum of the synthesised FeOl 99
Figure 6.20: FTIR spectra of nanoparticles produced from the B solution. From bottom to top, nanoparticles produced from residence periods of 2s (B2) and 4s (B4), three runs each. At the top are the FTIR curves of oleic acid (OA) and iron oleate (FeOl) for comparison 102
Figure 6.21: FTIR spectra of nanoparticles produced from the O solution. From bottom to top, nanoparticles produced from residence periods of 2s (O2), 4s (O4), 6s (O6), and 8s (O8), three runs each. At the top are the FTIR curves of oleic acid (OA) and iron oleate (FeOl) for comparison. 103
Figure 6.22: FTIR spectra of nanoparticles produced from the N solution. From bottom to top, nanoparticles produced from residence periods of 2s (N2), 4s (N4), 6s (N6), and 8s (N8), three runs each. At the top are the FTIR curves of oleic acid (OA) and iron oleate (FeOl) for comparison. 104
Figure 6.23: FTIR spectra of the O and N samples in the 1000 - 400 cm^{-1} region. The FeOl spectrum has been subtracted from all the spectra presented. 105

Figure 6.24: (Left) SEM image of sample B2-2. (Right) STEM image of sample B2-2. This sample was produced by microfluidic synthesis using the B solution with an average residence period of 2s. This sample was purified using method 1 and shows high levels of agglomeration. 107
Figure 6.25: STEM images of sample B2-3, produced by microfluidic synthesis using the B solution with an average residence period of 2s. This sample was purified using method 2 and shows lower agglomeration compared to sample B2-2. 107
Figure 6.26: STEM images of samples B4-1 (left) and B4-2 (right). These samples were produced by microfluidic synthesis using the B solution with an average residence period of 4s. 108
Figure 6.27: STEM images of sample B4-3, produced by microfluidic synthesis using the B solution with an average residence period of 4s. 108
Figure 6.28: (Top) SEM and (Bottom) STEM images of purified samples O2-1 and O2-2, produced by microfluidic synthesis using the O solution with an average residence period of 2s. 111
Figure 6.29: STEM and SEM images of samples O4-1 (top) and O4-3 (middle row), and O4-4 (bottom row), produced by microfluidic synthesis using the O solution with an average residence period of 4s. 112
Figure 6.30: STEM images of sample (top row) O6-1, (middle row) O6-2, (bottom row) O6-3, produced by microfluidic synthesis using the O solution with an average residence period of 6s. Denser iron oxide particles can be seen embedded in lighter organic networks. 113
Figure 6.31: STEM images of sample (top row) O8-1, (middle row) O8-2, (bottom row) O8-3, produced by microfluidic synthesis using the O solution with an average residence period of 8s. 114
Figure 6.32: SEM and STEM images from samples N2-1 (top) and N2-2 (bottom) , produced by microfluidic synthesis using the N solution with an average residence period of 2s. 116
Figure 6.33: Speculative outlines of overlapping cubes in samples N2-1 and N2-2. 117
Figure 6.34: Diluted, unpurified O6-1 solution showing individual spherical particles. 118
Figure 6.35: Possible explanation for the brightness gradient around the boundary of the particle. The estimated size of this particle is ~480 nm. 119
Figure 6.36: Diluted, unpurified N6-2 solution showing small (left) and large (right) particles. 119
Figure 6.37: Mean sizes across all samples. The error bars show standard deviation. 120
Figure 6.38: Particle size histogram of the O6-1 and N6-2 liquid samples. 122
Figure 7.1: The absorbedheat function overlaid onto the geometry of the device. Visualised on an XZ plane at Y = 0. 130
Figure 7.2: Final geometry used for the model. Image generated with transparency on. 131
Figure 7.3: Heat capacities of the O solution and its constituent materials, used for the simulation. 135

Figure 7.4: Cutaway view (y>0) of the final mesh used for the simulation. 143
Figure 7.5: Output time steps used in the transient study. 146
Figure 7.6: Velocity magnitude of unheated fluid (from Study 1) at 26.55 µL/min with arrows showing direction of flow. Visualised on an XZ plane at Y = 0. 147
Figure 7.7: Velocity magnitude of unheated fluid (from Study 1) in the device at different flow rates. Visualised on an XZ plane at Y = 0. 148
Figure 7.8: Velocity magnitude of the heated fluid (from Study 3) in the device at different flow rates. Visualised on an XZ plane at Y = 0. 149
Figure 7.9: Velocity magnitude of the heated fluid (from Study 3) in the device at different flow rates (synchronised scales). Visualised on an XZ plane at Y = 0. 150
Figure 7.10: Temperature field in the device (independent temperature scales). Visualised on an XZ plane at Y = 0. 152
Figure 7.11: Temperature field in the device at different flow rates (synchronised temperature scales). Visualised on an XZ plane at Y = 0. 153
Figure 7.12: Temperature field contours at different flow rates. The contour levels are chosen based on the nucleation and decomposition temperature ranges (Table 7.5). 154
Figure 7.13: Particle tracing in one half (y>0) of the channel (flow rate = 4.4250e-10 mm^3/s). The colour of the traces represents the temperature in degrees Celsius. 155
Figure 7.14: Particle tracing in one half (y>0) of the channel (flow rate = 2.2133e-10 mm^3/s). The colour of the traces represents the temperature in degrees Celsius. 156
Figure 7.15: Particle tracing in one half (y>0) of the channel (flow rate = 1.4750e-10 mm^3/s). The colour of the traces represents the temperature in degrees Celsius. 157
Figure 7.16: Particle tracing in one half (y>0) of the channel (flow rate = 1.1067e-10 mm^3/s). The colour of the traces represents the temperature in degrees Celsius. 158
Figure 7.17: Temperature on the inner surfaces of the channel at different flowrates. (synchronised scales) 159
Figure 7.18: Temperature contours on the inner surfaces of the channel. The contour levels are based on Table 7.6, and represent the acrylic glass transition temperature (70 °C), acrylic melting point (170 °C), ... 160
Figure 7.19: von Mises stress in the acrylic around the reaction chamber. Visualised on an XZ plane at Y = 0. 161
Figure 7.20: von Mises stress in the acrylic around the reaction chamber (synchronised scales). Visualised on an XZ plane at Y = 0. 162
Figure 7.21: 3D view of the von Mises stress on the channel surfaces (synchronised scales) 163

Figure 7.22: Temperature rise in the measured temperatures shown by the curves. The maximum temperatures from the simulated studies are shown higher up. 164
Figure 7.23: Temperature vs time plots of particle traces at the different flowrates. All curves are terminated when they reach x = 2e-3 m (i.e. the particle tracing is stopped when they leave the reaction chamber). 168
Figure 7.24: Percentage breakdown of traces in each temperature range. 168
Figure 7.25: Nucleation and growth periods calculated from particle tracing temperature data at different flowrates. Plots show periods of individual traces marked with a yellow x, and the mean periods and standard deviation error bars. 169
Figure 7.26: Heating rates (yellow x) at the different flow rates, along with the mean and standard deviation error bars. 170
Figure 7.27:Reactor damage seen after the experiments (left) compared with the simulation results (right). (Full simulation results can be seen in Figure 7.19) 172
Figure 8.1: Photo of an acrylic sample between two cross-polarised films showing the higher stress on the laser cut edges compared to the saw cut edge. 174
Figure 8.2 Acrylic layers clamped in the bonding jig. The three layers are kept in place using two dowel pins and sandwiched between two glass slides 175
Figure 8.3: The modified setup used for microfluidic CdSe synthesis. 176
Figure 8.4: (top) Elevated view and (bottom) side view of the experimental setup during alignment (the laser power is set to the minimum). 177
Figure 8.5: Measured laser output power vs PWM input signal, showing a fairly linear relationship between PWM value and output power. 178
Figure 8.6: Photograph of purified samples made from Mix342 under UV illumination (365 nm). From left to right: 17-184, 19-188, 21-191, 21-194, 23-198, 24-200. While the sample 21-194 appears much brighter, it is mostly due to a higher amount being produced. 182
Figure 8.7: Photograph of purified samples made from Mix431 under UV illumination (365 nm). From left to right: 15-180, 15-225, 15-255, 20-180, 20-190, 20-200 182
Figure 8.8: Photographs of purified samples made from Mix571 under UV illumination (365 nm). From left to right: 20-180, 37-134x, 65-255, 70-255, 75-255x 183
Figure 8.9: Photograph of purified samples generated from batch synthesis using Mix571 under UV illumination (365 nm). From left to right: 70c5d, 190C1m (purified with methanol), 190C1m (purified with ethanol), 220C0m, 240C5m. 184
Figure 8.10: FTIR spectra of pure s70_255 and the supernatant after purification. 185

Figure 8.11: Absorbance of purified CdSe quantum dot solutions from batch synthesis runs using three different precursors. 185
Figure 8.12: PL spectra (normalised) of purified CdSe quantum dot solutions produced via batch synthesis. From left to right, the samples are (Mix571) 190 °C 1 min, (Mix111) 240 °C 30 s, and (Mix461) 240 °C 5 min. 187
Figure 8.13: PL spectra (normalised) of aliquots taken at various temperatures during a batch synthesis run using Mix571. 187
Figure 8.14: Normalised fluorescence spectra of Mix342 and the purified samples produced from it via microfluidic synthesis..... 188
Figure 8.15: Normalised fluorescence spectra of Mix431 and the purified samples produced from it via microfluidic synthesis..... 188
Figure 8.16: Normalised fluorescence spectra of Mix571 and the purified samples produced from it via microfluidic synthesis..... 189
Figure 8.17: Photoluminescence spectra (coloured) and UV-VIS absorbance spectra (grey) of Mix571, and samples produced from it. Sample b190C1m_CME_pure was produced via a batch synthesis run, while the other samples were produced via microfluidic synthesis. All spectra are normalised. 190
Figure 8.18: Normalised fluorescence (PL365) and PLE spectra of sample s24_120_pure (made from Mix571) measured at various emission wavelengths. The absorption features at 355, 373, and 394 nm are the main contributors to the PL peaks seen below 460 nm. At higher wavelengths the contribution of these peaks is reduced and the PLE spectra around them broadens. 194
Figure 8.19 Normalised fluorescence (PL365) and PLE spectra of sample s37_134_pure (made from Mix571) measured at various emission wavelengths. The absorption features at 355, 373, and 394 nm are the main contributors to 410 nm PL peak. The 462 nm PL peak sees some absorption features between 433 – 450 nm, which decreases in intensity but does not exhibit a red shift when the emission wavelength is increased to 477 nm. 195
Figure 8.20: Normalised fluorescence (PL365) and PLE spectra of sample s65_255_pure (made from Mix571) measured at various emission wavelengths..... 196
Figure 8.21: Normalised fluorescence (PL365) and PLE spectra of sample 70_255 (made from Mix571) measured at various emission wavelengths. Red shifting can be seen in the weak band edge absorption hump going from EX458 to EX470. 197
Figure 8.22: : Normalised fluorescence (PL365) and PLE spectra of sample s75_255 _pure (made from Mix571) measured at various emission wavelengths. There is no observable change in the ratio of the excitation absorption peaks seen at 356, 373, and 394 nm at any of the emission wavelengths measured. 198

Figure 11.1: FTIR curves of iron oleate samples dried at 30 °C (FeOl-1), washed with ethanol and then dried at 30 °C (FeOl-3) and 70 °C (FeOl-4). 224
Figure 11.2: FTIR spectra of commercial powders of 100% hematite, maghemite and magnetite. The peak at 3642 cm^{-1} is from the CaO added for calibration. 225
Figure 11.3: FTIR spectra of magnetite nanoparticles annealed at different temperatures. The conversion from magnetite (A) to maghemite (B) to hematite (C and D) can be clearly seen. 226
Figure 11.4: FTIR curves of hematite, maghemite and magnetite nanoparticles (from Li et al (Li, et al., 2012)) over laid with the peak range obtained from the literature. The ranges show where the tip of the peak may lie, and not its entire breadth. 229
Figure 11.5: FTIR spectrum of 1-Octadecene. 230
Figure 11.6: FTIR transmission spectrum of liquid oleic acid. Peaks are labelled according to the bond that causes them. More details in Table 11.2. Source: NIST 230
Figure 11.7: STEM images of purified sample O2-3, produced by microfluidic synthesis using the O solution with an average residence period of 2s. 232
Figure 11.8: STEM and SEM images of sample O4-2 (bottom), produced by microfluidic synthesis using the O solution with an average residence period of 4s. 232
Figure 11.9: STEM images of sample O6-1, produced by microfluidic synthesis using the O solution with an average residence period of 6s. Denser iron oxide particles can be seen embedded in lighter organic networks. 233
Figure 11.10: STEM images of sample O6-2, produced by microfluidic synthesis using the O solution with an average residence period of 6s. 233
Figure 11.11: STEM images of sample O6-3, produced by microfluidic synthesis using the O solution with an average residence period of 6s. 234
Figure 11.12: STEM images of sample O8-1, produced by microfluidic synthesis using the O solution with an average residence period of 8s. 234
Figure 11.13: STEM images of sample O8-2, produced by microfluidic synthesis using the O solution with an average residence period of 8s. 235
Figure 11.14: STEM images of sample O8-3, produced by microfluidic synthesis using the O solution with an average residence period of 8s. 235
Figure 11.15: STEM images from samples N4-1 and N4-2, produced by microfluidic synthesis using the N solution with an average residence period of 4s. 236
Figure 11.16: STEM images from sample N4-3, produced by microfluidic synthesis using the O solution with an average residence period of 4s. 236

Figure 11.17: STEM images from sample N6-1 and N6-2, produced by microfluidic synthesis using the N solution with an average residence period of 6s. 237
Figure 11.18: STEM images from sample N6-3, produced by microfluidic synthesis using the N solution with an average residence period of 6s. 237
Figure 11.19: STEM images from samples N8-1 (top row), N8-2 (middle row), and N8-3 (bottom row), produced by microfluidic synthesis using the N solution with an average residence period of 8s. 238
Figure 11.20: Heat Capacity of PMMA. (Gauri et al) 239
Figure 11.21: Thermal conductivity of PMMA. (dos Santos et al) 239
Figure 11.22: Thermal conductivity of 1-octadecene (Yaw) 241
Figure 11.23: Density of 1-octadecene (Yaw) 241
Figure 11.24: Viscosity of 1-octadecene 242
Figure 11.25: UV-VIS absorbance spectra of the solvents used in CdSe synthesis, measured against air. 242
Figure 11.26: Fluorescence spectra of the various solvents used in the CdSe synthesis runs. These spectra in each subplot were measured using the same settings (photomultiplier voltage: (left) 950V, (right) 400V) and have not been normalised. 243
Figure 11.27: Normalised fluorescence (PL365) and PLE spectra of sample s17_184_pure (made from Mix342) measured at various emission wavelengths. No peaks stand out prominently in this case in either the PL or PLE spectra, but very weak band absorption peaks may be seen in the 550, 565, 580 and 600 nm PLE spectra. 244
Figure 11.28: Normalised fluorescence (PL365) and PLE spectra of sample s19_188_pure (made from Mix342) measured at various emission wavelengths. This sample is similar to s20_180_pure (Figure 11.36), with significant band edge absorption peaks, but very low yield. 245
Figure 11.29: Normalised fluorescence (PL365) and PLE spectra of sample s20_191_pure (made from Mix342) measured at various emission wavelengths. While the 329 nm and 372 nm peaks contribute the most to the PLE spectra, a sharp peak can be seen with in most of them with a constant stokes shift of ~40-55 nm. 246
Figure 11.30: Normalised fluorescence (PL365) and PLE spectra of sample s21_194x_pure (made from Mix342) measured at various emission wavelengths. The band edge absorption peaks seen here are negligible. Note: the chip was damaged during the synthesis of this sample. 247
Figure 11.31: Normalised fluorescence (PL365) and PLE spectra of sample s21_194x_pure (made from Mix342) measured at various emission wavelengths. The band edge absorption peaks can clearly be seen throughout the PLE spectra. 248

Figure 11.32: Normalised fluorescence (PL365) and PLE spectra of Mix431 aged at room temperature for 50 days, measured at various emission wavelengths. The PL365 spectrum of fresh Mix431 is included for comparison. An increase in the 432 nm and 455 nm PL peaks is seen after aging, while the 406 nm peak is reduced. 249
Figure 11.33: Normalised fluorescence (PL365) and PLE spectra of sample s15_180_pure (made from Mix431) measured at various emission wavelengths. A small but well-defined peak can be seen throughout the PLE spectra, with a constant Stokes shift of ~40 – 60 nm. 250
Figure 11.34: Normalised fluorescence (PL365) and PLE spectra of sample s15_225_pure (made from Mix431) measured at various emission wavelengths. A small but well-defined peak can be seen throughout the PLE spectra, with a constant Stokes shift of ~40 – 60 nm. 251
Figure 11.35: Normalised fluorescence (PL365) and PLE spectra of sample s15_250x_pure (made from Mix431) measured at various emission wavelengths. A small band edge absorption peak can be seen in the PLE spectra emitting at 442 nm to 464 nm. 252
Figure 11.36: Normalised fluorescence (PL365) and PLE spectra of sample s20_180_pure (made from Mix431) measured at various emission wavelengths. While this sample shows significant band edge emission, the overall amount is incredibly low. The peaks are visible due to normalisation, but compared to other samples, this is barely visible. 253
Figure 11.37: Normalised fluorescence (PL365) and PLE spectra of sample s20_190_pure (made from Mix431) measured at various emission wavelengths. 254
Figure 11.38: Normalised fluorescence (PL365) and PLE spectra of sample s20_190_pure (made from Mix431) measured at various emission wavelengths. Almost all the photoluminescence is due to the absorption features at 355, 373, and 394 nm. 255
Figure 11.39: Normalised fluorescence (PL365) and PLE spectra of sample s65_255_second_pure (made from Mix571) measured at various emission wavelengths. The second washing of this sample resulted in a small blue shift (-3 nm) of the main peak compared to sample s65_255_pure. 256
Figure 11.40: Normalised fluorescence (PL365) and PLE spectra of sample b70C5d_pure (made from Mix571) measured at various emission wavelengths. The PLE peaks at 355, 375, and 396 nm are major contributors to the fluorescence intensity up to 500 nm, above which another much broader PLE peak (444 nm) becomes the dominant contributor. 257

List of Tables

Table 3.1: Summary of mean diameters and standard deviations of particles obtained from the batch synthesis runs. 41
Table 5.1: Table showing the B, O, and N solutions with the amounts and type of surfactants in each. 66
Table 5.2: CNC settings used to fabricate the long-necked wells. 71
Table 5.3: Sweeping synthesis experiment details 72
Table 6.1: Residence periods and calculated flow rates for the preliminary microfluidic synthesis runs 82
Table 6.2: Average residence periods and calculated flow rates for the final batch. The total volume is 100 µL 87
Table 6.3: Names of samples produced. The purification method used is distinguished by the colour of the cells in the table. Method 2 is a gentler purification method adapted to reduce agglomeration during separation. These methods are explained in greater detail in section 6.2.1. 87
Table 6.4: Number of runs conducted per chip and the total time. 88
Table 6.5: Mean diameters and standard deviations seen in Figure 6.37. 121
Table 7.1: Parameters used in the model. 128
Table 7.2: List of solid geometry objects. All dimensions 132
Table 7.3: Boolean operations performed on the solid objects 133
Table 7.4: Details of the mesh sequence used for the model. The values in grayed out cells are the default predefined values that were left unchanged. 144
Table 7.5: List of significant temperatures for iron oleate. 151
Table 7.6: Significant temperatures for acrylic plastic 159
Table 7.7: Number and percentage of traces in each temperature range 168
Table 7.8: Mean durations and standard deviation of time periods spent by the traces in growth and nucleation temperature ranges 168
Table 7.9: Mean and standard deviation of heating rates of growth traces at different flow rates 170
Table 8.1: Precursor mixtures used for CdSe quantum dot synthesis 179
Table 8.2: Samples generated from each precursor mixture via microfluidic synthesis. For the samples with x at the end, the chip was found to be damaged after these samples. Hence their results may not be as expected. The samples are labelled using a combination of flow rate and PWM. 180
Table 8.3: Samples generated from each precursor mixture via batch synthesis. All times stated are the time at which the sample was taken after reaching that temperature. 180

Table 11.1: Calculated and observed vibrational modes of hematite, maghemite and magnetite from the literature. Only values of peaks observable above 400 cm^{-1} are shown. 228
Table 11.2: Prominent FTIR bands seen in the FTIR spectrum of oleic acid 231
Table 11.3: Heat capacity coefficients (J/mol.K) (Yaws, 2010) 240
Table 11.4: Thermal and physical properties of 1-octadecene (Source: Yaws) 240

1 Introduction

1.1 Background

Magnetic nanoparticles, especially single domain superparamagnetic nanoparticles, have a large variety of applications in various fields. They are most prominently used for medical and clinical purposes (Ito, et al., 2005) (Laurent, et al., 2008) (Mornet, et al., 2006) (Lu, et al., 2007), as MRI contrast enhancement agents (Shao, et al., 2010) (Patel, et al., 2008) and for cancer treatment via magnetic hyperthermia (Alphandery, et al., 2012) (Armijo, et al., 2012). Since they can be easily magnetically guided in an aqueous medium (e.g. blood), iron oxide nanoparticles have also been used for drug delivery and cell/tissue labelling and sorting. Non-biological applications include use in batteries, supercapacitors, ferrofluids and magnetic storage (Ievlev, et al., 2014) (Sheng-Nan, et al., 2014).

All of these applications have their own set of requirements when it comes to the nanoparticle morphology and properties. For the nanoparticles to be superparamagnetic, they must be comprised of a single domain per particle, which typically limits its size to less than 50 nm. In the case of cell labelling and certain drug delivery applications the particles must also be small enough to pass through the cell walls. For magnetic storage, the smaller the particle/domain size is, the denser the storage medium can be. In all of these cases, regardless of the size requirements, a monodisperse size distribution is desirable for predictable results.

Several colloidal synthesis methods have been reported for iron oxide nanoparticle production (Wu, et al., 2015). The coprecipitation method is one of the most commonly used method as it is fast, simple, and offers good size control, but rather poor shape control and crystallinity at room temperatures. The thermal decomposition method offers some the best results: highly crystalline particles with narrow size and shape distributions and a good amount of control over the particle shape and size. The morphology of the particles heavily depends on the conditions of the reaction, notably temperature, reaction time, and the presence of surfactants and other ions.

The process has several downsides: it is relatively slow, complicated, and depending on the reagents, requires an inert atmosphere and high temperatures. In a thermal decomposition synthesis run, a low heating rate is one of the conditions typically required to maintain a narrow size distribution. The growth temperature is one of the major factors controlling the final size of the particles grown. Both of these factors depend on temperature control during the process, which can exhibit significant

variations and is highly dependent on the knowledge and skill of the user, as well as the equipment used in the experiment.

Similarly, the diameter of cadmium selenide nanoparticles must be between ~1.5-9 nm to exhibit quantum confinement and fluoresce in the visible region (Murray, et al., 1993). CdSe quantum dots can also be synthesised by the same thermal decomposition process.

In this thesis, iron oxide nanoparticles and cadmium selenide quantum dots are produced in microfluidic devices via thermal decomposition. Rather than using a conventional heater which heats up the entire device, a laser is used for localised heating of the solution. The expected advantages of this are:

- Non-contact heating
    - Only the solution is directly heated
    - Larger choice of materials for the microfluidic chip
- Quick heat-up and cooldown
    - Decreased synthesis period
    - Greater degree of control over nucleation and growth
- Energy savings
- Safer operation

The use of localised optical heating results in a small heated region (less than 0.7 mm in diameter), which makes accurate temperature measurement unfeasible. A thermocouple embedded in the middle of the channel would block the laser. A thermocouple in or near the heated region would also act as a heat sink for the limited amount of energy (<0.5 W) being put into the system. Instead, simulations were performed to estimate the temperature distribution in the heated region within the channel.

To the best of the author's knowledge, laser-induced thermal decomposition of iron oleate, the use of continuous wave lasers for LRL nanoparticle synthesis, and the combination of these approaches within a microfluidic device, all have not been previously reported. The work in this thesis is presented as a first step in this area.

1.2 Aims and objectives

The ultimate aims of research in this area are:

1. Automated, scalable, on-demand, customised nanoparticle synthesis

2. Better tools to study the kinetics of nanoparticle and cluster formation

The objectives of this work are:

1. To find a suitable homogenous precursor solution for microfluidic nanoparticle synthesis.
2. Develop an experimental setup for safe and controlled laser irradiation of the solution.
3. Design and fabricate microfluidic chips suitable for thermal decomposition synthesis of nanocrystals by laser heating.
4. Synthesise iron oxide nanoparticles and cadmium selenide quantum dots in microfluidic chips at different flow rates and laser power levels and establish the relationship between process parameters and nanocrystal morphology.
5. Model the flow and temperature distribution within the channel at different flow rates and laser power levels to get a better understanding of the residence period distribution.

1.3 Thesis structure

Chapter 1: The current chapter introduces the work, its aims and objectives, and the structure of the thesis.

Chapter 2: Some experimental and theoretical background of the related fields is presented. Thermal decomposition synthesis, microfluidic synthesis, and laser synthesis are the three main fields that have been covered.

Chapter 3: The thermal decomposition synthesis process from the literature is reproduced using both FeO(OH) and iron oleate as iron sources. The use of olive oil as alternate solvent/surfactant has also been explored and a precursor suitable for microfluidic use was chosen.

Chapter 4: Design and fabrication of the continuous flow microfluidic chips used in Chapters 5 and 6.

Chapter 5: Preliminary tests of the thermal decomposition synthesis conducted within wells (stationary heating) and the straight channel chip (heating under flow).

Chapter 6: Thermal decomposition synthesis of iron oxide nanoparticles in the vertical flow chips, characterisation of the products, size analysis and discussion of the nanoparticles produced.

Chapter 7: Simulations conducted in COMSOL to provide an insight into the flow and temperature within the microfluidic device during synthesis.

Chapter 8: Thermal decomposition synthesis of cadmium selenide quantum dots in the vertical flow chips and characterisation of the product's optical properties and composition.

Chapter 9: A summary of the works presented in the thesis, as well as possible future improvements.

Chapter 10: References

Chapter 11: Appendix

2 Literature review

In this section, a comprehensive literature review is provided for the various fields that this project brings together. The main areas covered are:

1. The thermal decomposition synthesis process, and the various parameters (temperature, surfactant concentration, residence period, etc.) that affect the results for both iron oxide and cadmium selenide.
2. Microfluidic synthesis of iron oxide and cadmium selenide nanoparticles, as well as thermal decomposition synthesis within microfluidic systems.
3. Nanoparticles synthesis via laser heating, with the main focus being laser synthesis in a liquid medium.

2.1 Thermal decomposition synthesis of iron oxide nanoparticles

Iron oxide nanoparticles can be produced by high temperature thermal decomposition of organic iron complexes. In a typical synthesis run an iron precursor and a surfactant are mixed in a high boiling organic solvent. The mixture is then heated up to the decomposition temperature of the iron precursor and refluxed for a certain period of time. The iron precursor decomposes, releasing free monomers which then bind together and grow into larger nanoparticles. The presence of the surfactant is known to affect the formation and growth of the nanoparticles, and thus the particle size, size distribution, and shape. These results are also affected by the refluxing temperature and heating rate.

2.1.1 Nanoparticle growth mechanism

Colloidal nanoparticle growth can be divided into two major steps: nucleation and growth. The concentration of the monomer during this process is illustrated by a LaMer diagram (LaMer & Dinegar, 1950). Kwon and Hyeon (Kwon & Hyeon, 2011) present a detailed explanation and mathematical model of this phenomenon, and experimental verification for the case of iron oleate decomposition in octadecene.

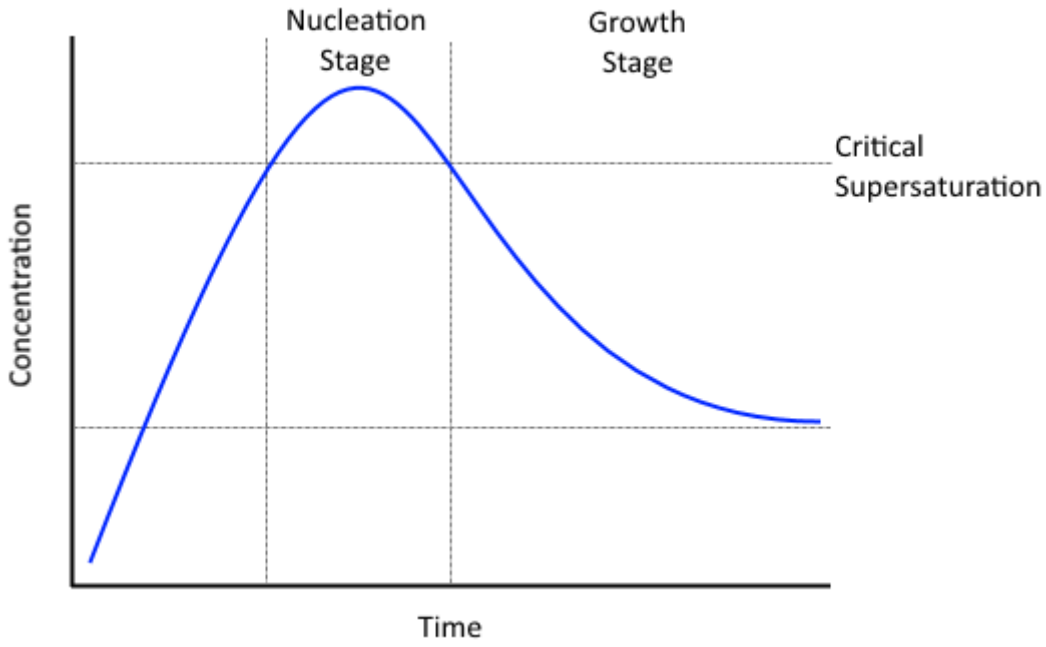


Figure 2.1: A basic LaMer diagram, outlining the nucleation and growth stages of the particle growth process. The y axis shows the concentration of monomers as it changes with time. Adapted from (Kwon & Hyeon, 2011)

In the thermal decomposition synthesis process, the precursor decomposes when reaching a certain temperature. This decomposition increases the concentration of monomers, molecules that act as building blocks for nanoparticle growth.

Nucleation occurs when the monomer concentration exceeds the supersaturation limit within the solvent. The free monomers join the nuclei, growing into larger nanoparticles and reducing concentration of free monomers. Nucleation of new particles ceases when the free monomer concentration drops below supersaturation.

From this point, the growth stage begins, where the remaining dissolved free monomers join the nuclei and are eventually exhausted.

When the nucleation stage is kept short (burst nucleation), the particles nucleate and grow at the same time resulting in a narrow size distribution. If nucleation continues for a long period, polydisperse particles may be expected. Hence, in a typical synthesis run a slow heating rate and adequate mixing is recommended.

During the growth stage, the smaller particles grow at a much faster rate than larger ones, i.e. the growth rate is non-linear. This is known as the “size focusing” effect (Peng, et al., 1998) which, assuming the continued availability of monomers, leads to a narrower size distribution as the particles

that nucleated later catch up to the earlier ones. Extending the growth stage can lead to the dissolution of the smaller particles leading to an increase in the average particle size (Ostwald ripening).

2.1.2 Comparison of iron source

A commonly cited work for this method is by Yu et al (Yu, et al., 2004), who synthesised highly monodisperse iron oxide nanoparticles by thermal decomposition of iron carboxylate salts. It was adapted from Yu and Peng's earlier work (Yu & Peng, 2002) detailing the use of a noncoordinating solvent (octadecene) for the synthesis of semiconductor nanoparticles, whereas earlier works typically used coordinating solvents. The use of the term "noncoordinating" in this case refers to the fact that the solvent of choice is not thought to influence the reaction or growth process significantly, and because the solvent mainly acts as a medium for mass and heat transfer, the concentrations of the reagents in the mixture can be freely changed (Yu & Peng, 2002).

Yu et al (Yu, et al., 2004) prepared a mixture of FeO(OH), oleic acid and 1-octadecene, which was then heated to 320^{o}C and held for varying periods of time. The FeO(OH) dissolved while heating, forming an intermediate compound which was determined (via FTIR) to be iron oleate. Further heating of this solution caused thermal decomposition of the iron oleate resulting in a clear black solution of iron oxide nanoparticles. The average particle size could be tuned from 7 – 28 nm by adjusting the oleic acid concentration. The size distribution varied between 5 – 10%. Although the reactions were carried out in an argon atmosphere, the presence of oxygen did not appear to have much of an effect on nanoparticle size and quality (size homogeneity, crystallinity, and magnetic properties).

The use of FeO(OH) as the iron source has also been documented by others (Chen, et al., 2014) (Song, et al., 2013) (Dreyer, et al., 2016) (Augustyn, et al., 2014) (Chalasani & Vasudevan, 2011) (Si, et al., 2008). Other iron sources such as iron pentacarbonyl (Woo, et al., 2004) (Park, et al., 2005) (Pei, et al., 2005) (Teng & Yang, 2004) (Hyeon, et al., 2001), iron (III) acetylacetonate (Sun & Zeng, 2002) (Hyeon, et al., 2001) (Calero-DdelC, et al., 2010), iron acetate (Augustyn, et al., 2014), ferrocene (Bhalerao, et al., 2009), in both coordinating and noncoordinating solvents, have also been reported.

There are a few issues with the use of these iron sources for synthesis. Some of these materials are sensitive to oxygen and require the mixture to be prepared in an inert atmosphere. Iron pentacarbonyl in particular is highly toxic. While the use of FeO(OH) is safe, some authors have reported issues with it. For example, Augustyn et al (Augustyn, et al., 2014) reported that the FeO(OH) did not completely dissolve when heated, that the synthesis had poor yield (<60%), and the samples showed settling with

time. Similar observations were made in our work with the repeatability of the synthesis when using FeO(OH) or $Fe(OH)_3$ (see Section 3.4.5).

When heated up in the presence of oleic acid, these compounds dissolve to form iron oleate as an intermediate compound anyway, so the use of iron oleate as a stable initial iron source is logical. When synthesised separately using lighter solvents, iron oleate is non-toxic, directly soluble in octadecene, and stable at room temperature for several months.

2.1.3 Synthesis

The process can be divided into two major steps:

1. Synthesis of a stable iron oleate complex
2. Thermal decomposition of the iron oleate

Several authors (Yu, et al., 2004) (Chen, et al., 2014) (Chen, 2014) (Park, et al., 2004) (Park, et al., 2005) (Kim, et al., 2011) (Bronstein, et al., 2011) (Hyeon, et al., 2001) (Chiu, et al., 2007) have reported the use of iron oleate for the synthesis of monodisperse iron oxide nanoparticles. The most commonly used surfactants in these works is oleic acid, which controls monodispersity and growth rate, resulting in spherical nanoparticles when properly controlled (Lassenberger, et al., 2017). Cubical nanoparticles can be grown with the addition of sodium oleate (Wetterskog, et al., 2014) (Bronstein, et al., 2011). Other shapes have been reported with the use of various solvent and surfactant combinations (Bronstein, et al., 2011) (AbuTalib, et al., 2021). The scope of this thesis largely limited to spherical and cubical nanoparticles.

Tests by Park et al (Park, et al., 2004) show that the minimum temperature required to form monodisperse, highly crystalline nanoparticles is 260 °C, although an aging period of 3 days was required. At 240 °C, three days of aging produced polydisperse particles, while at 200 °C, no particles were formed even after three days. At a higher temperature of 320 °C, as low as 10 minutes of aging was required to produce monodisperse 12nm particles. Interestingly, at an even higher temperature of 380 °C, 20nm iron oxide nanocubes were formed.

Chen (Chen, 2012) explored the effects of various parameters on particle formation. The refluxing temperature and oleic acid to iron oleate ratio were found to have the largest effects on the particle size, whereas the refluxing period had a very minor effect on the particle size. The heating rate affected the size distribution of the particles, and rates higher than 20 °C/min appeared to inhibit particle growth.

Wetterskog et al (Wetterskog, et al., 2014) synthesised spherical and cubical iron oxide nanoparticles using different combinations of oleic acid and sodium oleate as surfactants. The presence of any amount of sodium oleate led to cubical nanoparticles, with increasing sodium oleate concentrations leading to cubes with increasingly sharper edges. The use of sodium oleate to produce cubical nanoparticles was also studied by Kovalenko et al (Kovalenko, et al., 2007) and Bronstein et al (Bronstein, et al., 2011), among others.

Xu et al (Xu, et al., 2010) skipped the iron oleate synthesis step and heated up a mixture of iron (III) chloride, sodium oleate, oleic acid and octadecene to 317 °C to produce cubical nanoparticles.

A few other possible shapes are also found in the literature. Bronstein et al (Bronstein, et al., 2011) synthesised iron oxide nanoparticles from different iron carboxylate sources, including iron oleate, iron palmitate and iron myristate complexes, showing the formation of spheres, stars and cubes under different experimental parameters. Kovelenko et al (Kovalenko, et al., 2007) produced bipyramids using potassium oleate as a surfactant. Palchoudhury et al (Palchoudhury, et al., 2012) described the synthesis of iron oxide nanoplates and nanoflowers by heating up the iron oleate in the presence of TOPO (TriOctylPhosphine Oxide) and oleic acid. Xu et al (Xu, et al., 2010) varied the ratio of the cobalt (II) chloride and iron (III) chloride used as precursors to obtain triangular and polyhedral cobalt ferrite and cobalt oxide particles.

Recent work by Lassenberger et al (Lassenberger, et al., 2017) uses in-situ X-ray scattering to study the formation of iron oxide nanoparticles by thermal decomposition of $Fe(CO)_5$ in the presence of oleic acid, using dioctyl ether as the solvent. The iron pentacarbonyl decomposes and forms iron oleate as in intermediate compound, which then also decomposes at higher temperatures. They break down the nucleation stage into roughly three stages: formation of polyiron oxo cluster between ~220 – 240 °C, a heat-up lag phase between ~240 – 290 °C, and burst nucleation at 290 °C. These clusters are known to be the true precursors to the iron oxide nanoparticles, but their exact nature is still a matter of debate.

TEM imaging of these clusters has proven to be difficult as they tend to be smaller than 1 nm in size, however, work by Kim et al (Kim, et al., 2013) worked out a relationship between the particle size distribution and data from MALDI-TOF (Matrix-Assisted Laser Desorption/Ionization – Time of Flight) mass spectrometry results that accurately matches results obtained after TEM-based size analysis.

Branched iron oxide nanoparticles have also been synthesised by the decomposition of iron acetylacetonate using oleylamine and oleic acid as surfactants (AbuTalib, et al., 2021).

2.1.4 Iron oleate synthesis

A few different (but similar) routes have been described to synthesise the iron oleate (FeOL) precursor. Iron oleate is an organometallic complex with one iron ion with two or three oleate ligands attached to it. It is a stable precursor typically used in thermal decomposition synthesis as a source of iron.

The most commonly used method is the **two-phase synthesis** (Bear, et al., 2014) (Ding, et al., 2014) (Armijo, et al., 2012) (Bronstein, et al., 2011) (Patsula, et al., 2014) (Bau, et al., 2014) (Wetterskog, et al., 2014) (Chen, 2012) (Park, et al., 2004) (Chiu, et al., 2007). Ferric chloride and sodium/potassium oleate are dissolved in a 7:4:3 mixture of hexane, ethanol and water, and refluxed at 70^{o}C for four hours. The resultant iron oleate remains in the organic layer on top and the bottom water layer is discarded. The product is then washed with distilled water to remove the dissolved salts and unused reactants. The hexane is then evaporated in air or vacuum to yield iron oleate in the form of a waxy solid. Bear et al (Bear, et al., 2014) report a yield of ~70% using the above method.

Bronstein et al (Bronstein, et al., 2007) studied the Fe-Oleate synthesis method described above, reported the effect of drying temperature on the final product. Using FTIR analysis, they propose that Fe-Oleate dried at 30^{o}C still has some water attached, which was removed when dried at 70^{o}C. Some ethanol is also believed to be attached, which could be removed by washing with ethanol and acetone. It was found that excessive washing reduced the temperature difference between nucleation and growth, resulting in polydisperse particles.

Another route is described by Ding et al (Ding, et al., 2014), who refluxed a solution of sodium oleate and $FeCl_3.6H_2O$ in methanol for 3 hours. This formed a yellow brown rubbery solid, which was then washed several times with methanol to remove NaCl to obtain the iron oleate complex. This product was compared to the usual two-phase iron oleate synthesis method, which is typically a waxy solid. FTIR analysis showed free oleic acid in the iron oleate synthesised by the two-phase method. It also determined that the iron oleate made using this method had bidentate coordination as the dominating coordination mode, while the iron oleate produced with the two-phase method had both bidentate and bridging coordination modes. The decomposition of this precursor resulted in nanoplates rather than the usual spheres, at temperatures as low as 170^{o}C, with sizes increasing with temperature.

A third method is reported by Kovalenko et al (Kovalenko, et al., 2007). This method requires no heating (except for the drying stage) and is by far the quickest. $FeCl_3$ and NaOH solutions of equal molarity were prepared separately in methanol. Oleic acid was added to the $FeCl_3$ solution. The NaOH solution was slowly added, dropwise, under constant stirring, resulting in the formation of a gelatinous brown precipitate. The precipitate was washed with methanol, diluted in hexane, washed with warm

deionised water and then separated and dried resulting in a waxy product (dry iron oleate) with approximately 80% yield.

All of the above methods use iron (III) chloride as the iron source, however the use of other iron sources is also possible. For example, Chen et al (Chen, et al., 2009) synthesised iron oleate by heating up porous hematite powder in oleic acid at 290 °C for 4 hours.

2.1.5 Effect of experimental parameters on particle morphology

Surfactant concentration

The surfactant(s) used in the synthesis, as well as their concentrations effect the size and shape of the nanoparticles. When only oleic acid is used, particles typically grow into spheres. The oleic acid to iron oleate molar ratio has a significant positive effect on the particle size, when all other parameters are kept constant. Both Wetterskog et al (Wetterskog, et al., 2014) and Chen (Chen, 2012) report increasing particle sizes with an increasing oleic acid to iron oleate ratio. Chen also report an upper limit of 10 for the ratio, above which no particles were found.

With the addition of sodium oleate, the particles grow into nanocubes, with increasing concentrations leading to cubes with increasingly sharper edges. (Wetterskog, et al., 2014) (Kovalenko, et al., 2007).

Temperature

The nanoparticle growth has been shown to be affected by both the aging/growth temperature and heating rate.

The particle size has been shown to increase with an increase in aging temperature by several authors. Figure 2.2 shows this size dependence demonstrated in chosen publications (Chen, 2012) (Chen, et al., 2009) (Kovalenko, et al., 2007) (Park, et al., 2004) (Wetterskog, et al., 2014). All of these data points are taken from synthesis runs where:

- Only oleic acid was used as the surfactant (spherical nanoparticles).
- The refluxing temperature is determined by the choice of solvent (i.e. different non-coordinating solvents are used).
- The solutions were constantly stirred.

However, the collection of studies shown in Figure 2.2 does not consider differences in aging time, which also has an effect on the particle size and size distribution.

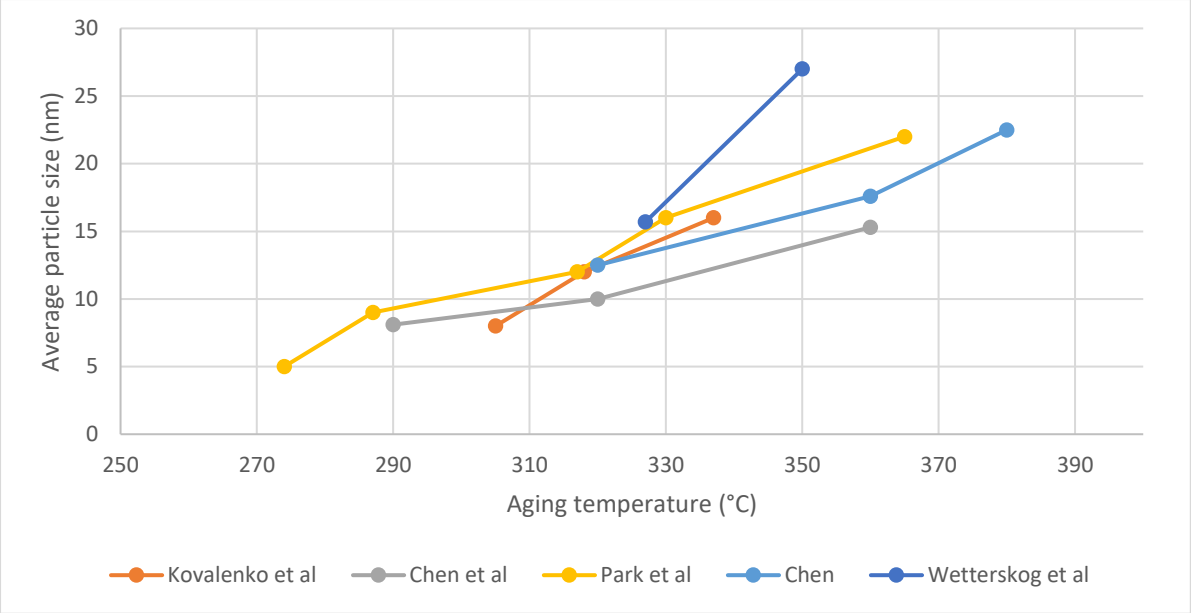


Figure 2.2: Aging temperature vs average particle size reported by various authors. The chosen data represents spherical nanoparticles produced by the thermal decomposition of iron oleate in the presence of oleic acid with the solution under constant stirring. (Chen, 2012) (Chen, et al., 2009) (Kovalenko, et al., 2007) (Park, et al., 2004) (Wetterskog, et al., 2014).

From graph in Figure 2.2, the average particle size ranges from 5 to 30 nm, when the aging temperature is varied between 270 °C to 380 °C. Smaller sizes were achieved at lower temperatures by Kim et al (Kim, et al., 2011) with a modification to the procedure. Oleyl alcohol was added to the reaction mixture which was thought to act as a reductant for the iron oleate, thus lowering its decomposition temperature. Particles in the 1.5 – 3.75 nm range were created by keeping the aging temperature lower, between 200 °C to 280 °C. In a typical synthesis run using iron oleate, this is considered to be the nucleation temperature range and little growth is seen below 270 °C.

The sizes of nanocubes produced by the addition of sodium oleate also showed a similar size increase with an increase in temperature but with an increased minimum growth temperature (Kovalenko, et al., 2007).

While these results show that the particle size generally increases with temperature, it is important to remember that the actual decomposition temperature of the iron oleate complex may vary based on the synthesis route chosen. For example, DSC traces of the iron oleate synthesised by Ding et al (Ding, et al., 2014) showed a final decomposition temperature of 380 °C, while Park et al's iron oleate (Park, et al., 2004) showed a single sharp dip at 320 °C. Bronstein et al's study (Bronstein, et al., 2007) showed the final decomposition temperature varying between 330 °C to 380 °C depending on the washing and drying parameters used when synthesising the iron oleate.

The heating rate in general is known to affect the size distribution of the particles, presumably due to temperature gradients, mass transfer, removal of volatiles, and decomposition kinetics. Most authors kept the heating rate below 3.3 °C/min. Chen (Chen, 2012) found that particles synthesised using a heating rate of 10 °C/min to be polydisperse. At 20 °C/min, no particles could be found. However, Lynch et al (Lynch, et al., 2011) found that monodisperse particles could be produced using a high heating rate of up to 25 °C/min if the iron oleate is treated (exposure to vacuum, and then aging in a dessicator) before use.

Boiling and bubbling

Lynch et al (Lynch, et al., 2011) performed synthesis runs with non-boiling solvents, argon bubbling, and under reduced pressure. At all temperatures, they found that the particles produced in non-boiling solvents were much larger, polydisperse, and had irregular polyhedral shapes. Results from runs with non-boiling solvents but with artificial argon bubbling were very similar to those from boiling solvents, suggesting the effect of the solvent composition on the particle formation was minimal.

Particles synthesised by Wetterskog et al (Wetterskog, et al., 2014) at 327 °C under constant stirring had an average size of 15.7 ± 1.7 nm. However, they also performed another synthesis run at 325 °C with argon bubbling, which resulted in particles with an average size of 5.3 ± 0.4 nm, which appears to contradict Lynch et al's results. However, they used a much lower heating rate of 3 °C/min.

Lassenberger et al (Lassenberger, et al., 2017) compared the effects of three different heating rates on the particle size distribution. They found that the 3 K/min was the optimal heating rate, as both the slow (1K/min) and faster (9 K/min) led to increased polydispersity.

2.2 Thermal decomposition synthesis of cadmium selenide quantum dots

Monodisperse CdX (where X is a chalgocen, typically Sulphur, Selenium or Tellurium) quantum dots have been synthesised based on work by Murray et al (Murray, et al., 1993). In fact, the iron oleate synthesis route was an adaptation of this work. The synthesis follows a similar route. In this case a mixture of organic cadmium compound and a chalcogen source is heated to high temperatures (~240 °C). For this study we are limited to the use of cadmium oleate and a selenium compound. While Murray et al used dimethyl cadmium, Yu and Peng (Yu & Peng, 2002) first used cadmium oxide to replace the much more dangerous dimethyl cadmium that was previously used in hot injection CdSe nanocrystal synthesis.

Hot injection is a common synthesis approach for CdSe nanoparticles, in which the selenium precursor solution is injected when the cadmium precursor solution reaches the nucleation temperature. This causes a burst of nucleation as well as a reduction in temperature. At this lower temperature, further nucleation is inhibited while growth can continue, resulting in monodisperse nanocrystals. However, heat-up methods, in which both precursors are premixed and heated up, have found similar success. Since we aim to perform this synthesis in microfluidics, we again limit our scope to "heat-up" or "one pot" methods.

Earlier, and indeed most current CdSe synthesis routes involve the use of trioctylphosphine (TOP) or tridecylphosphonic acid (TDPA), tributylphosphine (TBP) and other phosphine compounds, which are very expensive and are either already hazardous/toxic/corrosive or have the potential to form such compounds when reacted with. These are used as they readily dissolve elemental selenium to form a homogenous selenium stock solution for use in quantum dot synthesis, in addition to acting a ligand for the particles grown. In order to address these shortcomings, several authors have explored alternate phosphine-free routes to synthesise CdSe quantum dots.

Jasieniak et al (Jasieniak, et al., 2005) reported the use of elemental selenium dissolved in octadecene by heating at 200 °C under nitrogen for 2 hours. They found that this approach resulted in a lower nucleation, resulting in lower particle concentration. Nevertheless, high quality particles were still obtained. Bullen et al studied this precursor solution in greater detail and found that overheating it may cause a reduction in efficacy (Bullen, et al., 2010).

Deng et al (Deng, et al., 2005) produced CdSe nanoparticles using paraffin wax as the solvent. They proposed that the particles were formed by the reaction of H2Se gas generated in the solution with the cadmium oleate at 217 °C. To support this, they conducted a separate experiment where they produced H2Se gas by heating up selenium in paraffin wax to 300 °C, which was then directed to flow through a cadmium oleate solution, which resulted in the growth of CdSe nanoparticles.

Qu et al (Qu, et al., 2004) performed in-situ absorbance measurements during CdSe nanocrystal synthesis using a dip probe, and shows the quick growth in the first few seconds following injection of the Se solution.

2.2.1 Clusters

CdSe magic sized clusters (MSCs) are known to undergo sequential growth in discrete steps, instead of the continuous growth seen in the larger quantum dots (Kudera, et al., 2007). This gives rise to sharp absorption peaks which appear to move from ~300 nm to 450 nm as the solution is heated.

However, due to the discrete MSC sizes, as the solution is heated the peaks on the blue side fall in intensity while the peaks on the red side increase. This continues until ~440-450 nm above which continuous growth of quantum dots is seen. Hence, there is a good chance of small sized CdSe quantum dot samples containing MSCs (Li, et al., 2019). One way to differentiate between CdSe clusters and quantum dots is by comparing the absorbance and fluorescence curves. CdSe clusters absorb <450 nm with discrete peaks but have a broad emission spectrum between 400 – 700 nm, hence appearing to glow white. CdSe quantum dots, however, have an absorption spectrum that closely follows the narrow fluorescence peak, including a band edge peak with a stokes shift of 20-60 nm. Common CdSe clusters reported in literature have absorbance peaks at 335 nm, 350-360 nm, 381-384 nm, 391 nm, 406 nm, 415-418 nm, 431-437 nm, 450-455 nm, and 467 nm (Kudera, et al., 2007) (Li, et al., 2019) (Hsieh, et al., 2018).

CdS clusters (and even quantum dots) have also been made at low temperatures including room temperature (Li, et al., 2020) (Siy, et al., 2011). Zhang et al (Zhang, et al., 2018) proposed a framework of possible pathways between the formation of CdS precursors, immediate precursors, clusters, fragments, and quantum dots.

Kudera et al heated the reaction mixture at 80°C for over 40 hours, resulting in the formation of clusters in the solution. Up until 25 hours, only clusters were found in the solution, and finally at ~42 hours, small CdSe quantum dots were found. The absorbance spectra recorded are shown in **Error! Reference source not found.**. Similar behaviour is reported in earlier work by Platschek et al (Ptatschek, et al., 1998).

2.2.2 Purification

Hassinen et al (Hassinen, et al., 2012) showed that methanol as a non-solvent to precipitate the particles resulted in ligand loss and lowered quantum yields. These problems were avoided by using acetonitrile instead. Similarly, Shakeri and Meulenberg (Shakeri & Meulenberg, 2015) recommend using ethanol as the nonsolvent over methanol. Both studies reported that using methanol resulted in increasingly worse results with repeated purification steps. Purification of colloidal nanocrystal products is an area of active research (Shen, et al., 2017) (Shakeri & Meulenberg, 2015). Rosson et al (Rosson, et al., 2012) treated CdSe nanocrystal solutions with various carboxylic acids and found that treatment with formic acid resulted in a significant increase (up to 45%) in quantum yield.

Dhaene et al (Dhaene, et al., 2019) conducted a study on the polymerisation of 1-octadecene. Upon heating the solvent to temperatures between 120 °C and 320 °C (common temperature range for

thermal decomposition nanoparticle synthesis), the found that octadecene did indeed polymerise to a significant degree at higher temperatures. While the degree of conversion increased with increasing temperature, the molecular weight of the polymer product was found to be inversely related to temperature. Polymerised ODE was also concluded to be found in the purified nanocrystal product. To overcome this issue they proposed two solutions: (1) to use a saturated solvent, such as n-hexadecane, and (2) exchange the original oleate ligands on the nanocrystals with a more polar ligand (in this case, they used (6-[2-[2-(2-Methoxy-ethoxy)-ethoxy]-ethoxy]hexyl) phosphonic acid). The use of n-hexadecane did not have a noticeable effect on the synthesis of $CuInS_2$, CdS, and TiO_2. Fe_3O_4 synthesis was also successfully conducted in n-octadecane. However, ZnS:Mn nanocrystal synthesis in resulted in polydisperse particles, since octadecene acts to reduce sulfur in the reaction. CdS nanoparticles produced in octadecene could be purified to a higher degree by ligand exchange. Due to the presence of oleylamine on the surface of ZnS:Mn/ZnS core/shell nanocrystals, the ligand exchange process is not as straightforward, but still results in particles that precipitate easily by the addition of hexane.

2.3 Microfluidic synthesis

This section looks at microfluidic nanoparticle synthesis in the literature, particularly iron oxide and semiconductor nanoparticles. A small section is also dedicated to the coprecipitation synthesis in microfluidic devices as it is one of the most common methods used to produce iron oxide nanoparticles.

2.3.1 Microfluidic device fabrication

Our application has two major requirements from the material used to fabricate the device. The first requirement is that the material must not absorb or be dissolved by the solvent being used (octadecene). The second requirement is that the material must be optically clear at the wavelength of the laser being used. Other factors such as cost and ease of fabrication are also important.

Glass and silica were the materials used for some of the first microfluidic devices (Kangning, et al., 2013). Both materials fulfil the solvent resistance requirement, however silica is opaque in the visible spectrum. Fabrication of channel features in a glass device typically requires the use of hydrofluoric acid, which is extremely hazardous.

In recent years, PDMS (poly dimethyl siloxane) has emerged as the most common choice of material for aqueous microfluidics. However, octadecene, like many organic solvents (Lee, et al., 2003), has

been shown to swell and dissolve PDMS (Harley, 2011), even at room temperature. Fluoropolymers like PTFE offer better solvent resistance, but can be quite expensive and, more importantly, most are not optically clear. Bonding of fluoropolymers can also be complicated due to their inert nature.

Acrylic plastic (PMMA) offers decent solvent resistance, and a tolerably high melting point (170 °C), in addition to being inexpensive and easily obtained, making it suitable for quick prototyping. Thanks to the localised heating in our application, the use of acrylic can be considered. Common fabrication methods for acrylic devices include micromachining, laser etching, hot embossing, and injection molding. Bonding the separate layers can be done via thermal, solvent-assisted and adhesive bonding or laser/ultrasonic welding (Tsao & DeVoe, 2009).

Zhu et al (Zhu, et al., 2007) conducted a study on the thermal bonding parameters for PMMA. Higher temperatures and pressures did result in higher bond strengths but also increased the likelihood of feature deformation. They recommended a bonding temperature between 91-95 °C and a bonding pressure lower than 2.5 MPa for optimum results.

2.3.2 Coprecipitation

Salazar-Alvarez et al (Salazar-Alvarez, et al., 2006) synthesised iron oxide nanoparticles with sizes ranging between 2 and 7nm in a flow injection setup. A Fe^{3+}/Fe^{2+} solution was mixed with NaOH at 80 °C. Nanoparticles with an average diameter of 5nm were formed. The chemical parameters (concentrations of iron and NaOH solutions) were found to have a bigger effect on the final product than the physical parameters (flow rates, injection schemes).

Abou Hassan et al (Abou Hassan, et al., 2008) prepared iron oxide nanoparticles in a millifluidic mixer device using the coprecipitation method. An excess of TMAOH (Tetraethylammonium Hydroxide) was used to enhance dispersion and avoid the adsorption of the formed nanoparticles on the channel walls. The average particle size was 7nm. The nanoparticles formed by their method showed lower magnetisation than in nanoparticles formed in large scale. One of the reasons may be the shape (the TEM image shows elongated non-spherical particles). Abou Hassan et al (Abou Hassan, et al., 2012) also synthesised Cobalt Ferrite nanoparticles in a setup using a similar mixer followed by aging in a tube through a hot water bath. The nanoparticles formed had an average size of 6.67 nm after 16 minutes of aging in the microfluidic setup, compared to 12.11 nm after 2 hours in bulk synthesis and 16.18 nm after 50 minutes in a hydrothermal bomb.

Erdem et al (Erdem, et al., 2011) synthesised iron oxide nanoparticles with an average diameter of 5nm in a droplet-based microreactor. The device was made using laser printed polyurethane. The advantage of using this material is that there is no adsorption of materials, as is the case with PDMS.

Frenz et al (Frenz, et al., 2008) demonstrated a droplet based microreactor by synthesising iron oxide nanoparticles with an average diameter of 4±1 nm (compared to 9±3 nm for bulk synthesis). An interesting feature of this system is the electrically controlled mixing of two adjacent droplets. Two droplets (one droplet is NaOH and the other droplet is a stoichiometric solution of Fe(II)/Fe(III)) travelling together in an oil medium undergo coalescence when passing between two electrodes, starting the coprecipitation reaction and forming nanoparticles inside the new combined droplet.

Lee et al fabricated a peristaltic micromixer for controlled mixing of the reagent solutions. By adjusting the ratios of the 2 M $FeCl_2$, 1 M $FeCl_3$, and 5 M NaOH solutions, they were able to produce nanoparticles with sizes of 5.24 ± 0.85 nm (2:8:20), 6.69 ± 1.15 nm (5:5:23), and 4.83 ± 1.20 nm (8:2:25). The total synthesis time varied between 15 to 18 minutes depending on the total volume.

Kumar et al (Kumar, et al., 2012) synthesised dextran-coated iron oxide nanoparticles in a droplet reactor. An aqueous ammonia solution was combined with a mixture of $FeCl_2$, $FeCl_3$, and dextran in a glass capillary under flowing octadecene. This resulted in aqueous droplets, within which the coprecipitation reaction occurs, in an organic stream of octadecene. This two-phase stream was flowed through a 4 m long PTFE tubing at 1.7 cm/s, with the tubing being submerged in an oil bath at 60 °C. In a single-phase flow, particle deposits were found on the channel walls. The mean particle size was found to be 3.6 ± 0.8 nm.

2.3.3 Thermal Decomposition

A major challenge with achieving thermal decomposition synthesis in microfluidics is the fact that most polymers, including PDMS, are not suitable for use with the high boiling solvents used in this process. Additionally, most polymers cannot survive the high temperatures required.

Edel et al (Edel, et al., 2003) synthesised CdSe nanoparticles by thermal decomposition in a glass microfluidic device at high temperatures, ranging between 180^o and 240^{o}C. Although particle sizes were not given, spectroscopic measurements were given that indirectly hint at the production of “reasonably homogenous” CdSe particles when heated to 240^{o}C.

Yen et al (Yen, et al., 2005) synthesised CdSe nanoparticles in a microreactor with single-phase and gas-segmented flow at 260 °C. The products from the gas-segmented syntheses showed significant improvements in both yield and size distribution. Krishnadasan et al (Krishnadasan, et al., 2010)

describe the automation of quantum dot nanoparticle synthesis in a microfluidic device, with the aims of minimizing the drift in particle properties over time by adjusting the temperature and flow rate based on feedback from the in-line measurement of the emission spectra. Moghaddam et al (Moghaddam, et al., 2013) studied the effects of temperature, residence time, and flow rate, on the continuous synthesis of CdSe nanoparticles in a heated steel coil.

Some early work on microfluidic synthesis was done by Shestopalov et al (Shestopalov, et al., 2004) where CdS and CdS/CdSe nanoparticles were synthesised in an aqueous droplet based reactor. Most of the work focused on microreactor design and operation, and the particles produced were not analysed in detail as they used an aqueous approach that was known to produce amorphous particles.

Chan et al (Chan, et al., 2003) were one of the first to report droplet-based microfluidic synthesis of CdSe via high temperature thermal decomposition. They were able to produce particles with fluorescence peaks tunable between ~525 - 545 nm. However, the stability of the droplets depended on the surface coating applied to the microchannel walls, which was rendered unusable after ~5 hours of heating.

Nakamura et al (Nakamura, et al., 2004) from the Maeda group synthesised CdSe nanoparticles in a capillary submerged in an oil bath at varying temperatures (210 – 330 °C), and by adjusting the residence time, were able to tune fluorescence peak location between ~475 to 620 nm, with FWHM ranging from 40 – 80 nm. The group later also studied the synthesis of CdSe magic sized particles/clusters/seeds by ageing the solution at various temperatures, and its effect on synthesising larger nanoparticles using the same reactor setup (Wang, et al., 2004). They reported no growth of larger particles after 2 weeks of aging at 96 °C, but did find growth after 22 hours at 150 °C. Using a pre-seeded solution for nanoparticle synthesis increased the yield of the final product from 6% to 31%. The group has also published work detailing the coating of the synthesised CdSe nanoparticles with ZnS, again in a microfluidic capillary reactor (Wang, et al., 2004) (Wang, et al., 2005).

Luan et al (Luan, et al., 2007) synthesized CdSe nanoparticles in a PTFE tube passed through a tubular furnace. With the residence time fixed at 10s at 275 °C, they were able to produce particles which fluoresced between ~540 – 610 nm, when increasing Se:Cd ratios from 1 to 5. In a later article (Luan, et al., 2008), they used a capillary in an oil bath to coat these particles with a ZnS shell. They were able to coat the particles at relatively low temperatures (10 s at 120 °C), resulting in an increase of the quantum yield from 22% to 70%.

Nightingale et al (Nightingale, et al., 2011) generated droplets of the reaction mixture in a carrier fluid (PFPE), pumped through a PTFE tube immersed in an oil bath set to various temperatures. This is

similar to Chan et al's earlier work, except the heating is conducted in a PFTE tube instead of a microfluidic chip. They were able to obtain particles which fluoresced between ~510 – 570 nm by changing the temperature and/or residence times, however, changing the Cd:Se ratio did not have much of an effect on the peak location. They would later scale up the production (Nightingale, et al., 2013) by using multiple braided tubes in parallel, and were able to produce 54.4 g of CdTe in 9 hours.

Tian et al (Tian, et al., 2016) synthesised CdSe nanoparticles in a PTFE capillary reactor in an oil bath. They used a mixture of dodecyl amine and oleylamine as ligands. Since dodecyl amine has a lower boiling point (259 °C) than oleylamine (349 °C), it was theorised to vaporise above 250 °C once it has helped coordinate with nuclei, resulting in a more effective separation of the nucleation and growth stages. Tian et al (Tian, et al., 2018) also studied the effect of separating the nucleation stage at different temperatures (210 and 270 °C) while the growth stage was kept constant at 240 °C. They found that monodispersity was better when nucleated at 210 °C, due to monomer availability. It may be important to note that this set of experiments included n-hexylphosphonic acid to promote the growth of branched nanoparticles.

Wang et al (Wang, et al., 2017) synthesised CdSe nanoparticles in a PTFE capillary passed through a tubular furnace. The flow rate was fixed at 0.6 mL/min while the temperature was varied (150, 200, 250, 300 °C), resulting in particles that fluoresced at 533, 585, 642, and 653 nm respectively. The particles formed were not spherical, nonetheless they did show a very narrow size distribution and FWHM of the fluorescence peak. The quantum yield was not reported, although from the picture provided it appeared low except for the first sample (533 nm).

Richard et al (Richard, et al., 2020) synthesised HgS, CdS, and HgCdS particles via an aqueous route in a droplet based microfluidic reactor with a helical mixer. Although the reaction does take place at room temperature, increasing the temperature to 80 °C resulted in a decrease in the average particle size. The effects of other parameters were also tested.

Cheng et al (Cheng, et al., 2020) synthesised CdSe and CdSe/ZnS core/shell nanoparticles in a ferruginous (the exact material was not specified) microfluidic capillary that was heating using an induction coil (magnetothermal heating). By adjusting the power and flow rate, particles with fluorescence peaks between 490 – 625 nm could be produced.

Guidelli et al (Guidelli, et al., 2018) synthesised ZnSe nanoparticles in a stainless-steel tube wrapped around a heated cylinder. In this experiment, they heated the precursor solution (a mixture of zinc-stearate and selenium trioctylphosphine) at 160 °C for 40 min to cause nucleation. This was determined by measuring the absorbance of the solution at 300 nm. By adjusting the residence time

between 30 s – 10 min at growth temperature of 340 °C, particles fluorescing between ~375 – 415 nm could be produced.

Kwak et al (Kwak, et al., 2018) synthesised CdSe nanoparticles in a segmented flow droplet based capillary reactor where the precursor droplets were separated by N_2 gas. They reported 3 different products made with residence periods of 7 s, 15 s, and 30 s, which fluoresced at 510 nm, ~530 nm and 590 nm respectively.

Jeong et al (Jeong, et al., 2016) produced CdSe nanoparticles in a microfluidic reactor with separate pumps for the Cd and Se precursors. The Cd:Se ratio was adjusted by varying the flow rates of these individual pumps. The mixture then passed through a capillary in a furnace at different temperatures. At 220 °C and 240 °C, a 5:1 ratio of Cd:Se provided the highest quantum yield and a narrow fluorescence peak. At 260 °C, lower ratios provided higher quantum yield but their fluorescence peak varied with the ratio even when the flow rate was kept constant. The 5:1 ratio was chosen for further testing and could produce particles with fluorescence peaks at 546 nm (green), 578 nm (yellow), and 611 nm (red) by varying the flow rate.

Misuk et al (Misuk, et al., 2015) produced a seed solution by heating Cd and Se precursors separately to 300 °C, mixing them and passing them through a room temperature coil for quick cooling. This solution was then mixed with more Cd and Se precursors and flowed through a PTFE tube at 200 °C. Growth could occur at this temperature but not significant seed formation. The flow was segmented using PFPE as the continuous phase. From TEM images, the particles formed appeared to be more homogenous than those formed in bulk synthesis, however no optical characterisation (UV-VIS absorbance or photoluminescence) was presented.

Other examples of thermal decomposition synthesis of quantum dots are presented in a 2013 review by Krishna et al (Krishna, et al., 2013). In general, the quantum dot products show a decent amount of size tunability by adjusting the temperature and residence periods.

The examples above for the synthesis of CdSe quantum dots are presented due to the similarity of the process to the thermal decomposition of iron oleate. Factors affecting nucleation, mixing, and growth of the particles are likely to be similar in both processes. However, the decomposition temperatures used for CdSe nanoparticles is typically lower than 270 °C, while iron oleate decomposition temperatures typically start above 320 °C.

Kumar (Kumar, 2013) synthesised iron oxide nanoparticles by thermal decomposition in a droplet-based reactor. The reaction mixture, consisting of iron acetylacetonate and oleylamine in benzyl ether, was added to a stream of octadecene, forming droplets within a PTFE tube. The droplets then flowed

at different flow rates through a 4 m section of the tube immersed in silicone oil set to different temperatures. At temperatures of 175 °C, 200 °C, 220 °C, and 240 °C, particles had an average size of 1.5 nm, ~1.8 nm, ~2.7 nm, and 3 nm, respectively. At 240 °C, varying the residence time from 2 minutes to 60 minutes resulted in particle sizes increasing from ~2.5 nm to 3.8 nm.

Ren et al (Ren, et al., 2014) designed a ceramic microreactor from inorganic polymers for high temperature and pressure applications and present the only report so far of thermal decomposition of iron oleate in a microfluidic device. The device has a channel length of 10 cm, and the flow rate was adjusted to attain the required residence period. The device was made from PVSZ (polyvinylsilazane) using a polystyrene template. This was then heated to 500 °C, resulting in a yellowish transparent solvent-resistant ceramic material. The encased polystyrene template was completely decomposed at this temperature. A solution of iron oleate, oleic acid, and octadecene was flowed through the device at 320 °C for varying residence periods. At the residence periods of 12 min, 24 min, and 48 minutes, particles sizes of 5 ± 1 nm, 10 ± 2 nm, and 20 ± 2 nm were found. Rod shaped particles were produced with the addition of oleyl amine.

2.4 Laser synthesis

2.4.1 Laser synthesis in solid media

Laude's group (Baufay, et al., 1982) has synthesised semiconductor thin films by applying laser radiation to layers of elemental thin films deposited on a substrate.

Limosani et al (Limosani, et al., 2020) synthesised CdSe quantum dots by laser patterning of a single source precursor (2-(*N,N*-dimethylamino)ethylselenolate of cadmium) dispersed in a PMMA film. A 355 nm pulsed laser (10 ns, 40 kHz, beam diameter: 30 µm, power: 0.3 W) was used. The precursor was prepared according to a method described by Kedarnath et al (Kedarnath, et al., 2006), which may be considered as a candidate for future work with microfluidic laser synthesis of CdSe nanocrystals.

2.4.2 Laser synthesis in aerosol streams

Marcu et al (Marcu, et al., 2013) synthesised iron oxide nanoparticles using a focused CO_2 laser with an incident power of 250 W/cm^2. A mixture of $Fe(CO)_5$ vapour and ethylene gas (which absorbs the laser energy) was flowed across the laser beam. The pyrolisis of the iron pentacarbonyl resulted in mixed phase iron oxide nanoparticles of sizes between 8 to 10 nm.

Grimes et al (Grimes, et al., 2000) used a similar setup, with the addition of ammonia, to produce iron carbide and iron nitride particles (depending on pressure) nanoparticles with averages sizes varying between 19.15 to 35 nm, achieved using different parameters. Gavrila-Florescu et al (Gavrila-Florescu, et al., 2017) prepared particles with an iron-based core and ZnO shell using the same method. Similar experiments and a more detailed review of this method are also presented by Malumbres et al (Malumbres, et al., 2013).

2.4.3 Laser synthesis in liquid media

Laser Ablation in Liquids

Laser synthesis in liquids is a field that has garnered significant attention in recent years. An extensive recent review by Zhang et al (Zhang, et al., 2017) covers a wide range of laser synthesis methods and results. Continuous laser ablation synthesis is currently limited to second scale processing due to boiling of the solvent, and thus, the vast majority of the literature on laser-induced nanoparticle synthesis in liquid media is based on Pulsed Laser Ablation in Liquid (**LAL** or **PLAL**). In this process, a solid metal source is placed in a liquid and heated with a pulsed laser, which results in ablation of the surface, resulting in pure (depending on the liquid) metal nanoparticles.

Hasna et al (Hasna, et al., 2013) synthesised erbium doped hydroxyapatite nanoparticles by ablation in water using a 355 nm laser with an intensity of 3.9 J/cm^2. Zamiri et al (Zamiri, et al., 2013) produced silver nanoparticles in a starch solution using a 60 mJ, 532 nm pulsed laser at different repetition rates, and found the average particle size to increase with an increased repetition rate. In all cases, however, the particles had wide size distributions.

Henley et al (Henley, et al., 2009) used commercially obtained iron powder (<60 µm) as the metal source. A thin layer of the powder was made in a vessel filled with different solvents (water, ethanol, methanol, isopropanol, and acetone). UV (248 nm) and green (532 nm) lasers were used. The laser was scanned across the powder every 15 seconds, using 120 mJ pulses at a repetition rate of 20 Hz. Using the UV laser, spherical nanoparticles (~50 nm) were produced in water, whereas nanoribbons and nanowires were found in the methanol sample. Using the green laser, only spherical nanoparticles were found in methanol regardless of the annealing time, while smaller and smaller nanowires were found when the UV laser time was increased. The increased surface area of the powder, compared to a solid iron target, was thought to increase the decomposition of not only the powder, but the methanol as well (providing oxygen and hydroxide ions to the reaction).

Luo et al (Luo, et al., 2018) synthesised iron oxide nanoparticles via laser ablation of a fast-rotating iron rod (7500 rpm) within a glass tube with flowing water. A 1064 nm laser was used with a 5 ns pulse duration at pulse energy of 360 mJ. Particle sizes could be tuned from 15.4 ± 1.1 nm to 20.3 ± 0.2 nm by adjusting the flow rate from 0.1 mL/min to 1 mL/min (derived from XRD data). Confined experiments were also conducted, with no flow. The rotational speed was instead varied. A steady decrease in particle size from ~25.7 nm to 14.2 nm was seen when the rotational speed was increased from 3000 to 7200 rpm. However, the size saw a sudden increase to 19.1 nm at 8000 rpm. The particles formed were a mixture of spheres and hexagonal platelets.

Ruth and Young (Ruth & Young, 2006) produced CdSe and CdTe nanoparticles by ablation of the bulk material in different solvents. A Nd:YAG laser pulsed at 50 Hz with a pulse duration of 600 ns and energy ranging 1-7 mJ was used. Additional irradiation of the particle suspensions resulted in a change in colour, corresponding to a change in average particle size. It was found that depending on the material and laser parameters, the irradiation could cause the particle size to decrease or increase. In any case, photoluminescence, which would be expected from CdSe/CdTe particles in this size range, was not observed.

Horoz et al (Horoz, et al., 2012) synthesised CdSe nanoparticle by nanosecond pulsed laser ablation of a CdSe target in deionised water. An Nd:YAG laser (266 nm) with 10 ns pulses and a repetition rate of 10 Hz was focused on the target immersed in water in a quartz bowl for several hours. The estimated laser fluence was 1 J cm^{-1}. The particles formed had a mean diameter of 5.1 nm, and had a peak emission wavelength of 553 nm, and suspension in water was apparently stable in water up to 2 weeks.

A pico-second pulsed laser was used to produce nanocrystals from a suspension of CdSe powder by Zholudov et al (Zholudov, et al., 2015). A Yb:YAG (1030 nm) laser with a beam diameter of 6nm, pulse energy of up to 250 µJ at 10 kHz. The suspension was irradiated in a quartz cuvette under both magnetic stirring and manual agitation using a pipette. These measures were taken to avoid overheating the same spot and remove ablated particles from the heated area. In addition, the laser beam was also continuous moved using a galvanometric scanner to keep it from hitting cavitation bubbles. The surfaces of the particles were coated with different surfactants and re-dispersed in different solvents. Particles formed were in order of 1.5 – 2 nm and exhibited fluorescence peaks between 564 – 610 nm. These peaks were quite broad with FWHM of the fluorescence intensities being on the order of ~200 nm. The measured quantum yield was also quite low at ~2%.

Laser Reaction in Liquid

There are also a few examples of laser-induced decomposition of liquid precursors in the literature. This is commonly known as a Laser Reaction in Liquid (**LRL**) process.

Tangeysh et al (Tangeysh, et al., 2013) synthesised gold nanoparticles by decomposition of an aqueous $[AuCl_4]^-$ solution via femtosecond laser. A 790 nm laser with 35 fs pulses was focused down to a 20 µm spot, where the total pulse energy was set to 2.5 mJ (~200 J/cm^2). The beam was spatially dispersed using gratings and then refocused at the focal point within a cuvette. This spread out the beam energy and helped reduce heating of the cuvette and solvent except at the focal point. The solution was irradiated for various periods of time between 1 to 20 minutes. Samples showed large, irregular and highly polydisperse spherical and pyramidal particles. With the addition of PEG (polyethylene glycol) as a surfactant, spherical particles between 4 to 12 nm (depending on PEG concentration) particles were found.

The closest example to the work presented in this thesis is by Robinson et al (Robinson, et al., 2009), who synthesised cobalt nanoparticles by the thermal decomposition of a solution of cobalt carbonyl, oleic acid and TOPO (trioctylphosphine oxide) in 1,2-dichlorobenzene (DCB). A 266nm pulsed laser with a beam width of 5 mm and a pulse energy of 15 mJ was used to irradiate the reaction mixture for 30 minutes under stirring. Both the DCB and cobalt carbonyl showed absorbance peaks at this wavelength, which is why it was chosen. Oleic acid concentrations of 0.04 M and 0.02 M were used. The particles in these solutions were found to have an average size of 2.8 ± 0.5 nm and 3.6 ± 0.6 nm respectively.

Another similar work is reported by Okamoto et al (Okamoto, et al., 2018), where iron oxide nanoparticles were produced by femtosecond and nanosecond laser pulsed irradiation of a ferrocene solution in hexane. The femtosecond laser used a wavelength of 800 nm, pulse duration of 40 fs, pulse energy of 0.4 mJ, repeating at a rate of 1 kHz. The corresponding settings for the nanosecond laser were 355 nm, 8 ns, 45 mJ, and 10 Hz. The solution was irradiated in a quartz cuvette in ambient conditions. The femtosecond batch saw an increase in size from ~16 nm to ~33.3 ± 17.8 nm when increasing the irradiation time from 10 minutes to 30 minutes, but further increases up to 120 minutes did not have a significant effect. For the nanosecond batch, a similar increase in size from ~16 nm to ~25 nm was seen going from 10 minutes to 30 minutes. A small increase to ~30 nm was seen when the irradiation period was increased to 90 minutes. At 120 minutes, a large increase to ~47.2 ± 27.7 nm was seen.

Lin et al (Lin, et al., 2005) produced CdSe and CdSe/CdS (core/shell) quantum dots using a photoassisted synthesis method. A solution of cadmium nitrate and 1,1,-dimethylselenourua in water was used as the precursor solution. A sodium citrate solution was used as the surfactant, after adjusting its pH to 9 using NaOH. The mixture was heated at temperatures varying from 80-140 °C, under N_2 flow and constant stirring. Laser irradiation was provided using an Nd:YAG (532 nm) laser at 50 mW, 3000 Hz, as well as diode pumped solid state lasers (532 nm) at 15, 50, and 100 mW. The laser beam was focused on to a 2 cm spot in the centre of the flasks. However, the quantum yield did show significant improvements with increasing laser power. The highest quantum yield achieved was 0.044% for CdSe particles, 2.4% for core-shell CdSe/CdS particles, and 82% for core-shell CdSe-CdS particles after 24 hours of UV irradiation under a 100 W Xe-Hg lamp. The large spot size indicates that that laser does not contribute much to the heating of the material, and their results reflect as much, as varying the laser power did not have much of an effect on the particle size.

2.4.4 Energy absorbed by the solution

The Beer-Lambert law (Swinehart, 1962) defines the attenuation of light by the medium it is travelling through. For solutions, it relates the absorbance of the sample with its concentration and optical depth. When a light ray of incident energy I_0 travels through a liquid with absorbance A, the intensity of the beam at a depth z can be given by the relation $I = I_0 10^{-Az}$.

The energy absorbed by the solution from a laser beam can be calculated using this relation. First, the absolute absorbance of the solution at the laser's wavelength must be measured, which can be done using most desktop spectrophotometers. Since these instruments are designed for chemical analysis, the absorbance is typically reported in 1/cm (the optical length of a typical cuvette). Care must be taken to ensure proper conversion of the units before further use.

3 Batch synthesis of iron oxide nanoparticles

Small variations within the synthesis methods and materials can affect the nanoparticle morphology. Even with similar conditions, works from different authors have resulted in different particle sizes (section 2.1.5). This makes it important to recreate the synthesis from the literature using our synthesised precursors, lab conditions, and instruments.

In this section, batch synthesis of iron oxide nanoparticles is performed using the thermal decomposition method. Two different iron sources and solvents have been used. The main aim is to determine the suitability of the reaction mixtures for microfluidic synthesis, and to compare the results with those found in the literature. Additionally, the use of olive oil as an alternate solvent/surfactant has also been investigated.

3.1 Experimental setup

All bulk experiments were performed using the setup shown in Figure 3.1. A 500 mL three necked round flask was set up in a heating mantle. A condenser was attached to the central neck, and a thermocouple and a long needle were inserted through each of the side necks. The thermocouple is connected to a PID temperature controller. The top of the condenser was attached to a valve connected to a vacuum pump and a purified N_2 supply.

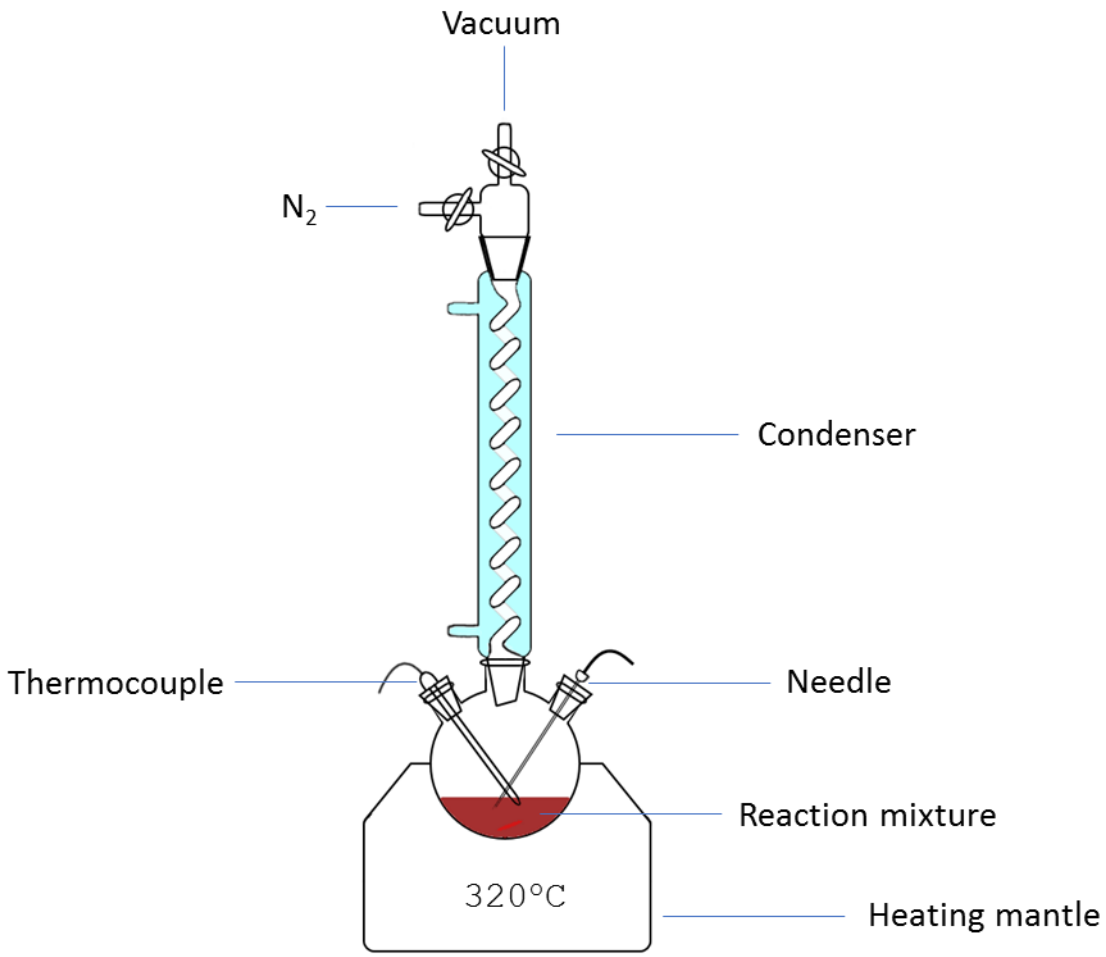


Figure 3.1: Diagram showing the experimental setup used for batch synthesis of iron oxide nanoparticles.

3.2 Precursor synthesis

This section details the synthesis of the precursors, the iron compounds used as iron sources for nanoparticle synthesis. The following reagents were purchased and used as-is unless otherwise noted:

1. $FeCl_3.6H_2O$ (Sigma-Aldrich)
2. NaOH (Fisher)
3. 1-Octadecene, >90% (Sigma-Aldrich)
4. Oleic Acid, technical grade (Sigma-Aldrich)
5. Methanol, 99% (Fisher)
6. Hexane, 99% (Fisher)

3.2.1 FeOOH Synthesis

FeOOH powder was prepared for use as an iron source. 0.61g of NaOH was dissolved in 8 mL deionised water. The solution was transferred to a centrifuge tube and 1.37g $FeCl_3.6H_2O$ was added, causing the precipitation of $Fe(OH)_3$.

The tube was centrifuged for 3 minutes at 7500 rpm and the supernatant was discarded. The precipitate was washed with fresh deionized water and centrifuged again. The washing step was repeated 5 times to remove water-soluble impurities.

The precipitate was then dried in a watch glass on a hotplate set to 75° for 6 hours, yielding dry iron oxyhydroxide (FeOOH) powder.

FTIR analysis of the powder (Figure 3.2) matched results from the literature (Silva, et al., 2006) (Rahimi, et al., 2014). The wide band between 3000 and 3500 cm^{-1} is typically associated with -OH group, while the 893 cm^{-1} and 798 cm^{-1} bands are typically found in goethite spectra. All vibrational features match those of goethite (α-FeO.OH) given by Silva et al (Silva, et al., 2006).

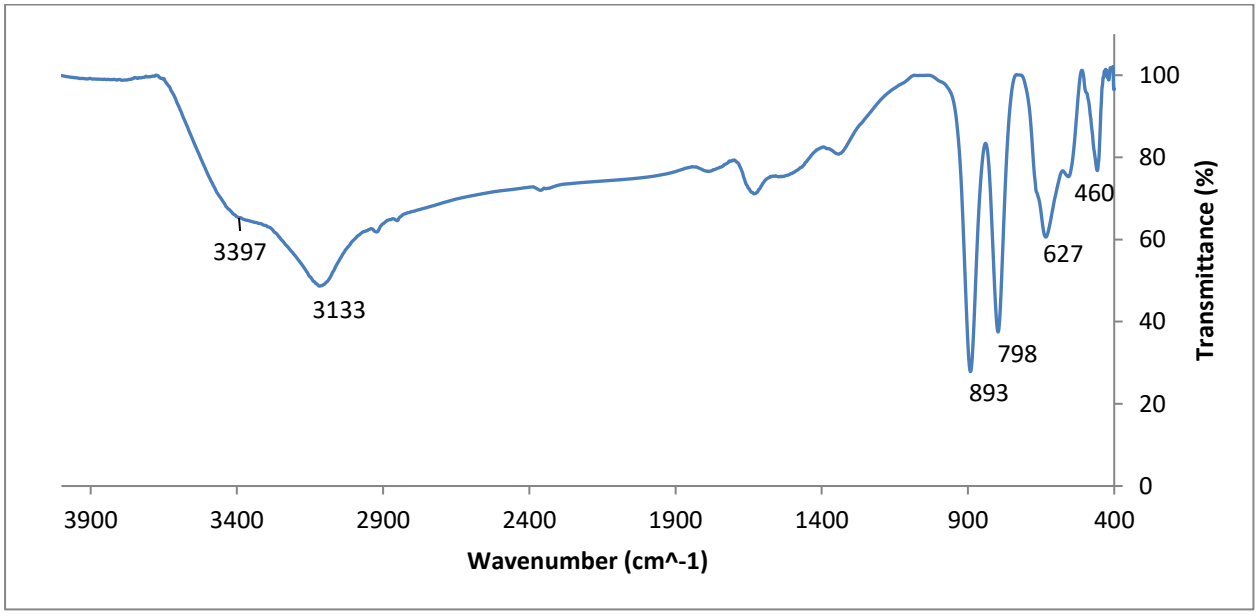


Figure 3.2: FTIR spectrum of the synthesised FeOOH powder

3.2.2 FeOl Synthesis

Iron oleate was synthesised using a procedure described by Kovalenko et al (Kovalenko, et al., 2007). All steps were performed at room temperature in ambient air.

69.37 mL of 0.4M $FeCl_3.6H_2O$ solution in methanol was prepared in a beaker and 26.28 g oleic acid was added to it. A magnetic stirrer bead was added to the solution and set to stir at 700 rpm.

208.1 mL of 0.4 M NaOH solution in methanol was prepared and poured into a separatory funnel set up above the first beaker. The stopcock was opened so that the NaOH solution was slowly added dropwise over a period of ~10 minutes.

As the NaOH solution was added, small brown droplets of iron oleate were formed which slowly precipitated if stirring was stopped. When all of the NaOH solution was added, the droplets merge to form a waxy brown precipitate (FeOl).

The supernatant was carefully decanted, and the precipitate was washed at least twice with fresh methanol to remove unreacted salts, fatty acid and byproducts. The precipitate was then dissolved in hexane and poured into a separatory funnel. Deionised water was added to the funnel and vigorously shaken. The water and hexane phases were allowed to separate, and the water was drained out. The water washing step was repeated at least 5 times.

The hexane solution was poured out into a petridish and evaporated on a hotplate at 70^{o}C until a thick paste was obtained. This was placed into a vacuum oven (Memmert) at dried at 70^{o}C at 50 mbar for at least 12 hours. A reddish brown waxy product was obtained (Figure 3.3).

FTIR analysis (Figure 3.4) of this product showed good agreement with literature (Bronstein, et al., 2007). A more detailed analysis of the FTIR results of this product and the other compounds used in the experiments is presented in section 6.4.3.



Figure 3.3: The synthesised FeOl after the final drying step.

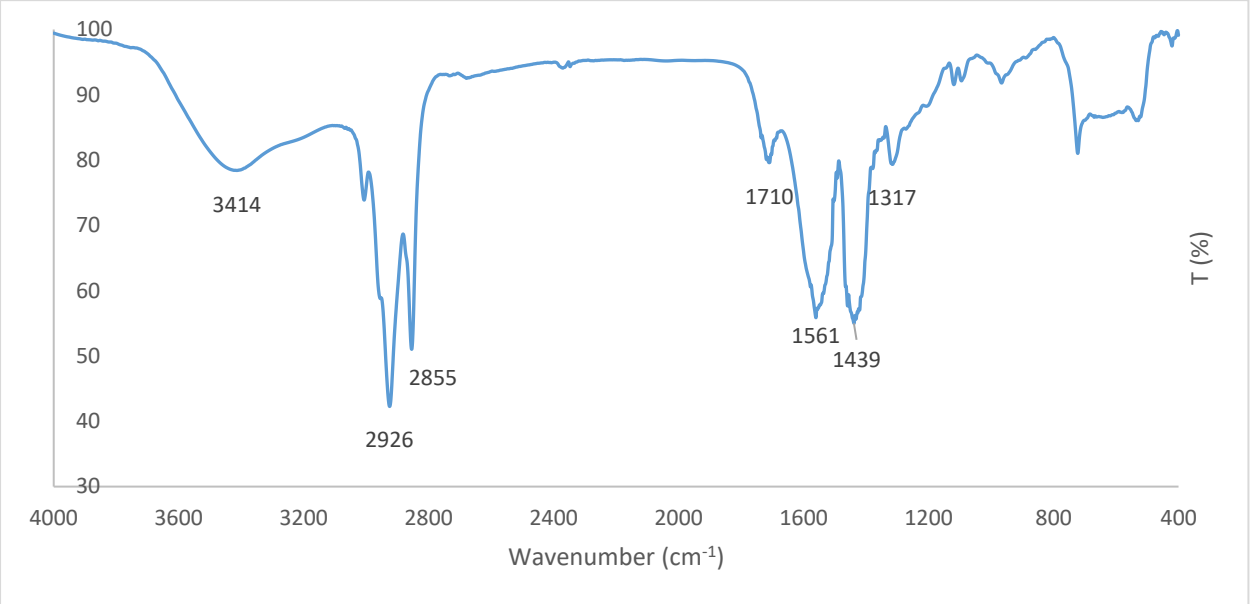


Figure 3.4: FTIR spectrum of the synthesised FeOl.

TGA and DSC analysis (Figure 3.5) was performed with the following parameters:

Temperature range : 30 °C to 550 °C

Heating rate : 20 °C/min

Atmosphere : N_2, 5 mL/min

As expected, the sample shows a large decrease in weight as soon as the temperature rises past 320°C as the oleate groups dissociate from the iron. Another major decrease can be seen starting from 390°C where the oleic acid starts to decompose. The final remaining mass at 550°C is ~25%.

The differential DSC curve (Figure 3.6) shows bands corresponding to the abovementioned events: decomposition of FeOl between 310°C to 330°C, dissociation and decomposition of oleic acid between 360°C to 450°C. There is however a band starting at 490°C which does not have a corresponding mass loss (and appears to continue beyond the scanning range). This band can be assigned to the phase change of Fe_3O_4 to Fe_2O_3.

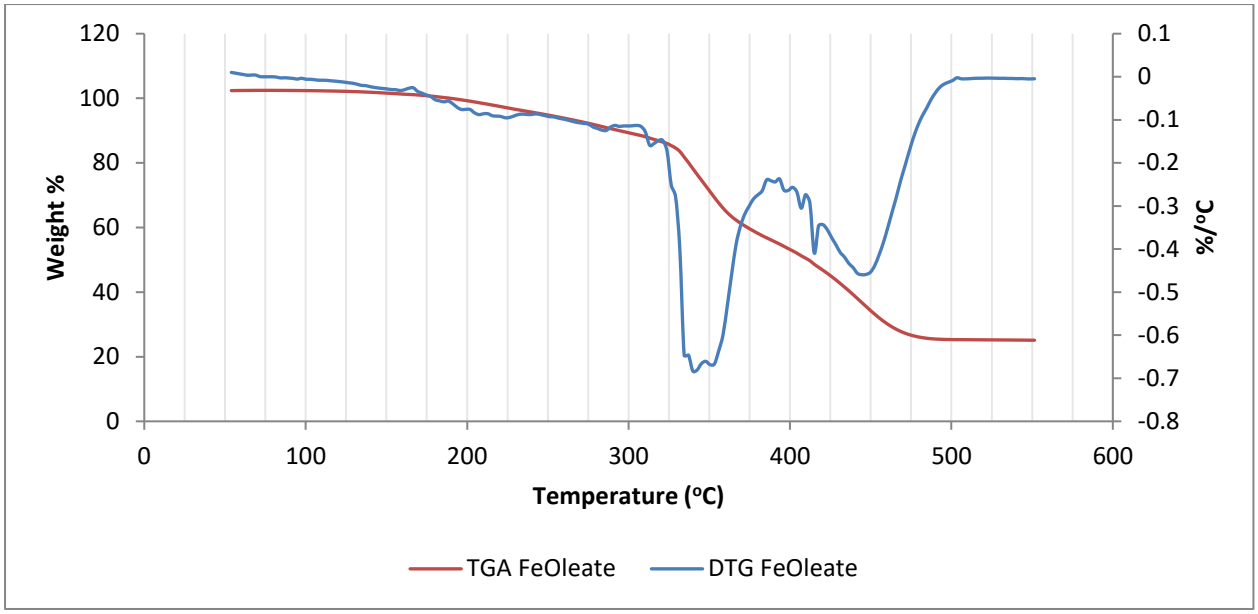


Figure 3.5: TGA/DTG curves for the synthesised FeOl. (Range: 30 – 550 °C, Rate: 2 °C/min, Atmosphere: N_2, 5 mL/min)

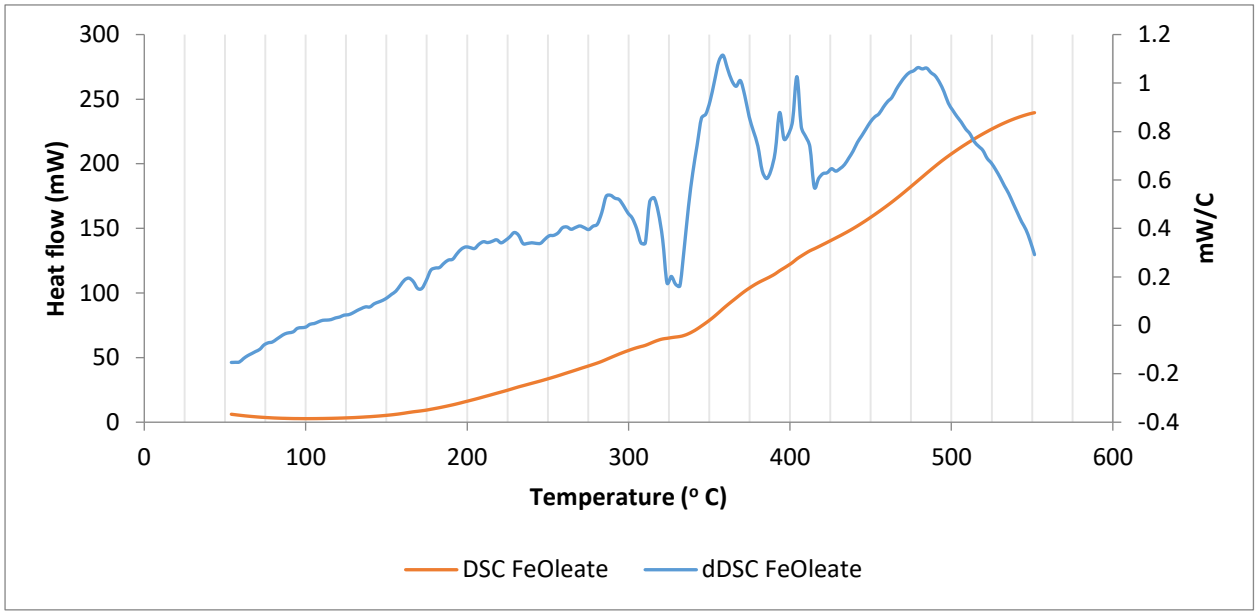


Figure 3.6: DSC curve for the synthesised FeOl and its first differential. (Range: 30 – 550 °C, Rate: 2 °C/min, Atmosphere: N_2, 5 mL/min)

3.3 Nanoparticle synthesis

3.3.1 Reaction mixtures

Two iron sources (FeOOH and FeOl) and two solvents (octadecene and olive oil) were used in our bulk synthesis tests, giving us a total of 4 combinations.

The list below shows the reaction mixtures prepared in each run:

1. **FeOOH in Octadecene:** 2g of FeOOH, 10.572g oleic acid (1:2 molar ratio of FeOOH:OA), and 12 mL octadecene.
2. **FeOOH in Olive Oil:** 1.94g FeOOH and 24 mL of extra virgin olive oil (Tesco).
3. **FeOl in Octadecene:** 0.5g FeOl, 0.3g oleic acid (1:2 molar ratio), and 15 mL octadecene.
4. **FeOl in Olive Oil:** 0.99g FeOl and 7g olive oil.

All reaction mixtures were degassed in the reaction vessel prior to heating. A vacuum pump was used to remove dissolved gases from the mixture, at room temperature and under magnetic stirring. The vacuum was applied until no more bubbles were observed, typically less than 10 – 15 minutes.

3.3.2 Heating conditions

For the synthesis runs using FeOOH (runs 1 and 2) as the iron source, the reactions were performed under ambient atmosphere, as according to Yu et al (Yu, et al., 2004), the was little difference in nanoparticle size and quality whether the synthesis was conducted under argon or air. When FeOl was used (runs 3 and 4), a constant flow of purified N_2 provided an inert gas blanket over the reaction.

After degassing, the temperature was increased to 320^o C over a period of 100 min and then kept constant for another 60 min. In the case of FeOl in Octadecene, the temperature was held at 220^{o}C for 30 min before proceeding. The heating mantle was then switched off and the solutions were allowed to cool down to room temperature before purification.

3.3.3 Purification

The purification process consists of:

1. Precipitation of the particles by the addition of acetone.
2. Removal of the solvent phase.
3. Redispersion of the particles in chloroform or hexane.

After step 1, the solvent phase consists of acetone, octadecene, excess oleic acid and reaction by-products. These are then removed in step 2 via careful decantation or pipetting. The precipitate now consists of nanoparticles but may still contain unwanted impurities. In step 3 the precipitate is redispersed in a small amount of hexane, and then steps 1-3 are repeated at least 3 times.

As the product gets cleaner in subsequent purification cycles, the solvent phase appears clearer. The precipitation step was accelerated by placing the sample near a strong neodymium magnet. The final product was then re-dispersed in hexane, except in the case of run 1 where chloroform was used.

For purification, we found that acetone as a precipitating solvent worked better than isopropanol or methanol, resulting in higher yield with a lower amount of solvent. The precipitant particles were found to be more soluble in hexane compared to chloroform.

3.4 Results

Magnetic nanoparticles were synthesised using all four reaction mixtures. Characterisation was done on the purified nanoparticle dispersion as follows:

SEM: The dispersion was dropped on to a piece of carbon tape on the SEM stub and allowed to dry.

STEM: The dispersion was dropped on to a 200-mesh formvar-carbon copper grid and covered with a petridish to slow down evaporation. This is done in order to create a single layer of nanoparticles.

FTIR: A few drops of the dispersion were dried on a glass slide, mixed with KCl and pressed into a tablet for FTIR analysis. FTIR spectra of iron oxides from the literature are presented in section 11.1.

3.4.1 FeOOH in octadecene

The particles from synthesis run 1 dispersed in chloroform showed more agglomeration than those from subsequent runs. Under SEM imaging, particles could be seen forming 100 – 200 nm sized agglomerates (Figure 3.7). Chloroform as a dispersing solvent was not suitable, despite several papers in literature doing so. Particles were seen to settle naturally after ~1-2 weeks. Another reason for the agglomeration is thought to the prolonged use of a magnet (up to 3 days) to precipitate the products. The particles were further diluted for STEM imaging. Although agglomerates were still found, the individual particles could be discerned. The largest particles had a diameter of ~29 nm, however very few of them were seen. The mean particle diameter was 11.2 nm with a standard deviation of 3.8 nm.

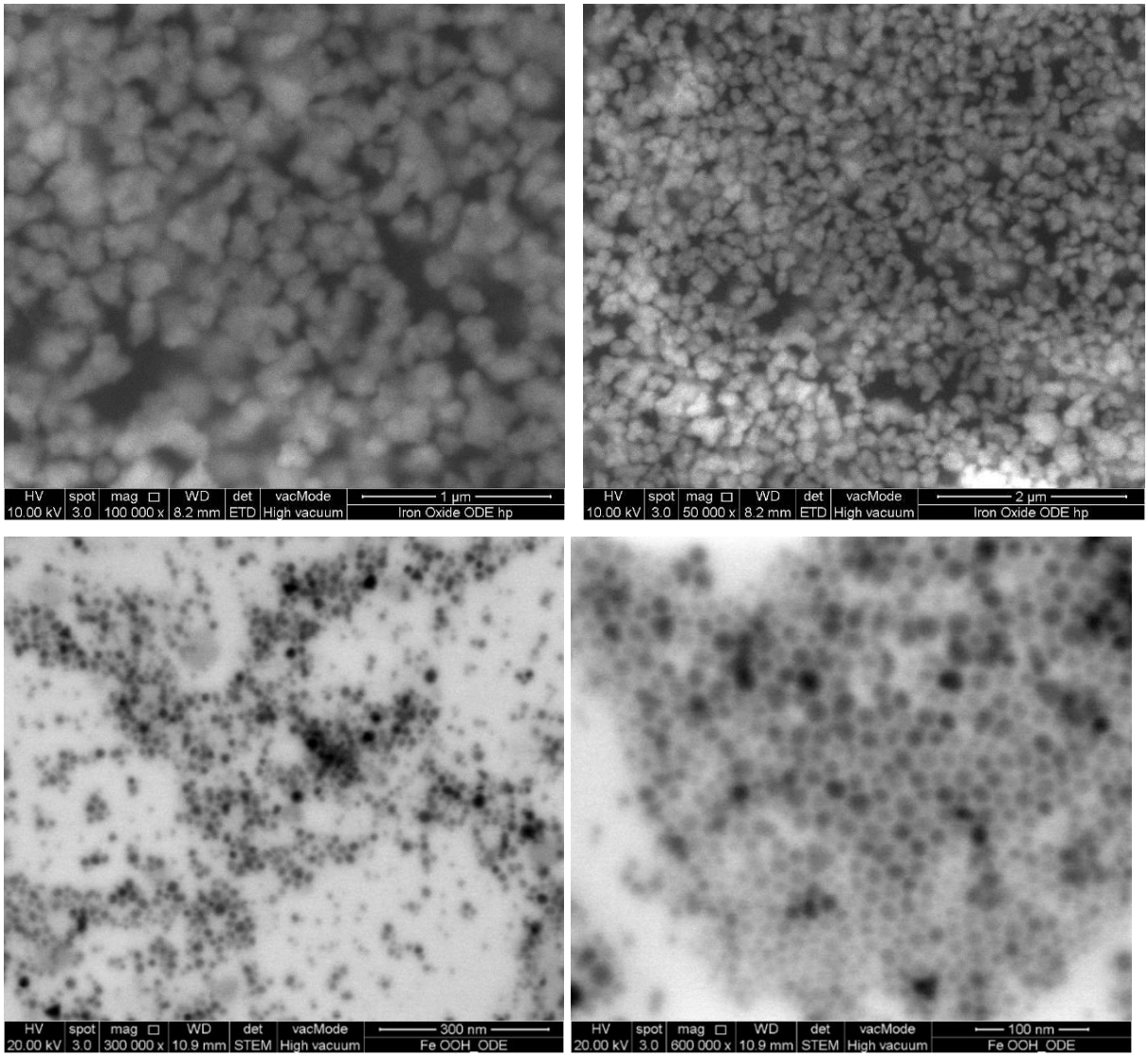


Figure 3.7: (top) SEM and (bottom) STEM imaging of iron oxide nanoparticles from run 1: FeOOH and oleic acid in octadecene.

3.4.2 FeOOH in olive oil

Particles formed in the second run showed little agglomeration. This improvement is attributed to two changes in the purification stage: use of hexane instead of chloroform, and limited exposure of the product to the magnet. After the addition of acetone, a magnet was kept beside the vial for ~1 minute to accelerate precipitation, after which it was removed. Under the SEM (Figure 3.8) particles were found to be uniformly spherical in shape, with sizes ranging between 10 to 40 nm. However, may more smaller particles can be seen using STEM imaging. While a few larger particles of ~46 nm were found, the mean diameter was 12.7 nm with a standard deviation of 7.3 nm.

The FTIR spectra of the nanoparticles is shown in Figure 3.9, showing a small amount of organic coating, evidenced by the weak peaks at 2923 cm^{-1} and 2853 cm^{-1} (CH_2 stretching). A very strong peak at 571 cm^{-1} points to the nanoparticles being magnetite.

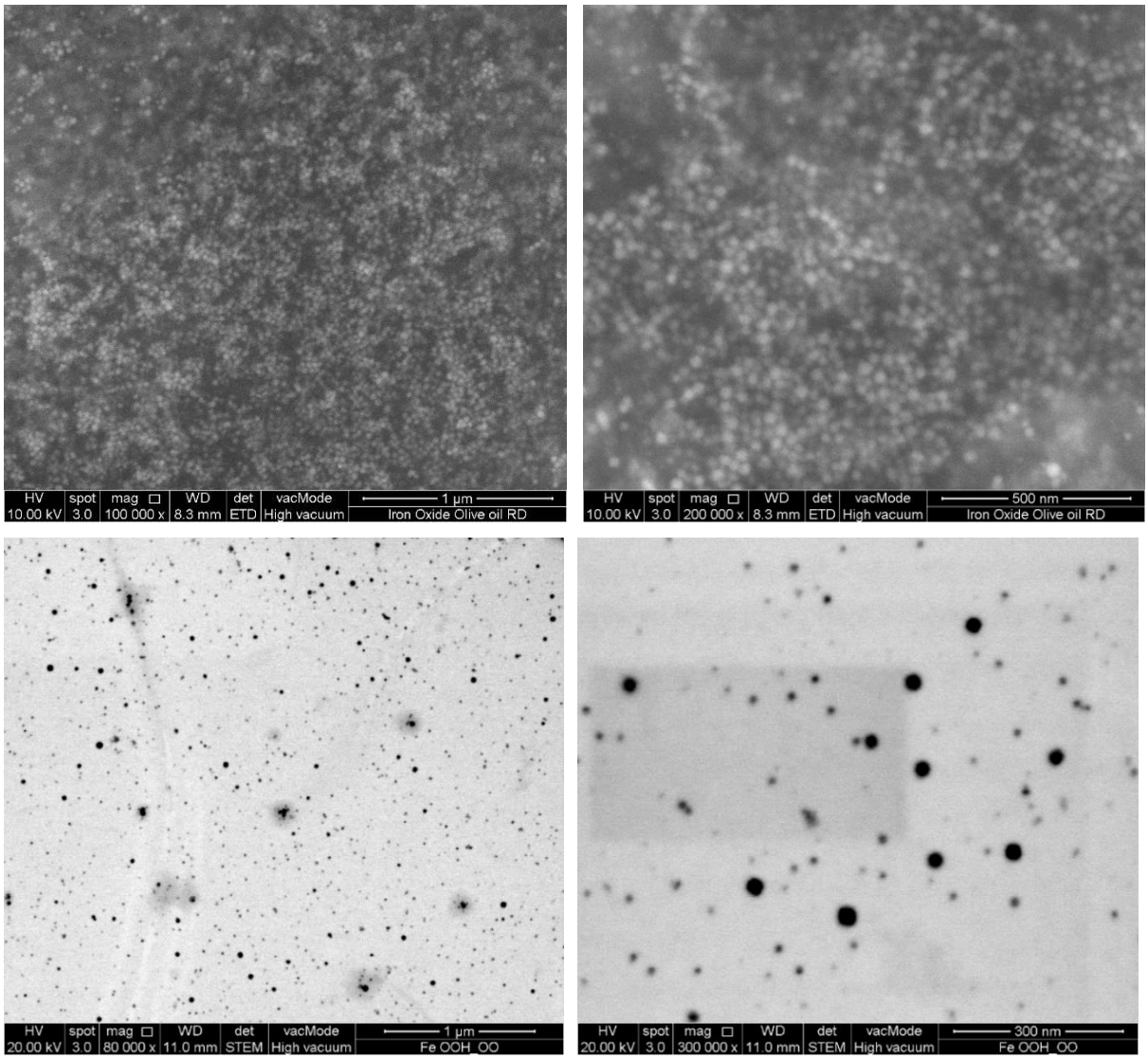


Figure 3.8: (top) SEM and (bottom) STEM imaging of iron oxide nanoparticle products from run 2: FeOOH in olive oil

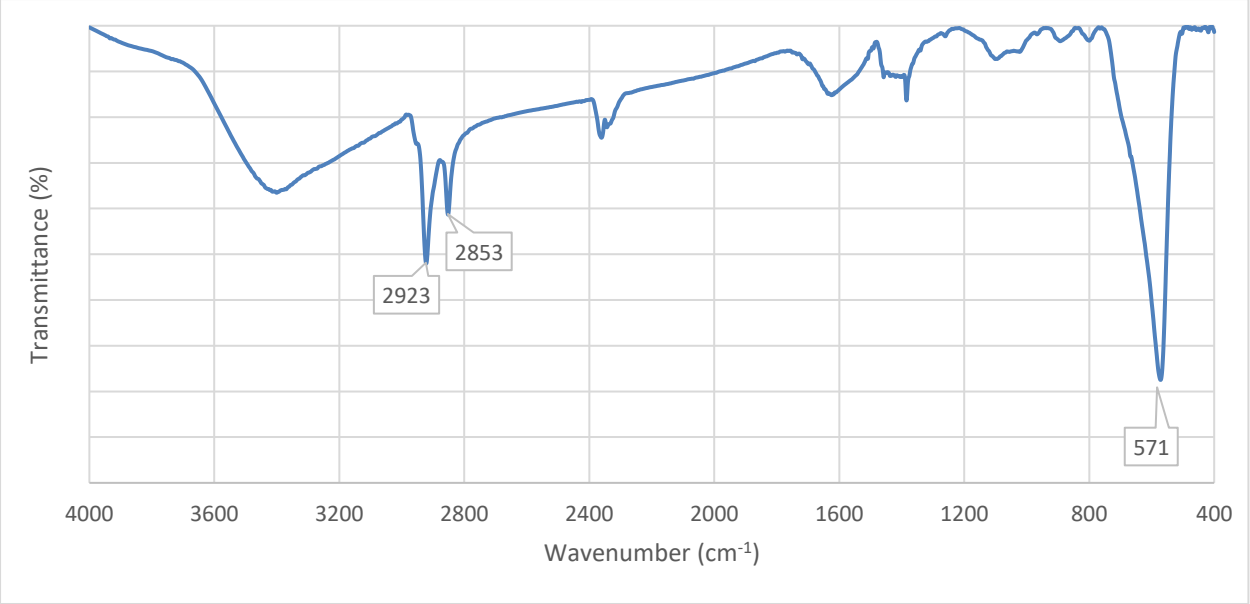


Figure 3.9: FTIR spectrum of the iron oxide nanoparticles synthesised from run 2 (FeOOH in olive oil).

3.4.3 FeOl in octadecene

The product from run 3 (FeOl and oleic acid in octadecene) yielded smaller but more uniform sized particles than all the other runs. SEM imaging shows a small amount of agglomeration (Figure 3.10), with the individual particles still visible. STEM imaging (Figure 3.10) shows individual particles more clearly. The mean particle size was determined to be 8.7 nm with a standard deviation of 2.3 nm, with a maximum observed size of 18.4 nm.

The FTIR spectrum of these nanoparticles (Figure 3.11) show a larger percentage of organic material compared to the results from run 2 (Figure 3.9). The peaks in the Fe-O region (400 cm^{-1} to 700 cm^{-1}) are closer to those of maghemite and hematite, suggesting oxidation of the particles. This is expected as the smaller size of the particles means the oleic acid coating them form a larger percentage of their weight. Their smaller size also makes them easier to oxidise.

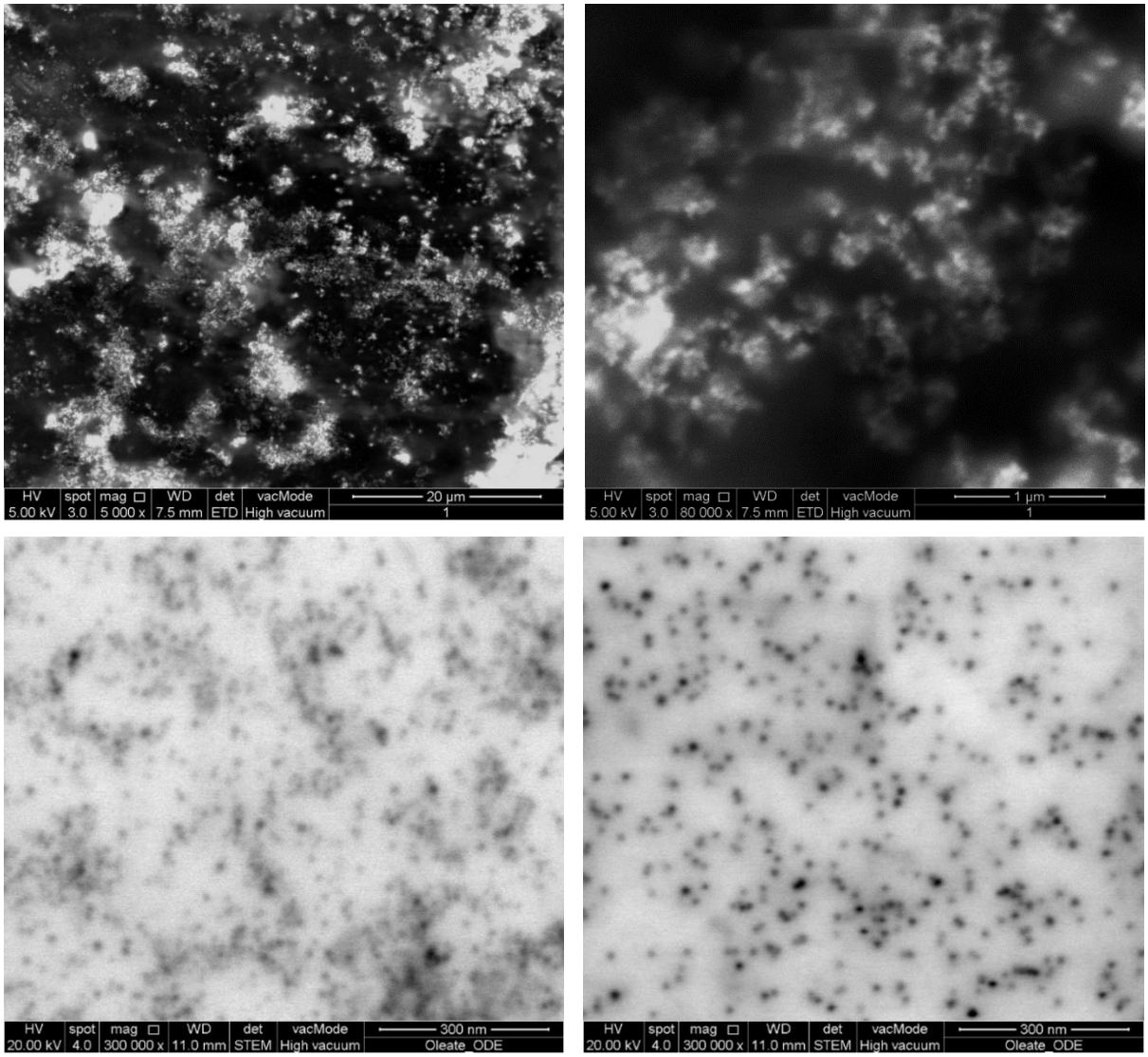


Figure 3.10: (top) SEM and (bottom) STEM imaging of iron oxide nanoparticles from run 3: FeOl and oleic acid in octadecene.

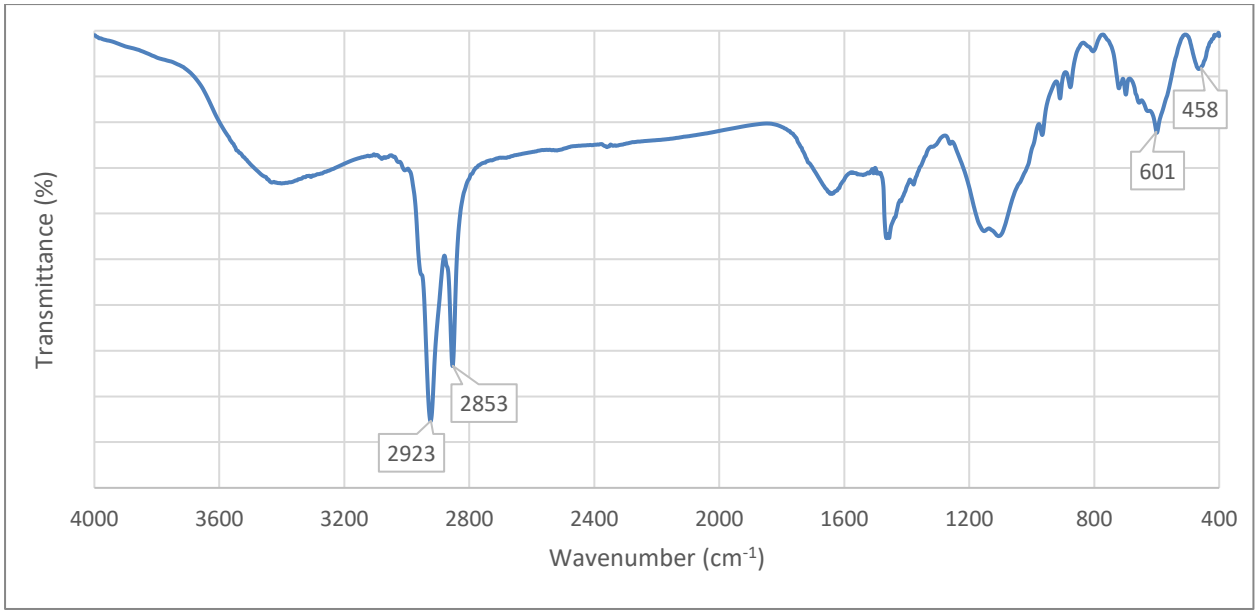


Figure 3.11: FTIR spectrum of the iron oxide nanoparticles synthesised from run 3 (FeOl in octadecene).

3.4.4 FeOl in olive oil

Magnetic particles were also found in the product from run 4 (FeOl in olive oil). The product in this case was highly polydisperse in both shape and size. Spherical, pyramidal and octahedral particles were found via SEM and STEM imaging of the product (Figure 3.12). A large amount of agglomeration was seen as well. No detailed size analysis was done for this sample, but the largest pyramidal particles were ~400 nm in size.

The SEM/STEM results are not surprising considering the difference between the reaction products from run 3 and 4. A significant amount of sedimentation can be seen in the reaction product from run 4 (Figure 3.13). During the purification step, non-magnetic solid by-products were also found, possibly a result of polymerisation of the fatty acids in the mixture. Only the nanomaterial still dissolved in the liquid was used for SEM analysis.

While the use of olive oil yielded good results with FeOOH, the lower density of FeOl required a much larger amount of olive oil to dissolve it, greatly decreasing the iron:surfactant ratio. This makes olive oil unsuitable as a solvent for FeOl decomposition.

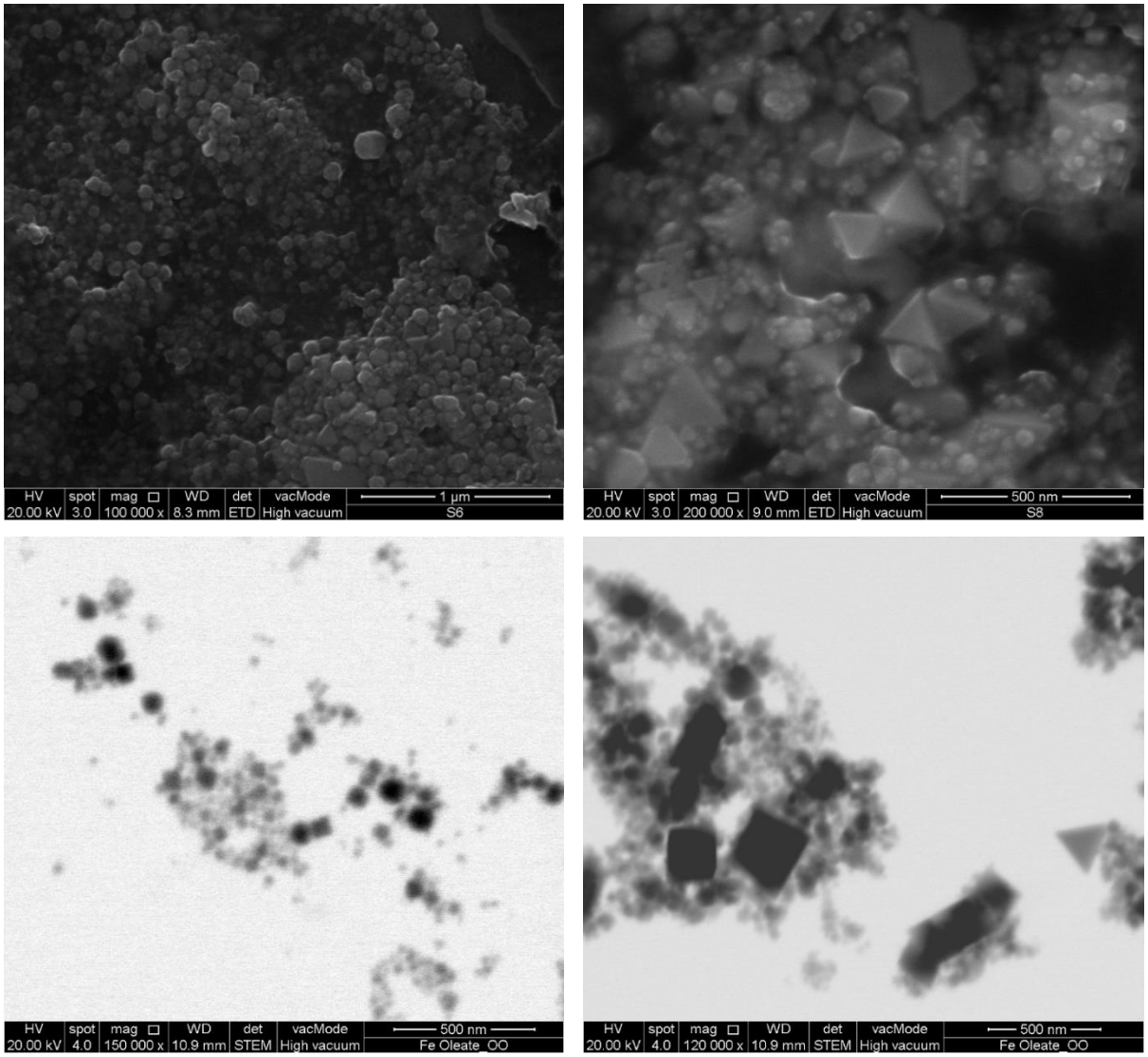


Figure 3.12: (top) SEM and (bottom) STEM imaging of iron oxide nanoparticles from run 4: FeOl in olive oil.



Figure 3.13: Difference between the reaction products obtained from run 3 (left) and run 4 (right) using FeOl as the iron source. Significant sedimentation (circled in red) can be seen in the olive oil based synthesis product in the vial on the right. This was not observed in run 2 (FeOOH in olive oil).

3.4.5 Choice of iron source for microfluidic synthesis

A summary of the particle sizes and standard deviations is given in Table 3.1. The results are close to those seen in the literature, as reported in section 2.1.2 and 2.1.5. Our run 3 synthesis at 320 °C resulted in a slight smaller average diameter (8.7 nm) than most works in the literature (10 – 13 nm).

Table 3.1: Summary of mean diameters and standard deviations of particles obtained from the batch synthesis runs.

Run	Iron source	Surfactant	Solvent	Mean diameter (nm)	Standard deviation (nm)	Standard deviation (%)	Agglome-ration
1	FeOOH	Oleic acid	Octadecene	11.2	3.8	34%	Medium
2	FeOOH	Olive oil		12.7	7.3	57%	Low
3	Iron oleate	Oleic acid	Octadecene	8.7	2.3	26%	Lowest
4	Iron oleate	Olive oil		-	-	-	Highest

Although our results using FeOOH as the precursor were acceptable (with some room for improvement), repeatability was low. New batches of FeOOH were prepared using the same method

as described in section 3.2. The results in subsequent runs were not as clean, most of the FeOOH did not dissolve, resulting in a mixture of spheres, hexagonal platelets, and rods. To eliminate the possibility of variations in the FeOOH synthesis, we purchased goethite from Sigma-Aldrich (CAS number 20344-49-4) and repeated the synthesis, however similar results were obtained: most of the powder did not dissolve. These experiments were also repeated under N_2 blanketing, with no noticeable difference.

Augustyn et al (Augustyn, et al., 2014) reported similar issues when using FeOOH as the precursor. They also found a significant amount of undissolved material at the end of the synthesis and their particles had a hexagonal shape, were of a different iron oxide phase, were much larger than expected.

The ability to form a homogenous solution from the reaction mixture is essential for use in our microfluidic device, and with these uncertain results, FeOOH was not a suitable source.

We did not face any of the above issues with iron oleate, which was a much more stable compound, can be easily dissolved in octadecene, and has a consistently repeatable synthesis route. Hence, the issue with the FeOOH was not investigated further.

3.5 Summary

Batch synthesis of iron oxide nanoparticles was performed using FeOOH and iron oleate as the iron sources, while oleic acid was used as the surfactant with octadecene. When using FeOOH, the mean particle size was 11.2 nm with a standard deviation of 3.8 nm (34%). With iron oleate, smaller particles with a mean size of 8.3 nm and standard deviation of 2.3 nm (26%) were found.

Olive oil was also tested as an alternate solvent/surfactant to 1-octadecene/oleic acid. The FeOOH + olive oil combination resulted in particles with a slightly larger mean size of 12.7 nm and a much larger standard deviation of 7.3 nm (57 %). The particles found when heating iron oleate in olive oil were highly polydisperse.

The results clearly show that the narrowest particle size distribution was obtained from run 3 (iron oleate and oleic acid in octadecene). Apart from a wider size distribution, the use of FeOOH also has another major problem, i.e. the incomplete dissolution of the iron source, which was also reported in the literature (Augustyn, et al., 2014).

The combination of iron oleate, oleic acid, and octadecene is the only one out of the four combinations (listed in Table 3.1) that reliably results in a homogenous solution that can be used for synthesis in

microfluidic chips, and also produced the best results. This is therefore the synthesis route chosen for the microfluidic synthesis in Chapters 5 and 6.

4 Design and fabrication of continuous flow microfluidic chips

The synthesis runs in Chapter 4 were carried out by laser heating in microfluidic chips. The fabrication of the continuous flow chips used in Chapters 5 and 6 is described in this chapter. Some of the preliminary work was done using microdroplet wells (section 5.2) and the fabrication of these wells is is described in their respective sections.

4.1 Thermal bonding Jig

The chips used in Chapters 5 and 6 were made of multiple layers of acrylic that were thermally bonded together using a custom-built jig.

The bonding setup is used as shown in Figure 4.2. The layers of the acrylic chip are brought together and clamped between the top and bottom platens. The two platens are made using 8 mm thick aluminium (6063) clamped together using four M5 bolts. Alignment pins can optionally be used to hold the acrylic layers together. The entire setup is then placed in an oven and heated.

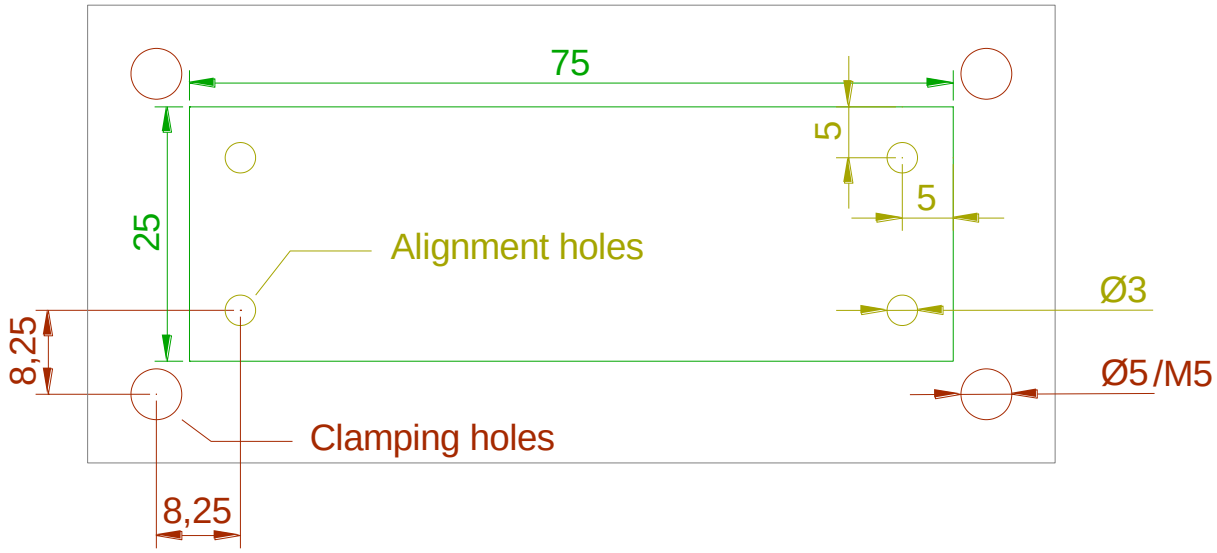


*Figure 4.1: Design of the platens used for cutting, milling, and drilling. **Green**: Chip dimensions used as a guideline. **Yellow**: 3mm alignment holes. **Red**: 5mm/M3 clamping holes.*

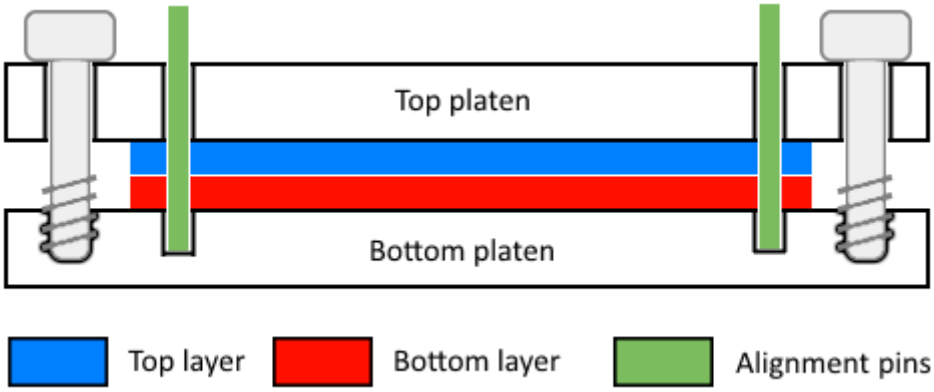
The overall dimensions of each platen are ~100 mm × ~60 mm × 8 mm. These were cut out using a vertical band saw and all faces were straightened using face cutter on a manual milling machine. A 25

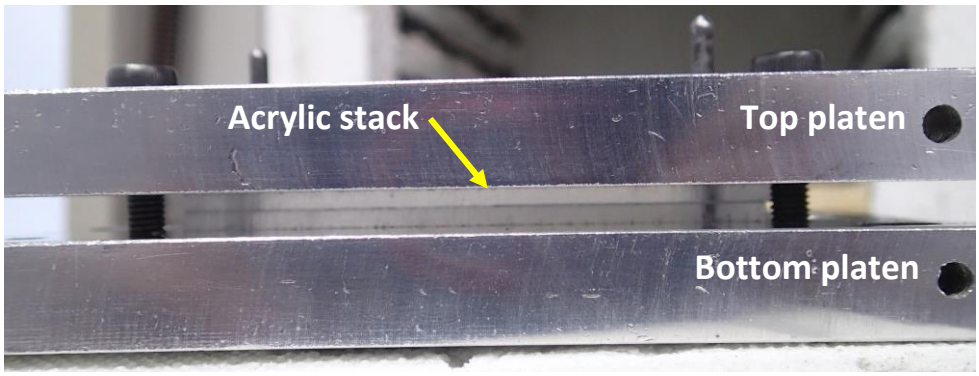
mm × 75 mm region was marked in the centre of each platen for the acrylic layers. Two sets of holes were drilled in each platen (Figure 4.1):

- **Alignment holes**: Four holes (3mm dia.) were made 5 mm inwards of each corner of the marked region to align the layers during the bonding process. They were drilled as ~3 mm deep blind holes on the bottom plate, and as through holes on the top platen (Figure 4.2).
- **Clamping holes**: Four holes (5mm dia.) were made 8.25 mm away on each axis, outside of each alignment hole. On the top platen, they were 5 mm through holes, and threaded M5 through holes on the bottom.

Platen Surface

As the acrylic under pressure is heated past its glass transition temperature, it will be moulded by any features found on the platen surface. Since we require the surface of the acrylic chip to be optically clear, the surface of the platen must be highly polished. The inner surfaces of the platens were thus wet sanded using increasingly fine sandpaper grades (up to 2000 grit), and then polished using a microfiber cloth and metal polish paste (Glosso).





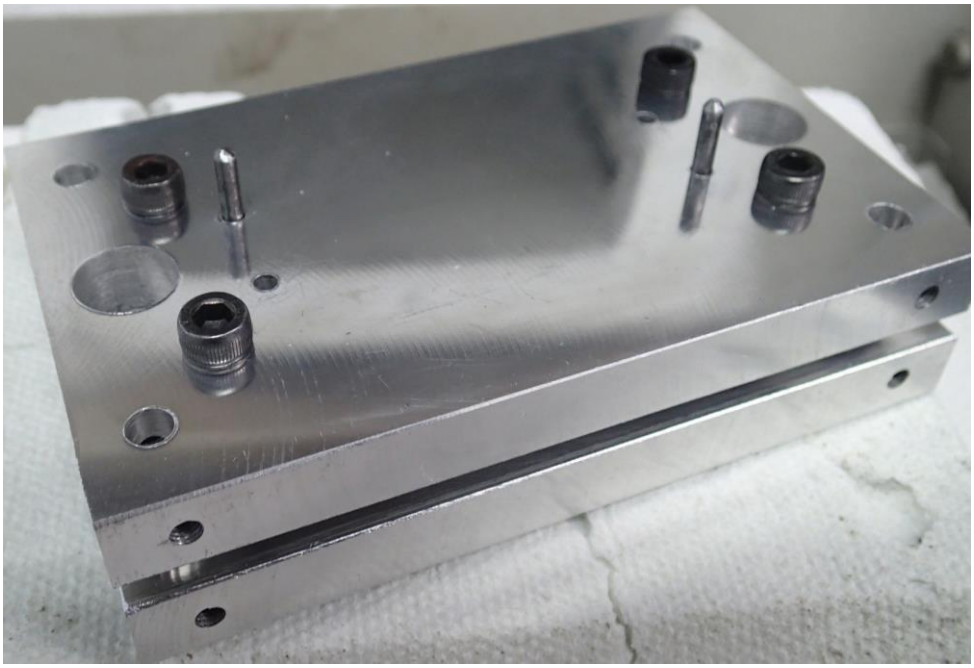


Figure 4.2: (top) Illustration and (bottom) photographs of the platens in use.

4.1.1 Thermal bonding parameters

The two major factors that affect thermal bonding of acrylic are the pressure and temperature. Since we do not have fine control over the pressure, this process was developed by somewhat fixing the pressure applied while adjusting the temperature for the best results.

Pressure

After stacking the layers, the top platen is put into position and the two platens are bolted together using the clamping holes. While holding down the top platen, the bolts are first tightened by hand. Then, using a screwdriver, a quarter turn is applied to each bolt in clockwise order until they cannot be tightened anymore. It is important to tighten the bolts in small increments to ensure that the pressure distribution is even.

While this approach does not allow us to quantify the pressure applied, we found the process repeatable without issue. As the acrylic layers heat up and bond together, the height of the stack decreases slightly, and excess pressure is relieved.

Temperature

The stack is placed in an oven (Memmert), which is then set to 93° C for 90 minutes. This duration includes the heat-up time of the oven itself. The stack is then removed and allowed to cool to room temperature for at least 1 hour.

Acrylic sheets (Ding Xing) were commercially obtained and cut to size. The bonding temperature was determined experimentally for this batch of acrylic; starting points for these tests were determined based on earlier work (Zhu, et al., 2007). Temperatures above or below this range resulted in deformed channels or failed bonding, respectively.

4.2 Straight channel chip

The first continuous flow chip design was a simple straight channel. The overall dimensions of the chip were chosen to match a standard microscope slide (25 mm * 75 mm). The design (Figure 4.3) consists of two layers. The channel itself is on the bottom layer, while the inlet and outlet holes are on the top layer. Both layers also have four alignment holes each.

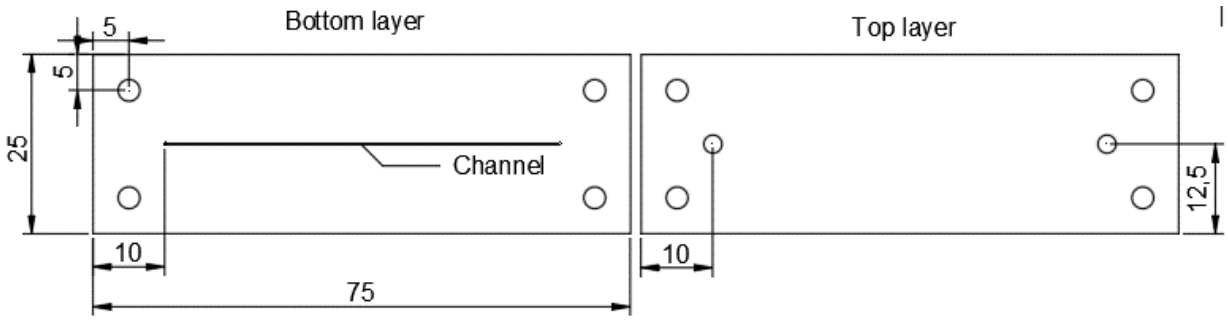


Figure 4.3: Design of the straight channel layers. The four holes on the corners of each layer are the alignment holes, and the two holes on the top layer are the inlet and outlet holes. All dimensions are in mm.

The chip was fabricated on a manual milling machine at a spindle speed of 3000 rpm. The base material is a 2.3 mm thick acrylic sheet. The fabrication steps are as shown below:

1. 2 plain slides (75 mm * 25 mm) were cut out of the acrylic sheet using a vertical band saw.
2. **Bottom layer:** The channel was milled on the bottom layer using a 10^{o} v-tip bit at a depth of 250 µm.
3. **Top layer:** The inlet and outlet holes were drilled through the top layer using a 2.5 mm drill bit and threaded using an M3 tap.
4. **Top and bottom layers:** The alignment holes were made on both layers using 3mm drill bits.

After the acrylic layers were fabricated, they were washed with soapy water, using a soft bristled brush to clear burrs and debris from the milled features. They were then thoroughly rinsed using isopropanol and distilled water and allowed to dry for several hours.

The channel dimensions were measured using a microscope (Olympus SZX7), and the channel was found to have a width of ~500 µm and a depth of ~250 - 300 µm.

The alignment pins were inserted into the bottom platen's alignment holes and the layers were stacked on top. The rest of the bonding process followed the description in section 4.1.1. After allowing the chip to cool for several hours it was leak tested using dyed water (Figure 4.4).

During the fabrication of this chip, it was found that small differences in the positions of the alignment holes in all the layers can cause unnecessary stress when preparing the setup. This approach might be more suitable when CNC machining is used in the fabrication of both the bonding jig and the acrylic layers.

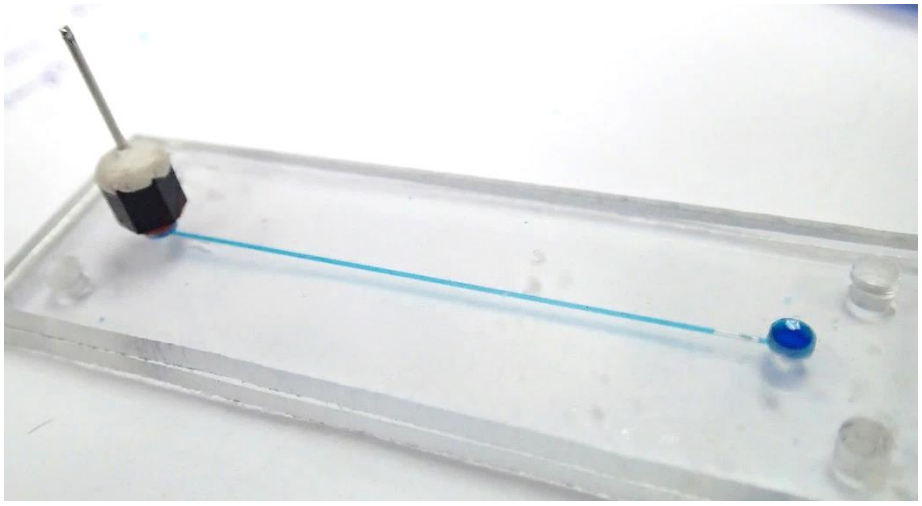


*Figure 4.4: A straight channel chip being leak tested using dyed water. The overall dimensions of the chip are 75 mm * 25 mm. The channel has a width of ~500 µm.*

4.3 Vertical flow chip

The main differentiating feature of this design is the reaction chamber, a section of the chip where the solution flows upwards while being heated by the laser beam (Figure 4.5). This design is essentially a custom flow cell, made with the overall setup and laser beam size in made. This allows us to increase the residence time under the laser from a few milliseconds in the straight channel chip to several seconds in the vertical flow chips.

The critical dimensions here are those of the cylindrical chamber, rather than the height and width of the channels. The height of the chamber is the thickness of the acrylic layer, and the diameter is determined by the diameter of the drill bit. This makes fabrication simple, controllable, and repeatable.

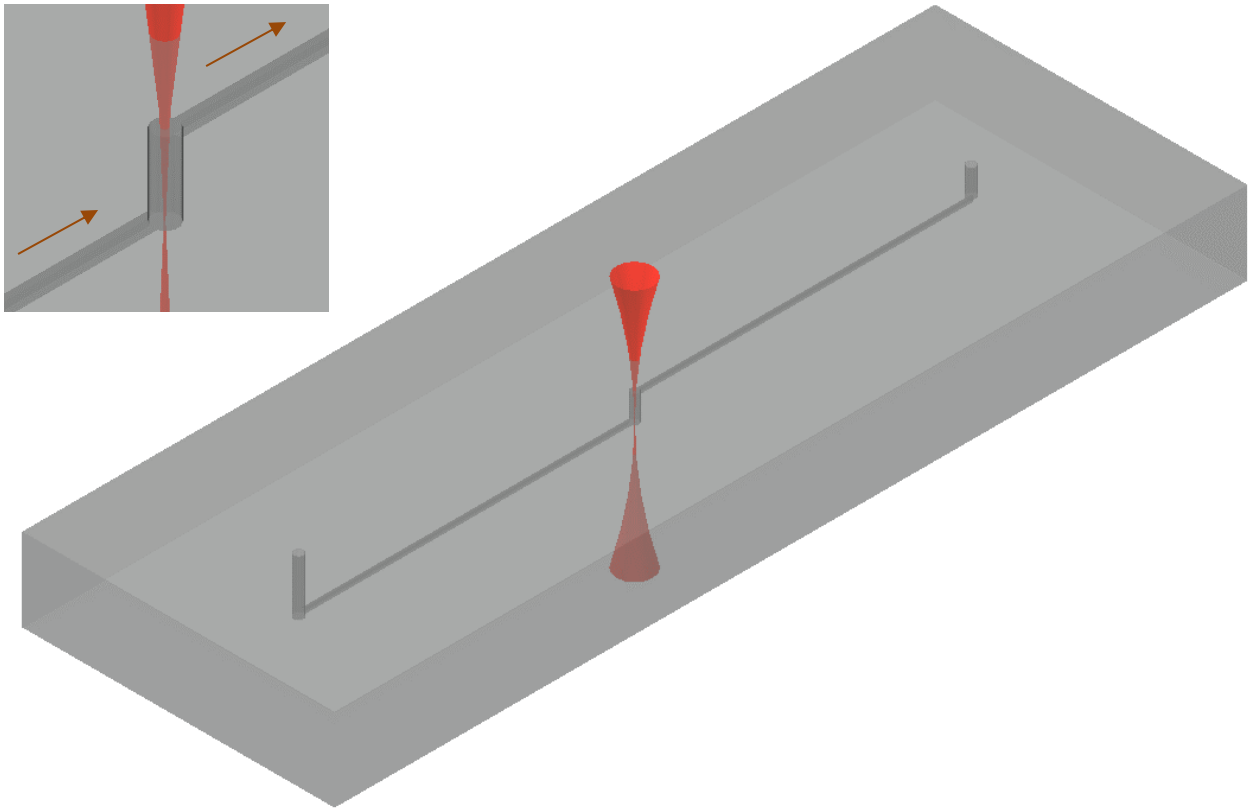


Figure 4.5: Illustration of the vertical flow chip with the focused laser beam. Inset: Close-up of the reaction chamber with arrows indicating the direction of fluid flow.

The chip is made up of three acrylic layers (shown in Figure 4.6):

1. The top layer with the inlet and outlet holes
2. The middle layer with the reaction chamber and the inlet and outlet channels
3. The bottom layer, a plain layer which seals the inlet channel and reaction chamber.

The chip was fabricated manually using a band saw, a drill press and an acrylic scoring tool. The base material was a 2.3 mm thick acrylic sheet. The fabrication steps are listed below and pointed out in Figure 4.6.

1. Three plain slides (75 mm * 25 mm) were first cut out using a band saw.
2. **Middle layer:** The reaction chamber was made by drilling through the centre of the middle layer using a 0.7 mm drill bit at 570 rpm. A low spindle speed is required when using sub-millimetre drill bits to avoid melting and deformation of the hole.
3. **Middle and top layers:** These two layers were stacked, and the inlet hole was drilled through using a 0.8 mm drill bit.
4. **Top layer:** The outlet hole was drilled using a 0.8 mm drill bit.

5. **Middle layer:** The inlet channel was created on the bottom side from the reaction chamber to the inlet hole. The outlet channel was created on the top side from the outlet hole to the reaction chamber.

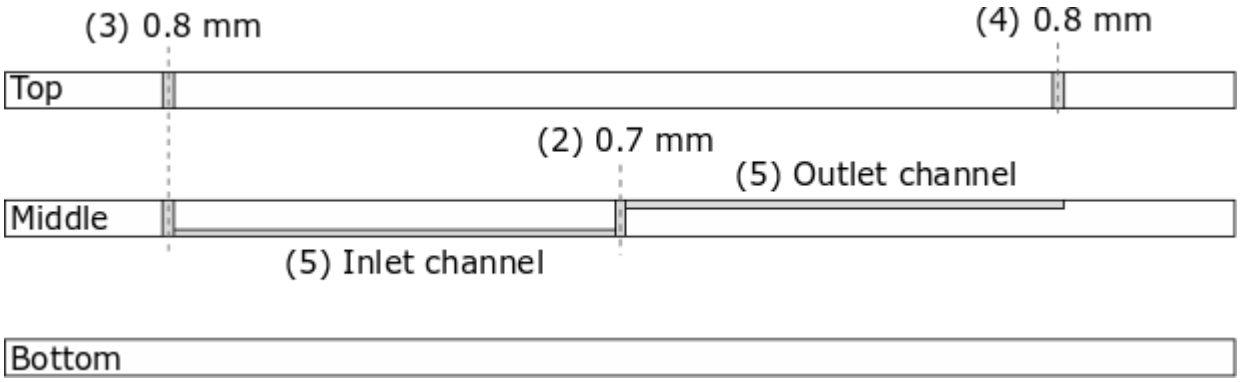


Figure 4.6: The three layers of the chip, showing the steps of fabrication. In the top layer, the hole on the left is the inlet, and the hole on the right is the outlet.

The inlet and outlet channels were created using an acrylic scoring tool, illustrated in Figure 4.7. Using a steel ruler as a guide, three passes were made with very light pressure applied. This method works well for creating straight channels with repeatable results (when the exact dimensions of the channels are not critical). The channels had an average depth and width of ~0.25 mm and ~0.3 mm respectively.

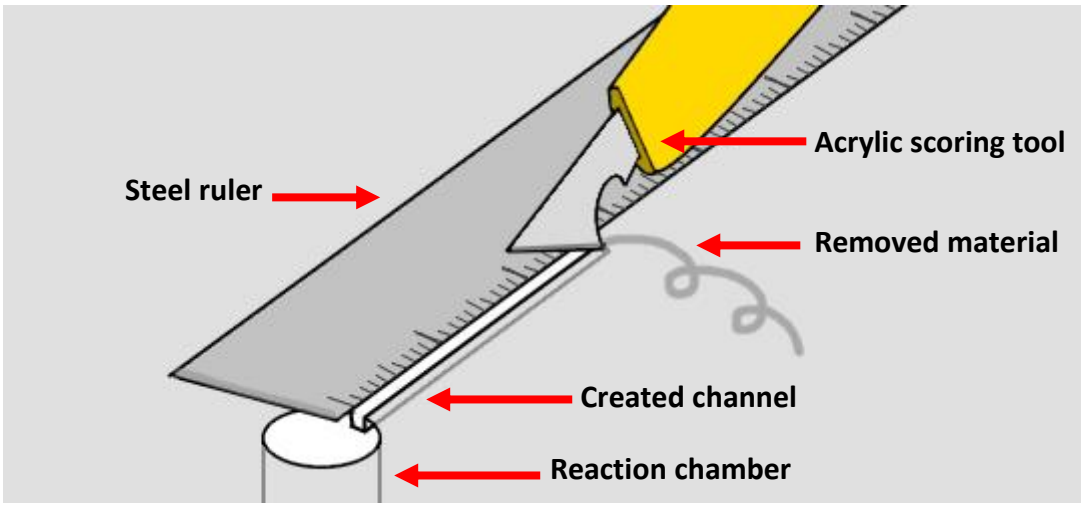


Figure 4.7: Illustration of the channel fabrication using an acrylic scoring tool.

The chip was bonded using the same procedure (section 4.1.1) with two minor changes to the alignment and surface finish of the platens.

Alignment

The three layers were aligned by hand and a drop of cyanoacrylate adhesive was applied on each corner, which was sufficient to hold the layers together during the bonding process. The alignment holes in the platens were not used when the chips were fabricated without a drill press. Even a slight difference in the hole positions between the layers can result in a large amount of stress on the acrylic, and with three layers the chances of a mismatch are increased. The only features that need to be matched are the 0.8 mm inlet and outlet holes, which does not require high precision.

Surface finish

The polish on the platens was not durable and needed to be re-sanded often. The stacked layers were instead sandwiched between two glass slides, which results in an optical quality finish on the surface of the chips. The slides tend to crack at the edges when pressure was applied, but they are inexpensive and quickly replaced.

After allowing the bonded chip to cool down for several hours, the inlet and outlet connections were installed. A 21G needle (Terumo), with a nominal outer diameter of 0.8192 mm was cut into several pieces and the ends were sanded to dull the edges. Two of these pieces were inserted into the 0.8 mm inlet and outlet holes. Since acrylic is a hard plastic, this press fit does not guarantee a perfect seal; a drop of cyanoacrylate adhesive was applied around the base of each needle. The adhesive was allowed to cure, and the chip was leak-tested using dyed water (Figure 4.9). A close-up of the reaction chamber can be seen in Figure 4.10. Multiple chips were made as needed.

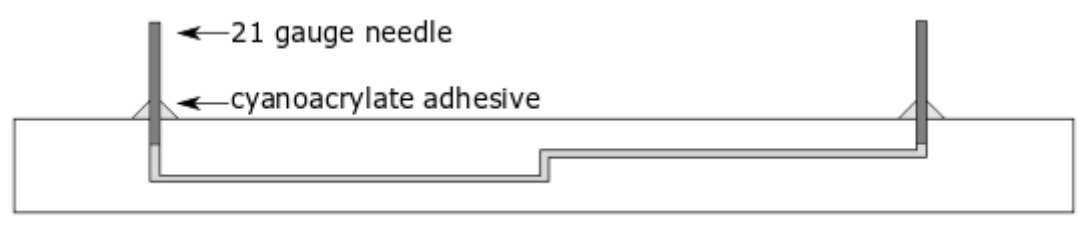


Figure 4.8: The bonded chip, showing the plugging of the inlet and outlet holes.



Figure 4.9: Leak testing of a vertical flow chip using dyed water.



Figure 4.10: Close-up of the reaction chamber showing the vertical flow region.

4.3.1 Solvent vapour bonding

While all the chips used to obtain results were made using the above process, an early prototype was made using solvothermal bonding. The layers were exposed to chloroform vapour within a closed petridish for 30s on each side and then immediately pressed together. This method was adopted from earlier work by Ogilvie et al (Ogilvie, et al., 2010). Thermal bonding was performed at a lower temperature of 80°C for 90 minutes and then the chip was allowed to cool overnight.

The advantage of this approach is that bonding is achieved at temperatures below the glass transition temperature, reducing the chance of channel deformation to occur. Additionally, the surface finish of the platens is not as important.

This chip worked well during leak tests with dyed water, and during the first synthesis run using the octadecene based solution. However, after this first run, the region around the reaction chamber developed stress cracking and clouding. This spread to the entire layer interface in rest of the chip within 2 days (Figure 4.11). It is unclear if this is due to inadequate drying of the chloroform after bonding or whether the chloroform causes permanent changes to the acrylic surface, making it more susceptible to attack by the octadecene. This approach was abandoned in favour of a purely thermal bonding process. This may still be a viable option if only aqueous solutions are to be used.

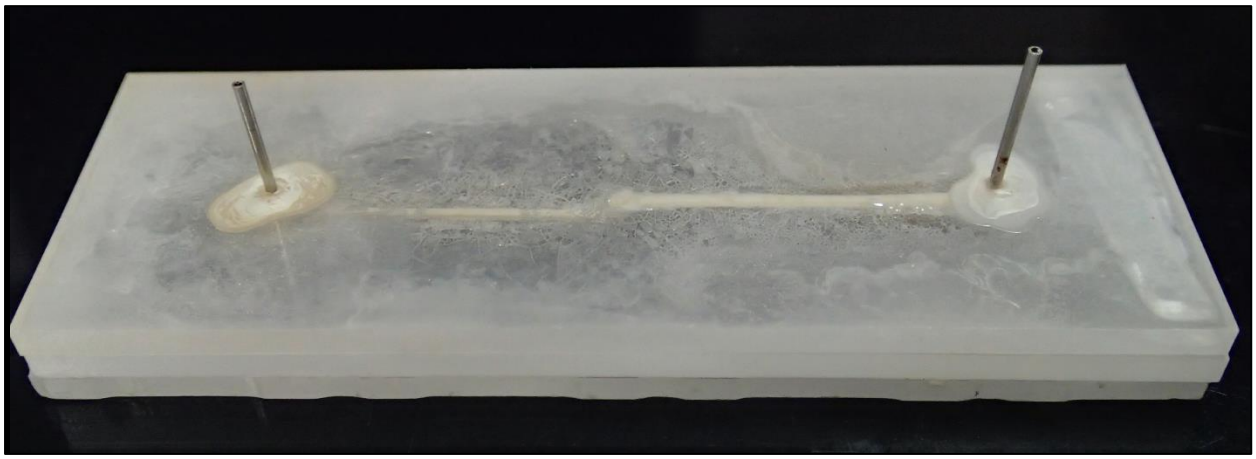


Figure 4.11: Solvent induced clouding observed in solvent bonded sample.

4.4 Summary

A simple route has been developed for the fabrication of vertical flow chips for microfluidic synthesis. The reaction chamber is made by drilling a 0.7 mm hole through the middle layer, while the inlet and outlet channels were made using an acrylic scoring tool. The inlet and outlet holes were drilled in the top layer using a 0.8 mm bit. The bottom, middle and top layers are thermally bonded using a custom-made jig, placed in a furnace for 90 minutes at 93 °C.

The critical dimensions (i.e. the central reaction chamber) are defined by the thickness of the acrylic sheet and the diameter of the drill bit, making it easily reproducible. The inlet and outlet channels only serve to transport the fluid and could be fabricated by hand. This approach avoids the need for expensive equipment like CNCs or laser cutters.

Solvent bonding of the layers was also tested and was successful in producing a sealed chip. However, the chip did not hold up to continued use with organic solvents. Hence, a purely thermal bonding method was chosen.

Compared with fabrication methods and materials used for microfluidic chips for thermal decomposition synthesis (Chan, 2006) (Edel, et al., 2003) (Yen, et al., 2005), this approach and design avoids the need for expensive high temperature materials (e.g. glass, silicon, PTFE) and multiple and potentially hazardous intermediate fabrication steps like masking, etching, CNC machining, etc.

5 Preliminary microfluidic synthesis of iron oxide nanoparticles

Previous attempts at reaction in liquid (LRL) syntheses were conducted in cuvettes with little or no flow control (Tangeysh, et al., 2013) (Robinson, et al., 2009) (Okamoto, et al., 2018). Robinson et al (Robinson, et al., 2009) irradiated a cobalt carbonyl solution under vigorous stirring, but they also recommended the use of a flow system to increase nanoparticle yield. All of these attempts use pulsed lasers to induce decomposition of the solution.

This chapter describes the nanoparticle synthesis achieved by heating the fluid using an inexpensive continuous wave laser. As a proof of concept, the solution was first heated by the laser in a small aluminium well, resulting in magnetic iron oxide nanoparticles. Other attempts at stationary synthesis were also made in shallow acrylic wells. Early attempts at continuous flow synthesis used a straight channel, which had a very low yield. The limitations of this approach led to the design of the vertical flow chip used in Chapter 6 which allowed for long residence periods and greater flow control.

This chapter also includes the preparation of the synthesis solutions and the experimental setup used in the experiments in Chapters 5 and 6.

5.1 Experimental Setup

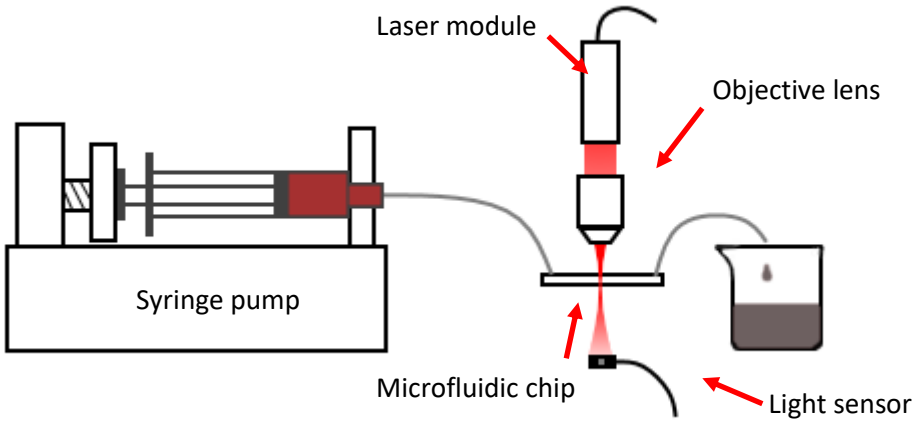


Figure 5.1: Illustration of the flow synthesis experimental setup used for microfluidic nanoparticle synthesis.

The experimental setup was made for the controlled laser irradiation of the solution. Simply put, there is a focused laser beam in a fixed position. A stage holds the microfluidic chip at the laser's focal point and allows for small movements (up to 4 mm on each axis) for fine adjustments.

In the stationary synthesis experiments (section 5.2), the solution is loaded into wells, which are then placed on the stage and heated for the desired period. For the continuous flow experiments (sections

5.4 and 6.3), the chip's inlet tube is connected to a syringe set in a syringe pump. The outlet tube drops the heated solution into a vial. An illustration of this setup is shown in Figure 5.1 and a photograph in Figure 5.2.

More details about these experiments are presented in their respective sections. This section describes the stage, its construction and characterisation.

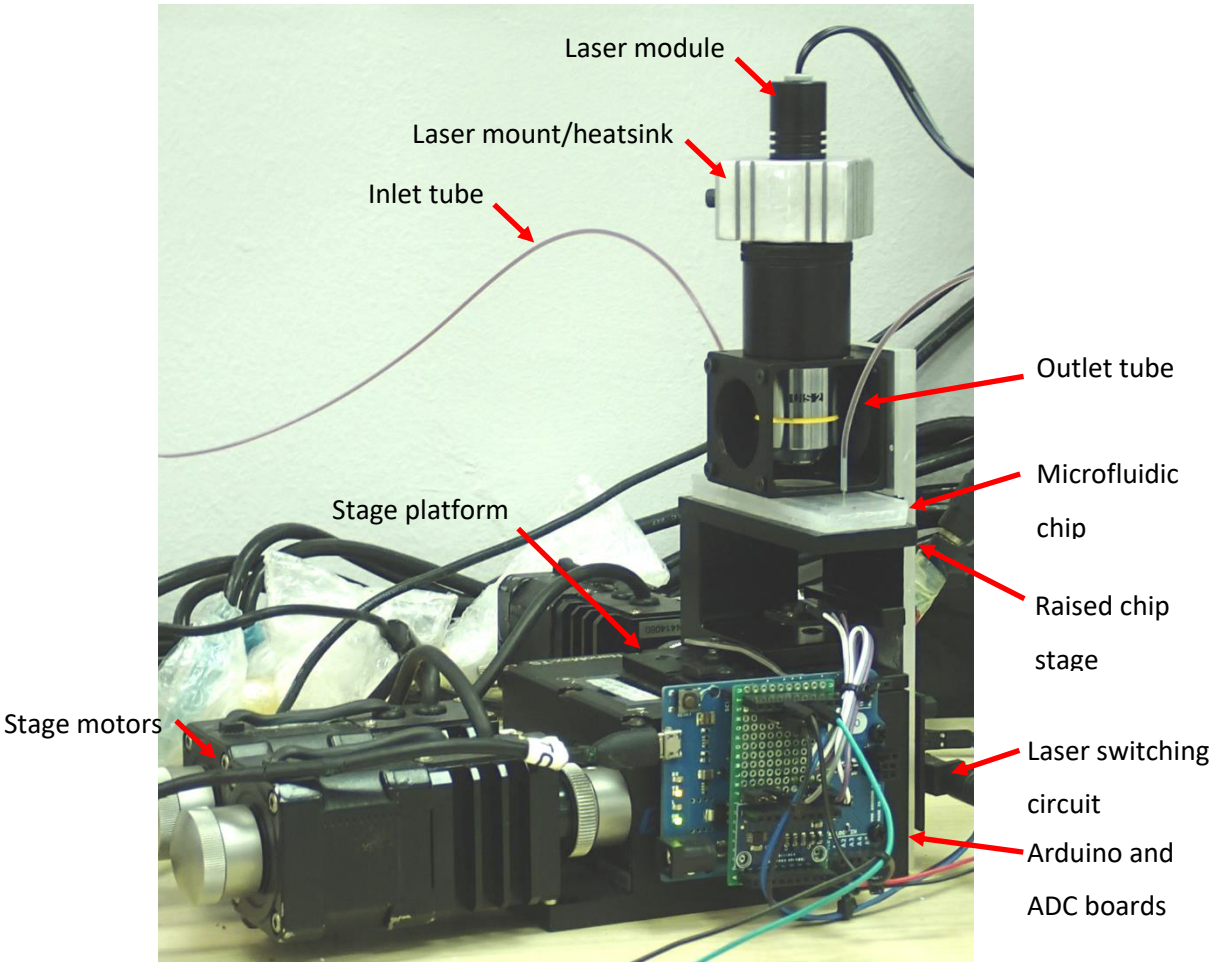


Figure 5.2: The experimental setup used continuous flow synthesis run of iron oxide nanoparticles.

The base of the experimental setup is a Thorlabs Nanomax MAX341/M motorised stage. The sides of the base, as well as the top platform (the moving stage) have several M3 and M2 threaded holes for mounting custom hardware. The manufacturer-provided AutoCAD drawings were used to design and fabricate our custom mounting hardware.

Apart from the stage these parts were used:

1. 250 mW 650 nm continuous wave laser module
2. Olympus RMS10x objective lens
3. Thorlabs SM1L10 lens tube
4. Thorlabs CM1-BS2 beam splitter housing (the beam splitter itself was removed)

Laser Safety: The laser module has an output power of 0.25 W, making it a Class 3B laser, meaning that eye exposure of any duration can result in blindness. The following precautions were taken:

- Laser safety goggles were worn at all times when operating the laser.
- Only the operator was present in the room when the laser was operated at full power.
- Any structural components that may be in the laser's path were painted matte black to eliminate specular reflections.
- The optical assembly and the stage were covered up whenever the laser was operated at full power, except during temperature measurements where only the hand was brought close to the stage.

While the laser module outputs a collimated beam, the optical assembly as a whole produces a diverging beam. The beam intensity is highest at the lens' working distance (10.5 mm from the lens surface). The intensity quickly drops after this point. At ~22 cm from the lens the intensity drops below 25 W/m^2, which is the M.P.E. (Maximum Permissible Exposure) limit for a Class 3A laser (i.e. it will not *immediately cause* blindness). At 34 cm or more the intensity drops below $10W/m^2$. At this power density the beam is eye safe and does not pose a risk to people farther away.

5.1.1 Optical assembly

The laser module is cylindrical in shape with a diameter of 16 mm. An adapter/heatsink was fabricated to mount the module in the open end of the lens tube, which has an internal diameter of 25.2 mm. The objective lens was mounted at the other end of the lens tube. The lens tube was then inserted into the beam splitter housing so that the object lens sits inside the cubical housing cage. The housing has M2 threaded mounting holes, which were used to mount this entire assembly. The assembly is shown in Figure 5.3, which shows the heatsink used with the first laser. This proved to be inadequate and a bigger version was made, shown in Figure 5.2.

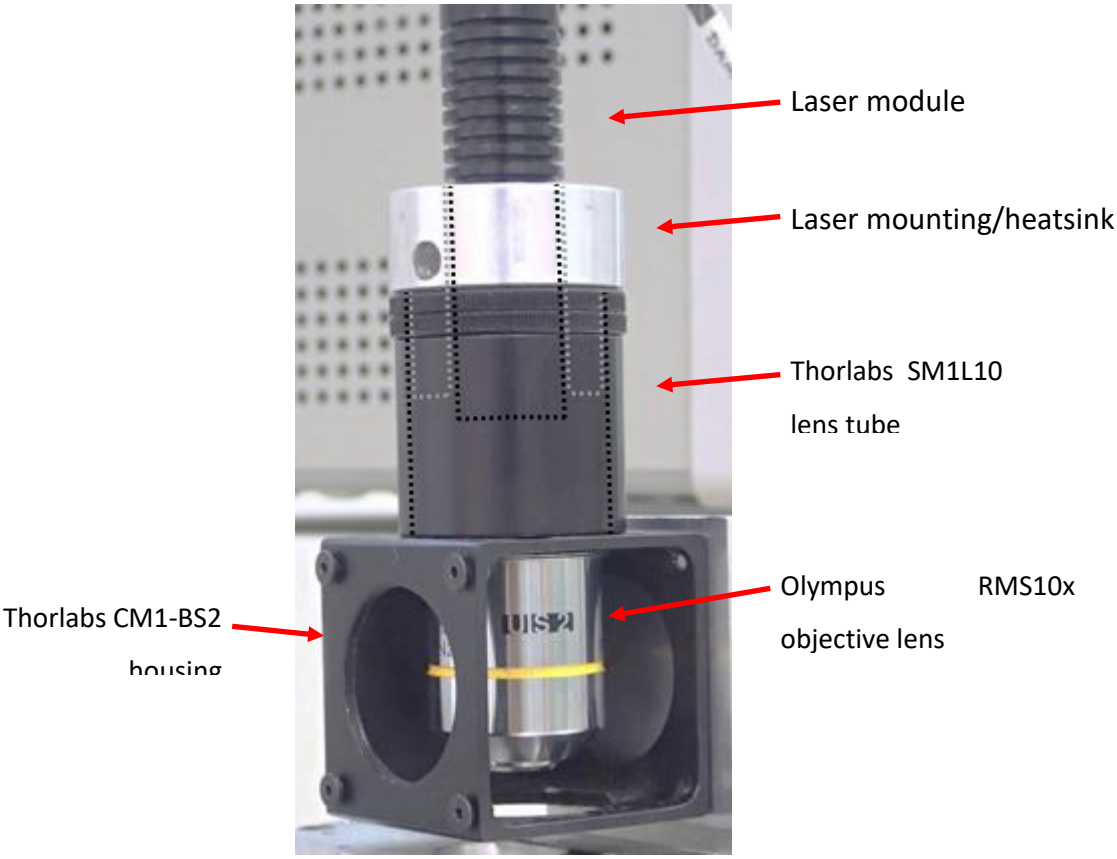


Figure 5.3: The optical assembly including the laser module, objective lens, and structural parts. The dotted lines show a cross-section of the internal structure of the assembly. This picture shows an earlier, smaller version of the heatsink.

5.1.2 Structural fabrication

The laser mounting in section 5.1.1 was turned on a lathe, while the remaining parts were fabricated on a manual milling machine:

1. Raised microfluidic chip stage: The chip rests on top of a raised stage mounted on the top platform, which allows the chip to be moved up to 4 mm in the X, Y, and Z directions. The stage is raised to allow an optical sensor to fit below the chip to monitor the transmitted light intensity. To allow the light to pass through a hole was drilling the centre of the stage.
2. Optical sensor holder: A thin plate that holds the optical sensor PCB (Sharp GA1A1S202WP light sensor) under the stage.
3. Mounting plate: This plate is mounted on the side of the platform. The optical assembly is mounted on this plate such the laser beam is pointed at the centre of the raised stage. The height of the assembly is chosen so that the chip lies within the working distance of the objective lens. The optical sensor holder is also mounted on this plate, directly below the objective lens.

The AutoCAD design models of these parts shown in Figure 5.4.

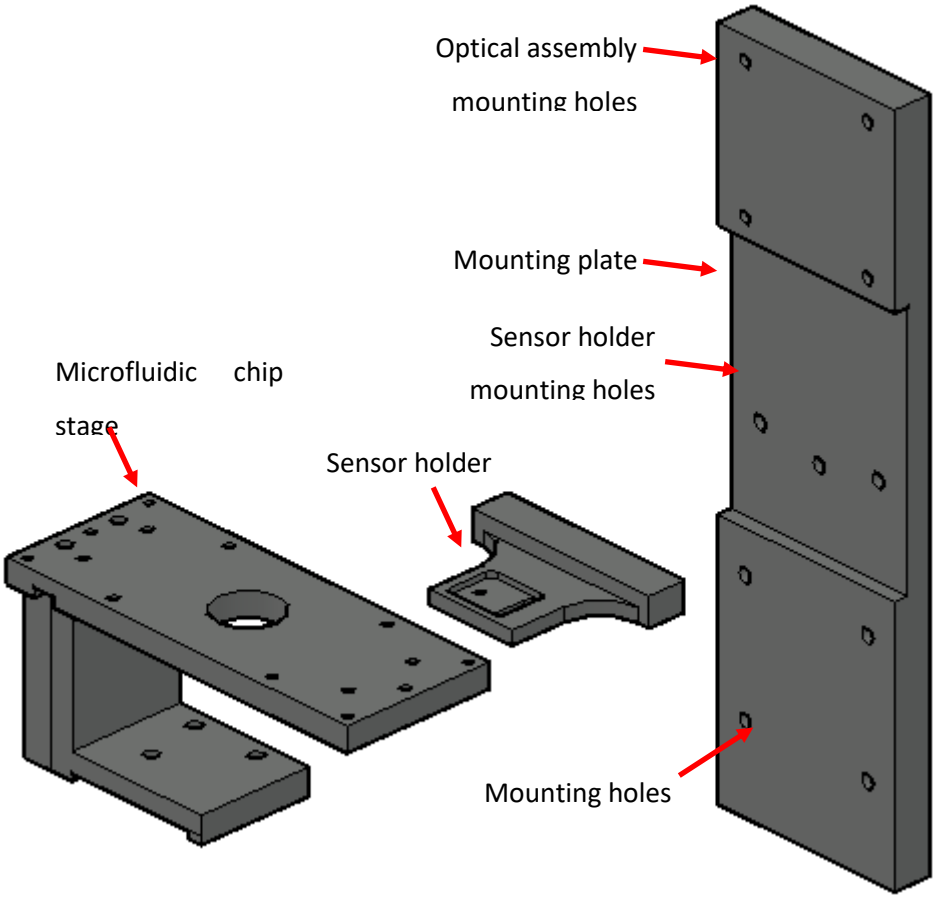


Figure 5.4: Fabricated structural parts. The mounting holes at the bottom attach the mounting plate to the stage base.

The stage and sensor holder were spray painted black after an acid bath treatment (in order to improved paint adhesion by increasing surface area). This was done to minimise reflections from the laser which might add noise to the sensor readings.

5.1.3 Control electronics

There are four electronics boards used in the system:

1. Arduino Leonardo
2. Adafruit ADS1115 ADC board
3. Sharp GA1A1S202WP light sensor

4. Laser switching circuit

The first three boards were purchased while the last one was fabricated.

Laser switching circuit: This board consists of a readymade switching voltage regulator circuit, a switching transistor, and status LEDs.

The voltage regulator takes in any voltage between 6 and 12 V and outputs a steady 5 V for the laser module. It was added as a safety feature and allows a separate power supply to be used for the laser.

The switching transistor takes a PWM input from the Arduino board and controls the 5 V power output connected to the laser.

The status LEDs simply show when the laser power and control signal are on.

The laser module has a built-in laser diode driver and so only needs to be supplied 4.5 – 5.5 V to turn on. The intensity can be controlled via PWM (pulse width modulation) of the power supply, which is achieved using the Arduino and the switching transistor.

Sharp GA1A1S202WP: The light sensor is mounted directly under the laser, and outputs a voltage between 0 and 3.3 V. The output is logarithmically related to the light intensity.

ADS1115 ADC: The ADC board reads the analogue voltage output of the light sensor and converts it to a digital value which can be read by the Arduino.

Arduino: The main job of the Arduino is to keep the laser running by controlling the switching circuit. The laser will not stay on without continuously receiving this signal. When the Arduino is programmed, it is given a default laser power level. It can then be run independent of the PC; however, it will not save the sensor readings.

When connected to a PC it can receive the digitised light sensor readings from the ADC and transmit them back to the PC. It can also receive new laser power values and change the PWM signal on the fly. This functionality is used to characterise the laser beam, as well as control the beam during the sweep synthesis (section 5.3.3).

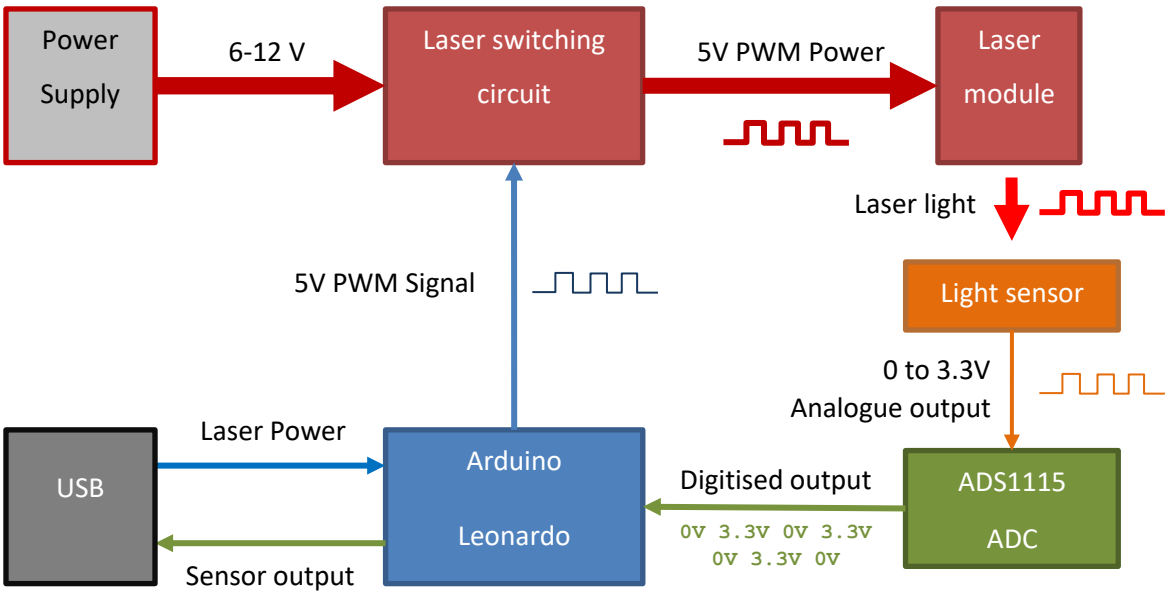


Figure 5.5: Illustration of the various electronics components of the setup. The thickness of the connecting arrows is indicative of the amount of current/energy being transferred.

5.1.4 Beam characterisation

A MATLAB GUI was made to measure the beam spot size at different heights using the knife edge method. The aim is to find the exact height of the focal point above the stage.

Figure 5.6 shows the setup used. The aim is to vary $h_{platform}$ until h_{stage} matches h_{focal}. The difference between h_{stage} and $h_{platform}$ is constant.

For this experiment, the laser's intensity is set to 1%. A razor blade's sharp edge is placed in the centre of the stage. In the beginning the stage is positioned so that the laser beam is completely covered up by the razor blade. The stage is then slowly moved in the x-direction so until the laser is completely unobscured. While this sweep is conducted, the GUI saves the position of the stage and the recorded light intensity from the sensor.

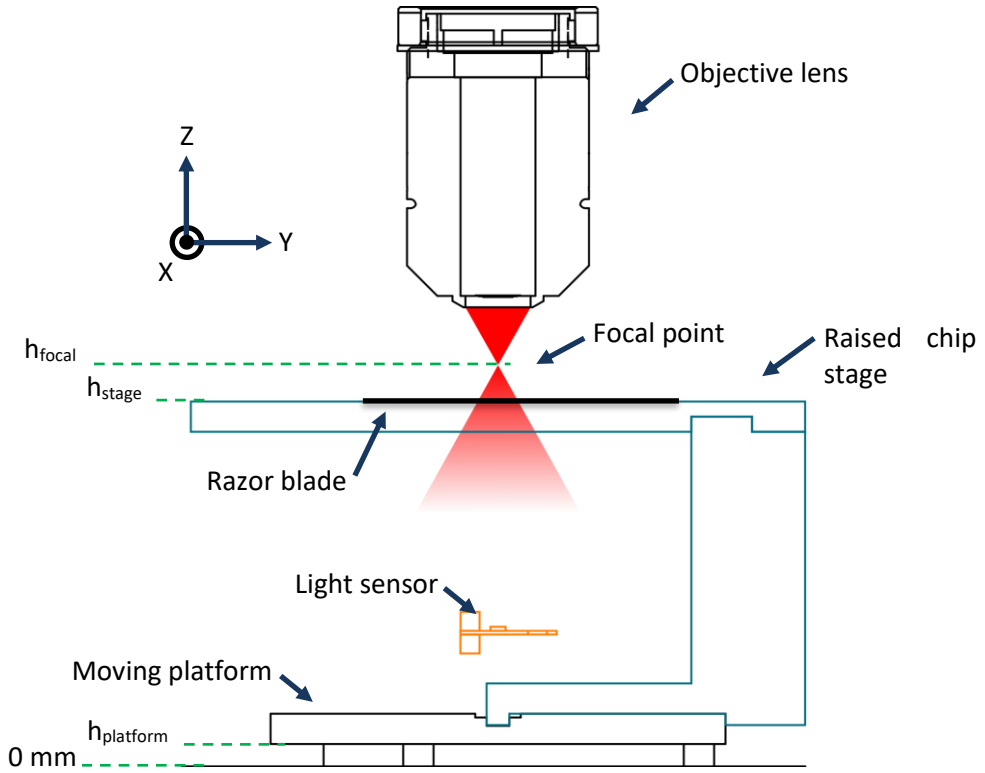


Figure 5.6: Diagram of the setup to find the height of the focal point and focal diameter for microfluidic synthesis.

Figure 5.7 illustrates this concept. At different heights, the laser beam will have different spot sizes. The stage is repeatedly moved across the beam at the same velocity. The time taken by the blade to completely clear the spot depends on the spot size. As the beam is uncovered, the sensor output will increase until the razor blade is completely out of the beam. By comparing the position vs intensity plots at various heights, we can zero in on the focal height. The plots have a sigmoidal profile, and typically the diameter of the spot is measured as the distance between 10% and 90% of the maximum intensity.

Sweeps were conducted between 2.25 and 2.45 mm at every 0.025 mm. The velocity of the stage was set to 0.025 mm/s. The data obtained was smoothed to reduce noise. The beam waist was found between a height of 2.2 and 2.5 mm with the minimum diameter of 19.5 µm at 2.35 mm in this case. This measurement is shown in Figure 5.8. The structural components were designed to have the focal point be at a stage height of 2 mm, so the results are quite close.

The laser module was replaced twice, and the measurements were repeated whenever the module was changed or adjusted. The scan in Figure 5.8 is from the first module, while the second and third modules showed average spot sizes of 43.41 and 39.44 µm. We assume this difference is due to manufacturing variances within the laser module's components as only the first module showed a

spot size smaller than 38 µm. Another reason for the increase may be a slight misalignment due to the new and larger laser mount/heatsink that was fabricated after the first module overheated.

The average focal height was 2.35 ± 0.05 mm across all measurements; we can attribute the small difference here to the layer of paint, thermal expansion and other minor changes made throughout the lifetime of the setup.

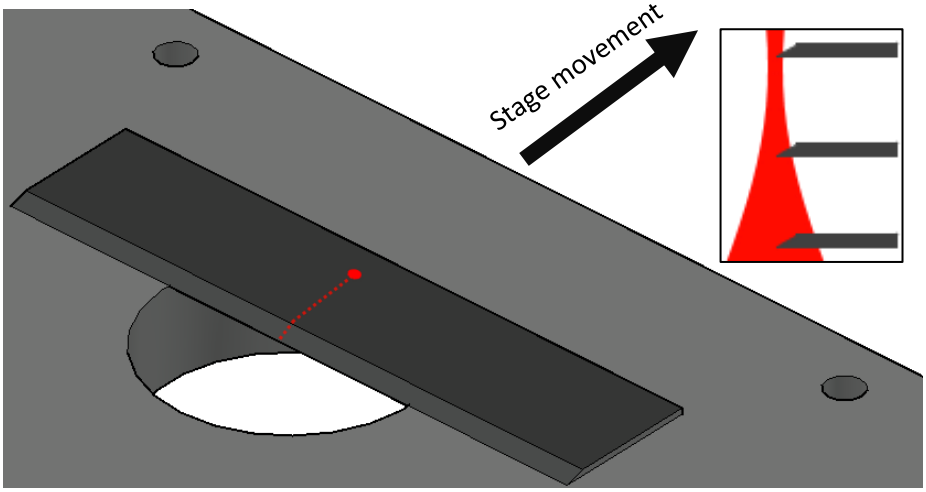


Figure 5.7: Illustration of the razor blade in the centre of the stage. As the stage moves, the laser spot is slowly uncovered. Inset: As the spot diameter changes with height, the time the blade takes to uncover the spot also changes.

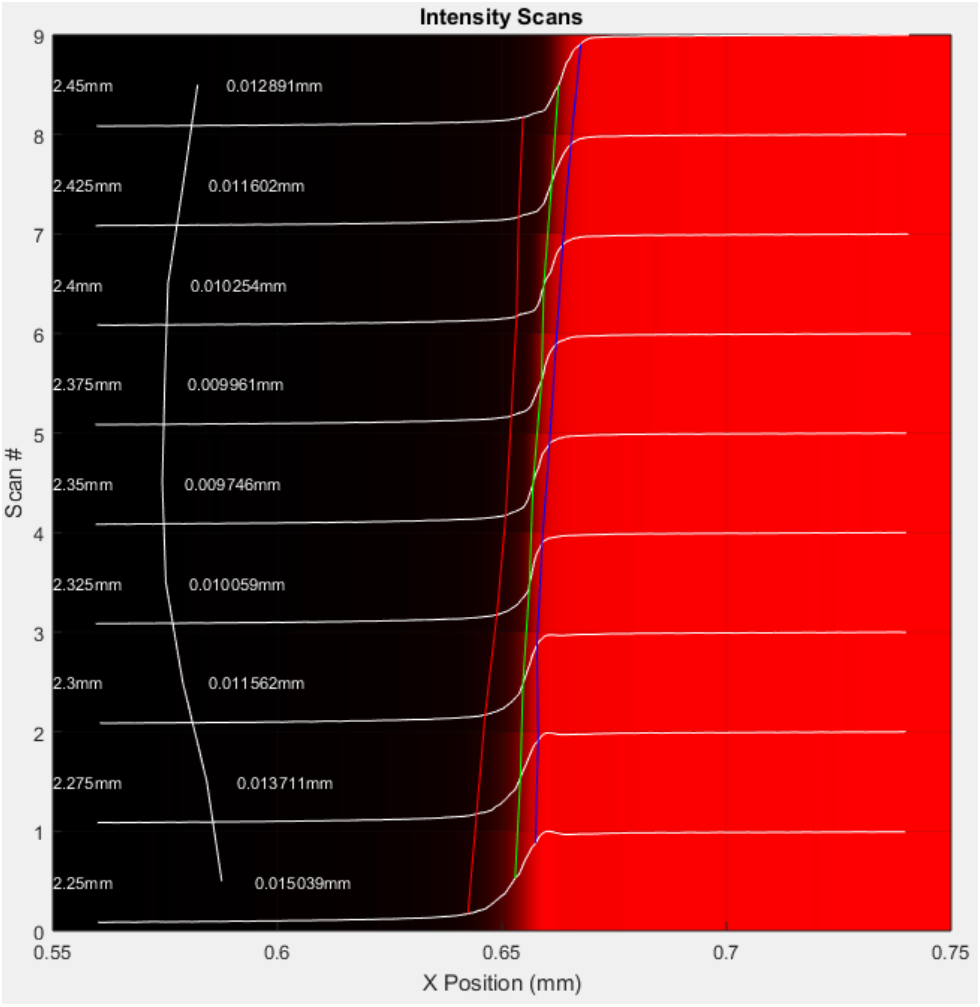


Figure 5.8: Intensity scans between 2.25 and 2.45 mm. The left most column shows the height of the scan ($h_{platform}$). To its right is the calculated beam radius at that height.

5.2 Solution preparation

Iron oleate was synthesised using the same method as before (section 3.2.2).

The same process was used to make three solutions, with the only difference being the surfactants added to the mixture. The three solutions are:

1. **B**: Stock solution with no surfactant; a mixture of FeOl and ODE.
2. **O**: Oleic acid added as surfactant. The molar ratio of FeOl to OA is 1:1.
3. **N**: Sodium oleate and oleic acid as surfactants. The molar ratio of FeOl to NaOl to OA is 1:0.5:0.5.

For each solution, the reactants were weighed and added to a glass vial. The vial was placed in a vacuum oven at (70°C at <100 mbar) for at least 3 hours to allow the iron oleate to dissolve while

simultaneously degassing the solution. Bubbling typically ceased within the first 20 minutes. The exact measurements of the reactants added to the solutions are given in Table 5.1.

Table 5.1: Table showing the B, O, and N solutions with the amounts and type of surfactants in each.

	B	O	N
FeOl conc.	0.154 M	0.154 M	0.154 M
ODE	4.5 mL	7.25 mL	4 mL
FeOl	0.626 g (0.695 mmol)	1.010 g (1.122 mmol)	0.556 g (0.618 mmol)
OA	-	0.317 g (1.122 mmol)	0.087 g (0.309 mmol)
NaOl	-	-	0.094 g (0.309 mmol)

5.3 Stationary synthesis

The premise of nanoparticle synthesis by laser heating was first tested using a simple stationary approach with a small amount of the solution being placed in a microwell and heated. These early attempts are documented in this subsection.

5.3.1 Aluminium well

A 3 mm thick aluminium plate was used as the substrate. Using a 3 mm drill bit, a well was drilled to a maximum depth of 1.5 mm.

The well was filled with a drop of the B solution (no surfactant) and sealed with a glass cover slip. A little extra solution was added to create a liquid seal. The plate was placed on the stage and the height was adjusted so that the laser's focal point was immediately below the cover sheet. An illustration of the setup is shown in Figure 5.9, and a photograph in Figure 5.10.

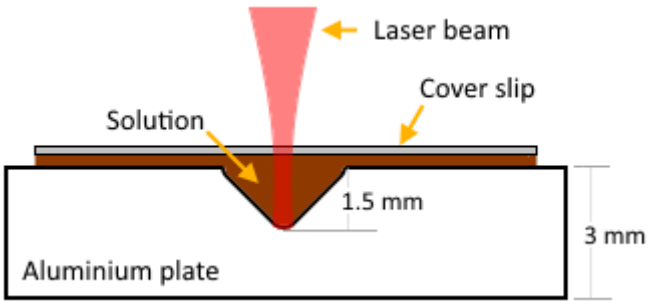


Figure 5.9: Illustration of the aluminium well synthesis setup.

The laser was turned on at full power for 30 s. The cover sheet was carefully removed, and the solution was pipetted out and poured into a vial. The sample was purified with 3 acetone-hexane wash cycles, and the precipitate was found to be magnetic (Figure 5.10). Compared to the precipitates found in all the other microfluidic syntheses, these are dark, nearly black in colour, suggesting near complete decomposition and formation of magnetite.



Figure 5.10: (Left) Photograph of the aluminium well with the reaction solution. (Right) Magnetic precipitates seen in the vial after purification.

Due to the small sample volume, only SEM analysis was done (Figure 5.11). A wide variety of shapes and sizes (~5-500 nm) were seen. Some agglomerates were found, although most of the particles were free. The larger particles were mostly bipyramidal shapes, and many of them were seen with smaller particles growing on their surfaces. Some of the smaller particles have a more rounded appearance.

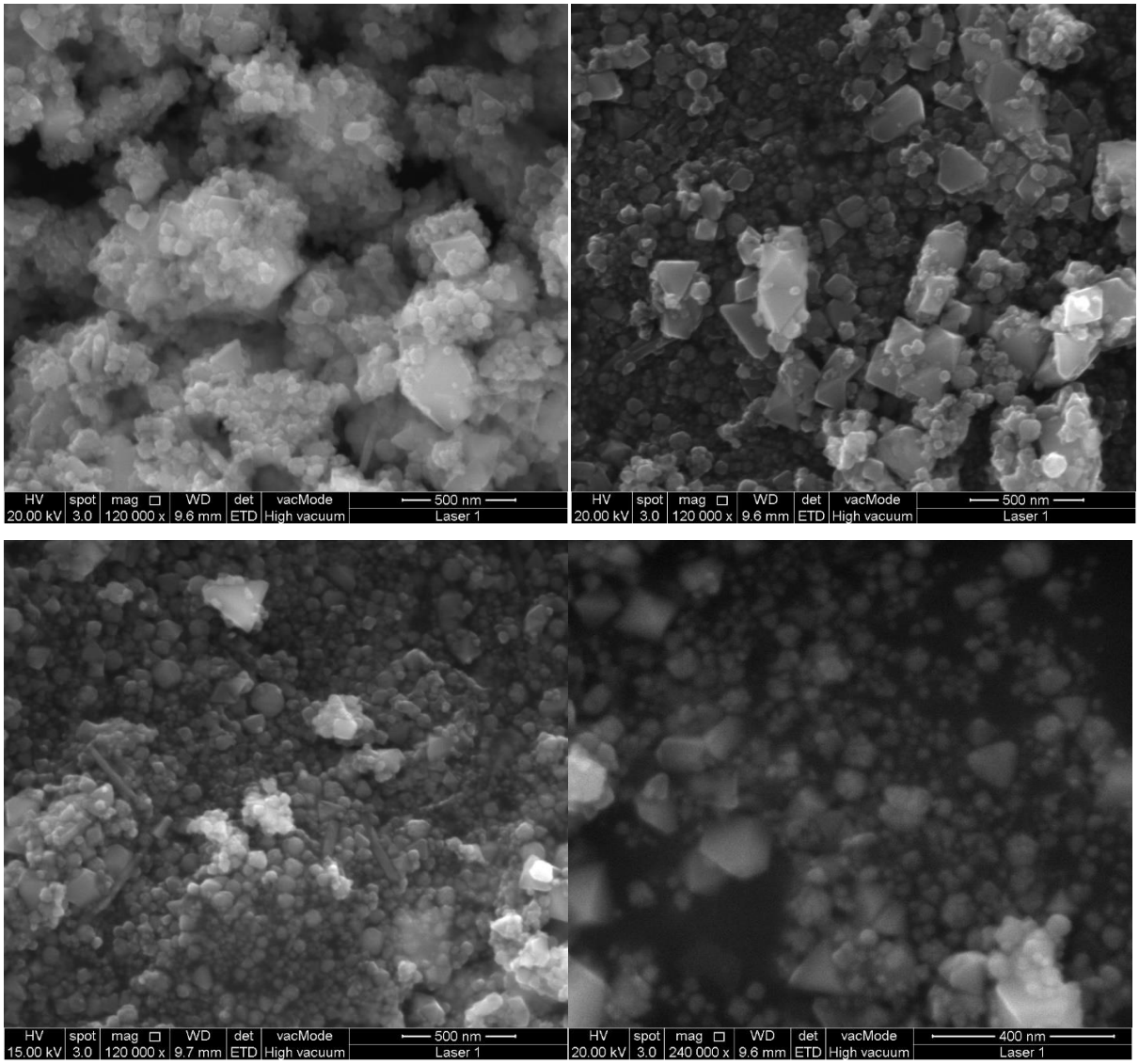


Figure 5.11: Nanoparticles produced in the aluminium well. Smaller spherical particles can be seen, but most of the larger ones are pyramidal/bipyramidal.

It should be noted that, unlike the rest of the devices, the aluminium well has an opaque, reflective bottom. The laser passes through the liquid twice, although it is likely defocused after reflection. Although the depth of the well is 1.5 mm, the effective optical path length here is longer, effectively increasing the intensity of the laser in the solution.

The polydispersity itself is not surprising when looking the difference between the well diameter (3 mm) and the laser beam diameter at the focal point (~20-40 µm). With a difference of 2 orders of magnitude, strong temperature gradients can be expected within the well.

The particle shapes and sizes are similar to those found after the decomposition of FeOl in olive oil (section 3.4.4) albeit cleaner and with less agglomeration. Many of the smaller particles appear to be

spherical, while the larger ones are exclusively pyramidal or bipyramidal. It is unclear if the growth of pyramidal shapes was due to the lack of surfactant, higher energy density or other factors such as the presence of the aluminium. As this stationary synthesis was not the main focus of the study, no further work was done. However, there is room for investigation here, as many of the larger particles show a well-defined bipyramidal shape.

5.3.2 Well array

A 5 mm thick acrylic plate was cut to the width of a standard microscope slide (26 mm). An array of wells was milled on to one side of the sheet. Each well has a diameter of 2 mm and a depth of 0.5 mm. They are arranged as a grid with a separation of 5 mm on each axis.

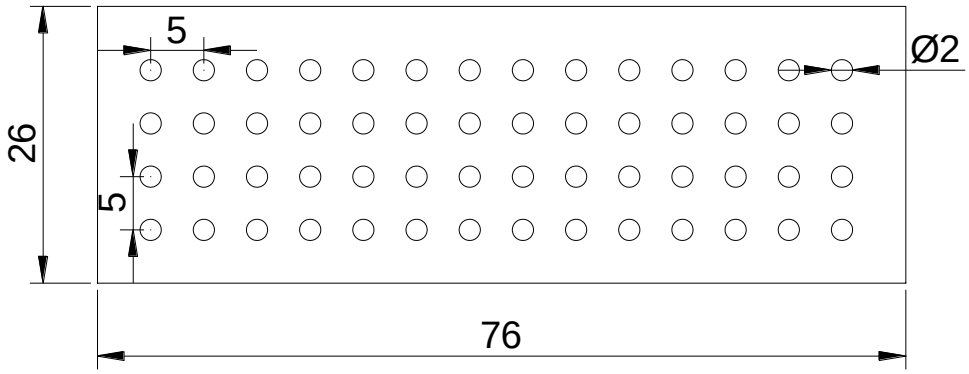


Figure 5.12: Design of the acrylic well array. All dimensions are in mm.

The wells were made using a 4-fluted endmill with a diameter of 2 mm, on a manual milling machine. The actual depths of the wells were found to vary from ~0.5 mm to ~0.7 mm.

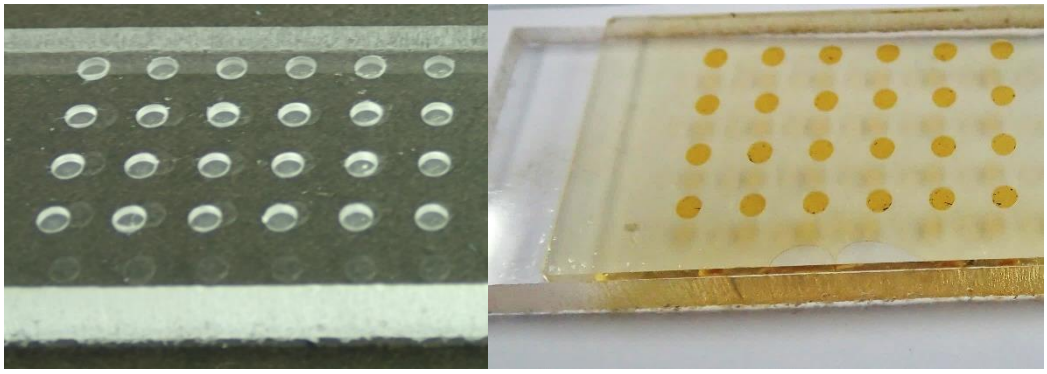


Figure 5.13: (Left) Acrylic well array as fabricated. (Right) Well array filled and sealed.

The wells were filled and sealed with a standard glass microscope slide (Figure 5.13) using the excess liquid. 18 wells of similar depth were chosen and divided into 6 groups. Each group was heated for different periods at full power: 30, 60, 90, 120, 180 and 300 seconds.

A magnet was held near the slide and it was observed under a microscope. Magnetic particles were observed in most cases, however there are several issues with this approach. The magnetic particles, following the magnet, were also found within the thin liquid layer sealing the chip, meaning that there was cross contamination among the wells. When remove the glass slide, most of the solution stuck to it due to surface tension, making it impossible to recover separately.

In general, the amount of magnetic material grew as the heating time was increased. As individual particles are too small to be seen with an optical microscope, we assume what was observed was agglomerations as they did not disperse when the magnet was removed. A large elongated particle, with an estimated size of ~400 µm * 40 µm, was seen in one of the 300s wells, with one end attached to the well bottom while the other end followed the magnet. The growth of such a large particle shows that the surfactant was ineffective at keeping the controlling particle growth at these temperatures.

5.3.3 Long-necked wells

Due to the difficulty in recovering samples from the well array, individual wells were made. The new design aimed to increase yield by increasing the depth of the well, and to improve sample recovery.

The wells were fabricated using 2.3 mm thick acrylic and each well has a diameter of 3mm and a depth of 1mm. The well is located at the end of a long thin neck (22.35 mm * 4.5 mm), which is designed to fit within the opening of a GC vial. The wells can be dipped in hexane within the vial to dilute the solution, recovering almost 100% of the sample.

The chips were fabricated on a Bungard CCD CNC machine, using the following settings:

Table 5.2: CNC settings used to fabricate the long-necked wells.

Spindle speed	30,000 rpm
XY speed (horizontal movement)	1000 mm/min
Z speed (vertical movement)	300 mm/min
Tool	Single-flute spiral endmill (carbide)
Tool diameter	3 mm

Fabricated wells were found to have depths between 1.00 mm to 1.10 mm, due to limitations of the machine and variations in the thickness of the acrylic sheet itself.

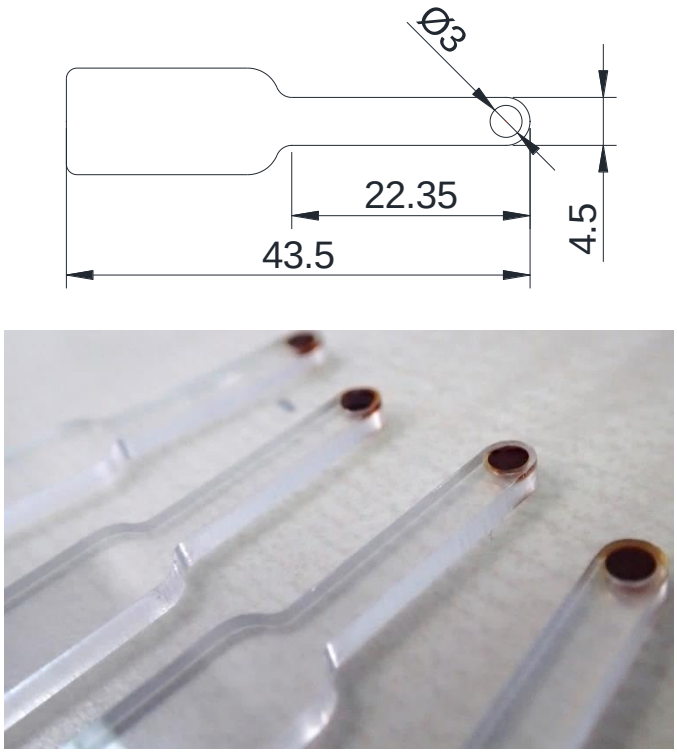


Figure 5.14: (Top) Design of the long necked well (units: mm). (Bottom) Fabricated and filled wells.

The typical volume of the well was ~7 µL. After loading the well, it was placed so that laser beam was pointed at the centre of the well. In this case the wells could not be sealed due to the small size of the neck. If the laser was focused on the surface of the liquid, it caused violent bubbling and evaporation. To avoid this the laser was focused 0.2 mm below the surface of the solution.

When heating the well in the centre, the yield was too low to be noticeable, and generally difficult to find in the SEM. The purification process which precipitated the FeOl as well made it even harder to find the particles. A program was developed in MATLAB to control the stage so that the laser sweeps across the well to heat up more of the solution (Figure 5.15). The smaller the spacing between the sweeps, the more sweeps are conducted across the well.

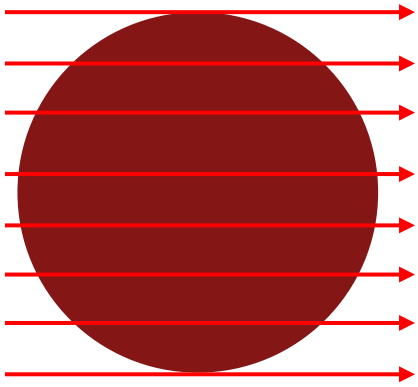


Figure 5.15: Laser sweep pattern across the 3mm well.

Different velocities and spacings were tried (Table 5.3). The solution was purified using multiple acetone-hexane cycles while allowing the particles to settle beside a magnet. Magnetic material was observed in most cases.

Table 5.3: Sweeping synthesis experiment details

Sample	Velocity (mm/s)	Spacing (mm)	Magnetic material seen	Individual particles seen in SEM
1	1.0	0.250	N	N
2	1.0	0.100	Y	N
3	1.0	0.050	Y	N
4	1.0	0.025	Y	Y
5	0.5	0.500	Y	N
6	0.5	0.100	Y	N
7	0.5	0.050	Y	Y

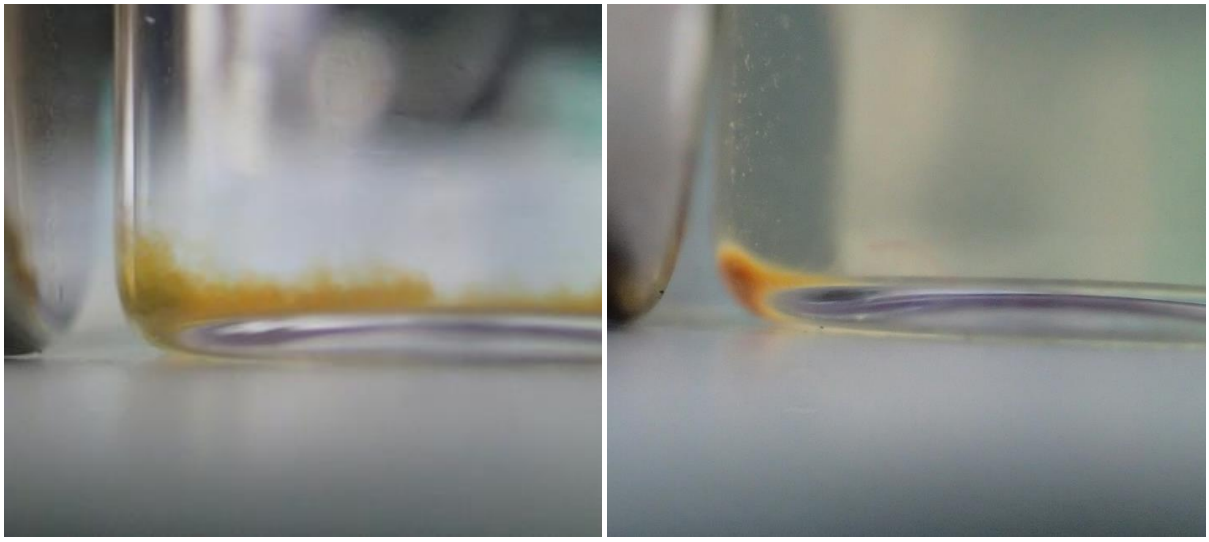


Figure 5.16: (left) Magnetic material seen in sample 2 and (right) sample 3 synthesised in the individual long necked wells. Synthesis parameters for these sample are presented in Table 5.3.

While this did result in an improved yield over the stationary heating route, results were found to be inconsistent and had poor repeatability. In most cases where magnetic material was seen, the particles observed in the SEM were highly agglomerated and embedded in the residual FeOl due to the incomplete decomposition. In two of the samples (4 and 7), we were able to observe individual particles (Figure 5.17 and Figure 5.18) although still agglomerated.

The stationary synthesis approach was discontinued after this set of experiments due to the low yields and inconsistent results. The residual FeOl and oleic acid sticking to particles is a problem that would continue to be an issue in future synthesis runs.

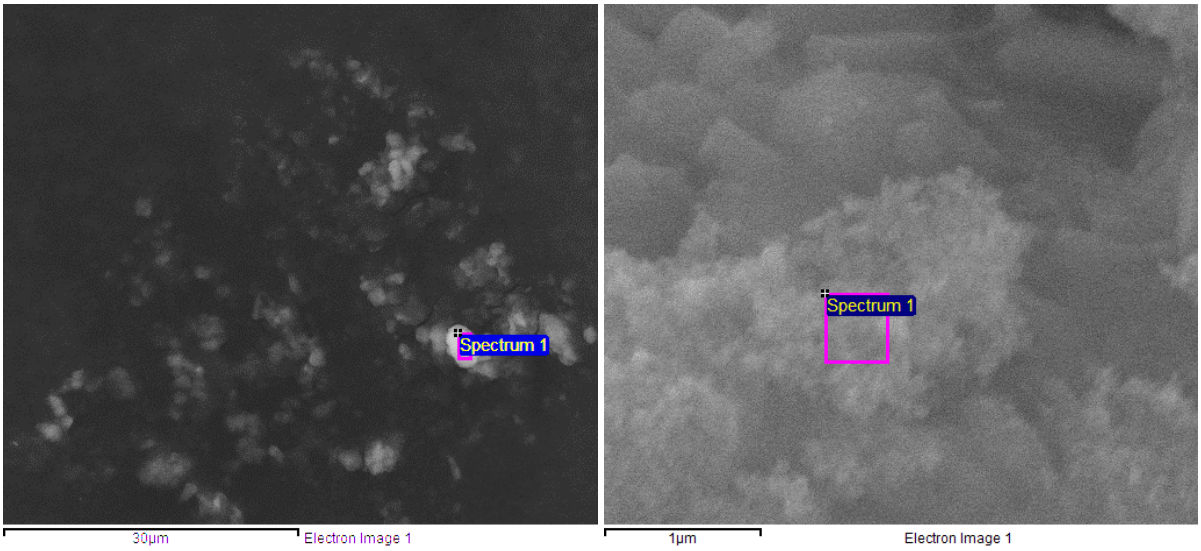


Figure 5.17: Particles seen in sample 4 synthesised in the long neck well. Particles are agglomerated and difficult to differentiate. Synthesis parameters for this sample are presented in Table 5.3.

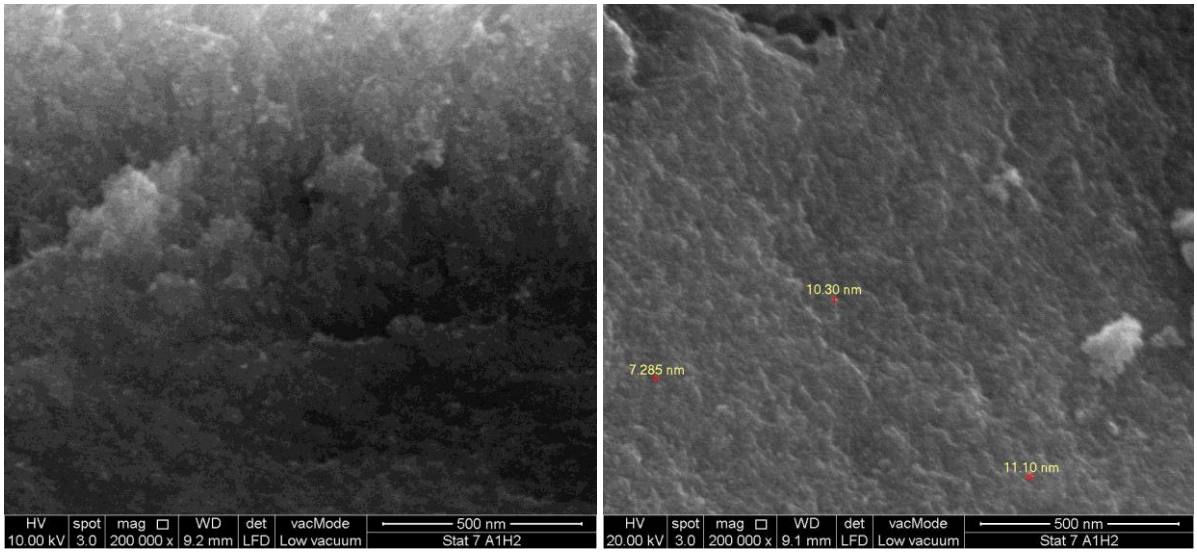


Figure 5.18: Particles seen in sample 7 synthesised in the long neck well. Particles are agglomerated but can be differentiated. The average size of the particles is in the 10 nm range. Synthesis parameters for this sample are presented in Table 5.3.

5.4 Straight channel continuous flow device

This section describes synthesis runs carried out in the straight channel chips. The fabrication of these chips is detailed in in section 4.2.

5.4.1 Synthesis

After bonding, and before each run, the chip was cleaned as follows:

1. Rinse with hexane.
2. Rinse with distilled water.
3. Rinse with isopropanol.
4. Dried overnight in a dryer set to 70° C

The solution used in this synthesis run was the O solution (section 5.2), which contains iron oleate and oleic acid in a 1:1 molar ratio in octadecene. 1.5 mL of the solution was loaded in a 5 mL syringe (Terumo) and connected to the inlet via a 0.8 (I.D.) mm tube. The syringe was placed in a syringe pump (KD Scientific KDS-200) which was set to 50 µL/min. The chip was placed on the stage with the laser pointed at the centre of the channel. The height of the stage was set so that the top of the channel was in the focal plane. For safety reasons, during all alignment processes the laser power is set to 5% (13/255), the minimum value at which the beam was visible.

The pump was then started. After the solution passed the focal point, the laser power was set to 100%. The solution dropped into a vial after leaving the chip. After 30 minutes, the entire volume was pumped through and the laser was turned off.

5.4.2 Results and discussion

From our experiences with the stationary synthesis, purification using acetone would most likely cause sample loss as the residual FeOl would also precipitate with the nanoparticles. In this case, the solution was diluted in 5 mL of hexane and a magnet was brought near the vial. A few fuzzy looking translucent grey specks were observed moving towards the magnet. Once they were pulled together, they did not separate after the magnet was removed. The overall amount was extremely small for the volume of solution used; the particle appeared no bigger than 1 mm^3. When trying to recover this particle it broke up and redissolved. This was likely a collection of iron oxo-clusters.

The main cause for the low yield is the size of the laser spot compared to the width of the channel. A 40 µm laser spot in a 500 µm wide channel only heats up ~8% (0.12/1.5 mL) of the flowing solution.

In addition, due to the shallowness of the channel, the linear velocity of the solution is quite high:

$$Channel\ cross-sectional\ area = apprx.\ 500\ \mu m * 200\ \mu m = 0.1\ mm^2$$

$$Flow\ rate\ = 50\ \mu L/min\ = 50\ mm^3/min$$

$$Average\ velocity\ = \frac{(Flow\ rate)}{(Cross-sectional\ area)}$$

$$= \frac{50\ mm^3/min}{0.1\ mm^2} = 8.3\ mm/s$$

The peak velocity in a laminar flow profile is twice the average velocity. As the laser was pointed at the centre of the channel, the velocity can be expected to be close to 16 mm/s. At that velocity the solution crosses the ~40 µm beam in approximately 2.5 ms.

The experiment suggests this is not enough time for particle growth to progress. Nucleation does occur as the particle is clearly magnetic. Its translucent appearance suggests the presence of very small particles bound together by oleate groups.

A point to note is that because only a small portion of the solution is heated, the nucleating particles possibly experience a much higher Fe:Oleic acid ratio than the bulk mixture would suggest.

Two more synthesis runs at lower flow rates (10 µL/min and 5 µL/min) were conducted with no noticeable improvement in results.

Due to fabrication limitations we were unable to make the channel smaller. Without that major improvement, this approach was too inefficient and thus discontinued. This led to the design of the vertical flow channel described in section 4.3.

5.5 Summary

Laser synthesis was successfully carried out in an aluminium well, however the particles had a wide range of shapes (spherical, bipyramidal, among others) and sizes (~5-500 nm) due to the uneven heating and complete lack of flow. Stationary synthesis was also attempted in shallower wells made in acrylic but found limited success. While magnetic particles were seen within the wells using a microscope, further analysis was not always possible because recovery of the solution was difficult due to the extremely small volumes. Attempts were made to improve the yield by sweeping the laser beam across the well to heat up more of the solution, but this approach was not consistently repeatable.

Using the straight channel device, nucleation and minimal growth of magnetic material was observed. Due to the width of the channel, only a small portion of the solution was heated under the laser, resulting in a very low yield which could not be recovered. Even if this problem was overcome with a narrower channel, the residence period of the solution under the laser was too low to allow for significant growth. The shortcomings of the straight channel device led to the design of the vertical flow channel used in Chapter 6.

6 Microfluidic synthesis of iron oxide nanoparticles in vertical flow chips

This section describes the synthesis carried out in the vertical flow chips. The design and fabrication of these chips is described in section 4.3.

6.1 Flow rate and residence times

The main advantage of this design is greater control over the residence time of the solution under the laser. The relationship between the residence period and volumetric flow rate (set on the syringe pump) is determined by the volume of the reaction chamber.

The diameter of the cylindrical chamber is determined by the diameter of the drill bit (0.7 mm). Its height is the same as the height of the middle layer. Its volume V_{rc} is therefore:

$$V_{rc} = \pi r^2 h$$

$$V_{rc} = \pi * \left(\frac{0.7\ mm}{2}\right)^2 * 2.3\ mm$$

$$V_{rc} = 0.885\ mm^3$$

The volumetric flow rate Q is set in the syringe pump. Since the chip only has a single fluid path, it can also be defined as:

$$Q = V_{rc}/t_r$$

Where t_r is the residence period of the solution in the reaction chamber. We can use this relationship to calculate the required volumetric flow rate from the desired residence period.

Note that this is based on simplified calculations based on volumetric flow rates, for the sake of determining different flow rates. It is assumed that a parabolic velocity field exists within the cylindrical channel, hence the velocity at the centre of the channel will be higher than the average velocity. Thus, the solution is expected to experience a range of residence periods.

6.2 Methodology

This section details the continuous flow synthesis done using the vertical flow chips. The B, O, and N solutions prepared as described in section 5.2 were pumped through the chip at different flow rates while being heated by the laser. The same experimental setup (section 5.1) is also used here.

All synthesis runs were completed using 100 µL of the solution. This amount was chosen based on observations from previous experiments (Chapter 5), as well as preliminary tests conducted in the vertical flow channel. The amount results in sufficient yield for analysis, limits reactor damage (especially in high residence period runs), and limits laser on-time which helped avoid overheating.

A 1 mL syringe (Terumo) was filled with the required solution and connected to the inlet of the chip. The syringe was placed in the syringe pump and manually pushed until the reaction chamber was filled and solution had flowed beyond it. The required flow rate and volume was entered.

The stage height was set to 0 mm, and the chip was placed on the stage. The laser was turned on at 5% intensity and the chip was positioned so that the laser hit the centre of the reaction chamber. The syringe pump and the laser, now at 100%, were turned on simultaneously. After 100 µL of the solution had flowed through, the pump the laser was turned off together. The solution was pumped out using air. This typical flow synthesis process for a single run is shown in Figure 6.1.

After each run the chip was cleaned by flowing ~1 mL of hexane through the channel. The remaining hexane is pumped out using air and the channel was either dried overnight or using compressed air if used immediately.

In some cases, notably when using the B solution, precipitates were seen in the channel even after washing. They were broken up by filling the channel with hexane and placing the chip in a bath sonicator for 10 minutes.

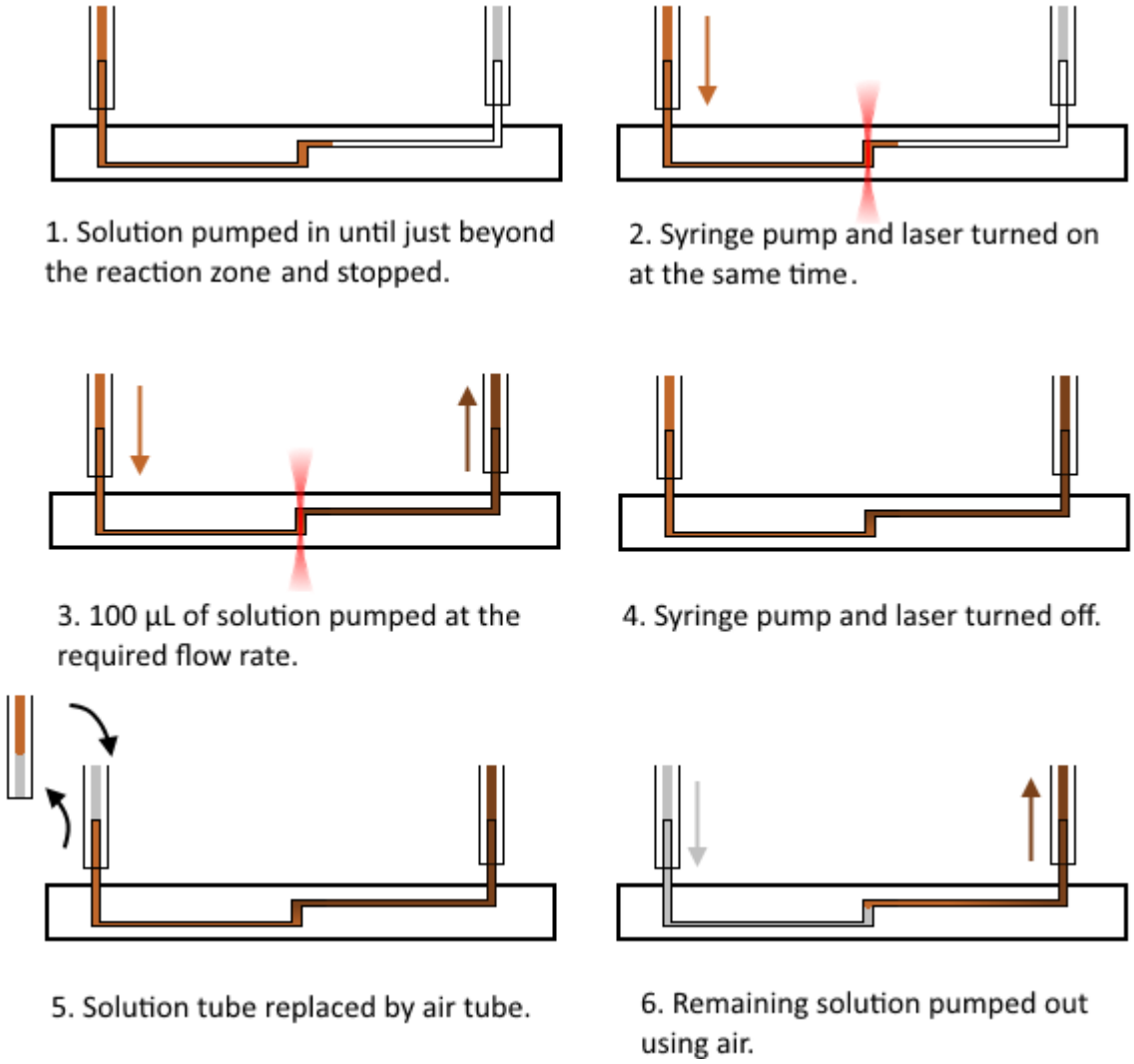


Figure 6.1: Typical flow synthesis process for 100 µL runs in the vertical flow chips.

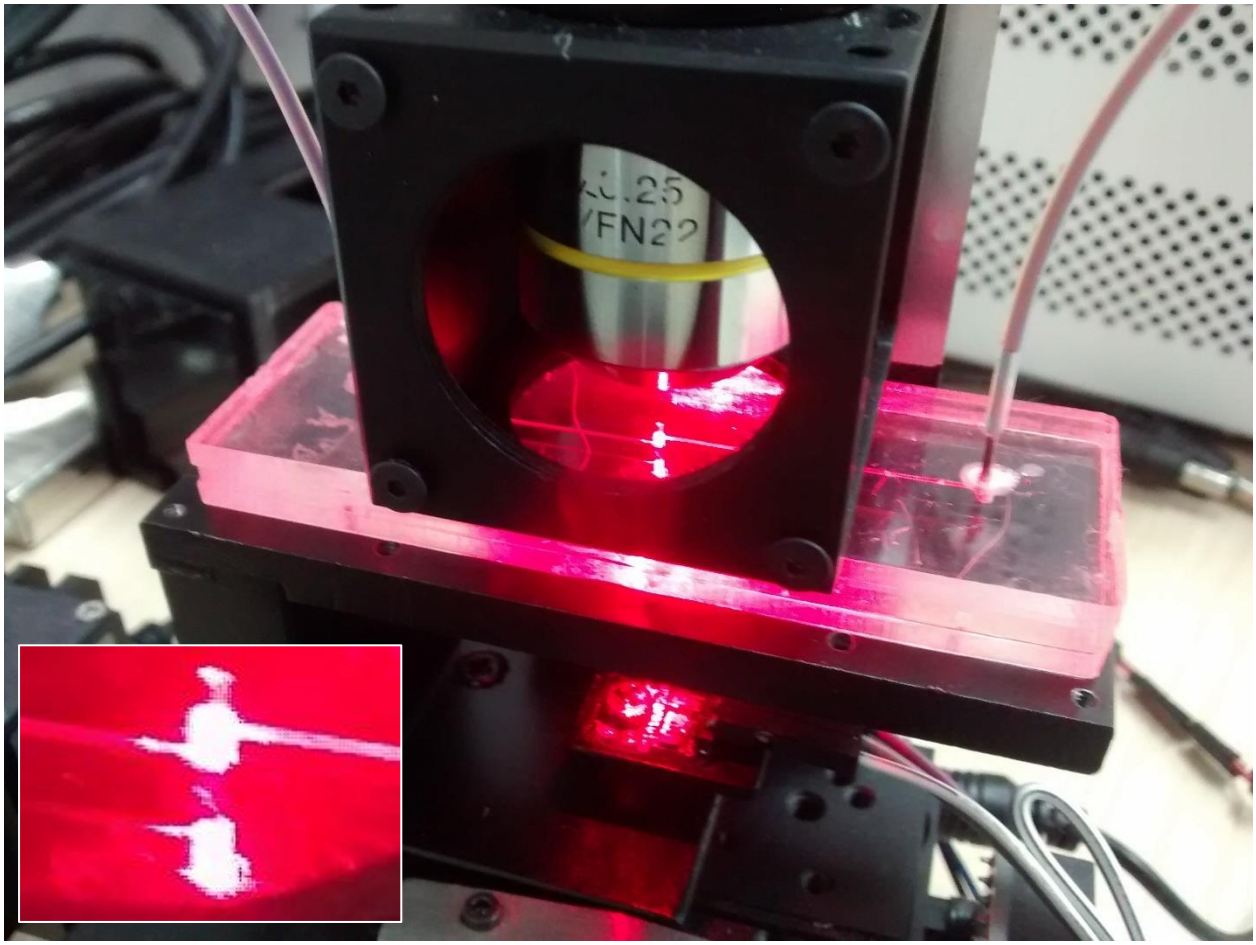


Figure 6.2: The vertical flow chip setup after a synthesis run (the laser power is set to minimum while taking this photograph). Inset: A close-up of the reaction chamber. The inlet, reaction chamber, and outlet channels can be clearly seen. The image at the bottom is the reflection of the channel from the bottom surface of the chip.

6.2.1 Purification

The use of pure acetone for nanoparticle precipitation works well for batch synthesis products when the solution has little or no remaining FeOl. However, in our microfluidic synthesis runs so far have resulted in partial decomposition and even though the yield is much higher, the samples from this section are no exception.

Early tests using just acetone for purification resulted in large spherical FeOl bubbles or “micelles” being formed which trapped the formed particles within them. It was possible to break up them up by sonication, but they usually resulted in the formation of smaller ones. This has not been problem for most authors in the literature as bulk synthesis typically results in complete decomposition. In this case, we have several by-products including remaining FeOl, FeOl decomposition products, and saturated and polymerised OA (further details can be found in section 6.5).

The samples produced in this chip were purified instead using a solvent/precipitant mixture which aims to prevent the formation of the micelles in the first place. There are two methods that were followed:

Method 1 used a 3:1 mixture (by volume) of ACE:HEX. For each run:

1. 1 mL of the mixture was added to the heated solution and shaken by hand.
2. The vials were placed next to a strong neodymium magnet and allowed to settle for several hours.
3. The supernatant was carefully pipetted out. This step removes most of the original ODE and soluble by-products.
4. 1 mL of the mixture was added to the precipitates and shaken.
5. The vials were placed next to a magnet until settling occurred.
6. The magnetic particles settle next to the magnet while the non-magnetic by-products settle down.
7. The supernatant and free by-products are carefully pipetted out.
8. Steps 4-7 are repeated three more times.
9. Finally, pure HEX was added, and the precipitates were dispersed by 30s of sonication using a probe sonicator.

This method often resulted in the formation of large FeOl spheres and a largely organic network, especially in the O solutions. The probe sonication was determined to be a major cause of this. Additionally, magnetic separation in the presence of octadecene was very slow. For some of the higher residence period samples (t_r = 6,8), the 3:1 mixture was inadequate in inducing precipitation. Thus, the second method was developed.

Method 2 used a 7:1 mixture of ACE:HEX:

1. 1 mL of the mixture was added to the heated solution and shaken.
2. The solution was gently centrifuged at 1500 rpm for 30 minutes.
3. The supernatant was carefully pipetted out. This removes the original ODE much faster.
4. 1 mL of the mixture was added to the precipitates and shaken.
5. The vials were placed next to a magnet until settling occurred.
6. The magnetic particles settle next to the magnet while the free by-products settle down.
7. The supernatant and free by-products are carefully pipetted out.
8. Steps 4-7 are repeated three more times.

9. After the addition of pure HEX, the precipitates were dispersed by low power sonication in a water bath.

The precipitates were insoluble in HEX in both cases, however, they stayed suspended for a longer time using the second method and resulted in cleaner STEM images as well.

6.3 Synthesis

6.3.1 Preliminary tests

Preliminary synthesis runs were performed to determine a suitable starting point for the flow rate. These samples were not analysed in detail. The first four chosen residence periods and their corresponding flow rates are shown in Table 6.1.

Table 6.1: Residence periods and calculated flow rates for the preliminary microfluidic synthesis runs

Sample	Residence period (s)	Flow rate (µL/s)	Flow rate (µL/min)	Total time (s)	Total time
1	0.5	1.770	106.22	56	57s
2	1.0	0.885	53.11	113	1m 53s
3	1.5	0.590	35.41	169	2m 50s
4	2.0	0.443	26.55	226	3m 46s

The O solution (using only OA as the surfactant) was used in this batch. Samples were prepared using the flow rates in Table 6.1. All samples were purified using Method 1 detailed in section 6.2. Samples were prepared for SEM by dropping ~5 µL of the HEX-based suspension on a stub covered with carbon tape and allowing the solvent to evaporate. No further analysis was done for this batch of samples.

Photographs were taken of the vials after step 2 of the purification process, i.e., the first precipitation was done, but no material was removed. This was done to visually compare the extent of the reaction. Figure 6.3 shows these photographs. A clear increase in the amount of magnetic material can be seen going from sample 1 to 4. Additionally, sample 4 shows a clear separation of the particles from the residual FeOl, while in the other samples the entire body of the precipitate is attracted to the magnet. Due to this separation, sample 4 could be purified to greater extent.

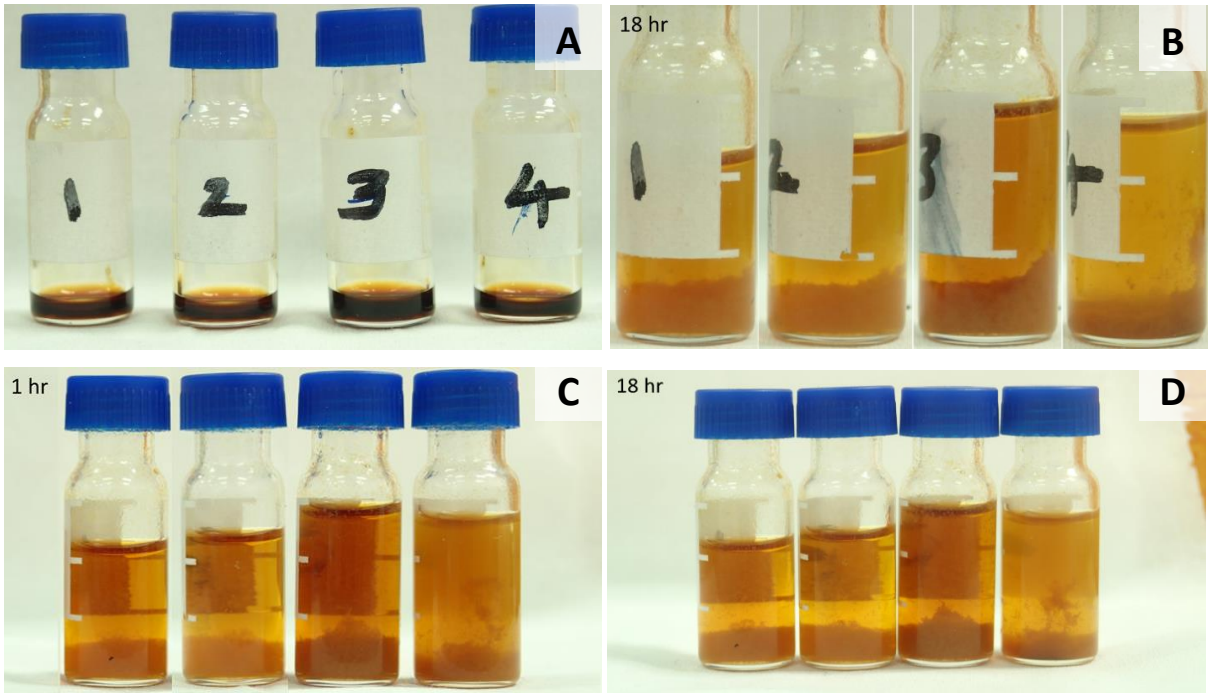


Figure 6.3: (A) The four preliminary samples (from Table 6.1) after synthesis. Each vial has ~100 uL of the heated solution. The samples were purified twice and allowed to settle beside a magnet. (C) Front view of the precipitates after 1 hour. (B) Side view of the precipitates after 18 hours. (D) Front view of the precipitates after 18 hours of settling.

The SEM results show a similar trend. Individual particles could not be found in samples 1 and 2. A few individual particles could be seen in sample 3 (Figure 6.4) but they were part of a larger network. Large spheres (2-3 µM) were also found. EDX analysis of the sphere confirmed higher amount of iron and oxygen than in the network.

Although the particles in sample 4 were purified more, they still form agglomerations. The SEM images show spheres as large as large as 500 nm, however the thick coating binding them together makes it unclear whether they are large individual particles or a multiple smaller ones together. The true size of the particles cannot be determined by surface imaging alone.

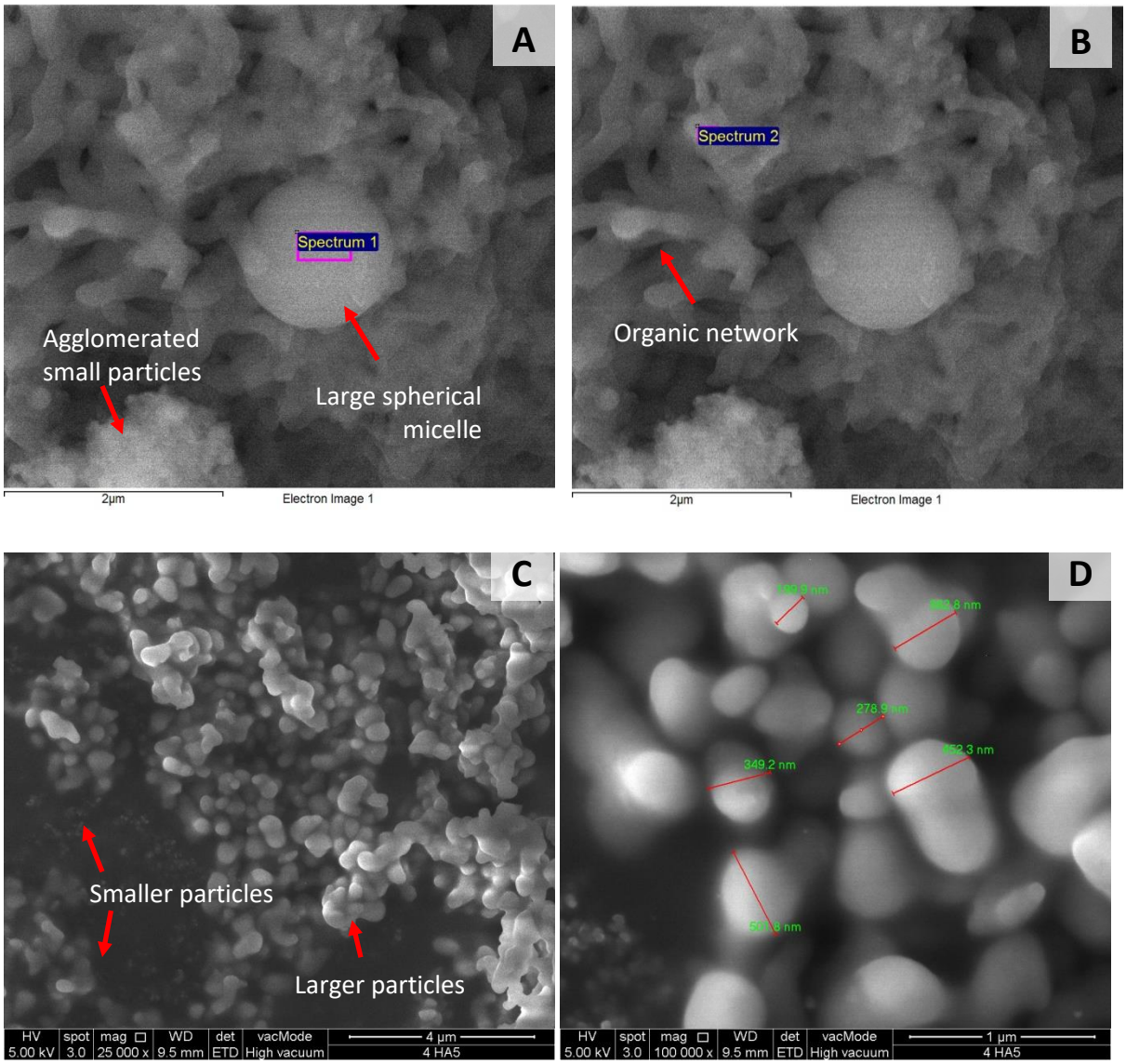


Figure 6.4: (A and B) Two sites chosen for EDX analysis in sample 3. (C and D) Particles seen in sample 4. Sample 3 shows few individual particles. While spherical particles can be seen in sample 4, they are still agglomerated and coated in a thick layer of FeOl and/or oleic acid.

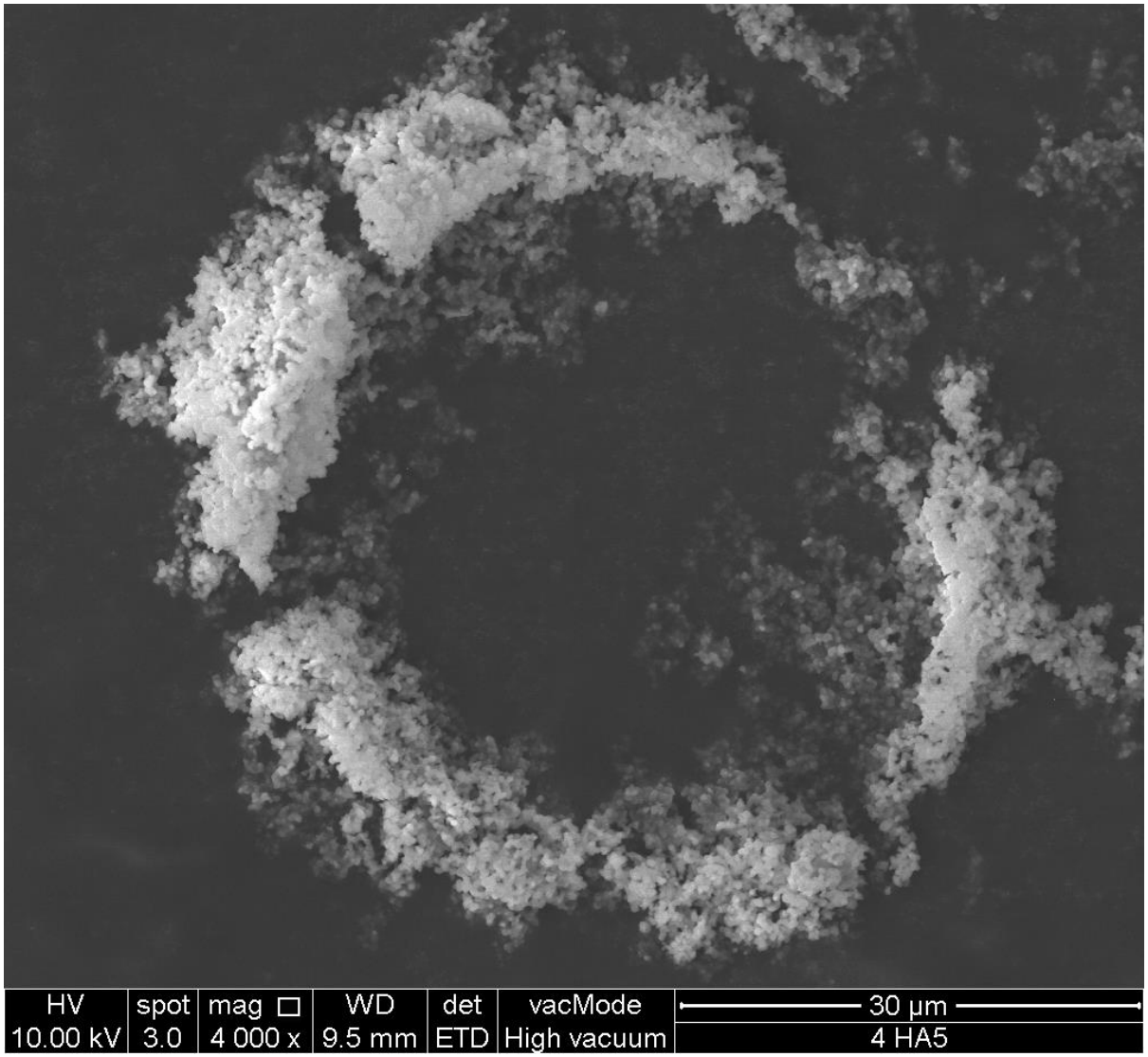


Figure 6.5: Low magnification SEM view of the iron oxide nanoparticles in sample 4, produced by microfluidic laser synthesis.

Figure 6.5 shows an overall view of one of the deposition sites of the particles found in sample 4. EDX elemental mapping of this view was conducted, shown in Figure 6.6. As expected from iron oxide, iron is clustered at the deposition site, which also shows a higher oxygen concentration compared to the rest of the region. The carbon tape substrate accounts for most of the carbon seen here.

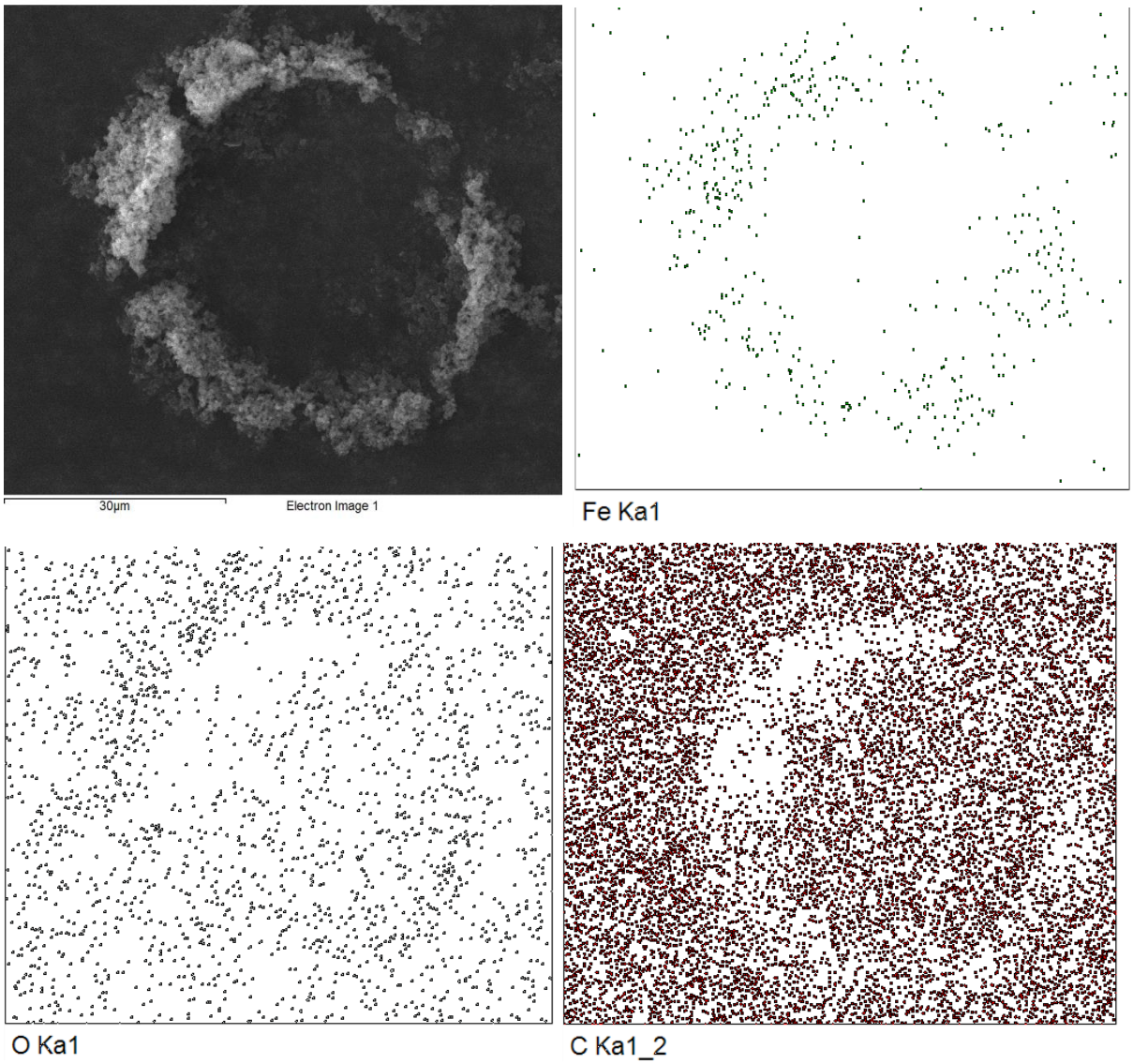


Figure 6.6: EDX elemental mapping of the region seen in Figure 6.5, showing nanoparticles from sample 4, produced by microfluidic synthesis. Iron (Fe) and oxygen (O) can be seen on the particles, while most of the carbon (C) counts come from the carbon tape that the sample was deposited on.

6.3.2 Final batch

The B, O, and N solutions were prepared as described in section 5.2. Following the results from the preliminary tests, a residence time of 2s was chosen as the minimum. The O and N solutions were heated for 2, 4, 6, and 8 seconds. The B solution was only heated for 2 and 4 seconds; synthesis with higher residence periods were cancelled for this solution due to high levels of sedimentation and agglomeration. The flow rates were calculated as described in section 6.1 and are listed in Table 6.2.

Table 6.2: Average residence periods and calculated flow rates for the final batch. The total volume is 100 µL

Average residence period	Flow Rate (µL/min)	Total time (s)	Total time
2 s	26.55	226	3m 46s
4 s	13.28	452	7m 32s
6 s	8.85	678	11m 18s
8 s	6.64	904	15m 04s

The experiment was repeated three times for each solution and residence period. Early samples were purified using the first method. The later samples could not be precipitated using the first method hence the second method was developed. These methods are described in section 6.2.1.

The list of samples, as well as the purification method used is shown in Table 6.3. The samples are named using the format (*solution*)(*residence period*) – (*repetition*), e.g. sample O6-2 is produced from the O solution, its residence period is 6s, and it is the second repetition of this combination.

Table 6.3: Names of samples produced. The purification method used is distinguished by the colour of the cells in the table. Method 2 is a gentler purification method adapted to reduce agglomeration during separation. These methods are explained in greater detail in section 6.2.1.

Method 1		**Method 2**			
Solution	**Residence period**	**Repetitions**			
		1	**2**	**3**	**4**
B	**2 s**	B2-1	B2-2	B2-3	
	4 s	B4-1	B4-2	B4-3	
O	**2 s**	O2-1	O2-2	~~O2-3~~	O2-4
	4 s	O4-1	O4-2	~~O4-3~~	O4-4
	6 s	O6-1	O6-2	O6-3	
	8 s	O8-1	O8-2	O8-3	
N	**2 s**	N2-1	N2-2	N2-3	
	4 s	N4-1	N4-2	N4-3	
	6 s	N6-1	N6-2	N6-3	
	8 s	N8-1	N8-2	N8-3	

6.3.3 Reactor damage

The samples were prepared using three identical chips. Each chip was used until it was blocked or damaged, rendering it unusable. The samples were prepared as follows:

Chip 1: B2-1, B2-2, B2-3, O2-1, O2-2, O2-3, O2-4, N2-1, N2-2, N2-3, B4-1, B4-2, B4-3*

Chip 2: N4-1, N4-2, N4-2, N6-1, N6-2, N6-3, O4-1 (repeat), O6-1, O6-2, O6-3, O8-1**

Chip 3: O8-2, O8-3, N8-1, N8-2, N8-3**

* The chip was found to be blocked after this sample was prepared.

** After this sample the window of the chip was too damaged for the laser to pass through.

Table 6.4 shows the number of runs at different flow rates conducted in each chip and he total heating time.

Table 6.4: Number of runs conducted per chip and the total time.

		Chip 1		Chip 2		Chip 3	
Residence period	**Run time (s)**	**Runs**	**Total time**	**Runs**	**Total time**	**Runs**	**Total time**
2 s	**226**	14	52 m 40 s	-	-	-	-
4 s	**452**	3	22 m 36 s	4	30 m 08 s	-	-
6 s	**678**	-	-	6	67 m 48 s	-	-
8 s	**904**	-	-	1	15 m 04 s	5	75 m 20 s

The chips were observed under a reflected light microscope (Olympus SZX-7) at various points during their lifespan. In all cases, the diameter of the reaction chamber was found to be 725±35 µm. As more runs were conducted in a chip, an increasing amount of damage was seen on in the acrylic around the reaction chamber. The chip was discontinued from use if the cracks were enough to cause the laser to scatter and cause the edges to glow.

The first chip was blocked after the B4-3 sample was prepared (Figure 6.7). It can be seen that the damage is not only around the reaction chamber, but also above the outlet channel for a short distance downstream.

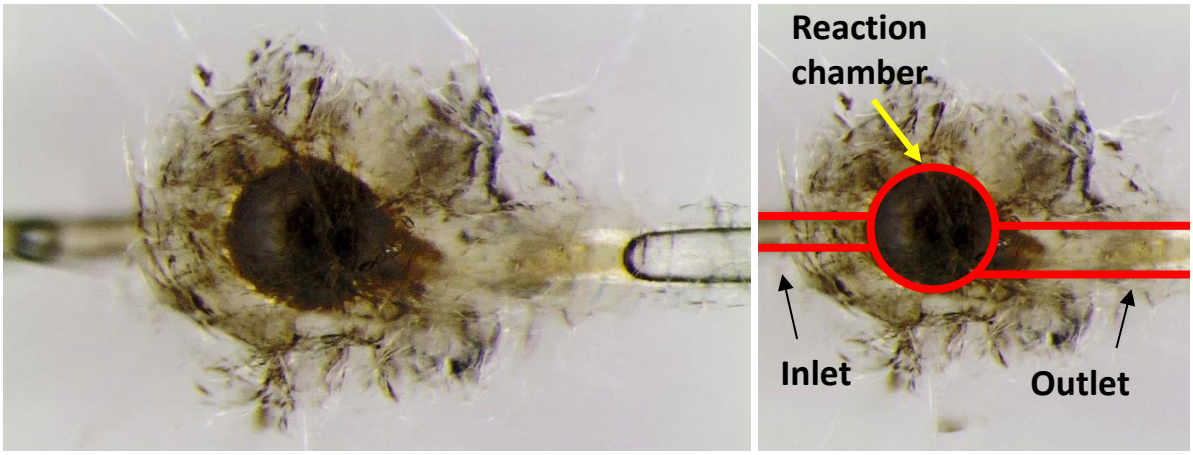


Figure 6.7: (Left) Close-up of chip 1's reaction chamber after it was blocked. (Right) Outlines showing the location of the inlet channel, reaction chamber, and outlet channel.

The second chip showed significant damage around the reaction zone, but its window remained fairly clear until sample O8-1 was synthesised. When synthesising the next sample, the chip was blocked and upon inspection, cracks were seen on the top surface of the reaction zone (Figure 6.8).

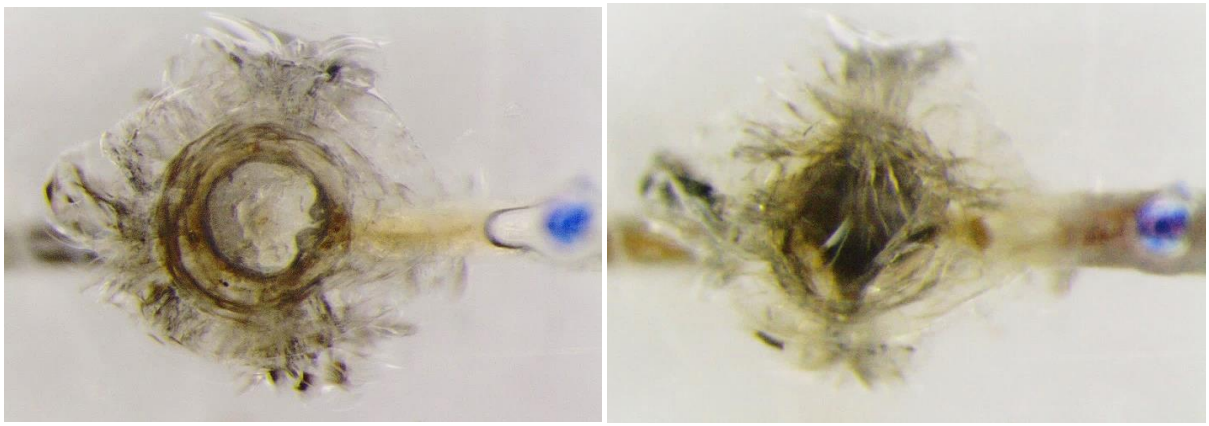


Figure 6.8: Close up of chip 2's reaction zone (left) before O8-1, and (right) after O8-1. The laser beam is pointed at the centre of the circular region, the top window of the reaction zone.

The third chip was used for two O8 and three N8 samples, which placed a lot of stress on it, and we noticed significant damage to the window of the chip after sample N8-3 (Figure 6.9). Cracks can also be seen originating from the outlet channel, showing that the exiting fluid is still hot enough to cause stress fractures in the material.

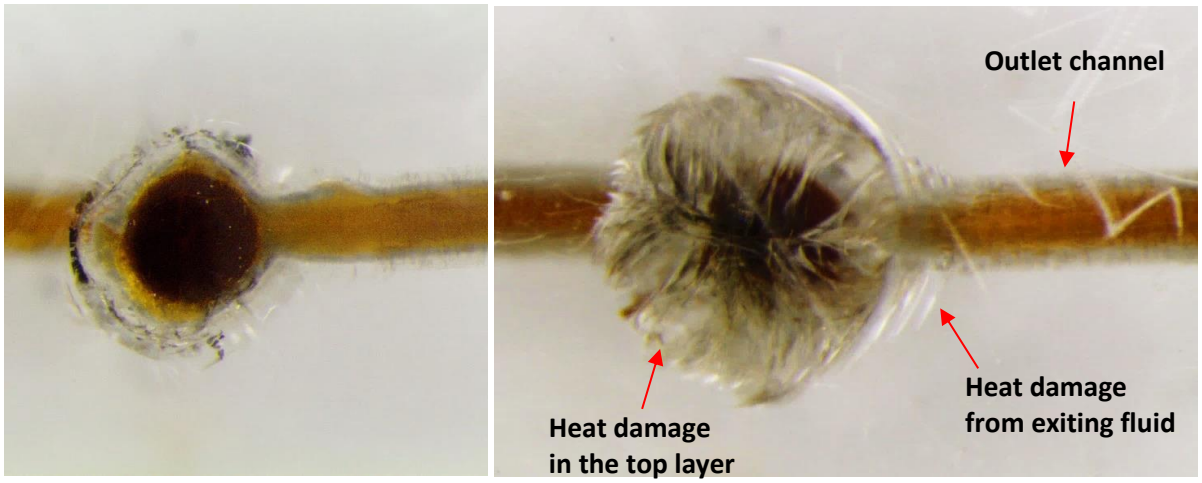


Figure 6.9: Close up of chip 3's reaction zone (left) after O8-2 and O8-3, and (right) after O8-2, O8-3, N8-1, N8-2, and N8-3

Chip 3's sides were sanded and polished, and an image was obtained to observe the damage from the side (Figure 6.10). The damage to the top layer is clearly seen. It appears that some of the solution has in fact risen into a large crack in the top layer.

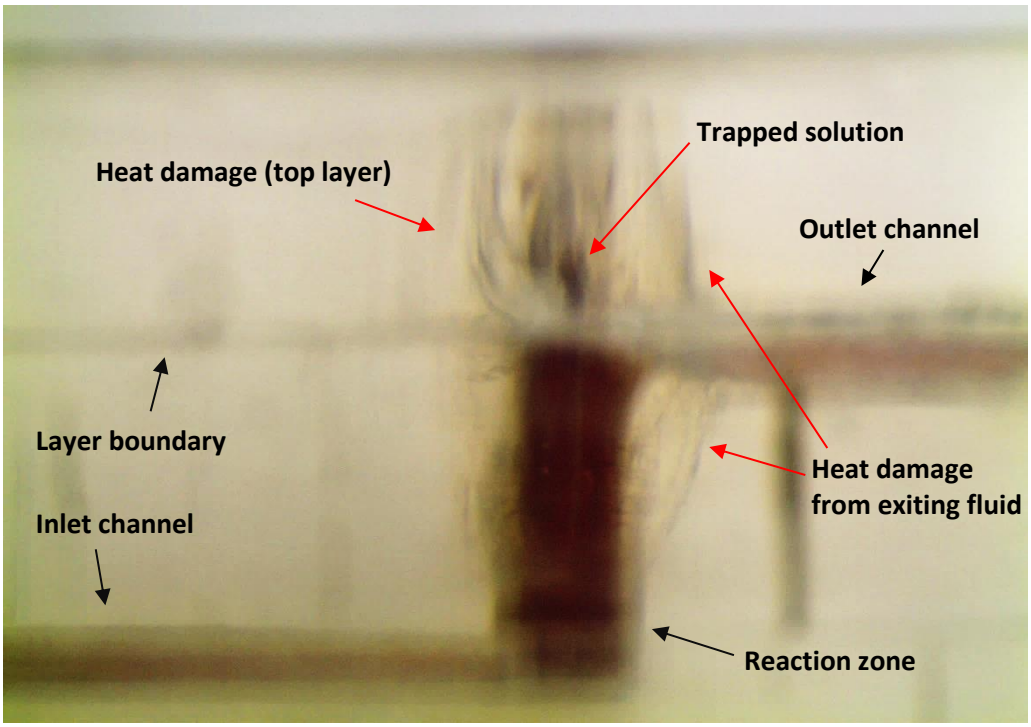


Figure 6.10: Side view of chip 3's reaction zone after sample N8-3. Fracturing can be seen in both the top and middle layers.

It appears the flow rate used for the O8 and N8 experiments approaches the upper limit of what the acrylic chip can handle. The damage in chip 3, compared to chips 1 and 2, is much more focused around the reaction chamber. Since this is the slowest flow rate, it reaches a higher temperature faster and damages the chip quicker, before the heat can spread farther. Once cracks form in the top layer, the solution is sucked in and gets superheated with nowhere to go, causing further damage and blockage of the channel.

We can conclude that using acrylic as a material for this chip, while cheap and usable for quick prototyping and testing, is unsuitable for continuous synthesis, especially at the slower flow rates used for the 6 s and 8 s residence period runs. However, at higher flow rates the chip can last up to ~55 minutes.

6.3.4 Temperature measurement

Temperature measurements were taken during some of the synthesis runs using an IR thermometer (GM320). The measurements were taken by pointing the thermometer at the top surface of the chip centred at the entry point of the laser beam. The thermometer measures the average temperature in a circular area in front of its lens. In our case, the circular area turns into an oval due to the angle of measurement.

Due to the limitations of our setup, the area of measurement also includes parts of the objective lens and the stage. For our calculations we will assume the temperature of those objects does not change. Since they are still part of the average temperature, they will have a dampening effect on the temperature rise seen during the experiment.

Each synthesis run is completed by flowing 100 µL of the sample through the chip. Measurements were taken before starting the flow and after every 10 µL. Immediately after finishing the flow, the chip was removed from the stage, and the actual surface temperature of the chip was measured by holding it up against the thermometer. The chip was allowed to cool to room temperature after each run.

Seen in Figure 6.11 is the temperature rise seen during the flow (the initial temperature subtracted from the measured temperature at each point). The trend can immediately be seen. The final surface temperature rise was ~2 °C, 2.8 °C, 3.7 °C and 4 °C for the 2s, 4s, 6s, and 8s synthesis runs respectively (using the O solution).

It can also be seen that after 100 µL, the system is yet to achieve a steady state as the trend points to further increases in the surface temperature. This is supported by the simulation results in Chapter 7.

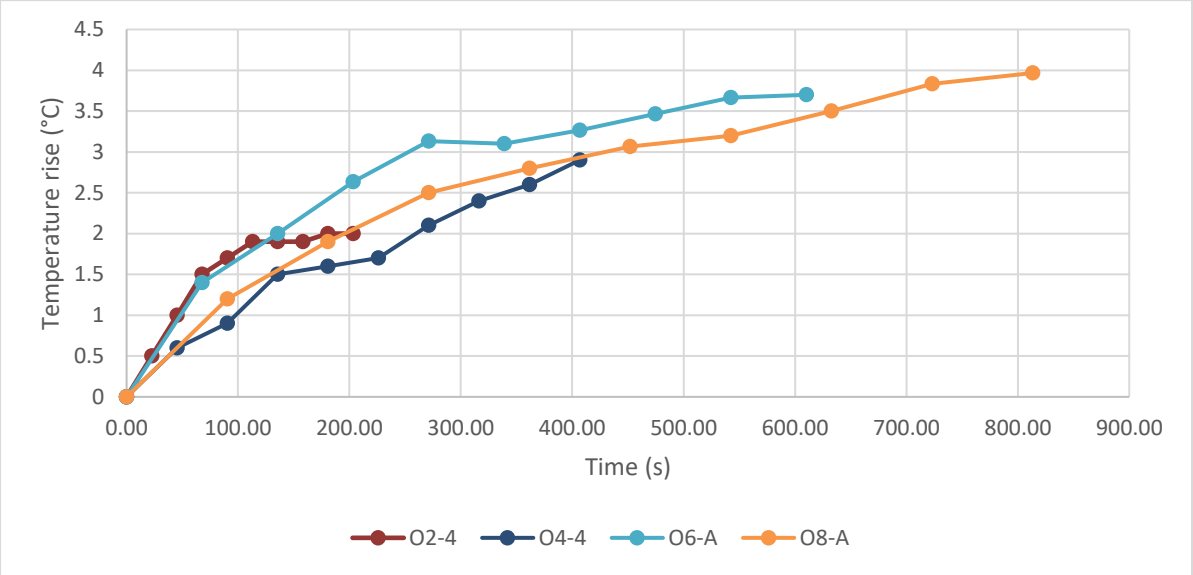


Figure 6.11: Measured surface temperature increase at four different flow rates for the O solution. O8-A and O6-A measurements are averages of 3 runs.

6.4 Results

Regardless of the purification method used, at a macroscopic level the purified material showed the same physical characteristics:

- The B samples precipitated quickly and showed high levels of agglomeration in the form of thick flakes. The precipitates could be broken up by gentle sonication but settled quickly and agglomerated again. This behaviour is not surprising considering the lack of surfactant in this solution.
- The O samples formed a light, cloudy precipitate several times the volume of the original solution, with a small amount of denser agglomerations. If allowed to settle naturally, the precipitate maintained its light cloudy form (Figure 6.12). When the samples were settled beside a magnet, the precipitates compressed under the magnetic field (Figure 6.13), indicating that the by-products form a compressible matrix around the magnetic nanoparticles.
- The N samples produced the densest precipitates (Figure 6.13) which also showed some agglomeration after prolonged settling under acetone. These were easily broken up via low powered sonication.

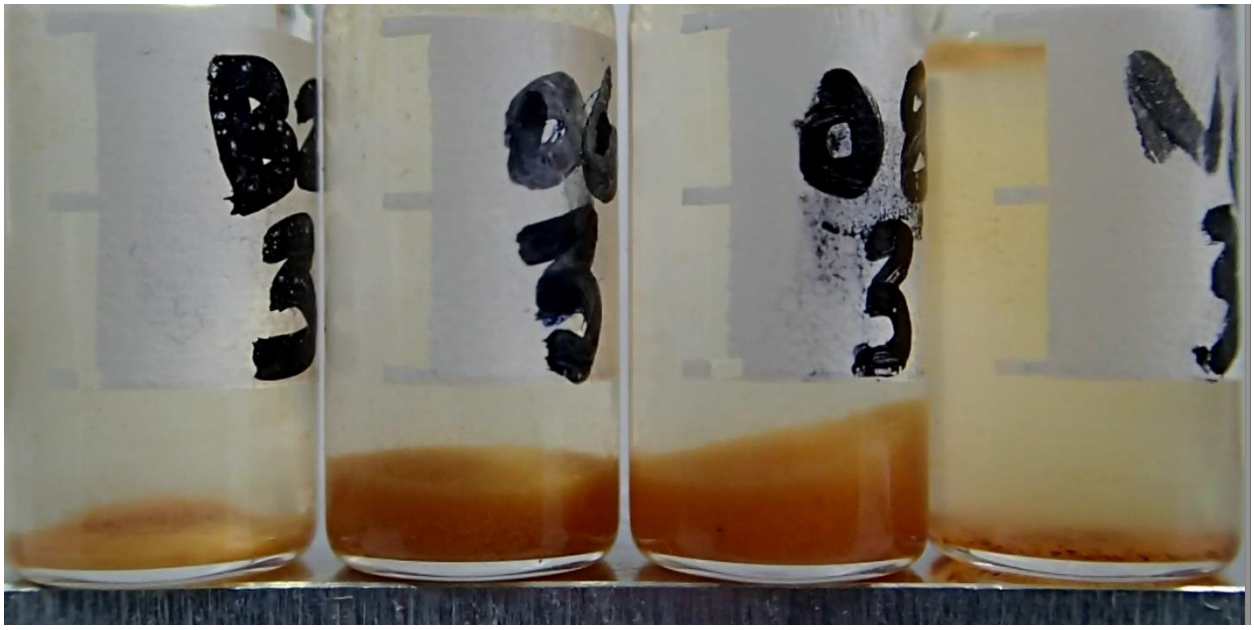


Figure 6.12: Left to right: Samples B2-3, O6-3, O8-3, N8-3 settled after 3 rounds of purification.



Figure 6.13: Left to right: Samples B2-3, O6-3, O8-3, N8-3 after 2 rounds of purification. In this picture, the samples were precipitated beside a magnet.

Characterisation

The reaction solutions were characterised using UV-VIS spectrophotometry. The products obtained after the purification process were characterised using XRD, FTIR, and SEM/STEM imaging. The processing done for each sample is shown below:

UV-VIS: 10 µL of the solution was diluted in 5 mL octadecene. The cuvettes were placed in an ultrasonic bath sonicator for 30 s before placing it in the instrument.

SEM/STEM: The purified hexane suspension was gently sonicated (10% power, 35 kHz, Elma TI-H-15) in a water bath for 5 minutes. 5 µL of this suspension was dropped on to:

- SEM: A carbon tape coated SEM stub
- STEM: A TEM grid (EMS FCF200-Cu, 200 mesh, formvar/carbon coated)

FTIR: A small amount of the purified precipitate was dropped onto the ATR-FTIR window and allowed to dry.

XRD: This was the final characterisation done. The products from all repetitions were combined and dried on a zero-background holder.

6.4.1 UV-VIS

In batch synthesis, the solution changes from a reddish brown to a brownish black solution. This does not give rise to any particular peaks in the UV-VIS spectrum, only a general increase in absorbance. Kwon et al (Kwon, et al., 2007) measured the absorbance at a single wavelength (400 nm) of samples taken from the reaction at multiple intervals and found it to rise with time as particles nucleated and grew. This shows that the absorbance can be used as a general indicator of the progress of the reaction, however, it is difficult to use it to identify any compounds or molecular structure.

The absorbance of diluted solutions was measured at 400 nm on a Perkin Elmer Lambda 35 UV-VIS spectrophotometer. All measurements were taken with the unheated solution as the 'blank', so the results only show the change in absorbance rather than the absolute absorbance.

The average rise in absorbance at a wavelength of 400 nm for each solution and residence period is plotted in Figure 6.14.

B solutions: Both groups of B solutions (B2 and B4) show an increase in absorbance. The average absorbance of the B4 solutions is slightly lower than that of B2, but that is explained by a higher level of agglomeration and sedimentation.

O solutions: The average absorbance of the O solutions shows a clear and continued increase in absorbance with increasing residence period, as expected.

N solutions: For the N solutions, there does not seem to be any significant increase in absorbance when the residence period is increased beyond 4 s, suggesting that the reaction might be reaching its limit at that flow rate.

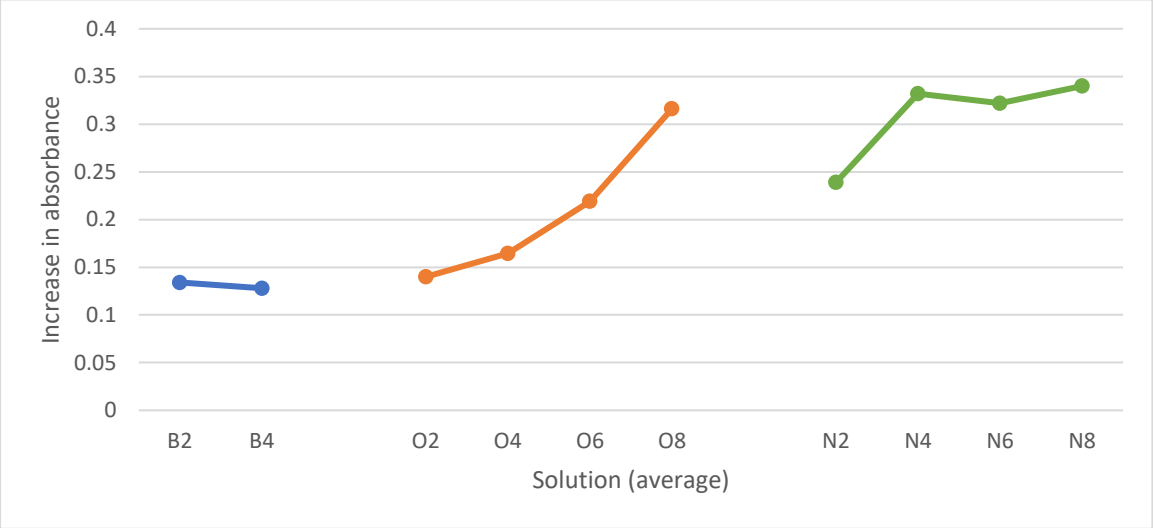


Figure 6.14: Increase in absorbance at 400 nm with increasing residence period using the B, O, and N solutions (average of all 3 repetitions).

6.4.2 XRD

XRD measurements were taken by combining the precipitates from all 3 repetitions for each residence time. In some cases, this amount was still insufficient. The samples from which a reading was obtained are shown here (Figure 6.15).

The by-products surrounding in the samples makes it difficult to observe the XRD peaks of the relatively lower amount of iron oxide. In all the samples, the hump at 20 degrees and the slope rising towards 10 degrees is typical of iron oleate's amorphous structure. The hump is much smaller in magnitude in the N samples, which is in agreement with the observations in Figure 6.12. Although the samples are magnetic, it is difficult to make conclusions about its crystallinity as the by-products coating it seems to absorb most of the X-ray radiation. Since this is a new synthesis method, the product being amorphous is also a possibility to consider. It is only in sample O8 that iron oxide peaks can be seen to emerge, most notably at 42° and 62°, however these are still too weak to confirm the phase.

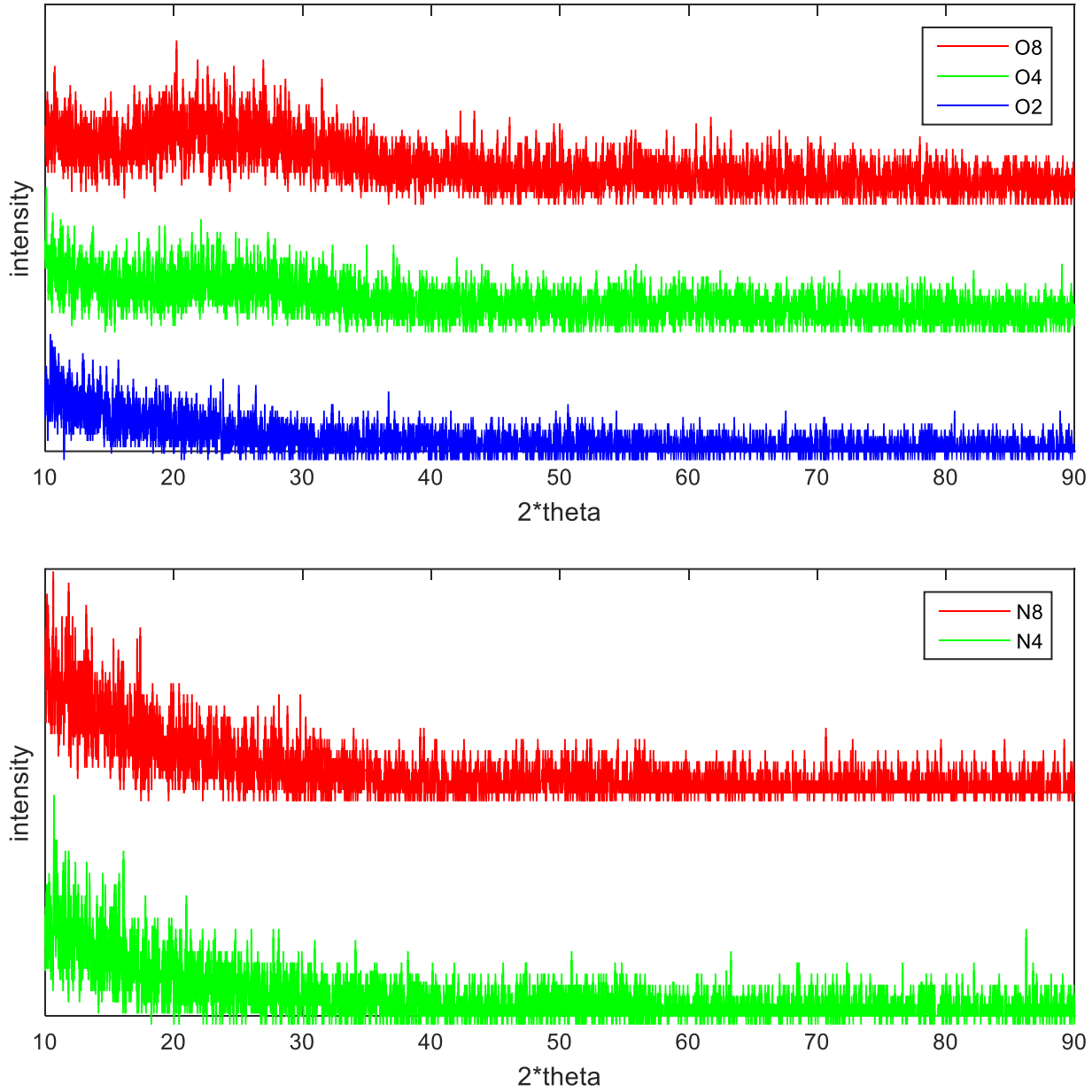


Figure 6.15: XRD measurements of some of the O and N samples

A relatively large amount (~15 mL each) of the leftover B and N solutions were heated in the chip at a flow rate of 24 µL/min and laser power of 250 mW, using the 405 nm laser (described in section 8.1.2). The samples were diluted in more octadecene until the absorbance of the solution at 405 nm reached 2.63. The purified samples were magnetic, however very weak XRD peaks were seen. They were then heated in a furnace at 350 °C for 10 hours, after which iron oxide peaks could be observed (Figure 6.16), however there is still a large amount of amorphous material in the samples. Using the HighScore (Malvern Panalytical) XRD pattern matching software, the product from the B solution was matched with hematite, while the product from the N solution showed a weaker match with magnetite. The

peaks detected in the samples and matched in the software's database are shown in Figure 6.17 and Figure 6.18. Both samples still show amorphous humps in their spectra.

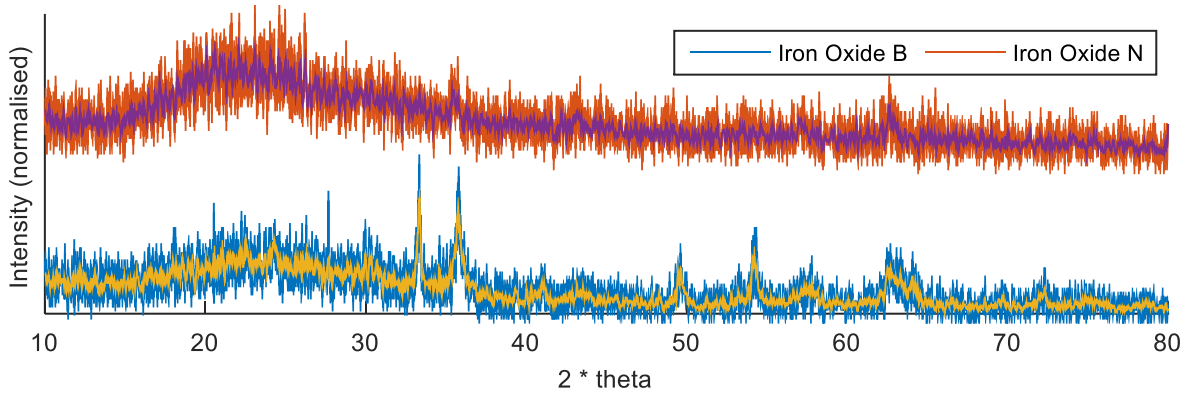


*Figure 6.16: XRD spectra of specially made samples (flow rate of 24 µL/min, laser power 250 mW) from the B and N solutions, **after** heating at 350 °C for 10 hours.*

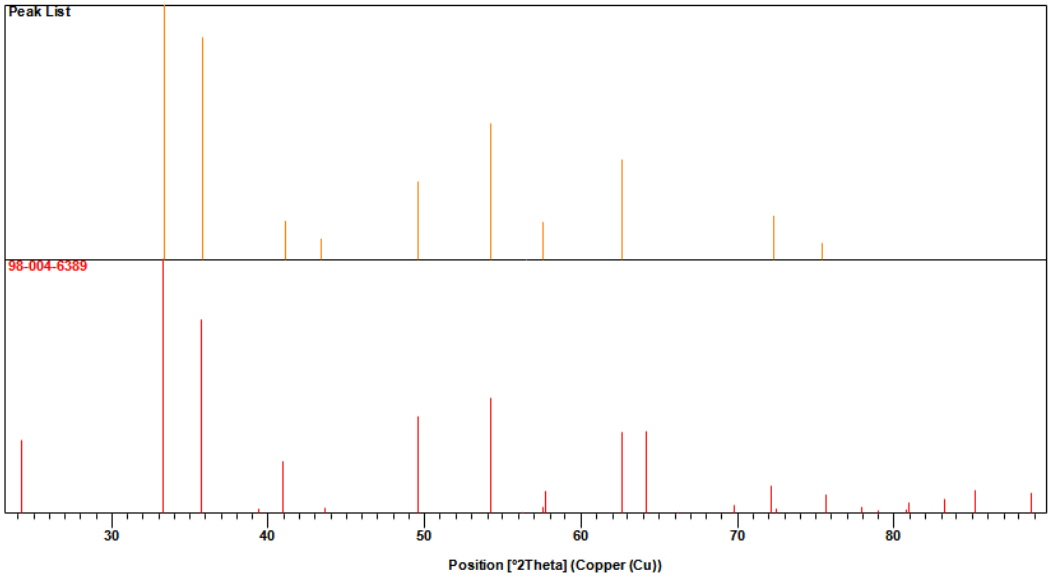


Figure 6.17: (top) Peaks detected in sample iron oxide B, and (bottom) Magnetite peaks from the HighScore database

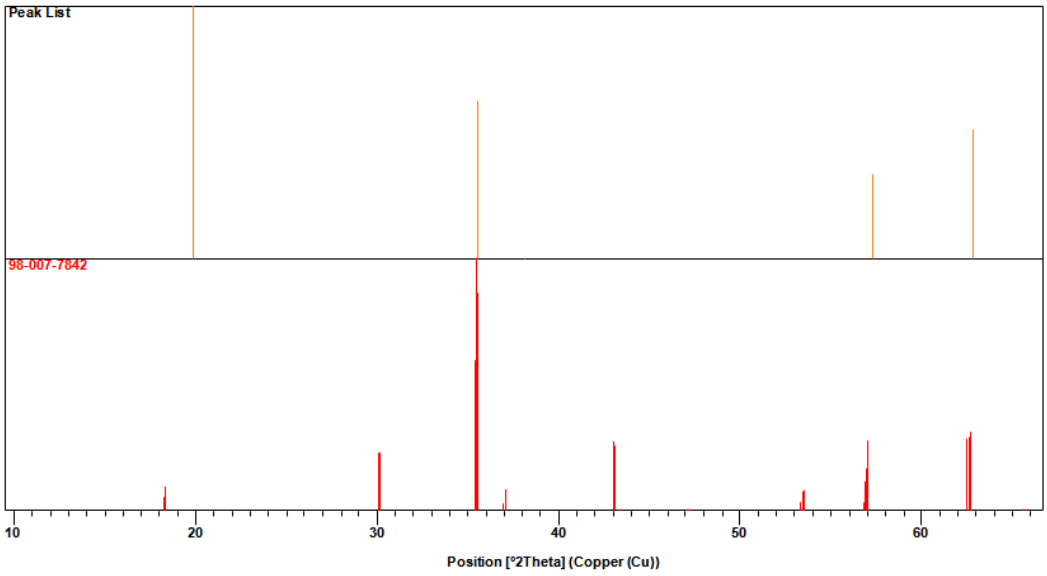


Figure 6.18: (top) Peaks detected in sample iron oxide N, and (bottom) Hematite peaks from the HighScore database.

6.4.3 FTIR

In this section, the FTIR spectra of the major components of our study are presented, analysed and compared. The discussion in this section only makes a distinction between bands caused by stretching and bands caused by bending but does not go into detail about the type of bending. Some background on the FTIR spectra of iron oleate and iron oxide phases found in the literature is presented in section 11.1. Analysis of the spectra of purchased solvents is shown in the appendix (section 11.2).

All FTIR measurements were taken on a Perkin Elmer Spectrum 400 spectrometer using a PIKE GladiATR ATR accessory. Transmission data was recorded in the 4000 cm^{-1} to 400 cm^{-1} range at a measurement speed of 0.5 cm^{-1}/s at and resolution of 4 cm^{-1}. Each spectrum is an average of 16 scans. Background scans were taken before each measurement session.

Liquid samples ODE, OA were dropped onto the ATR. A small amount of FeOl was placed on the ATR window and pressed using the weighted arm.

The nanoparticles were suspended in hexane and then ~10 µL of each sample's suspension was dropped onto the ATR window and allowed to dry. In some cases, repeated applications were required to get a clean measurement. After the hexane was completely evaporated, the sample was pressed down using the weighted arm.

6.4.3.1 Iron Oleate

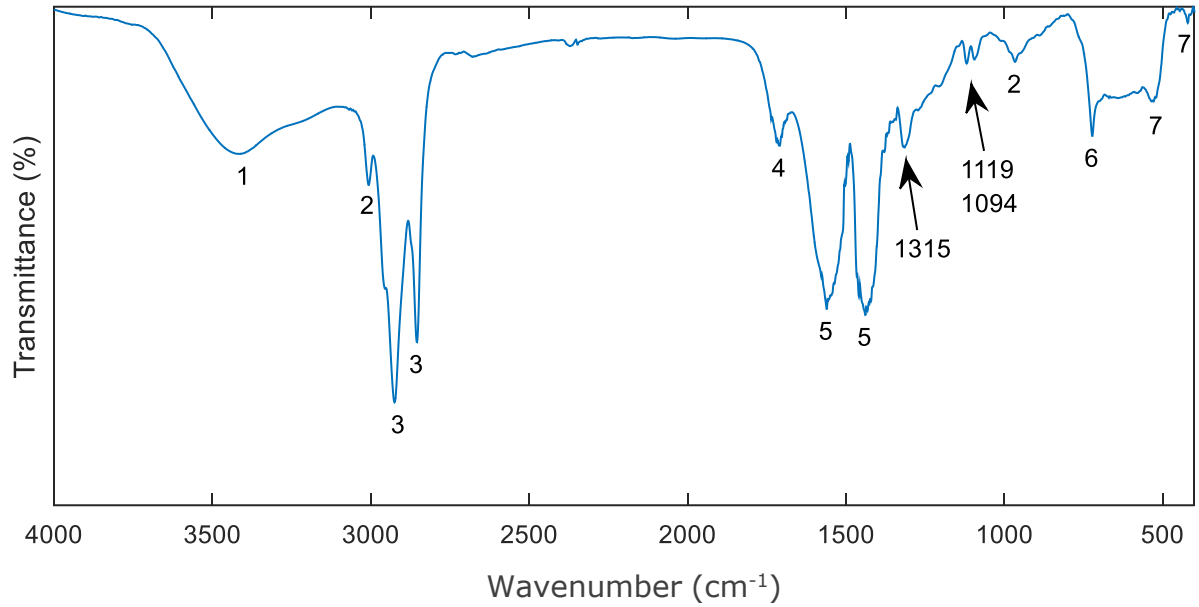


Figure 6.19: FTIR spectrum of the synthesised FeOl.

The FTIR spectrum of our sample is presented in Figure 6.19. The spectrum is very similar to some presented by Bronstein et al (Bronstein, et al., 2007) and Chen et al (Chen, et al., 2009). The following features are observed:

	Wavenumber	**Shape and Strength**	**Assignment**
1	3413 cm^{-1}	Broad band, medium	Oleic acid dimers
2	3006 cm^{-1} 966 cm^{-1}	Sharp, weak Sharp, weak	O-H stretching O-H bending
3	2925 cm^{-1} 2854 cm^{-1}	Sharp, strong	Asymmetric CH_2 stretching Symmetric CH_2 stretching
4	1711 cm^{-1}	Sharp, medium	C=O stretching
5	1560 cm^{-1} 1439 cm^{-1}	Sharp, strong	Asymmetrical carboxylate stretching Symmetrical carboxylate stretching
6	722 cm^{-1}	Sharp, medium, weak	C-H bending
7	529 cm^{-1} 421 cm^{-1}	Sharp, slightly broadened, weak Sharp, very weak	Fe-O bond stretching

1. A broad band is seen peaking at 3413 cm^{-1}, assigned to oleic acid dimers.

2. The O-H stretching peak at 3006 cm^{-1}, also seen in oleic acid, is present in our iron oleate sample as well. However, now it is much weaker and narrower suggesting a much lower amount of non-interacting OH groups. Similarly, the O-H bending vibration at 966 cm^{-1} is much weaker as well.
3. The CH_2 asymmetric and symmetric peaks at 2925 and 2854 cm^{-1} are present in the same position as in oleic acid.
4. The carbonyl peak at 1711 cm^{-1} is much weaker than in oleic acid; its presence in iron oleate indicates a small amount of free oleic acid trapped within. The amount in our sample is much lower compared to the iron oleate produced by Bronstein et al, where the carboxylate bands and carbonyl bands were of similar magnitude.
5. The asymmetrical band appears as a singlet at 1560 cm^{-1} and the symmetrical band at 1439 cm^{-1}. These show a separation of 122 cm^{-1}, suggesting largely bridging coordination. Lu and Miller also mention that these bands may appear at higher wavenumbers in samples with bridging coordination. This does appear to be the case when compared to the results by Bronstein et al (Bronstein, et al., 2007), who observed bands at 1527 cm^{-1} and 1436 cm^{-1} in bidentate coordination mode.
6. The weak peak at 722 cm^{-1} is assigned to C-H bending, as was the case in oleic acid.
7. The weak peaks at 529 cm^{-1} and 421 cm^{-1} are typical of Fe-O bond stretching (Chen, et al., 2009).

Overall, this spectrum shows weakening of peaks associated with free oleic acid (2,4), and strong new peaks corresponding to carboxylate bonding (5), particularly in bridging coordination mode. Other oleic acid related peaks from the saturated chain remain unchanged (2,6), except for the addition of peak 1 caused by oleic acid dimers. Fe-O peaks are also seen (7) from the carboxylate group bonding to the iron atom.

There are two other regions of possible significance: one peak at 1315 cm^{-1} and a doublet at 1119 cm^{-1} and 1094 cm^{-1}, which are characteristic of carboxylic acids, typically caused by its C-O single bond.

6.4.3.2 B samples

Figure 6.20 shows the FTIR spectra of samples B2 and B4, compared with OA and FeOl. The iron oxide peaks can be seen in each sample.

What stands out here is the inconsistent presence of the oleate groups in the samples. B2-2 was purified using a 1:3 HEX:ACE mixture, and shows a lower degree of carboxylate coordination (peaks at 1553 and 1431) compared to B2-3, yet a higher amount of CH_2 stretching, indicating the presence of hydrocarbon chains. It is possible that the free oleic acid in the sample were saturated during the workup process, or the CH_2 stretching vibrations come from other decomposition products. The broad peak at 3354 indicates oleic acid dimer formation.

B4-1 and B4-2 were processed in the same manner yet show different peaks. B4-1 appears to have the largest amount of coordinated carboxylate content, whether it be oleic acid on the surface of the particles, or from trapped iron oleate.

Bronstein et al (Bronstein, et al., 2011) withdrew probes of the solution at various intervals. In the FTIR spectra probes taken *before* the solution reached the final decomposition temperature, they noticed peaks at 1260 cm^{-1} and 799 cm^{-1}. They assigned these peaks to the formation of iron hydroxides as intermediate compounds, based on Ishikawa et al's (Ishikawa, et al., 1992) earlier publication which shows the peaks disappearing as δ-FeOOH was transformed to α-Fe_2O_3. These peaks are also seen in our 2s and 4s samples, mostly in the runs purified with the first method. It is unclear whether the hydroxides are formed during the workup process of the first method or are better washed away with the gentler workup of the second method.

It also shows a strong pair of merged peaks at 1096 cm^{-1} and 1020 cm^{-1}. These peaks are also seen in other samples made from the O and N solutions, but do not appear in either precursor, FeOl and OA, or the solvent ODE. The source of these peaks remains unknown, but it is again likely caused by the workup method. In the O and N batches, none of the samples purified with the second method show strong peaks at these wavenumbers. It may be that the first method results in unknown coordination of the oleic acids with intermediate decomposition products within the solution.

The second purification method did not work as well for sample B4-3 but given the high level of agglomeration seen in all the B samples, a considerable amount of trapped impurities can be expected.

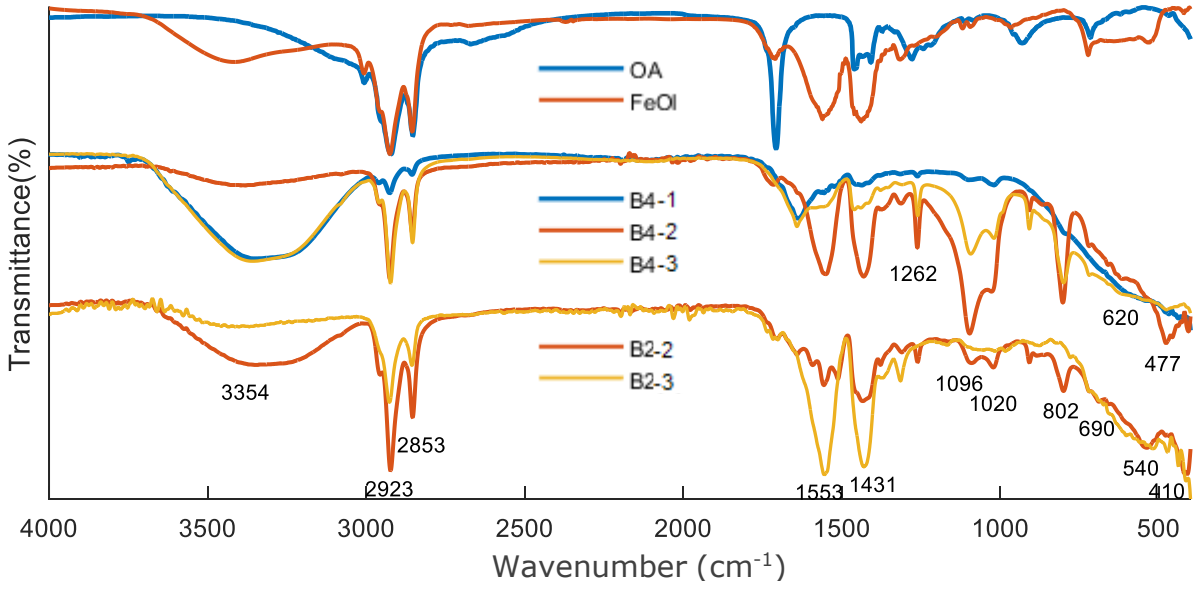


Figure 6.20: FTIR spectra of nanoparticles produced from the B solution. From bottom to top, nanoparticles produced from residence periods of 2s (B2) and 4s (B4), three runs each. At the top are the FTIR curves of oleic acid (OA) and iron oleate (FeOl) for comparison.

6.4.3.3 O Samples

Figure 6.21 shows the FTIR curves of all the nanoparticle produced from the O solution. We see the same pattern as the B samples; samples purified by the first method (O2-1, O2-2, O4-1, O4-2) show smaller CH_2 and oleate coordination peaks and more prominent peaks at 1097 cm^{-1} and 802 cm^{-1} (associated with hydroxides and unknown byproducts) compared to the other samples. The O6 and O8 samples show fairly consistent ratios of oleate to iron oxide. The slightly larger ratio seen in some of the samples is partly due to differing baselines.

The peaks at 720 and 540 are partly from the remaining FeOl coating the particles and have been subtracted from the spectra to get a better look at the iron oxide features (6.4.3.5).

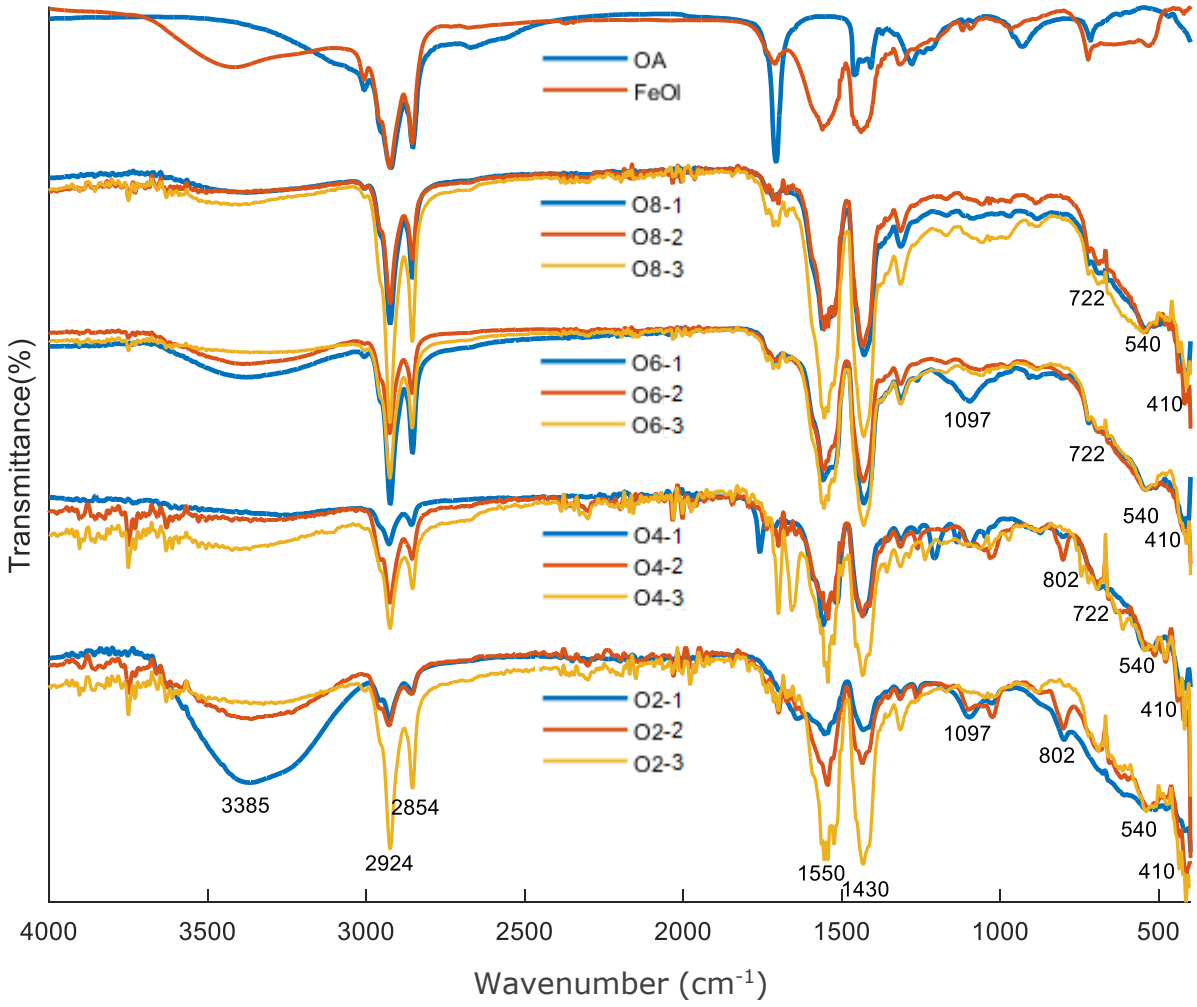


Figure 6.21: FTIR spectra of nanoparticles produced from the O solution. From bottom to top, nanoparticles produced from residence periods of 2s (O2), 4s (O4), 6s (O6), and 8s (O8), three runs each. At the top are the FTIR curves of oleic acid (OA) and iron oleate (FeOl) for comparison.

6.4.3.4 N Samples

Figure 6.22 shows the spectra of the N samples. They spectra shows features similar to those of the O samples, albeit with fewer byproduct peaks in the 1300 – 800 cm^{-1} range (only N4-1 shows the presence of the hydroxide peaks at 1260 cm^{-1} and 800 cm^{-1}).

The "cleanness" of the N samples (lower amount of FeOl/oleic acid compared to the O samples) is reflected here in the weaker CH_2 stretching peaks (2924 cm^{-1} and 2954 cm^{-1}) and carboxylate coordination peaks (1550 cm^{-1} and 1430 cm^{-1}). However, these peaks are still much stronger than those seen in batch synthesis samples.

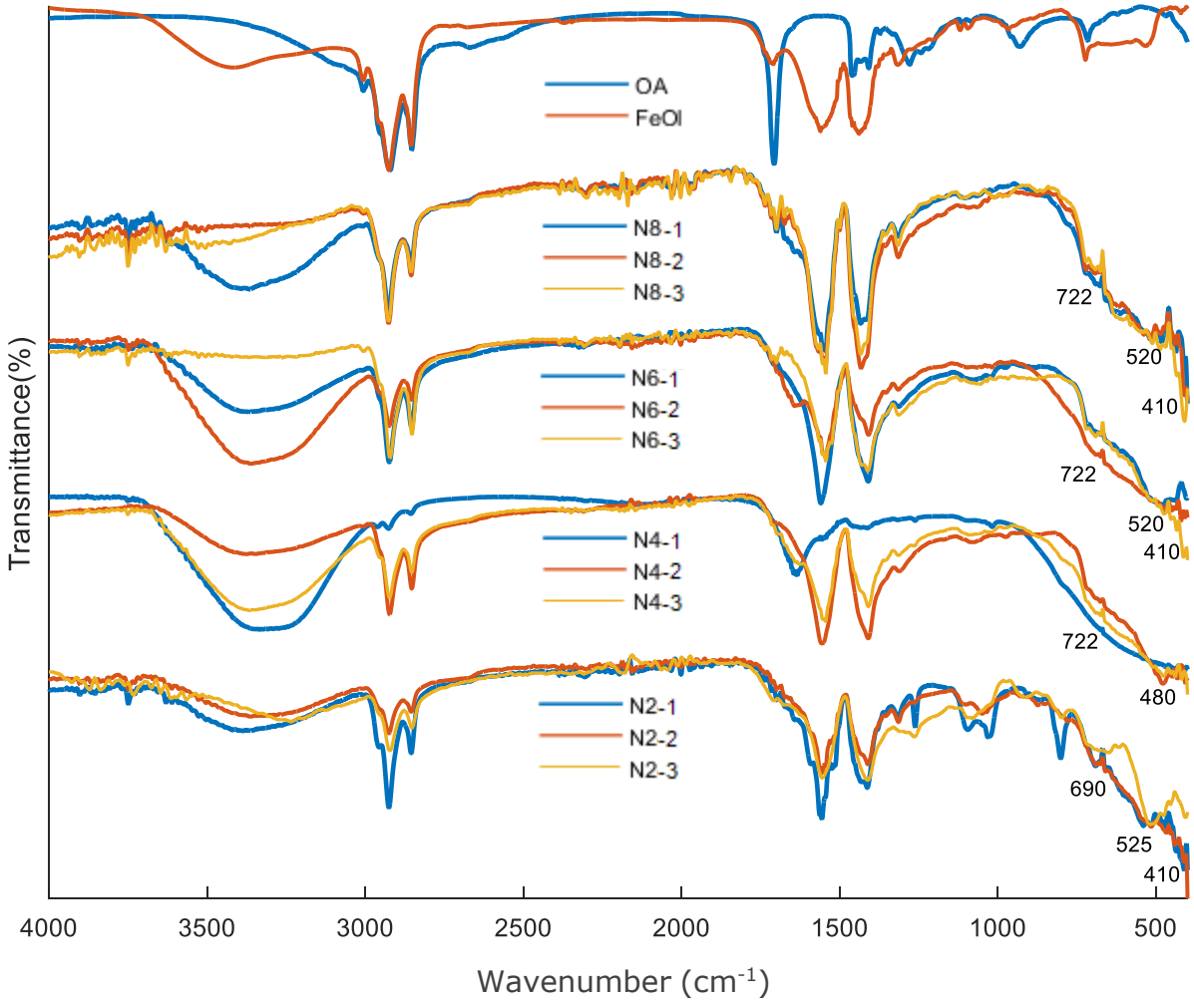


Figure 6.22: FTIR spectra of nanoparticles produced from the N solution. From bottom to top, nanoparticles produced from residence periods of 2s (N2), 4s (N4), 6s (N6), and 8s (N8), three runs each. At the top are the FTIR curves of oleic acid (OA) and iron oleate (FeOl) for comparison.

6.4.3.5 Subtraction of residual FeOl peaks

It can be seen in most of the sample spectra that the weak peak at 722 cm^{-1} is shared with FeOl, while pure iron oxides have no peaks beyond ~693 cm^{-1}. The peak at 966 cm^{-1} seen in the oleic acid spectrum is absent in all the samples, suggesting that there is little, if any, free oleic acid in the purified particles.

Subtraction from the spectra of the B samples did not reveal any useful information due to the excessive noise from other peaks.

The FeOl spectra was subtracted from the O and N samples in the 1000 cm^{-1} - 400 cm^{-1} region (Figure 6.23), where the Fe-O bonds are expected. In these cases, the subtraction revealed several weak peaks that correspond to the FTIR spectrum of iron oxides.

In all the samples, the width of the slope, in addition to the bump at 693 cm^{-1} suggests the presence of some amount of maghemite. N2-3 appears to be an exception here.

In the N4, N6 and especially the N8 samples, the peak at 476-480 cm^{-1} is more prominent, suggesting an increase in the amount of hematite.

Further peaks at ~410 cm^{-1} and <400 cm^{-1} beyond the instrument range (indicated by the strong downwards slope after 437 cm^{-1}), indicate there might still be some magnetite in the sample.

The peak at ~802 cm^{-1} is most likely cause by intermediate production of hydroxides, as indicated by Bronstein et al (Bronstein, et al., 2007).

Overall, quantification of the precise amounts of the phases of the final product is difficult using FTIR results as the different phases have similar spectra in the same region, with peaks that are known to vary with particle morphology.

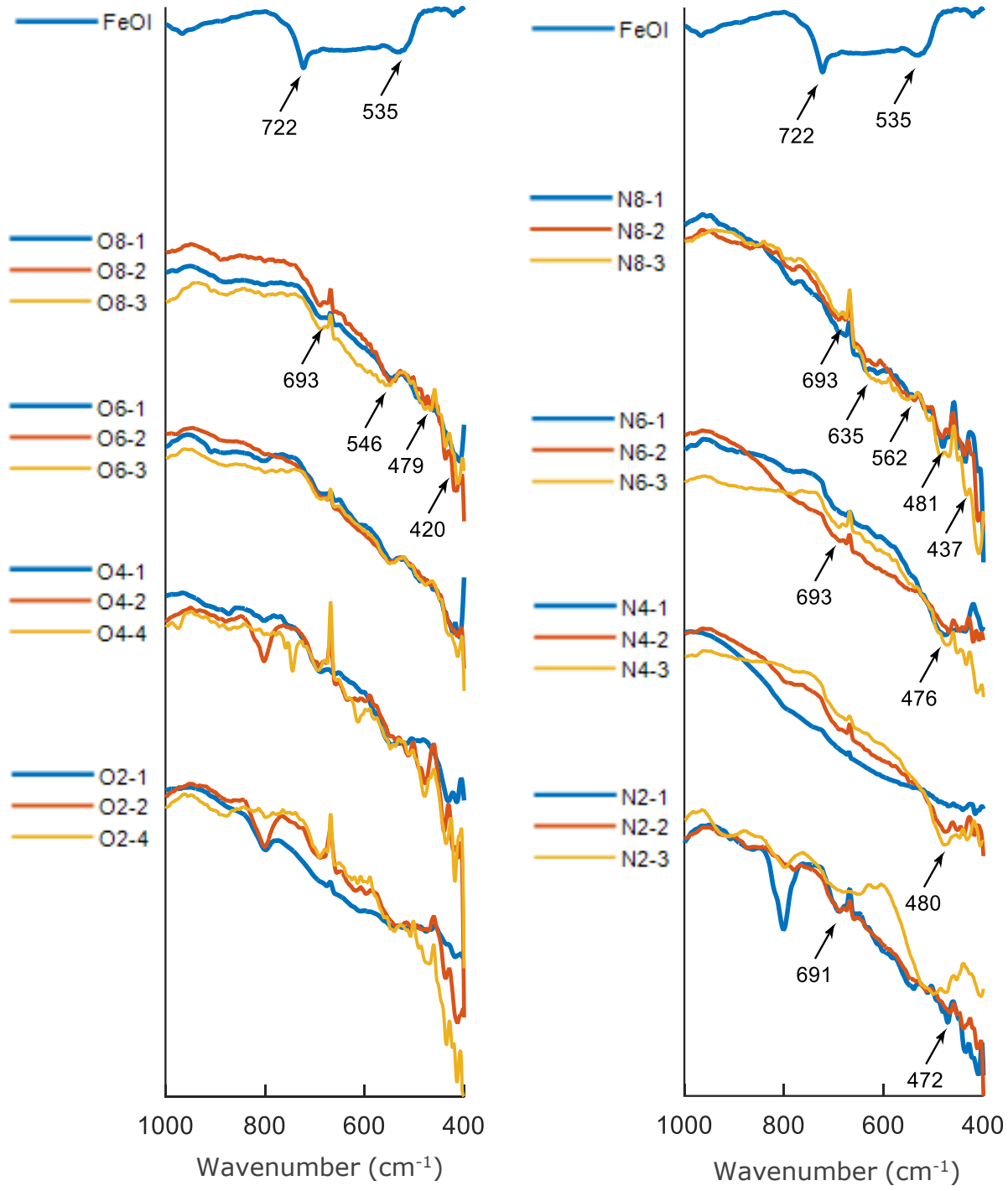


Figure 6.23: FTIR spectra of the O and N samples in the 1000 - 400 cm^{-1} region. The FeOl spectrum has been subtracted from all the spectra presented.

6.4.4 SEM/STEM

This section presents the SEM and STEM imaging results for the samples synthesised in this chapter. For the sake of conciseness, the images presented in this section are some of the best results obtained, however several others can be found in the Appendix (section 11.3) and have been referred to in this section.

6.4.4.1 B samples

B2

The B2-2 sample was purified using the first method, which has caused a large amount of agglomeration. Spheres of varying diameters are seen (thought to be FeOl micelles formed during purification) in addition to the network spread throughout (Figure 6.24 - Left). Additionally, aggregates of free smaller particles were found in STEM observations (Figure 6.24 - Right). FTIR peaks suggest that while there is some amount of free hydrocarbon material, it is not attached to the iron oxide surfaces (section 6.4.3.2). This is backed by EDX measurements that show the highest Fe:O ratio (0.28) out of all the samples (it is typically lower in other samples due to a larger amount of FeOl coating the particles). However, the structure of the particles is lost in most of the sample.

The second purification method is gentler and makes a significant difference in the B samples which do not have any added surfactant. In this sample, the particles are still agglomerated, but it is possible to make out individual spheres (Figure 6.25).

B4

With an increased residence period an increase in agglomeration can be observed in the B4-1 and B4-2 samples (Figure 6.26), compared to B2-2. In both samples, individual particles could be discerned, but only within thick agglomerates or FeOl ribbons. EDX analysis of the darker areas show a higher Fe:O ratio.

Sample B4-3 (Figure 6.27) also shows an increase in agglomeration, along with an increase in the average particle size, however the improvement in purification method allows us to view the particles in some areas of the sample.

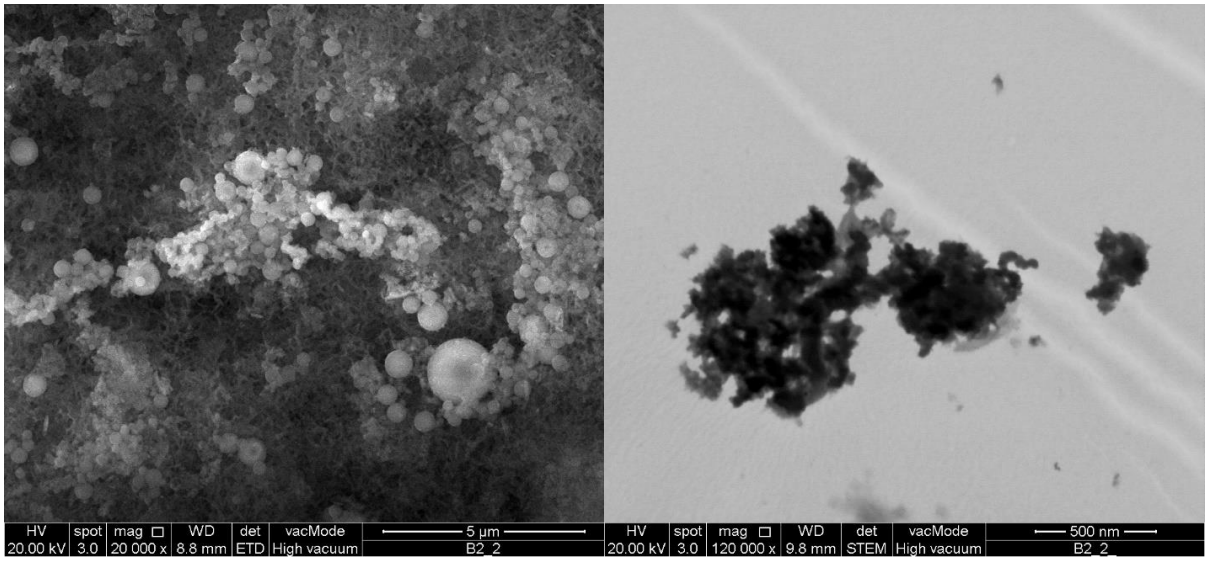


Figure 6.24: (Left) SEM image of sample B2-2. (Right) STEM image of sample B2-2. This sample was produced by microfluidic synthesis using the B solution with an average residence period of 2s. This sample was purified using method 1 and shows high levels of agglomeration.

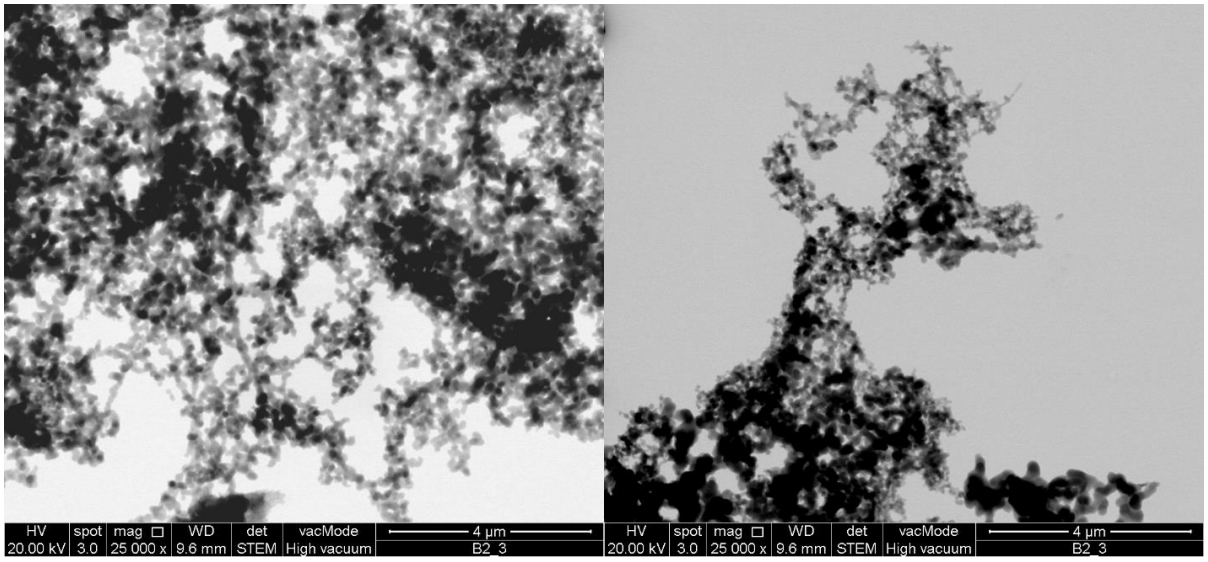


Figure 6.25: STEM images of sample B2-3, produced by microfluidic synthesis using the B solution with an average residence period of 2s. This sample was purified using method 2 and shows lower agglomeration compared to sample B2-2.

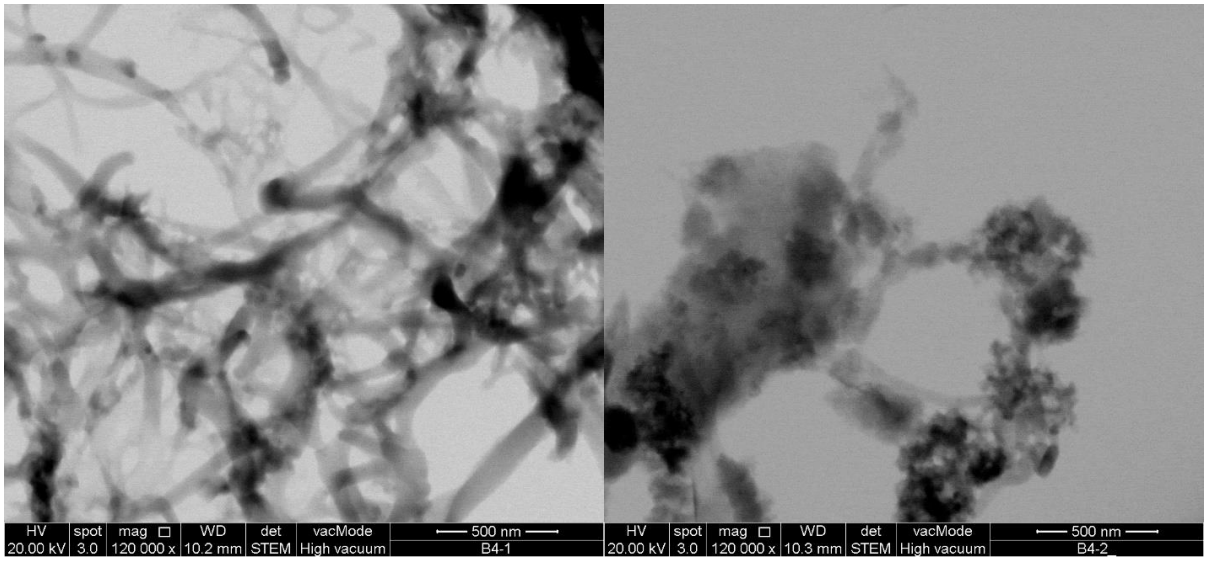


Figure 6.26: STEM images of samples B4-1 (left) and B4-2 (right). These samples were produced by microfluidic synthesis using the B solution with an average residence period of 4s.

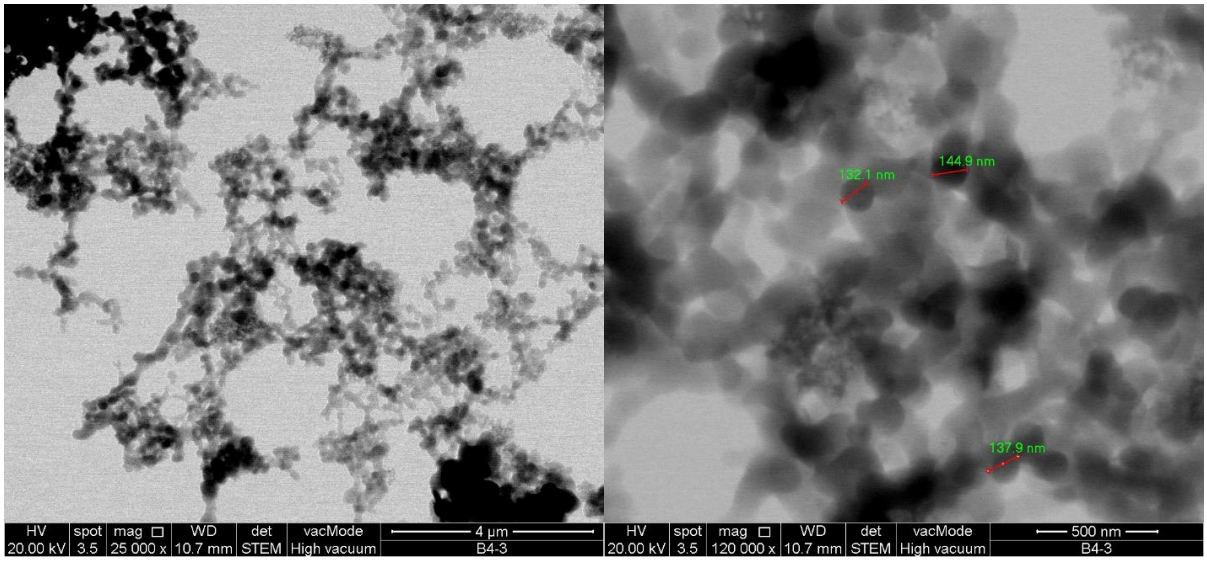


Figure 6.27: STEM images of sample B4-3, produced by microfluidic synthesis using the B solution with an average residence period of 4s.

6.4.4.2 O Samples

The excess oleic acid/iron oleate is a problem in all the O samples as they tend to form a network upon precipitation (which results in the spongy compressible precipitate seen in Figure 6.12) which is not easy to break up. Under strong probe sonication (first purification method) these could be broken up but resulted in the formation of large spherical micelles instead. With the second purification method, using a gentler bath sonicator avoided micelle/network formation, giving better results. However, all samples made from the O solution show excessive organic material in some form. The structures seen in these samples have been described as fibrils, wormlike-micelles, micellar networks, and gels (Lin, 1996) (Raghavan, 2009) (Dai, et al., 2017), however further study of these is beyond the scope of this work.

O2

Both O2-1 and O2-2 (Figure 6.28) showed similar structures, with short micelles of vary widths throughout the sample. Through STEM imaging the presence of individual particles was confirmed. Although the high level of agglomeration makes it difficult to determine precise sizes, most particles appear to be smaller than ~100 nm.

This sample O2-3, seen in Figure 11.7, was dried out and redispersed in hexane using a probe sonicator, which resulted in the formation of large (up to 2 um) spherical micelles in addition to the organic network seen earlier. The few individual particles seen are of similar sizes as in O2-1 and O2-2. This sample is not representative of the typical product.

O4

O4-1 (Figure 6.29) and O4-2 (Figure 11.8) were purified using the first method, and they both show similar characteristics: larger particles (>100 nm) were clustered together while smaller particles could be found within the thinner organic network.

Images from sample O4-3 and O4-4 are also shown in Figure 6.29. Sample O4-3, like O2-3, was also redispersed in hexane using the bath sonicator at low power. This avoided the formation of micelles or networks, however an organic layer could be seen in some areas with particles embedded in it. Particles of up to 400 nm in diameter were observed. O4-4 was purified using the second method. As in O2-4, particles were observed clustered together, but with the spherical boundaries clearly visible.

A few larger particles of up to 500 nm were seen in this sample, but most particles were between 150-350 nm in size.

O6

Figure 6.30 shows sample O6-1, O6-2, and O6-3. There are areas where the FeOl layer was thinner and spread out (the top two images) where individual particles mostly smaller than ~200 nm could be seen. There are also areas with higher agglomeration (bottom two images) with larger particles. It may be that the larger particles, having more FeOl surrounding them, result in higher levels of agglomeration making them difficult to observe individually in the purified samples.

STEM images of sample O6-2 show separate particles between ~70-155 nm. FeOl networks were also present, but agglomeration seemed lower overall with smaller particles being visible even in denser agglomerates (bottom right image).

Particles in sample O6-3 showed similar size distribution (~60-130 nm), and while agglomeration seemed a bit higher, once again particles in dense agglomerations were still visible.

O8

Samples O8-1, O8-2, and O8-3 are shown in Figure 6.31. Particles from sample O8-1 show similar size distribution (~60-130 nm) as the O6 samples, however there is a much larger degree of agglomeration which may be hiding larger sized particles within. Sample O8-2 shows a lower degree of agglomeration compared to O8-1 which reveals a wider variety of particles sizes of up 310 nm. A few particles as big as 1 um were also seen (bottom right image). Sample O8-3 shows a particle size distribution between 50-120 nm with seemingly fewer larger particles than in O8-2.

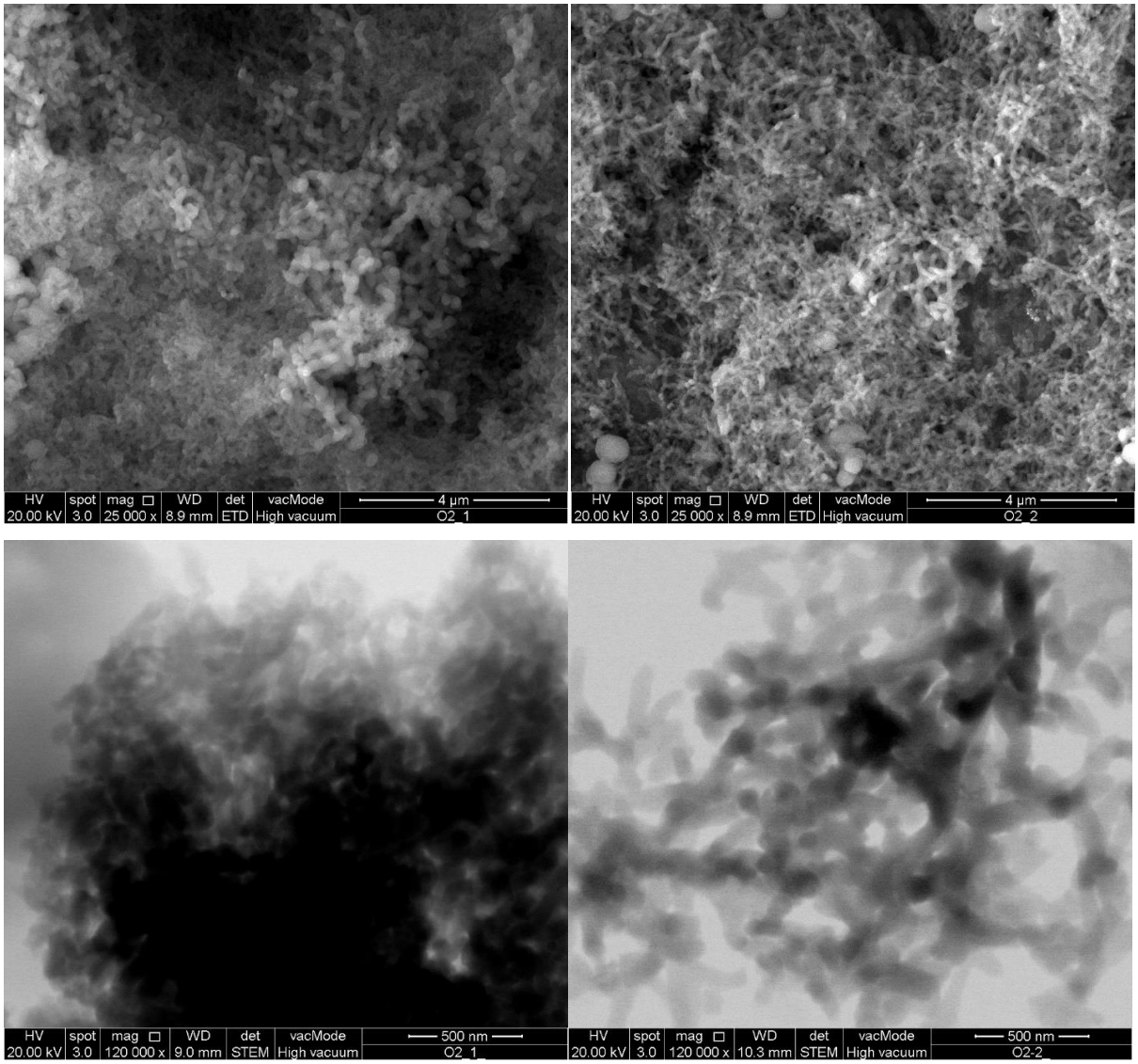


Figure 6.28: (Top) SEM and (Bottom) STEM images of purified samples O2-1 and O2-2, produced by microfluidic synthesis using the O solution with an average residence period of 2s.

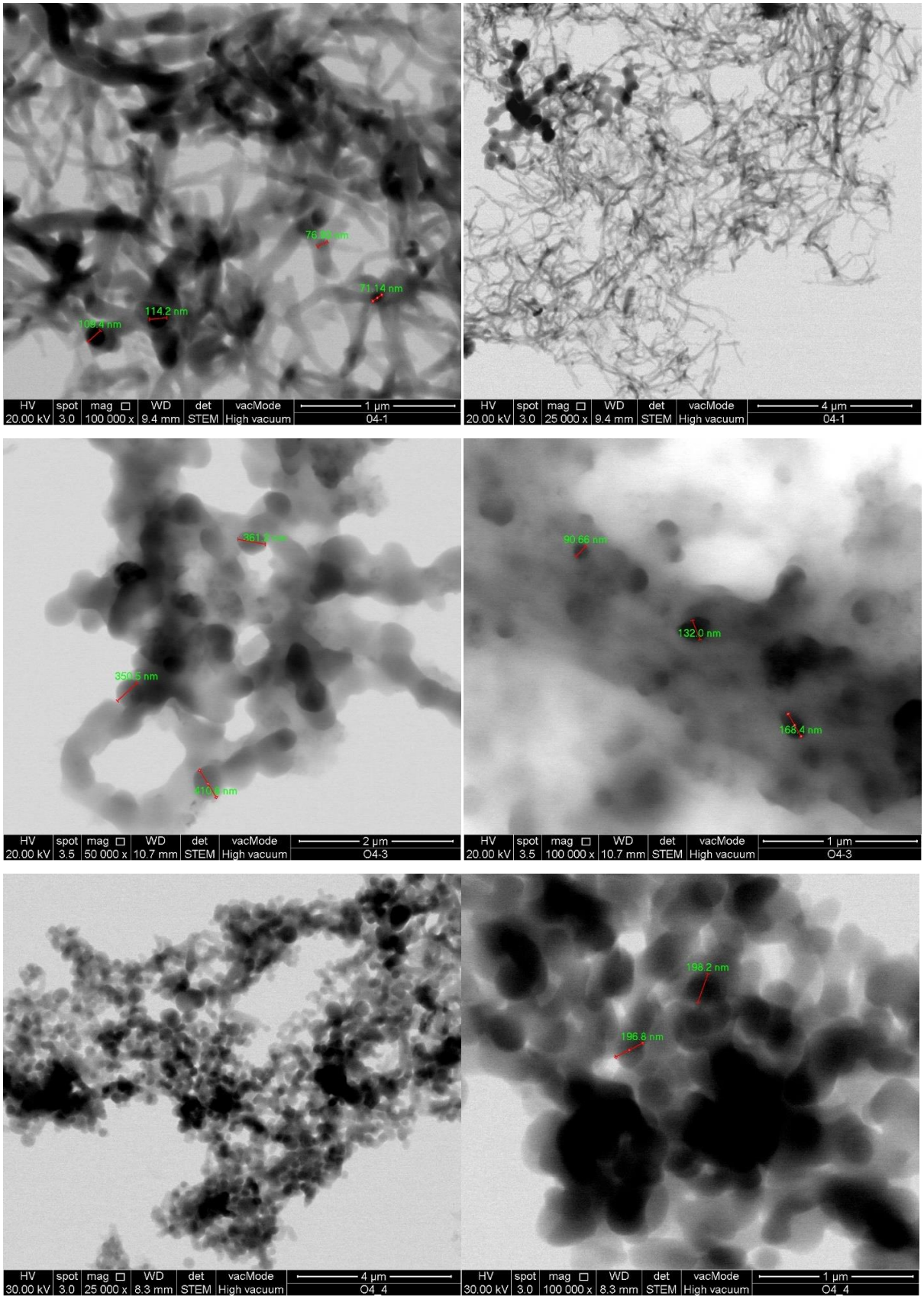


Figure 6.29: STEM and SEM images of samples O4-1 (top) and O4-3 (middle row), and O4-4 (bottom row), produced by microfluidic synthesis using the O solution with an average residence period of 4s.

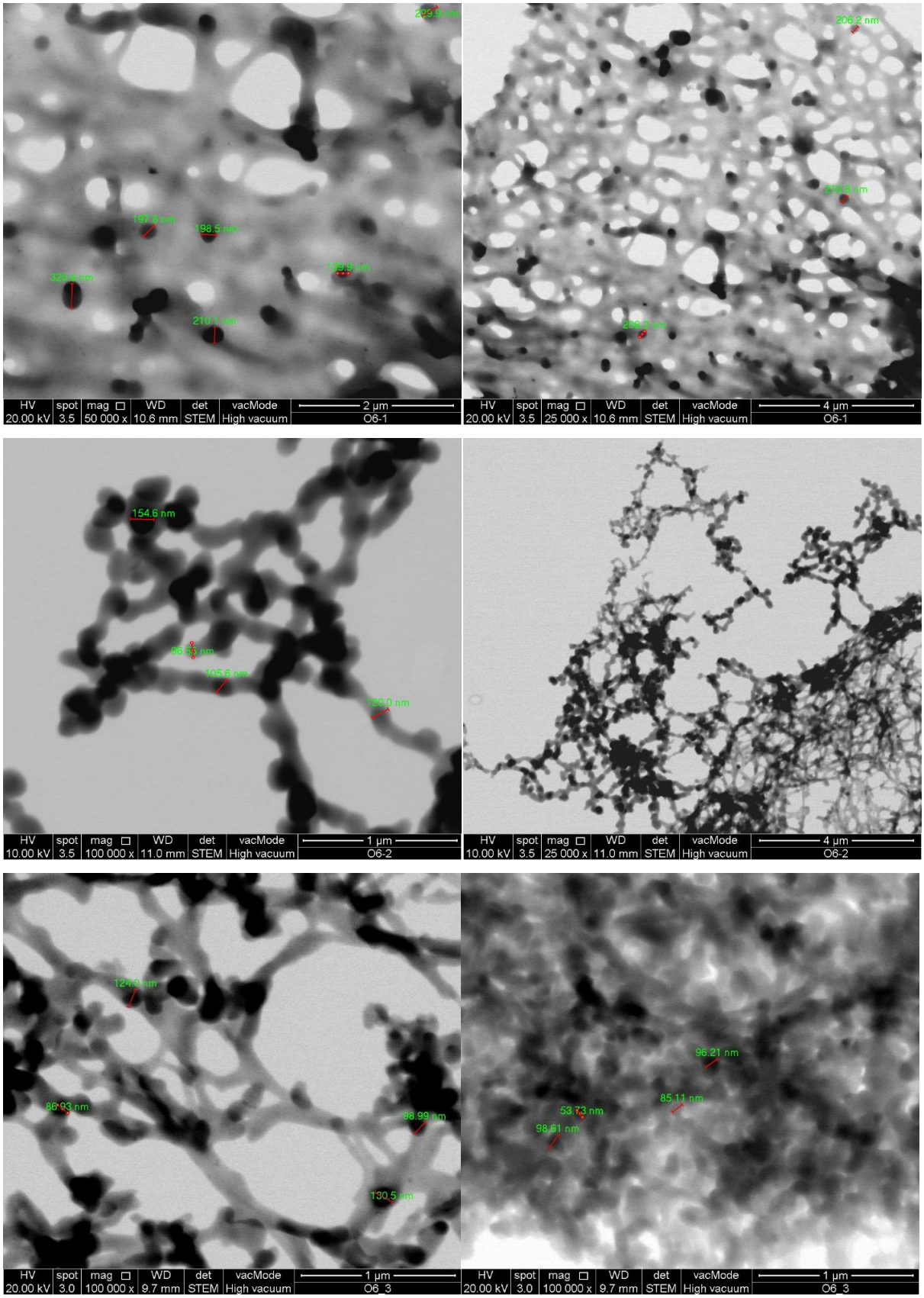


Figure 6.30: STEM images of sample (top row) O6-1, (middle row) O6-2, (bottom row) O6-3, produced by microfluidic synthesis using the O solution with an average residence period of 6s. Denser iron oxide particles can be seen embedded in lighter organic networks.

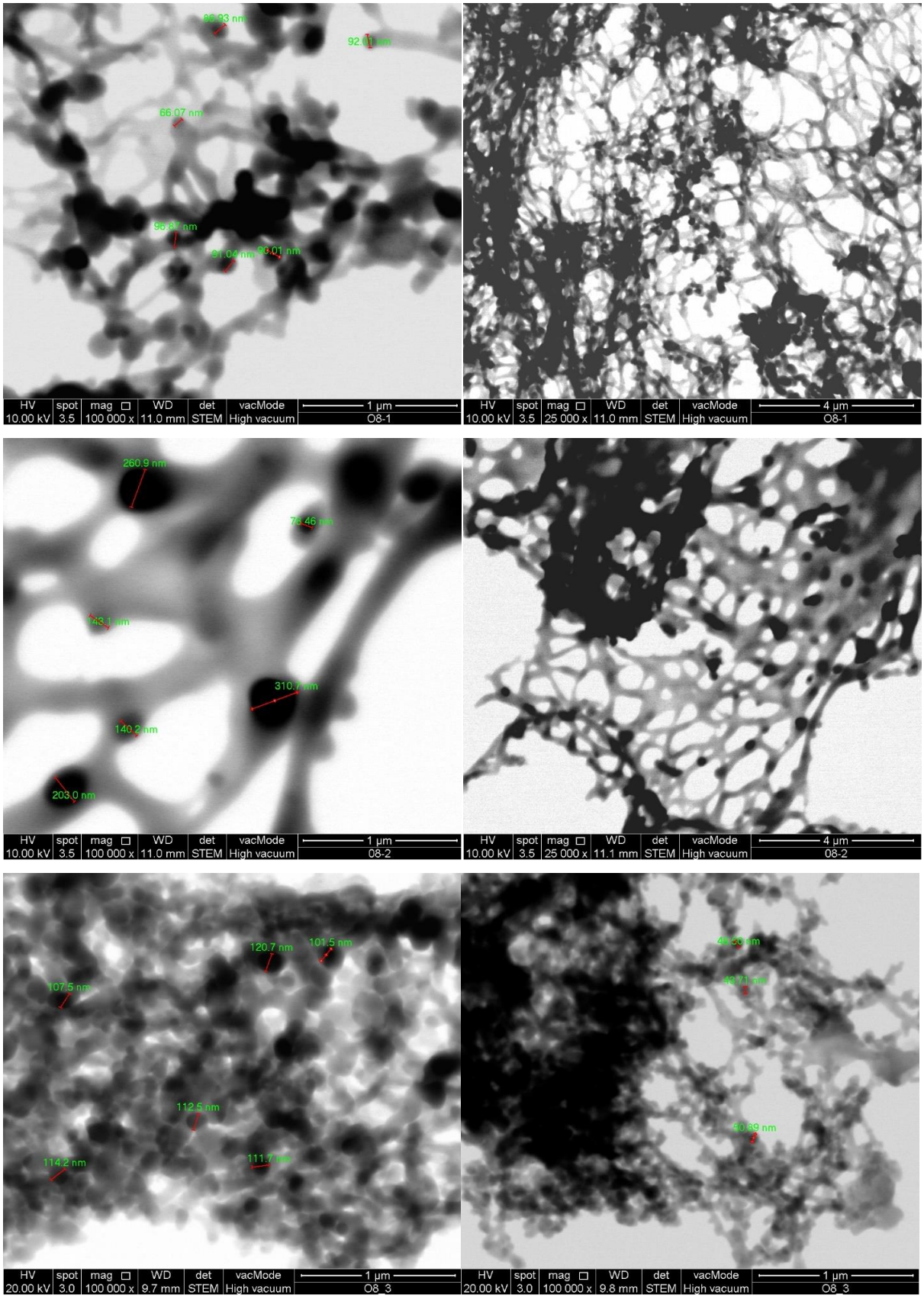


Figure 6.31: STEM images of sample (top row) O8-1, (middle row) O8-2, (bottom row) O8-3, produced by microfluidic synthesis using the O solution with an average residence period of 8s.

6.4.4.3 N Samples

The precipitates produced from the N solution are denser and "cleaner" than the ones produced from the O solution. However, they still have some organic material bound to the particles and none of the samples show completely free nanoparticles. In terms of size distribution, the best results were obtained at the lowest residence period (2s) where particles were largely around 70-120 nm or smaller.

N2

The images obtained from samples N2-1 and N2-2 (Figure 6.32) both show similar particle sizes and agglomeration tendencies. Although the organic network seen in the O samples is not present here, the precipitated particles are still insoluble in hexane and stick to one another.

Using sodium oleate as the surfactant, we expect to find cubical nanoparticles. It is clear from the STEM images that the particles are faceted. Since they have not been deposited as a monolayer on the TEM grid, not all of them show a square outline as they do not lie flat. The angles of the individual particle outlines are consistent with cubical shapes of different sizes viewed from different perspectives, illustrated in Figure 6.33. The corners of the cubes are not sharp, but the organic layer coating the particles hides the true shape as well.

N4 and N6

The N4 and N6 samples show similar morphologies. The particles are either severely agglomerated (Figure 11.15 and Figure 11.18) or are seen as large spheres (Figure 11.16 and Figure 11.17) which may be largely composed of FeOl. It is unclear what the cause of the agglomeration in these two cases is.

N8

Particle morphologies were consistent across the three N8 samples (Figure 11.19). Large spherical particles (>200 nm) made up the bulk of the sample by volume, however many smaller particles still exist.

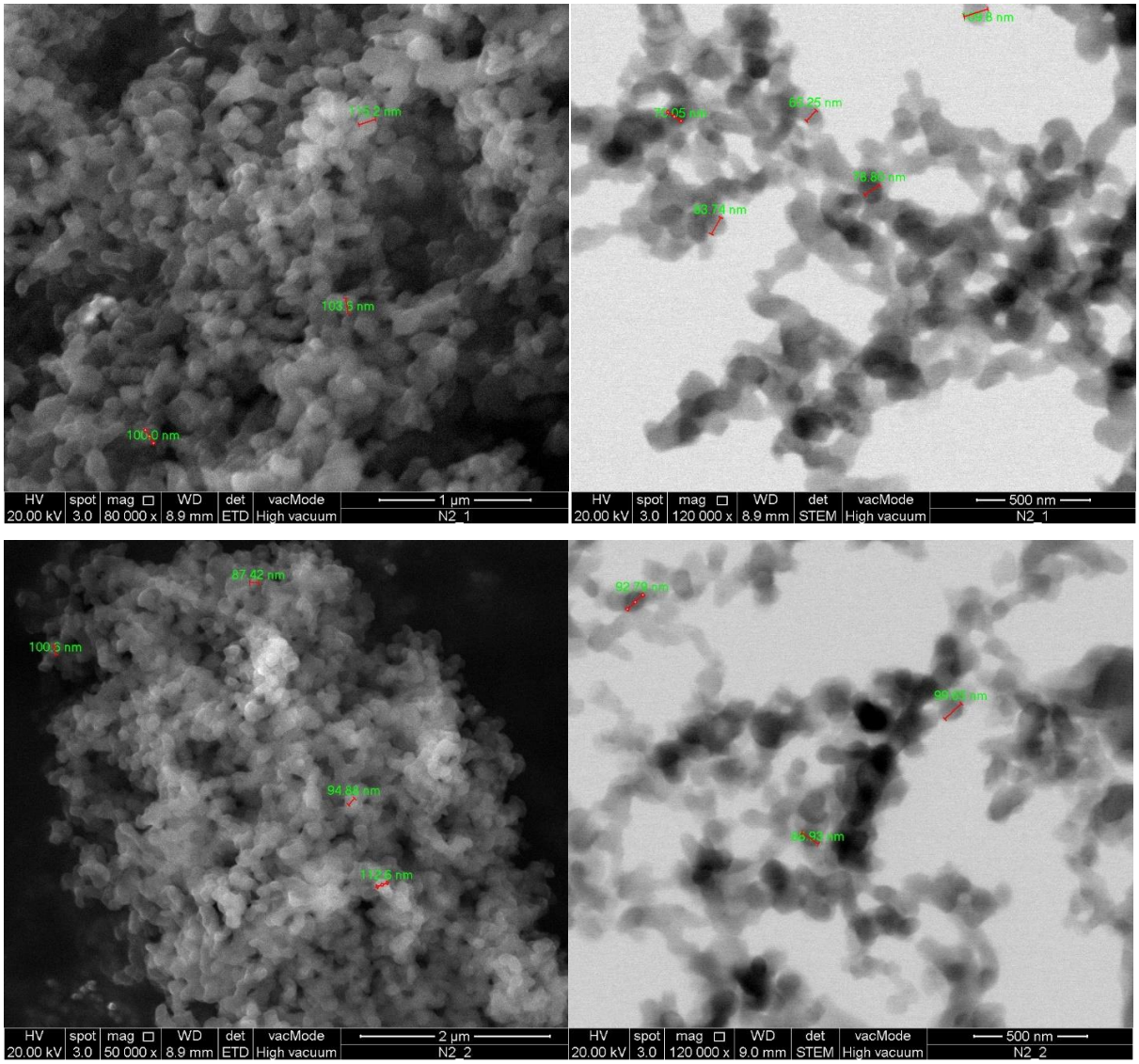


Figure 6.32: SEM and STEM images from samples N2-1 (top) and N2-2 (bottom) , produced by microfluidic synthesis using the N solution with an average residence period of 2s.

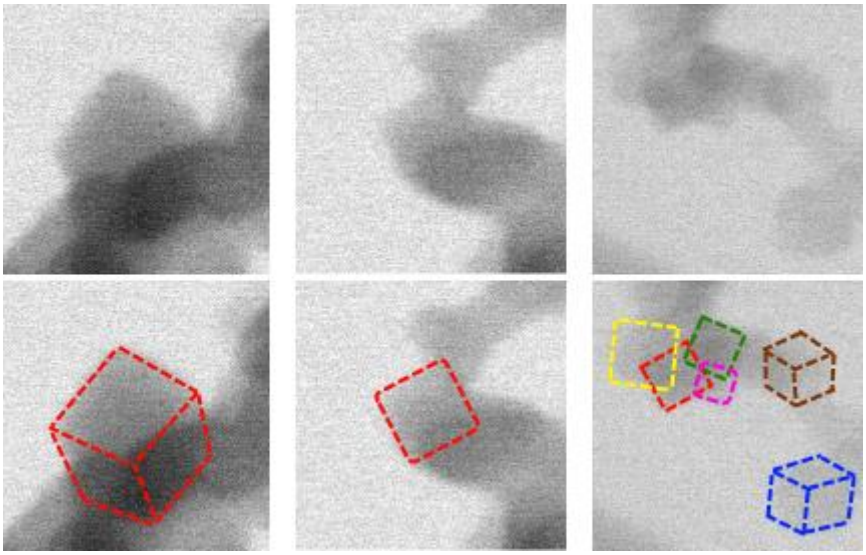


Figure 6.33: Speculative outlines of overlapping cubes in samples N2-1 and N2-2.

6.4.4.4 Liquid Samples

Two of the samples, O6-1 and N6-2, were imaged before purification. 5 µL of the original heated solutions were diluted in 1 mL of hexane and dropped on the TEM grid and dried. The hexane helps spread out the solution on the TEM grid and then evaporates, leaving behind the non-agglomerated particles covered by a thin homogenous layer consisting of octadecene, FeOl, surfactants and by-products.

Figure 6.34 shows some of the images obtained from sample O6-1. Individual particles of varying sizes between 3 nm to over 500 nm are seen. All of them have a distinct boundary, but also show a gradual reduction in absorption beyond the boundary. This suggest that while the particle is discrete, the remaining FeOl is strongly bound to it, illustrated in Figure 6.35.

Similarly, sample N6-2 was also prepared this way, and both small and large particles were found (Figure 6.36).

These two samples confirm that:

- The particles are indeed discrete spherical iron oxide particles.
- There are a significant number of smaller particles that are not easily discerned in the purified samples. However, they might not be significant in volume.
- The purification is responsible for agglomeration and micelles seen in the purified samples.

- The remaining FeOl, oleic acid and/or by-products stick to the surface of the particles even within the solution, and especially so under the repelling effect of the acetone during purification.

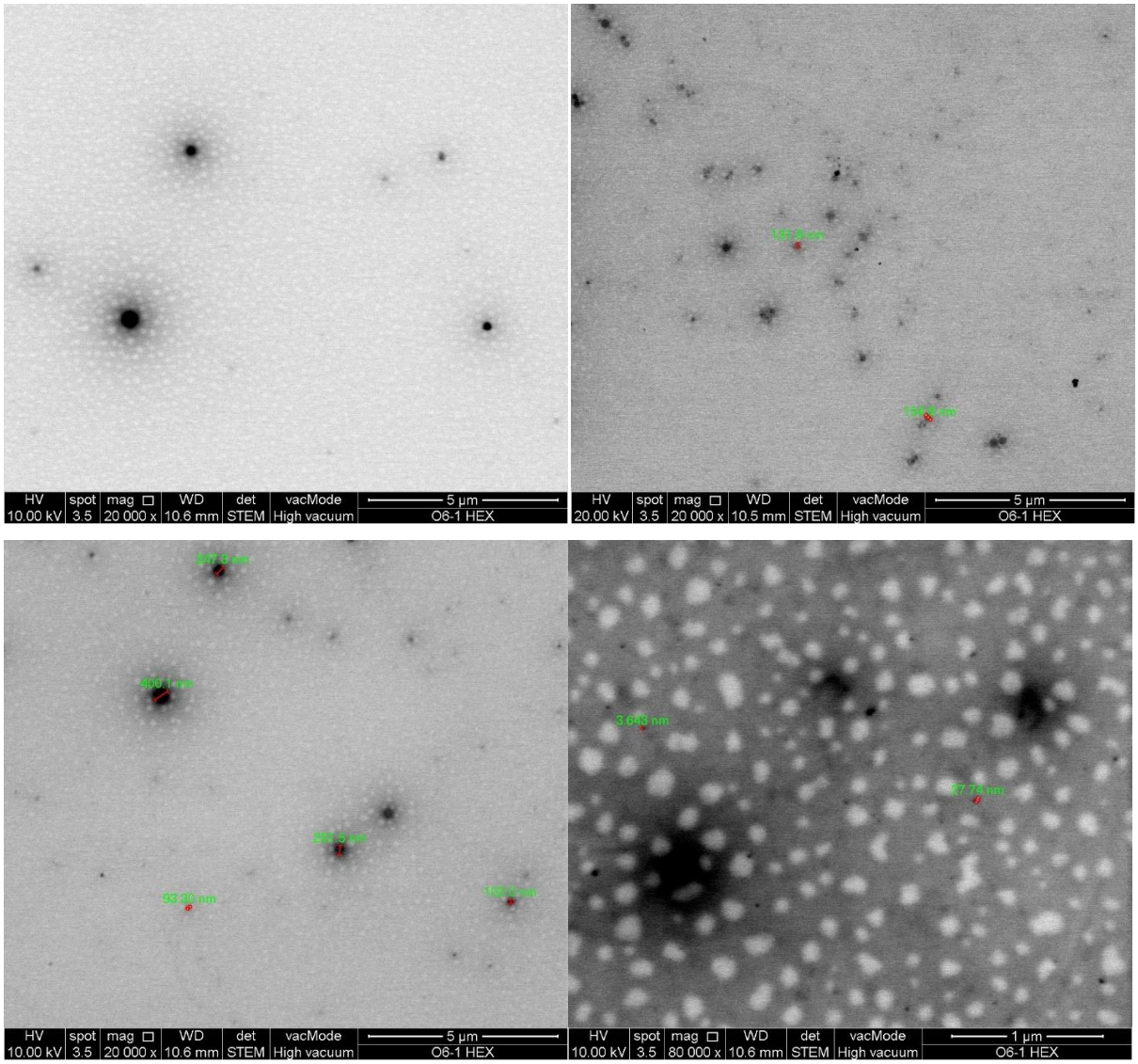


Figure 6.34: Diluted, unpurified O6-1 solution showing individual spherical particles.

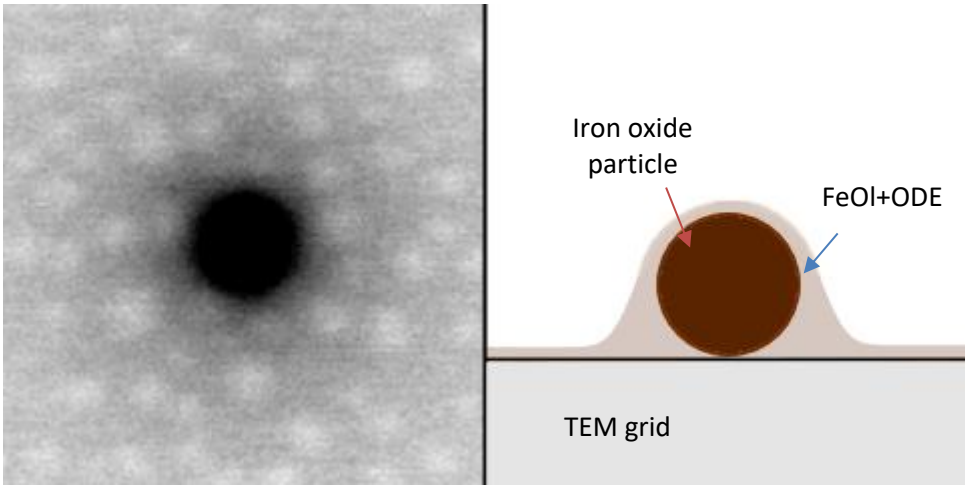


Figure 6.35: Possible explanation for the brightness gradient around the boundary of the particle. The estimated size of this particle is ~480 nm.

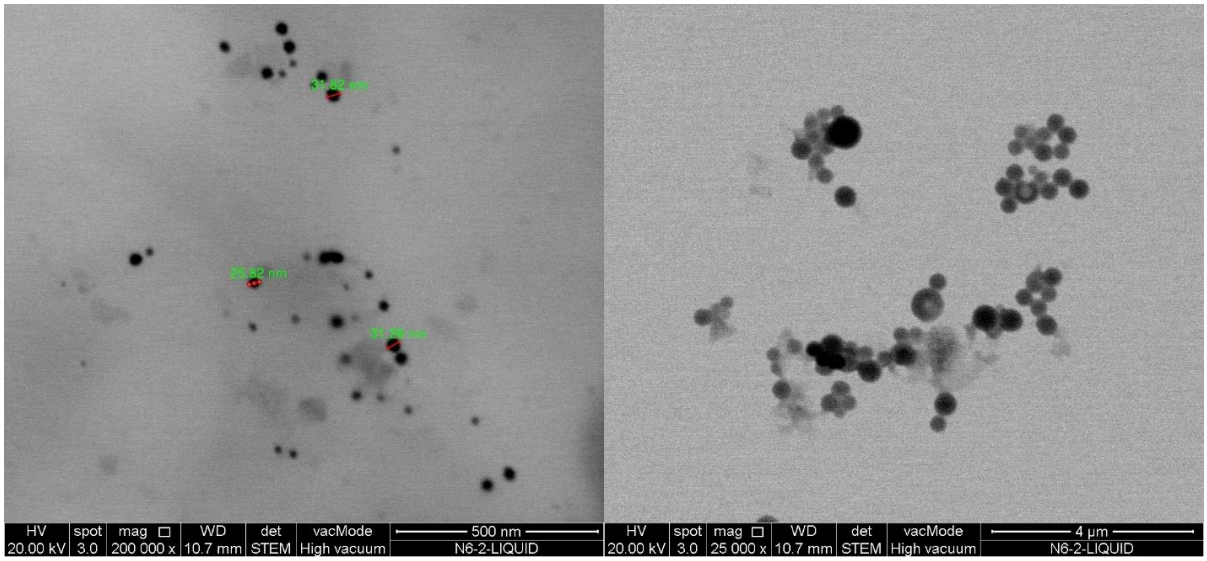


Figure 6.36: Diluted, unpurified N6-2 solution showing small (left) and large (right) particles.

Due to the thin film coating the particles, we could not obtain clear images at higher magnifications. Unfortunately, this method could not be repeated for all the samples, as the presence of the solvent (ODE) is not recommended in the SEM because it can slowly evaporate in the high vacuum environment.

6.4.4.5 *Size analysis*

The particles visible in the SEM/STEM imaging are mostly larger ones. Smaller particles have a higher tendency to agglomerate during the purification process and are much more unlikely to be visible in the SEM/STEM. The two liquid samples O6-1 and N6-1 prove that these smaller particles do exist. These particles are significant in number, but not in volume.

A particle size count was performed on selected images where individual particles could be discerned. The diameters of 5222 particles across all samples were measured. In this case the liquid samples are not counted, so this figure only considers larger particles. The mean sizes and standard deviations were calculated across all repetitions of a sample, shown in Figure 6.37 and listed in Table 6.5.

In all cases, larger agglomerations were not counted unless the individual particles were visible. In the 2 s and 4 s samples this skews the analysis somewhat to favour measurements from the third repetition which used the second purification method as more particles could be counted from them.

Due to the high level of agglomeration, it is also likely that the actual average particle sizes in the O2 and O4 samples are smaller than reported here.

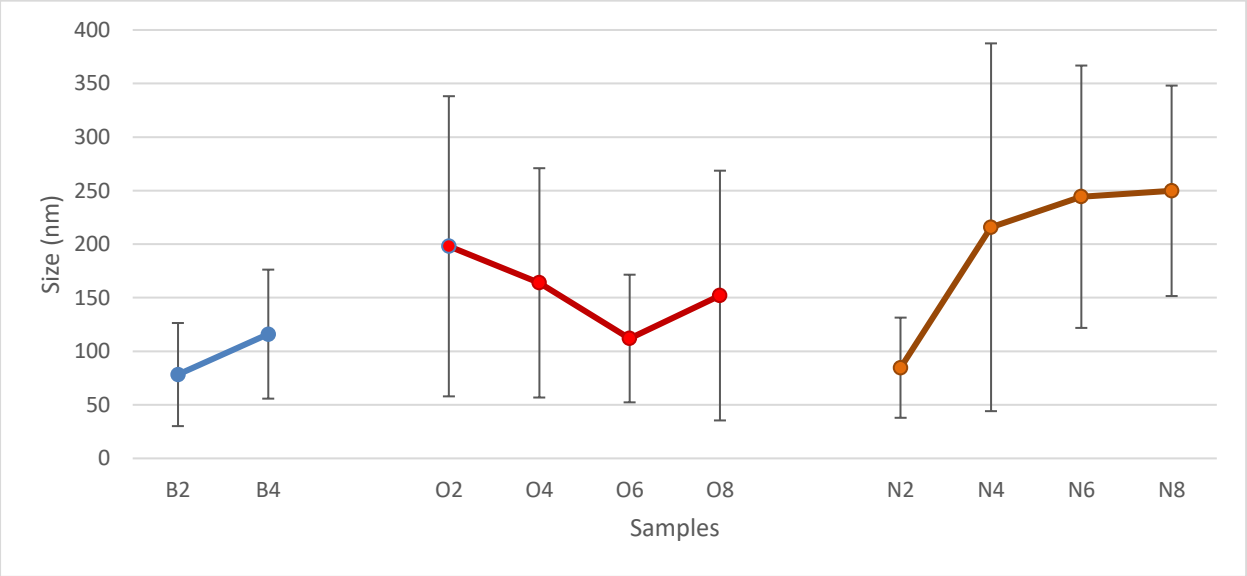


Figure 6.37: Mean sizes across all samples. The error bars show standard deviation.

Table 6.5: Mean diameters and standard deviations seen in Figure 6.37.

Sample name	Flow rate (µL/min)	Mean diameter (nm)	Standard deviation (nm)	Standard deviation (%)
B2	**26.55**	**78.3**	**48.1**	**61.4**
B4	13.68	116.0	60.2	51.9
O2	26.55	198.1	140.1	70.7
O4	13.28	163.9	107.0	65.3
O6	8.85	111.9	59.6	53.3
O8	6.64	152.0	116.6	76.7
N2	**26.55**	**84.7**	**46.8**	**55.3**
N4	13.28	215.8	171.7	79.6
N6	8.85	244.3	122.5	50.1
N8	6.64	249.8	98.3	39.4

The B samples show a steady increase in mean particle size from 78.3 nm in the B2 samples to 116.0 nm in the B4 samples, with a small increase in standard deviation from 48.1 nm to 60.2 nm.

The O samples surprisingly show a decline in size from O2 to O6, and then an increase in O8. The size distribution sees the same trend, with the O6 samples showing the smallest standard deviation. However, the heavy agglomeration and coating in the O samples makes it difficult to make solid conclusions about particle sizes.

The N samples show the best result in N2, with the smallest mean particle size (84.7 nm) and size distribution (46.8 nm). In N4, a large increase is seen to a mean size of 215.8 nm and a S.D. of 171.7 nm. The mean size increases slightly going to N6 (244.3 nm) and N8 (249.8 nm), however a much larger decrease in S.D. is observed (122.5 nm in N6 and 98.3 nm in N8). These results agree very well with

the UV-VIS measurements where similarly only a small difference was found between the N4, N6, and N8 samples.

Figure 6.38 shows the histogram of particle sizes seen in the liquid samples O6-1 and N6-2, showing the presence of a much larger number of smaller particles which are not visible in the purified samples.

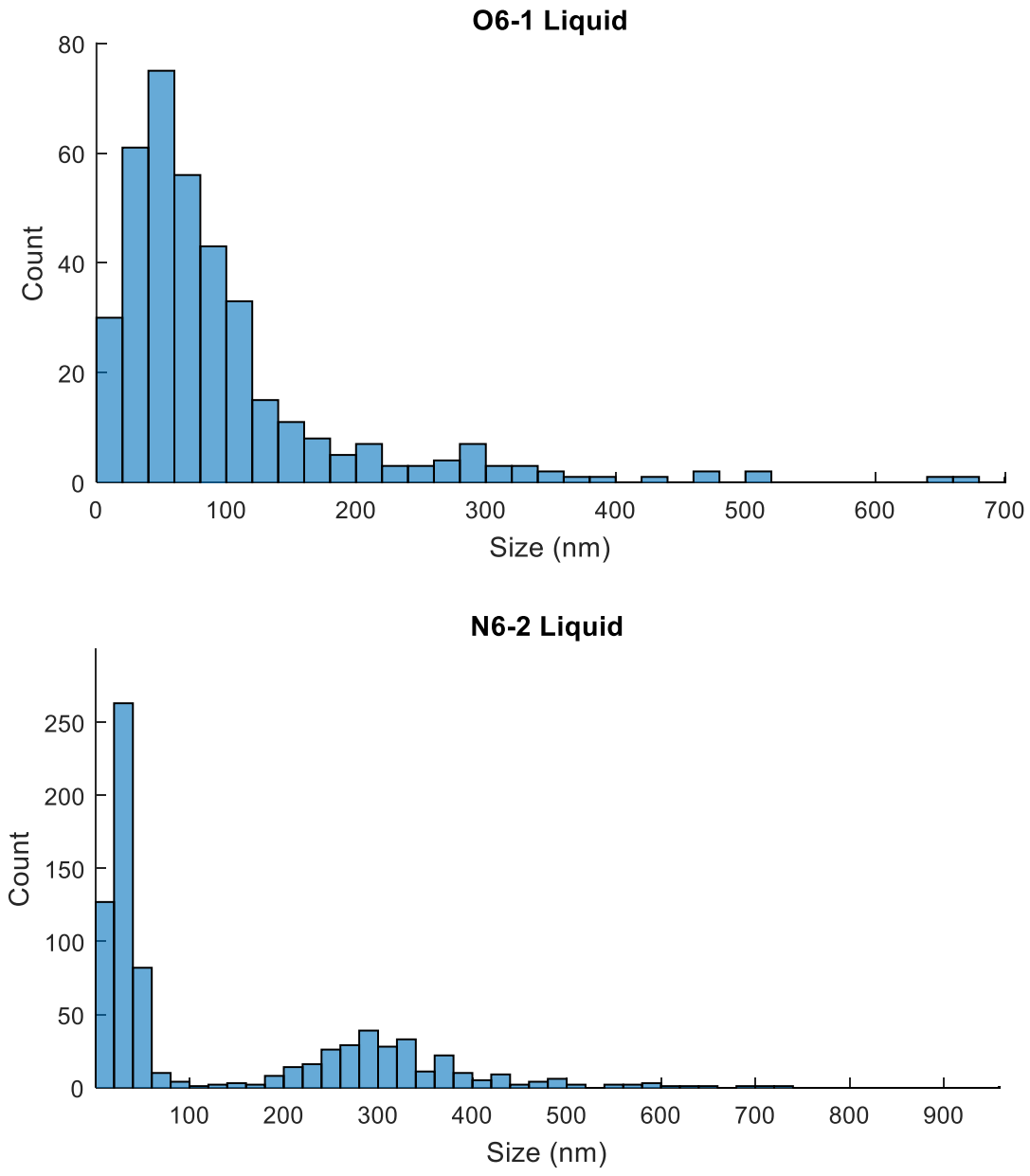


Figure 6.38: Particle size histogram of the O6-1 and N6-2 liquid samples.

6.5 Discussion

To address the limitations of the straight channel chip, the vertical flow chip was designed and fabricated. This design allowed for an increase in the residence period from a few (<10) ms to several seconds. Preliminary synthesis work using this chip design was performed to choose a suitable starting point to use for the flow rates. A flow rate of 2.26 µL/min was chosen as the starting point as it resulted in individually discernible nanoparticles.

Synthesis in vertical flow chips

Three different solutions with different surfactants were heated by the laser at four different flow rates. All of these combinations resulted in magnetic nanoparticles. With increasing residence periods, an increase in average particle size was seen in the B and N solutions. The O solutions showed a non-linear trend, likely due to the agglomeration caused by oleic acid polymerisation and byproducts. UV-VIS measurements of the N samples agree with the trend seen in the STEM size analysis. Also seen with increasing residence periods was a general increase in agglomeration for the samples purified with the first method. The agglomeration was kept under control by adopting a gentler purification method. However, no amount of purification was able to completely remove the excess organic material in the samples. This points to possible changes in the structure of the adsorbed and free oleic acid, such as polymerisation (Osman & Suter, 2002), isomerisation or saturation (Willis, et al., 2005).

This supports the simulation results in Chapter 7 which suggest that the amount of the solution that has exceeded 320 °C greatly increases when the flowrate is changed from 26.55 µL/min (O2) to 13.28 µL/min (O4). While this change in the oleic acid structure is expected in thermal decomposition synthesis (Willis, et al., 2005), there is still a significant portion of the solution that reaches the nucleation temperatures but does not get hot enough for particle growth (see table Table 7.7). This would mean that the oleic acid would bind to the small nuclei and the polyiron oxo clusters (precursors to the iron oxide nuclei, which are known to have oleic acid shells during the nucleation stage (Lassenberger, et al., 2017)). The clusters and nanocrystals below 2 nm in size are known to be paramagnetic (Kim, et al., 2013), which also explains the overall weak magnetisation of the sample (evidenced by the long settling periods required for separation). As seen in size analysis of the unpurified liquid samples (section 6.4.4.4), smaller particles that are lost during purification make up a significant part of the population, although they only form a small part by volume. These smaller particles may also be hidden within the organic matrix of the polymerised and/or micellized oleic acid.

The absence of the organic network in the B and N samples supports the hypothesis that the agglomeration is caused by excess oleic acid. This makes the O solutions unsuitable for synthesis via localised heating with the current setup, however, if the heating is made more uniform, they might still be used. There has been significant interest in wormlike micelles in the last two decades (Dreiss & Feng, 2017) (Dai, et al., 2017), and considering its resiliency, the magnetic wormlike micellar system obtained here could have future applications.

For the B and N samples, the 2s residence period (flow rate = 26.55 µL/min) provided the best results, but the lowest yield of magnetic material. Consequently, they have larger amounts of partially decomposed iron oleate and excess surfactants. These were removed more easily as the oleic acid did not polymerise to a great degree. This is again consistent with the simulation results in Chapter 7, which indicate that a maximum temperature of ~340 °C was reached. Slower flow rates do result in more of the solution reaching decomposition temperatures, however the peak temperatures exceed 500 °C which may result in the formation of hematite, and further decomposition of the oleic acid.

In the purified samples, FTIR analysis suggests the presence of iron oxides. The maghemite phase is seen in most particles, while the higher residence period samples, especially in the N samples, show more signs of hematite. This is expected as maghemite is known to oxidise to hematite at higher temperatures (Roonasi & Holmgren, 2009). XRD analysis for the purified samples was inconclusive: it is unclear if the amorphous nature of the spectrum was due to the particles themselves or the mixture of iron oleate, precursor clusters (also known to be amorphous) and oleic acid coating them. XRD peaks for magnetite and hematite were observed after heating purified samples in a furnace, with a significant amount of amorphous material still being part of the sample.

Particle morphology

The particle size and size distribution has been shown to be affected by the temperature in the channel, controlled by changing the flow rate. The B and N solutions show an increase in size with an increase in temperature, as expected. The increase in particle size does not continue with a continued decrease in flow rate beyond using the N solutions, however, it does result in a narrower size distribution.

In all cases, the mean particle sizes are much larger than the ones obtained in the batch synthesis. This is again explained by the uneven temperature distribution. There are many areas within the reaction chamber where the solution gets hot enough to cause precursor cluster formation, but not hot enough for sustained growth. The clusters formed in this area can act as monomers for growth taking place in

hotter areas, resulting in larger than average particles. Not all of the monomers/nuclei will reach the growth regions, hence we also find a significant number of small particles. The streamline analysis in Chapter 7 helps better illustrate this point.

The narrowest size distribution was obtained with the N2 samples (84.7 ± 46.8 nm), with the B2 sample being a close second (78.3 ± 48.1 nm), the mean size and size distribution are still much larger than what was obtained in the batch synthesis using iron oleate in octadecene (section 3.4.3). This fact, along with the undesired organic by-products, makes these particles unsuitable for further use without processing.

The particle shapes were largely spherical in most cases. Cubical particles were observed in the N2 samples, but further growth at slower flow rates resulted in particles growing into spheres.

Reactor damage

The acrylic chips can withstand roughly over an hour of heating in total, depending on the flow rate. At slower flow rates, significant fracturing was noted, however at even the fastest flow rate, the damage accumulates and degrades the quality of the laser. While this disqualifies the use of acrylic for continued continuous flow synthesis using this method, thanks to the localised laser heating an acrylic chip is usable for quick testing and characterisation.

6.6 Summary

Nanoparticles were successfully synthesised by thermal decomposition in microfluidic chips using localised heating with a focused laser beam. The best results were obtained by heating the N solution at a flow rate of 26.55 µL/min. The particles synthesised in this run had a mean particle size of 84.7 nm with a standard deviation of 46.8 nm. The B solution at the same flow rate resulted in particles with a similar size and size distribution (78.3 nm ± 46.8 nm), but experienced heavy agglomeration and sedimentation due to the lack of surfactant. At slower flow rates, the particle sizes increased to mean sizes of up to ~250 nm using the N solution, but also results in wider size distributions.

The O solutions, when heated, resulted in a large amount of organic by-product that made it difficult to properly characterise the products. The sizes reported for this group of results only represents the visible larger particles. This by-product contamination was also seen in the results from the N solutions, albeit in smaller amounts. The contamination is proposed to be a result of the partial

decomposition of the excess oleic acid, resulting in its saturation and possible polymerisation, as well as micellization of the oleic acid during the purification process.

Compared with the results from the batch synthesis experiments, the particle sizes are several times larger and have a wider size distribution. This is thought to be due to a small growth zone surrounded by a larger nucleation zone. This provides the growth zone a much larger amount of free monomers than there would normally be available.

7 Simulation of fluid flow and heat transfer in microfluidic synthesis

This chapter details the multi-physics simulation performed to obtain a better understanding of the within the device. The experiments performed in Chapter 6 are recreated as closely as possible.

The laser beam is modelled as a focused 3D gaussian beam with its intensity decreasing with height (the z-axis) according the Beer-Lambert law, using the measured absorbance of the 0.154M O solution at 650 nm. The partial derivative of the intensity (along the z-axis) is used as the heat source for the heat transfer equations.

The geometry for the device is simple and was constructed entirely within COMSOL. Temperature-dependent material properties were taken from the literature and put together to create a custom material for the solution.

A “physics interface” or “interface” in COMSOL refers to a physics module that can be added and simulated in a COMSOL model. Fluid flow was handled using the Laminar Flow interface, fully coupled with a Heat Transfer in Fluids interface. The four different flow rates used in the experiments are used as the input parameters, while all other variables are kept constant. The main results obtained from these physics interfaces are the velocity and temperature fields, which were used for further analysis. Additionally, a Solid Mechanics interface was added, coupled with the Heat Transfer interface, to solve for the stress due to thermal expansion within the acrylic chip.

Three studies were performed. Study 1 was a Stationary study that solved only the Laminar Flow physics, i.e. unheated fluid flow within the chip. Study 2 was a stationary study that solved all three physics. Study 3 was a time dependent study that solved the Laminar Flow and Heat Transfer physics.

The results presented from Study 1 show the laminar flow profile in the device. These results were used as initial values for Study 2 and Study 3. Results from Study 2 include temperature slices, fluid particle temperature tracing (streamlines) and analysis, and acrylic temperature and stress fields. Finally, Study 3 compares the measured temperature rise with the simulated results.

7.1 Model setup

The model was designed to mimic the actual setup as closely as possible. The entire chip is modelled; in addition, a slab of aluminium is added at the bottom to factor in the heat lost to the chip stage.

7.1.1 Parameters

The parameters added to the model are listed in Table 7.1. These parameters are used in various interfaces throughout the model.

Table 7.1: Parameters used in the model.

Name	Expression	Description
P	0.25[W]	Laser output power
w_0	30e-6[m]	Radius at beam waist
z_r	400e-6[m]	Rayleigh length
A	0.415[1/mm]	Absorbance of 0.154M solution
h_channel	0.25[mm]	Inlet/outlet channel height
d_channel	0.3[mm]	Inlet/outlet channel width
l_chip	75e-3[m]	Length of chip
w_chip	20e-3[m]	Width of chip
h_chip	2.3*3e-3[m]	Height of chip
h_stage	5e-3[m]	Height of stage plate
flowrate_2s	26.6[ul/min]	Flow rate at Tr = 2s
flowrate_4s	13.28[ul/min]	Flow rate at Tr = 4s
flowrate_6s	8.85[ul/min]	Flow rate at Tr = 6s
flowrate_8s	6.64[ul/min]	Flow rate at Tr = 8s
flowrate	flowrate_8s	Current flow rate
v_inlet	flowrate/A_inletneedle	Linear velocity at inlet
alphacrylic	7.0e-5[1/K]	Thermal expansion coefficient of acrylic
A_inletneedle	pi*0.8*0.8[mm^2]	Needle Inlet cross sectional area
T_room	297[K]	Room temperature
T0_acrylic	297[K]	Initial temperature of acrylic

7.1.2 Functions

7.1.2.1 Radius (w)

Defines the radius of the beam along the z axis. The beam focus is at z = 0, the bottom of the reaction chamber.

Expression : `w_0` * sqrt(1+(z/`z_r`)^2)

Arguments : z

7.1.2.2 Gaussian beam (gp)

The beam intensity distributed along a gaussian profile. The radius of the profile is determined using the radius function w(z). The total power is multiplied by 0.94 and 0.92 to account for the reflection losses at the obtjective lens and acrylic surfaces respectively.

Expression : 0.96*0.92*P/(pi * (w(z))^2/2) * exp(-2*(x^2+y^2)/(w(z))^2)

Arguments : x,y,z

7.1.2.3 Intensity (intensity)

The intensity vs depth profile of a collimated beam with an initial intensity of 1 W/m^2. The expression uses the Beer-Lambert relation to calculate the intensity of the beam at a certain depth. The function is translated along the z axis so that the incident height is 2.3 mm (the top of the reaction chamber.

Expression : 1*10^(-A*(2.3e-3-z))

Arguments : z

7.1.2.4 Intensity_dz (intensity_dz)

The first derivative of the intensity(z) function along the z direction. This determines the absorbed energy at each “slice” (dz).

Expression : d(intensity(z),z)

Arguments : z

7.1.2.5 *Absorbed Heat (absorbedheat)*

This function multiplies the gaussian beam profile with the intensity_dz function to approximate the absorbed energy of the gaussian beam. This is an approximation because the path length of a focused beam would be slightly longer. The final function is plotted in Figure 7.1. Note that this shows where the heat is absorbed in the fluid, however the final temperature profile will also depend on the fluid flow.

Expression : gp(x,y,z) * intensity_dz(z)

Arguments : x,y,z

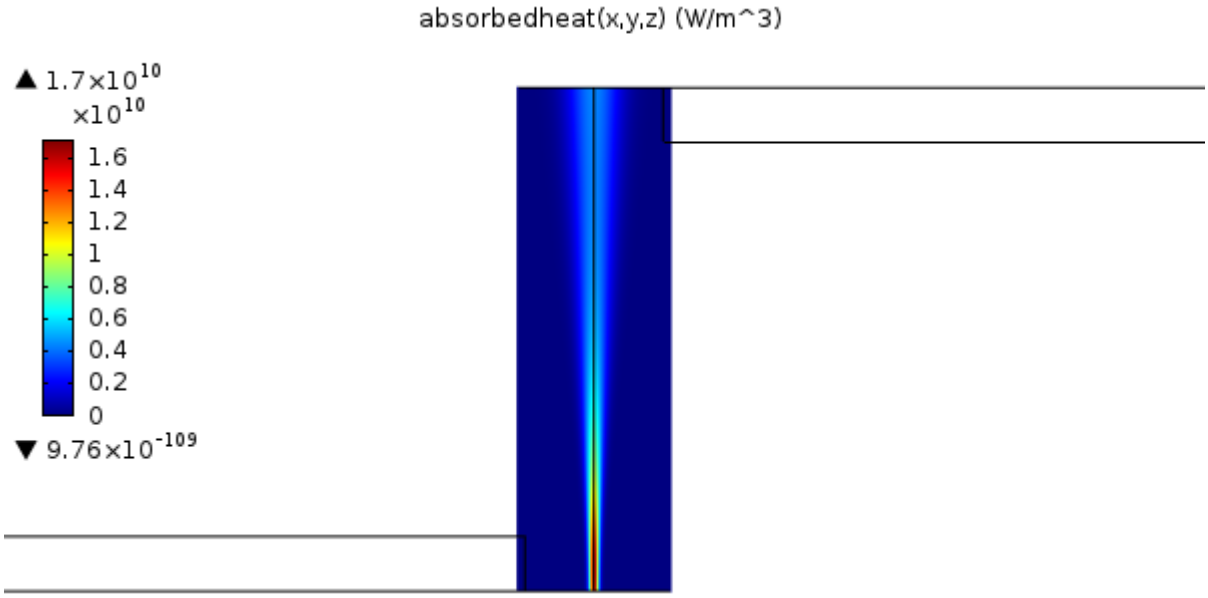


Figure 7.1: The absorbedheat function overlaid onto the geometry of the device. Visualised on an XZ plane at Y = 0.

7.1.3 Geometry

The geometry of the model was produced using COMSOL's built-in geometry builder. The final geometry used for the simulation is shown in Figure 7.2.

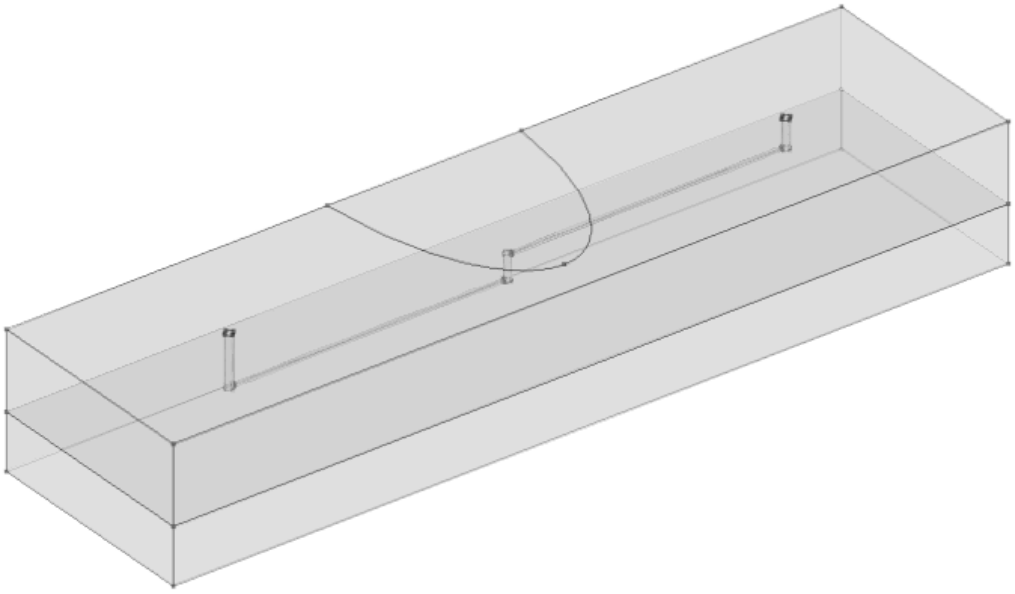


Figure 7.2: Final geometry used for the model. Image generated with transparency on.

The geometry definition is given in Table 7.2 and Table 7.3. Table 7.2 lists the solid primitives in the model, and Table 7.3 lists the operations performed on the primitive objects to produce the final geometry. The Partition Objects 1 operation (Table 7.3, #10) partitions the acrylic block with all the fluid domain primitive objects. The inlet and outlet channel blocks overlap with the inlet, outlet, and reaction chamber cylinder objects.

Work Plane 1 and its sub-object Ellipse 1 are used to partition the top surface of the chip. It does not affect the simulation; this partition is only used to emulate the surface temperature measurement as done in section 6.3.4.

The Ignore Faces 1 operation (Table 7.3, 11) selects the faces of the overlapping areas so that the three cylindrical fluid domains remain cylindrical. The Mesh Control Faces 1 operation (Table 7.3, 12) selects the vertical faces of the Beam cylinder and makes it so that the Reaction Chamber and Beam cylinder appear as a single domain except when meshing, allowing a finer mesh to be easily applied to the Beam domain. Finally, the two selections (Table 7.3, #13 and #14) are made to allow quick selection when setting up physics and meshes.

Table 7.2: List of solid geometry objects. All dimensions

Cylinders			**Size and Shape**		**Position**		
	Label	**Name**	**Radius**	**Height**	**x**	**y**	**z**
1	Reaction Chamber	cyl1	0.35e-3	h_layer	0	0	0
2	Beam	cyl2	0.1e-3	h_layer	0	0	0
3	Inlet	cyl3	0.4e-3	h_layer*2	-25e-3	0	0
4	Outlet	cyl4	0.4e-3	h_layer+h_channel	25e-3	0	h_layer-h_channel

Blocks			**Size and Shape**			**Position**		
	Label	**Name**	**Width**	**Depth**	**Height**	**x**	**y**	**z**
5	Inlet Channel	blk1	25e-3	d_channel	h_channel	-25.2e-3	-d_channel/2	0
6	Outlet Channel	blk2	25e-3	d_channel	h_channel	0.2e-3	-d_channel/2	h_layer-h_channel
7	Acrylic	blk3	l_chip	w_chip	h_chip	-l_chip/2	-w_chip/2	-h_layer
8	Aluminium stage	blk4	l_chip	w_chip	h_stage	-l_chip/2	-w_chip/2	h_layer-h_stage

Work Planes					
	Label	**Name**	**Plane type**	**Planar face**	
9	Work Plane 1	wp1	Face Parallel	par1, 4	

	Work Plane 1 Objects		**Size and Shape**			**Position**		
	Label		**Name**	**a-semiaxis**	**b-semiaxis**	**Sector angle**	**Base**	**xw**	**yw**
	9a	Ellipse 1	e1	8.8e-3	19.4e-3	360	Center	0	-12.6e-3

Table 7.3: Boolean operations performed on the solid objects

Partitions				
	Label	**Name**	**Objects to partition**	**Tool objects**
10	Partition Objects 1	par1	blk3	cyl1, cyl2, cyl3, cyl4, blk1, blk2
Virtual Operations				
	Label	**Name**	**Faces to ignore**	
11	Ignore Faces 1	igf1	14, 15, 17, 18, 27, 34, 36, 38, 39, 48, 49, 50, 52, 64, 66, 68, 71	
	Label	**Name**	**Faces to include**	
12	Mesh Control Faces 1	mcf1	29, 30, 34, 35	
Selections				
	Label	**Name**	**Geometric Entity Level**	**Entities Selected**
13	Fluid Domains	sel1	Domain	3, 4, 5, 6, 7
14	Solid domains	sel2	Domain	1, 2

7.1.4 Materials

The model makes use of three main materials:

1. Acrylic: the material used to fabricate the microfluidic chip
2. Aluminium: The stage on which the microfluidic chip rests
3. O solution: A mixture of iron oleate and oleic acid dissolved in 1-octadecene.

For aluminium, "Aluminium 6063-T83" was used from COMSOL's built-in material library. For acrylic, COMSOL's built-in "Acrylic" was used as a base material; however, its thermodynamic properties were static, making it unsuitable for our simulation in which it which would see a large temperature change.

Temperature dependent heat capacity and thermal conductivity values were taken from Gauri et al (Gaur, et al., 1982) and dos Santos et al respectively. Linear extrapolation was used for the heat capacity function, while the thermal conductivity function was set to constant extrapolation.

7.1.4.1 Heat capacity

The heat capacities of oleic acid and octadecene were used from reference data (Yaws, 2010). The heat capacity curves were described by the polynomial equation $C_p = A + B.T + C.T^2 + D.T^3 + E.T^4 + F.T^5 + G.T^6$, where T is the temperature in Kelvin and the coefficients (listed in Table 11.3) yield the heat capacity in J/mol.K. The properties of iron oleate ($FeC_{36}H_{66}O_4$) were not available and thus the nearest compound (cobalt (II) oleate – $CoC_{36}H_{66}O_4$) were used instead. The data provided does not include its heat of decomposition, however the iron oleate is a relatively small fraction of the mixture by weight and is not expected to make a large difference overall. Additionally, since the solution is heated in a closed area there is no loss of mass unlike what is observed in a typical TGA/DSC run.

The heat capacity of each material was first converted to J/kg.K by dividing by its molar mass. The converted values were scaled to the amounts of each material used in the O solution (5.72025 g octadecene, 0.316912 g oleic acid, and 1.01 g iron oleate). The values were added and normalised to obtain the heat capacity in J/kg.K (shown in Figure 7.3).

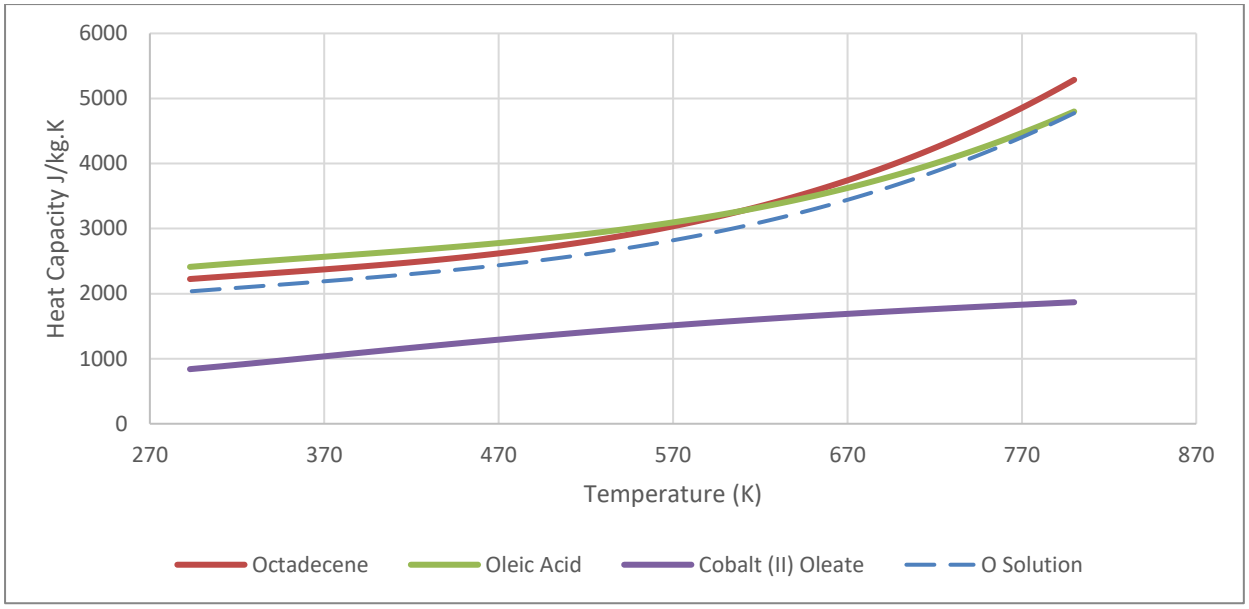


Figure 7.3: Heat capacities of the O solution and its constituent materials, used for the simulation.

7.1.4.2 Other properties

Other required thermal and physical properties were taken from Yaws' (Yaws, 2010) (Yaws, 2010) as well. The equations and coefficients are shown in Table 11.4. After adding the conversion factor to each equation, they were entered into COMSOL as the fluid's material properties. Graphs of the final properties are shown in Figure 11.22, Figure 11.23 and Figure 11.24.

7.1.5 Laminar Flow (spf)

The Laminar Flow interface solves the Navier-Stokes equations

$$\rho\left(\frac{\partial u}{\partial t}+u.\nabla u\right)=-\nabla \mathrm{p}+\nabla.\left(\mu\left(\nabla \mathrm{u}+(\nabla \mathrm{u})^{\mathrm{T}}\right)-\frac{2}{3}\mu(\nabla.u)I\right)+F \qquad 1$$

$$\frac{\partial \rho}{\partial t}+\nabla.(\rho u)=0 \qquad 2$$

Briefly put, the terms of the equation represent the various forces affecting the fluid flow:

- Inertial forces $\rho\left(\frac{\partial u}{\partial t}+u.\nabla u\right)$
- Pressure forces $-\mathrm{pI}$
- Viscous forces $\mu\left(\nabla \mathrm{u}+(\nabla \mathrm{u})^{\mathrm{T}}\right)$
- External forces F

In our case we have very low velocities and no noticeable evaporation, hence we can assume a laminar, incompressible flow. For an incompressible flow, the divergence of the velocity field is zero ($\nabla . u = 0$), reducing the momentum equation to:

$$\rho\left(\frac{\partial u}{\partial t} + u.\nabla u\right) = \nabla.\left[-\mathrm{pI} + \mu\left(\nabla \mathrm{u} + (\nabla \mathrm{u})^{\mathrm{T}}\right)\right] + F$$

The dependent variables being solved are u (velocity) and p (pressure).

7.1.5.1 Boundary Conditions

Walls

With the exception of the inlet and outlet boundaries, all other boundaries are default walls using a no-slip boundary condition, where $\mathrm{u} = 0$.

Inlet

The inlet boundary is assigned the Laminar inflow boundary condition, described using the flow rate option. The inputs are:

1. Flow rate (V_0) : `flowrate` m^3/s
2. Entrance length (L_{entr}) : 1 m

Outlet

The outlet boundary is assigned a pressure condition with $p_0 = 0\ Pa$

Initial Values 1

The use of appropriate initial values closer to the solution helps the solver to converge faster. The initial values of the velocity fields were set separately for the different fluid domains. The Initial Values 1 boundary condition was applied to the inlet domain with the following values:

1. u_x : 0 m/s
2. u_y : 0 m/s
3. u_z : -v_inlet m/s
4. Pressure : 10 Pa

Initial Values 2

The Initial Values 2 boundary condition was applied to the outlet and reaction chamber domains where the fluid flows upwards with the following values:

1. u_x : 0 m/s
2. u_y : 0 m/s
3. u_z : v_inlet m/s
4. Pressure : 5 Pa

Initial Values 3

The Initial Values 2 boundary condition was applied to the inlet and outlet channel domains where the fluid flows upwards with the following values:

1. u_x : v_inlet*3 m/s
2. u_y : 0 m/s
3. u_z : 0 m/s
4. Pressure : 5 Pa

7.1.6 Heat Transfer in Fluids (ht)

The Heat Transfer in Fluids physics interface handles heat transfer for all domains. A Heat Transfer in Solids sub-node is added to handle the solid domains.

The main equation being solved in the solid domains is the heat equation:

$$\rho C_p \frac{\partial T}{\partial t} = \nabla.(k\nabla T) + Q$$

In the fluid domains a few terms are added to represent the energy being transported by the moving fluid.

$$\rho C_p \frac{\partial T}{\partial t} + \rho C_p u.\nabla T = \nabla.(k\nabla T) + Q + Q_{vd} + Q_p$$

ρ Density

T Temperature

u Velocity field

C_p Heat capacity at constant pressure

Q External heat flux

Q_{vd} Viscous dissipation

Q_p Pressure work

7.1.6.1 Boundary Conditions

Initial Values 1

All domains were given an initial value of T_room (297 K), the room temperature.

Heat Source 1

A heat source condition was applied to the reaction chamber domain. The General source option was chosen, with a user defined value of Q being assigned.

1. Q : absorbedheat(x,y,z) W/m^3

Outflow 1

The outlet face was assigned the outflow boundary condition.

Diffuse Surface 1

The diffuse surface condition models the radiation of heat from an external surface. This condition was applied to all external surfaces of the acrylic chip. The inputs are:

1. Ambient temperature : T0 K
2. Surface emissivity : 0.94

Diffuse Surface 2

This condition was applied to all external surfaces of the aluminium stage. The inputs are:

1. Ambient temperature : T0 K
2. Surface emissivity : 0.96

The surface emissivity value is of the black paint coating the aluminium stage, rather than the aluminium itself.

Thermal Contact 1

This condition was applied to the interface between the acrylic chip and the aluminium stage. It models the lower heat conduction at the interface due to surface roughness and microscopic interstitial gas (air) pockets. The contact models chosen are:

1. Constriction conductance correlation : Cooper-Mikic-Yovanovich correlation
2. Gap conductance correlation : Parralel-plate-gap gas conductance

The inputs are:

1. Surface roughness, asperities average height : 1[μm] m
2. Surface roughness, asperities average slope : m_{asp}
3. Contact pressure : 0.8[kPa] Pa
4. Microhardness : 20.6[kPa] Pa

The contact pressure was estimated from the weight and area of the acrylic chip. Other values were estimated from values of anodised aluminium. Due to the low contact pressure the effect of the other values is greatly reduced. The gap properties were left to the default values for air.

Heat Flux Top

This boundary condition is applied to the top surface of the acrylic chip. The Convective heat flux option was chosen with the following inputs:

The heat flux modes chosen are:

1. Heat Flux : Convective heat flux
2. Heat transfer coefficient : External natural convection, Horizontal plate, upside
3. Fluid : Air

The inputs are:

1. Plate diameter L : `l_chip*w_chip/(2*l_chip + 2*w_chip)`
2. Absolute pressure p_A : 1[atm] Pa
3. External temperature T : `T0` K

Heat Flux Long Side 1

This condition was applied to the rear long sides of the acrylic chip and aluminium stage.

The heat flux modes chosen are:

1. Heat Flux : Convective heat flux
2. Heat transfer coefficient : External natural convection, Vertical wall
3. Fluid : Air

The inputs are:

1. Plate diameter L :
   `l_chip*(h_chip+h_stage)/(2*(l_chip+h_chip+h_stage))`
2. Absolute pressure p_A : 1[atm] Pa

3. External temperature T : `T0` K

Heat Flux Long Side 2

A duplicate of the previous boundary condition but applied to the front long sides of the chip and aluminium stage.

Heat Flux Short Side 1

This condition was applied to the short sides of the acrylic chip and aluminium stage on the left.

The heat flux modes chosen are:

1. Heat Flux : Convective heat flux
2. Heat transfer coefficient : External natural convection, Vertical wall
3. Fluid : Air

The inputs are:

1. Plate diameter L :
   `w_chip*(h_chip+h_stage)/(2*(w_chip+h_chip+h_stage))`
2. Absolute pressure p_A : 1[atm] Pa
3. External temperature T : `T0` K

Heat Flux Short Side 2

A duplicate of the previous boundary condition but applied to the short sides on the right side of chip and aluminium stage.

Heat Flux Bottom

This condition was applied to the bottom of the aluminium stage.

The heat flux modes chosen are:

1. Heat Flux : Convective heat flux
4. Heat transfer coefficient : External natural convection, Horizontal plate, downside
5. Fluid : Air

The inputs are:

4. Plate diameter L : `l_chip*w_chip/(2*l_chip + 2*w_chip)`
5. Absolute pressure p_A : 1[atm] Pa

6. External temperature T : T0 K

7.1.7 Solid Mechanics (solid)

The Solid Mechanics physics interface was applied to the acrylic domain only. The thermal expansion of the acrylic was defined by manually editing the variables being solved.

This was done by enabling Equation View in the model. The Solid Mechanics interface adds a Linear Elastic Material node by default. Opening the equation view for this node, three variables were edited:

Variable	Default value	Edited value
solid.eXX	u2X	u2X-alphacrylic*(T-T0)
solid.eYY	u2Y	u2Y-alphacrylic*(T-T0)
solid.eZZ	u2Z	u2Z-alphacrylic*(T-T0)

The three variables are the x, y, and z components of the strain tensor of the domain. The modified expressions add the thermal expansion term to the strain tensor, which is then used by the physics interface to calculate the stress in the domain. This approach is adapted from a COMSOL model example (COMSOL Inc., n.d.), which describes how to model thermal expansion using a basic COMSOL installation.

7.1.7.1 Boundary Conditions

Fixed Constraint 1

This condition was applied to the bottom face of the acrylic chip.

7.1.8 Multiphysics couplings

Multiphysics couplings are used to share variables between the various physics interfaces in the model. The following couplings were added:

Temperature coupling 1

Source : Heat Transfer in Fluids (ht)

Destination : Laminar Flow (spf)

Flow coupling 1

Source : Laminar Flow (spf)

Destination : Heat Transfer in Fluids (ht)

Temperature coupling 2

Source : Heat Transfer in Fluids (ht)

Destination : Solid Mechanics (solid)

7.1.9 Mesh

The final mesh parameters were tuned based on trial-and-error by balancing physics requirements, memory usage, result quality and solving time.

The Beam domain was created to have a dense mesh in the laser beam area, while the rest of the reaction chamber and the inlet and outlet ports were meshed with a slightly coarser mesh. The inlet and outlet channels were also given a fine mesh. More details can be found in Table 7.4.

Figure 7.4 shows a cutaway view of the final mesh showing the different mesh densities in the different domains.

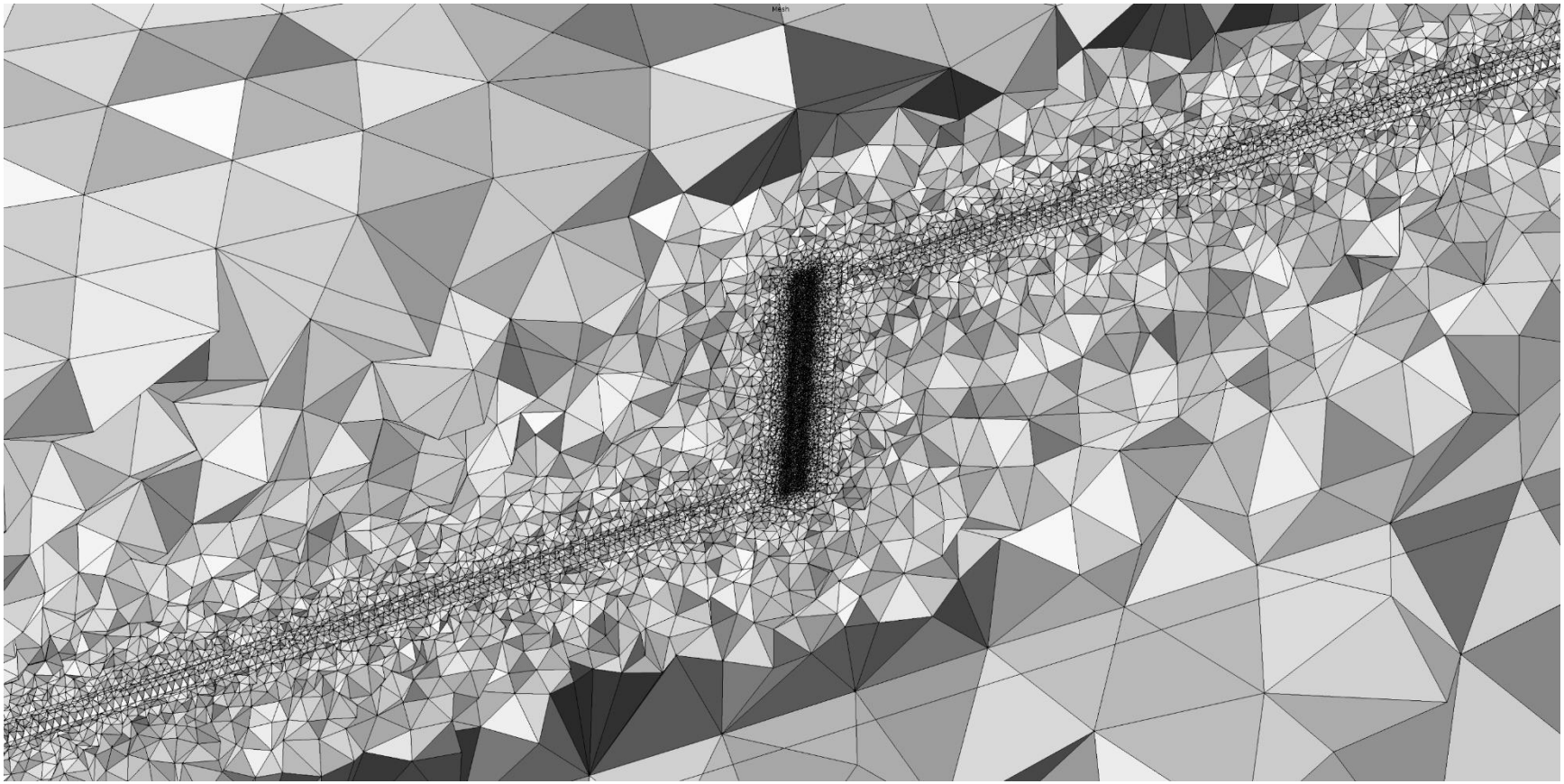


Figure 7.4: Cutaway view (y>0) of the final mesh used for the simulation.

Table 7.4: Details of the mesh sequence used for the model. The values in grayed out cells are the default predefined values that were left unchanged.

Mesh nodes	**Free Tetrahedral 1**				**Free Tetrahedral 2**	
Geometric entity level	Domain				Domain	
Selection	Fluid Domains				Solid Domains	
Size sub-nodes	**Beam**	**Chamber**	**Channels**	**Ports**	**Acrylic**	**Aluminium**
Geometric entity level	Domain	Domain	Domain	Domain	Domain	Domain
Selection	8	5	4, 6	3, 7	2	1
Calibrate for	Fluid dynamics	Fluid dynamics	Fluid dynamics	Fluid dynamics	General physics	General physics
Predefined/Custom	Extremely fine	Custom (Finer)	Custom (Extra fine)	Custom (Finer)	Custom (Finer)	Extra fine
Maximum element size	0.291e-3	0.8e-3	h_channel/3	0.7e-3	1.5e-3	2.63e-3
Minimum element size	4.47e-6	0.05e-3	h_channel/4	0.7e-5	0.8e-3	0.113e-3
Maximum element growth rate	1.05	1.2	1.15	1.1	1.3	1.35
Curvature factor	0.2	0.4	0.3	0.4	0.4	0.3
Resolution of narrow regions	1	0.9	0.95	0.9	0.7	0.85

7.2 Studies

Three COMSOL studies were computed using different physics interfaces for each case.

7.2.1 Study 1: LF, Stationary

In the stationary step settings, the solving of the Heat Transfer in Fluids and Solid Mechanics physics interfaces was disabled. The room temperatures and initial acrylic temperatures are set according to the measured temperatures during the actual synthesis runs.

A parametric sweep node was added to the study with the following settings:

Sweep type: Specified combinations

Parameter name	Parameter value list	Parameter unit
Flowrate	26.55, 13.28, 8.85, 6.64	ul/min
T_room	24, 24, 23.5, 26.5	degC
T0_acrylic	24.6, 24.3, 23.5, 27	degC

No other changes were made.

7.2.2 Study 2: LF, HT, and SM, Stationary

In this study, all physics interfaces were solved. The default solver was shown and within the Direct solver node, the Out-of-core option was enabled. Solving the Solid Mechanics equations require a lot of memory. This option allows the matrix factorisations to be stored on the hard drive and is useful for systems with insufficient memory.

The same parametric sweep node from section 7.2.1 was added again.

No other changes were made.

7.2.3 Study 3: LF and HT, Transient Study

A transient study was performed solving the Laminar Flow and Heat Transfer in Fluids physics. The default solver generated by COMSOL was used without any changes.

The output time steps were generated using an exponential function in order to improve temporal resolution during the first few seconds when most of the temperature rise occurs. The MATLAB

function used was t = [0 1000*exp((1:0.5:15)-15)], which generates 30 time steps ranging from 0 to 1000, shown in Figure 7.5

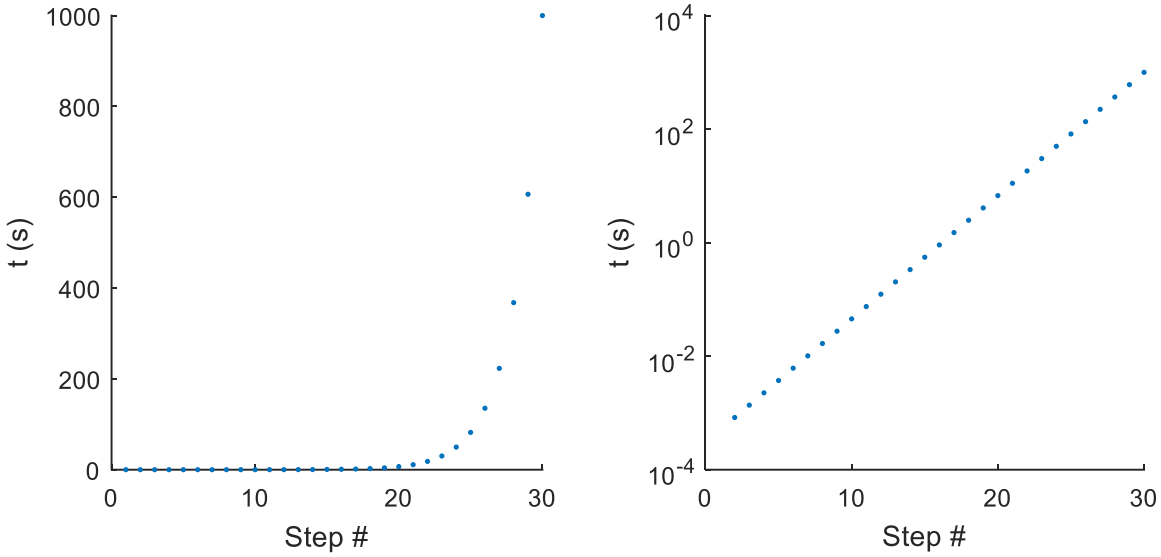


Figure 7.5: Output time steps used in the transient study.

The same parametric sweep node from section 7.2.1 was added again.

No other changes were made.

7.3 Results

7.3.1 Study 1: LF Stationary

7.3.1.1 Velocity - slice

Figure 7.6 and Figure 7.7 show results from Study 1, where only the Laminar Flow physics was solved, i.e. isothermal flow. Arrows are plotted in Figure 7.6 to illustrate the direction of flow. Apart from the overall magnitude, the velocity pattern is identical between all four flowrates.

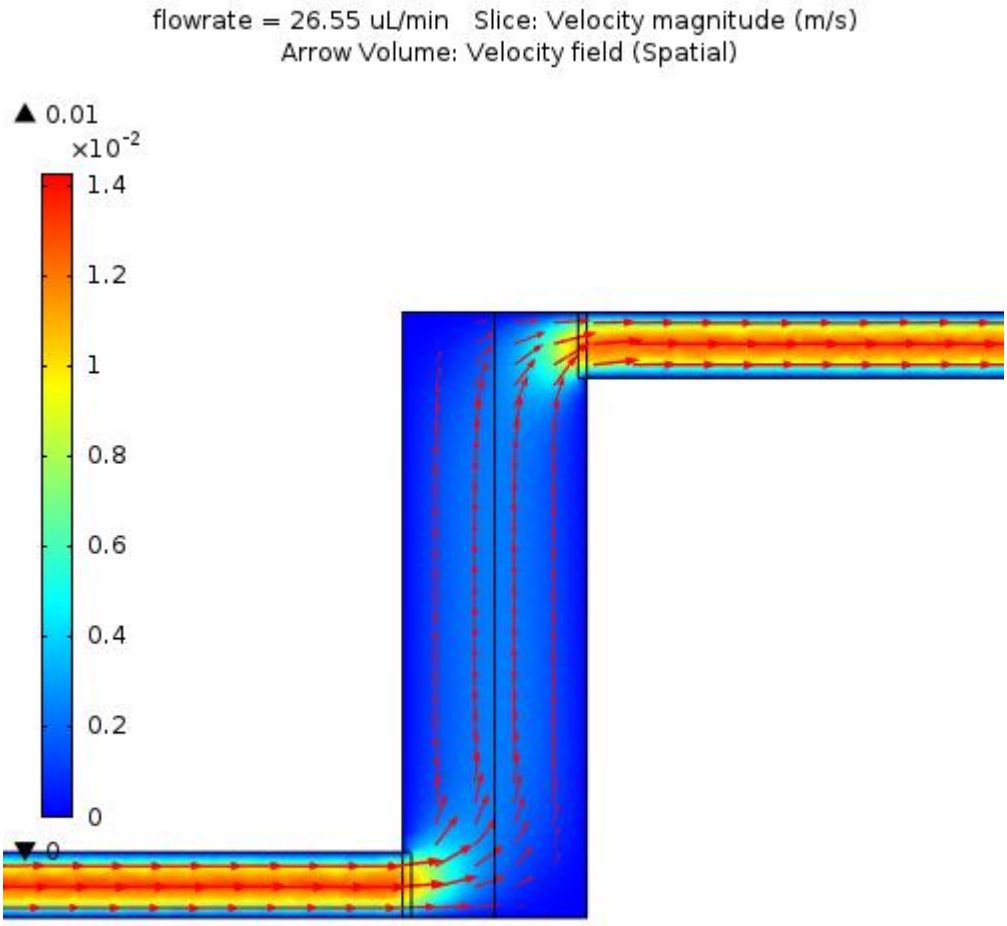


Figure 7.6: Velocity magnitude of unheated fluid (from Study 1) at 26.55 µL/min with arrows showing direction of flow. Visualised on an XZ plane at Y = 0.

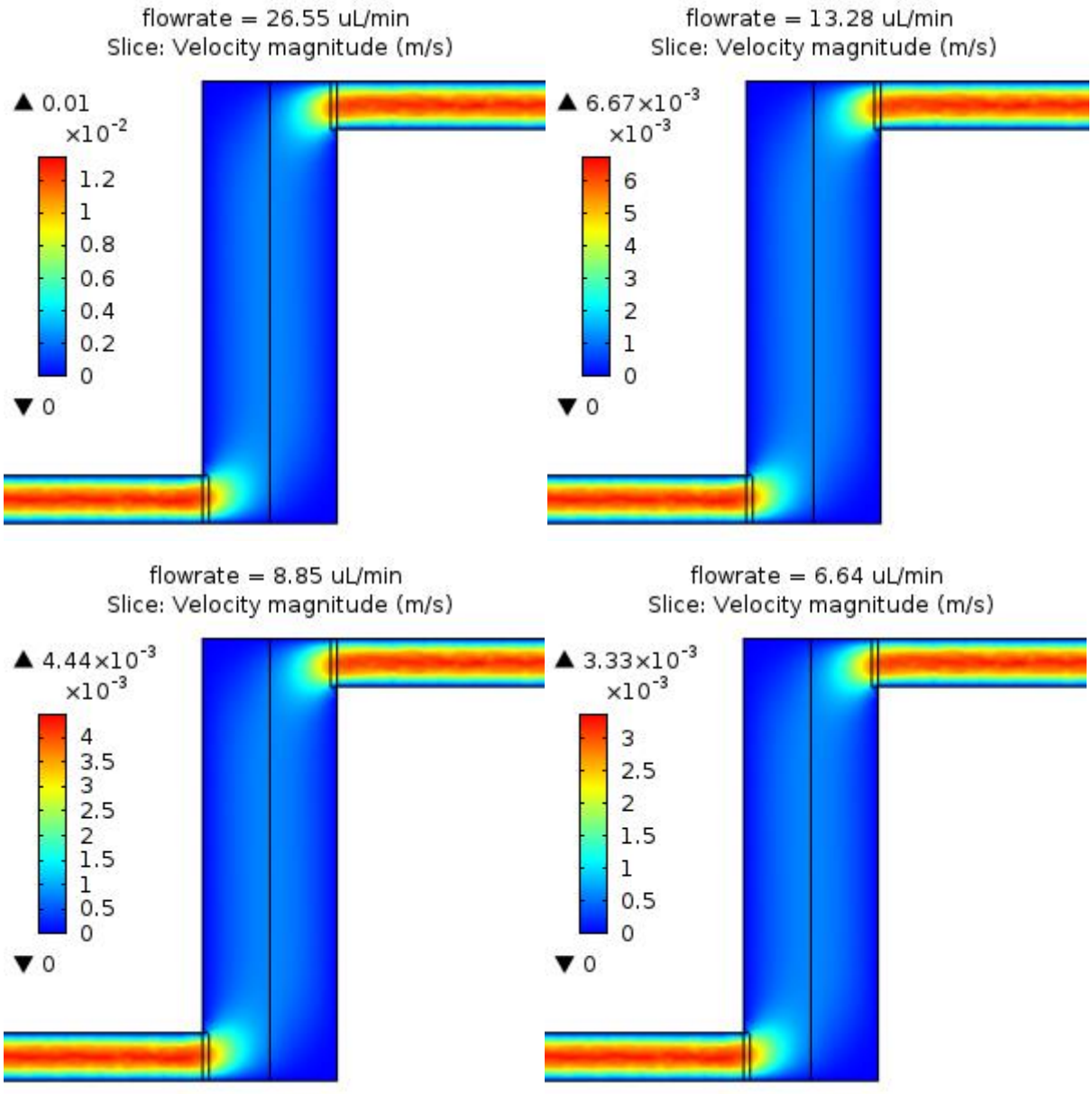


Figure 7.7: Velocity magnitude of unheated fluid (from Study 1) in the device at different flow rates. Visualised on an XZ plane at Y = 0.

7.3.2 Study 2: LF, HT, and SM Stationary

7.3.2.1 Velocity - slice

Figure 7.8 shows the results from Study 3, where the heat transfer and laminar flow physics are conjugated. Compared to the unheated flow (Figure 7.7) the velocity in the centre of the reaction chamber shows small increases with increasing temperatures. Figure 7.9 shows the same results but with synchronised scales, for easier comparison between the different flow rates.

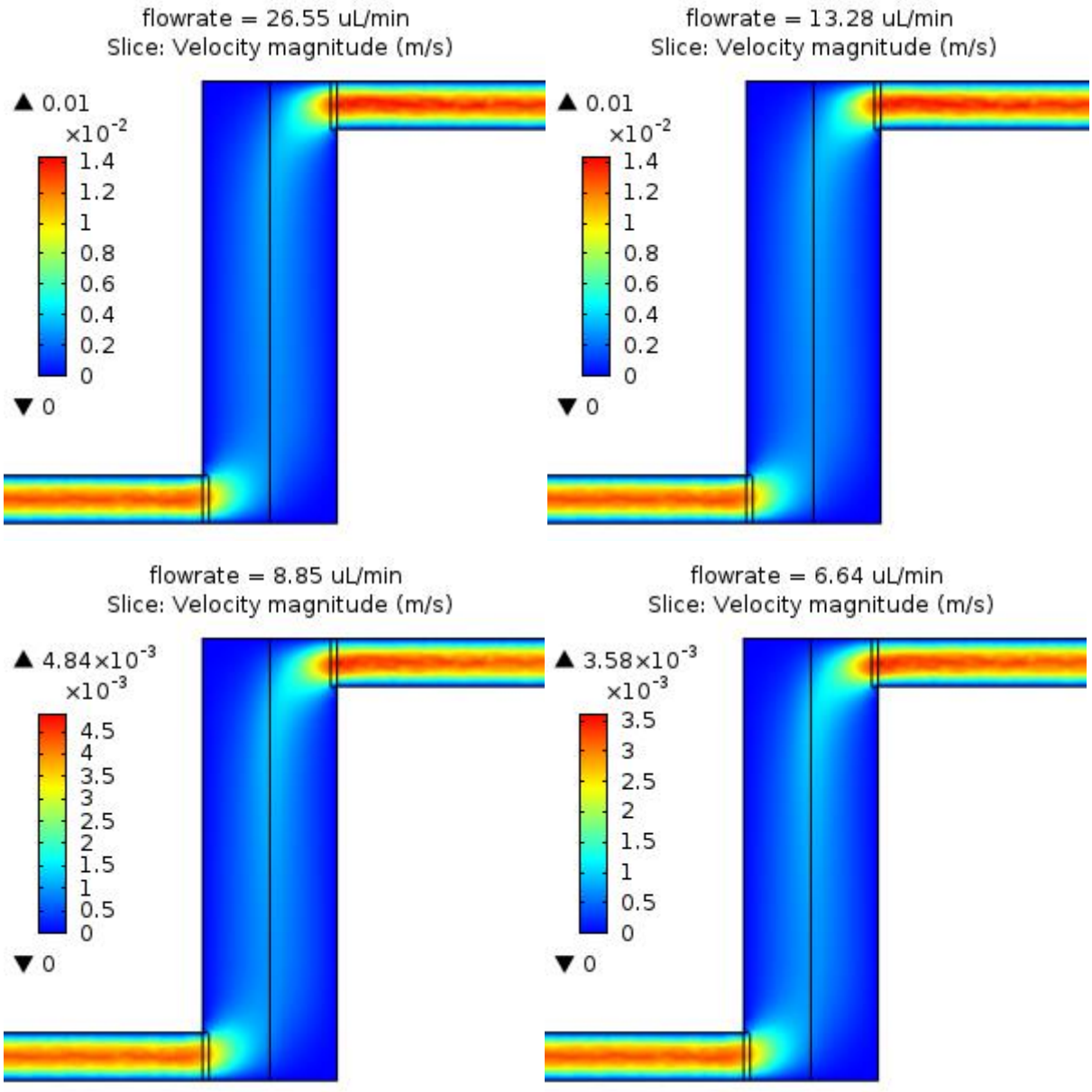


Figure 7.8: Velocity magnitude of the heated fluid (from Study 3) in the device at different flow rates. Visualised on an XZ plane at Y = 0.

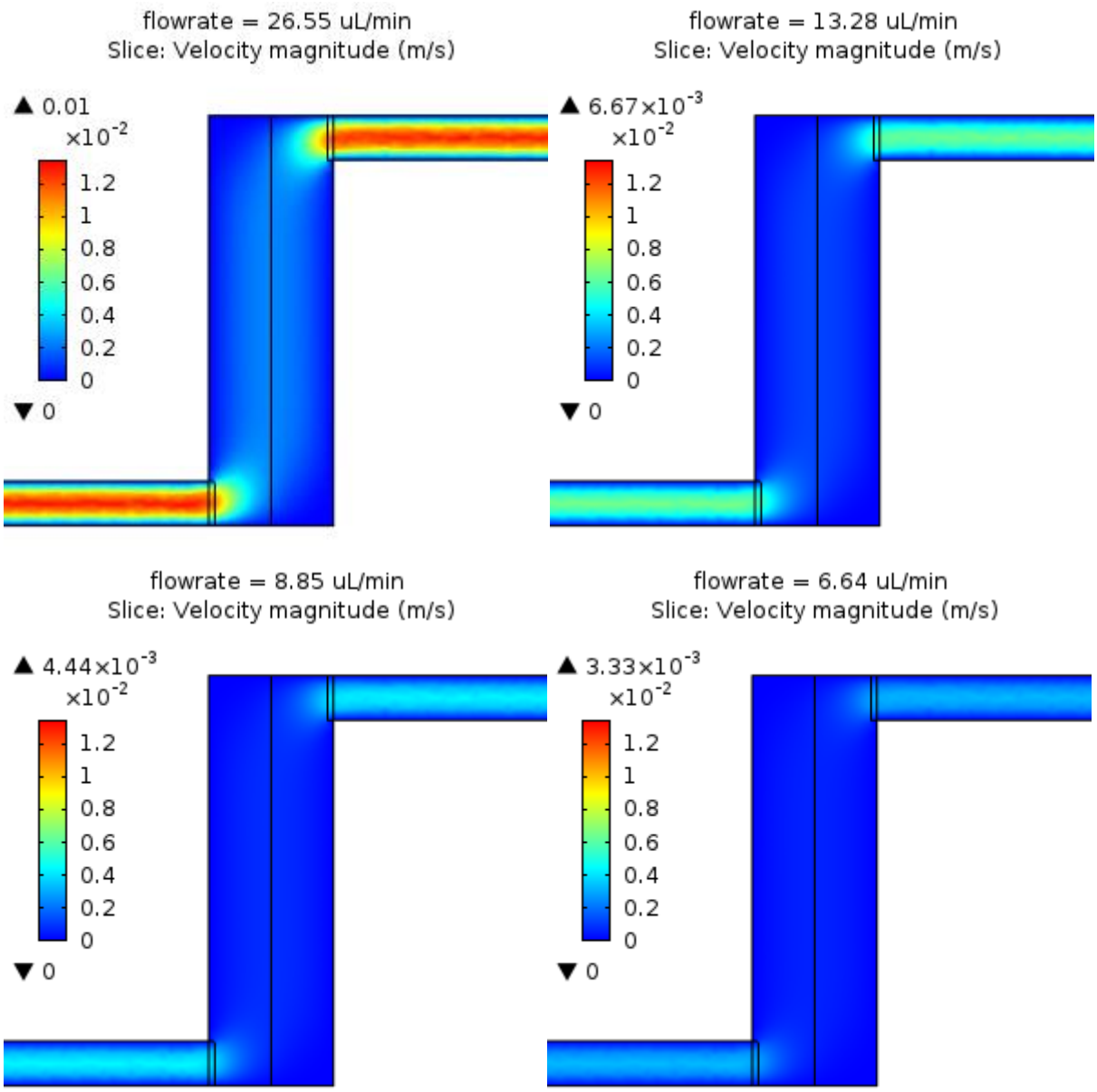


Figure 7.9: Velocity magnitude of the heated fluid (from Study 3) in the device at different flow rates (synchronised scales). Visualised on an XZ plane at Y = 0.

7.3.2.2 Temperature - slice

The temperature field was visualised on a slice on the ZX plane at Y = 0, shown in Figure 7.11, Figure 7.10, and Figure 7.12.

In Figure 7.10, the colour tables are scaled independently, highlighting the effect of the flow rate on the temperature distribution within the channel. In Figure 7.11, the scales are synchronised, emphasising the absolute temperature differences between the four cases.

Figure 7.12 reduces these temperature fields to filled contours based on significant temperature points in the thermal decomposition process (shown in Table 7.5). Most of the growth occurs in regions above 320°C, and temperatures as high as 351°C have been reported for growth in iron oleate thermal decomposition synthesis.

Table 7.5: List of significant temperatures for iron oleate.

Significant temperatures	
220° C	Nucleation temperature (lower bound)
250° C	Nucleation temperature (upper bound)
320° C	Decomposition temperature (lower bound)
350° C	Decomposition temperature (upper bound)

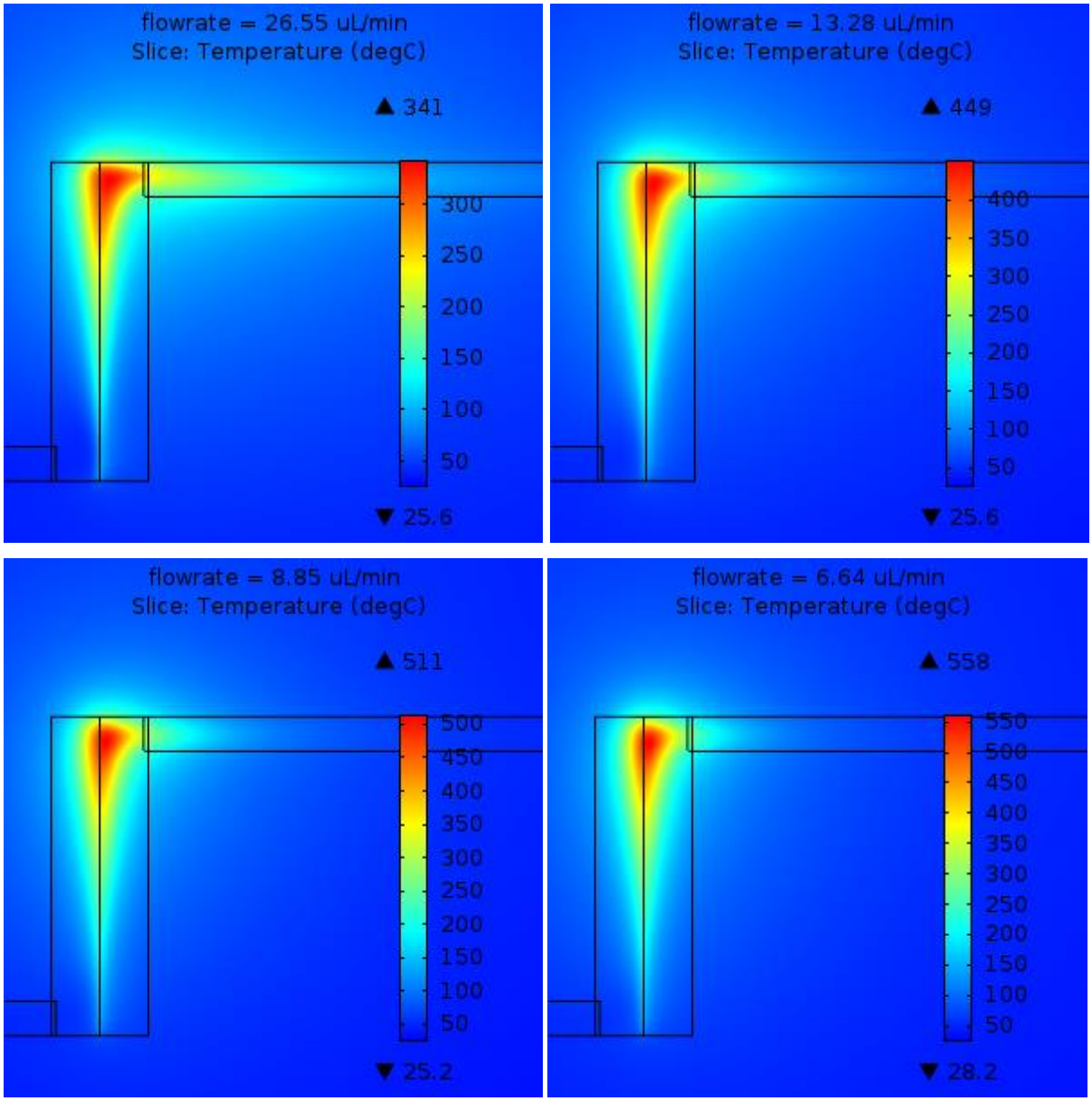


Figure 7.10: Temperature field in the device (independent temperature scales). Visualised on an XZ plane at Y = 0.

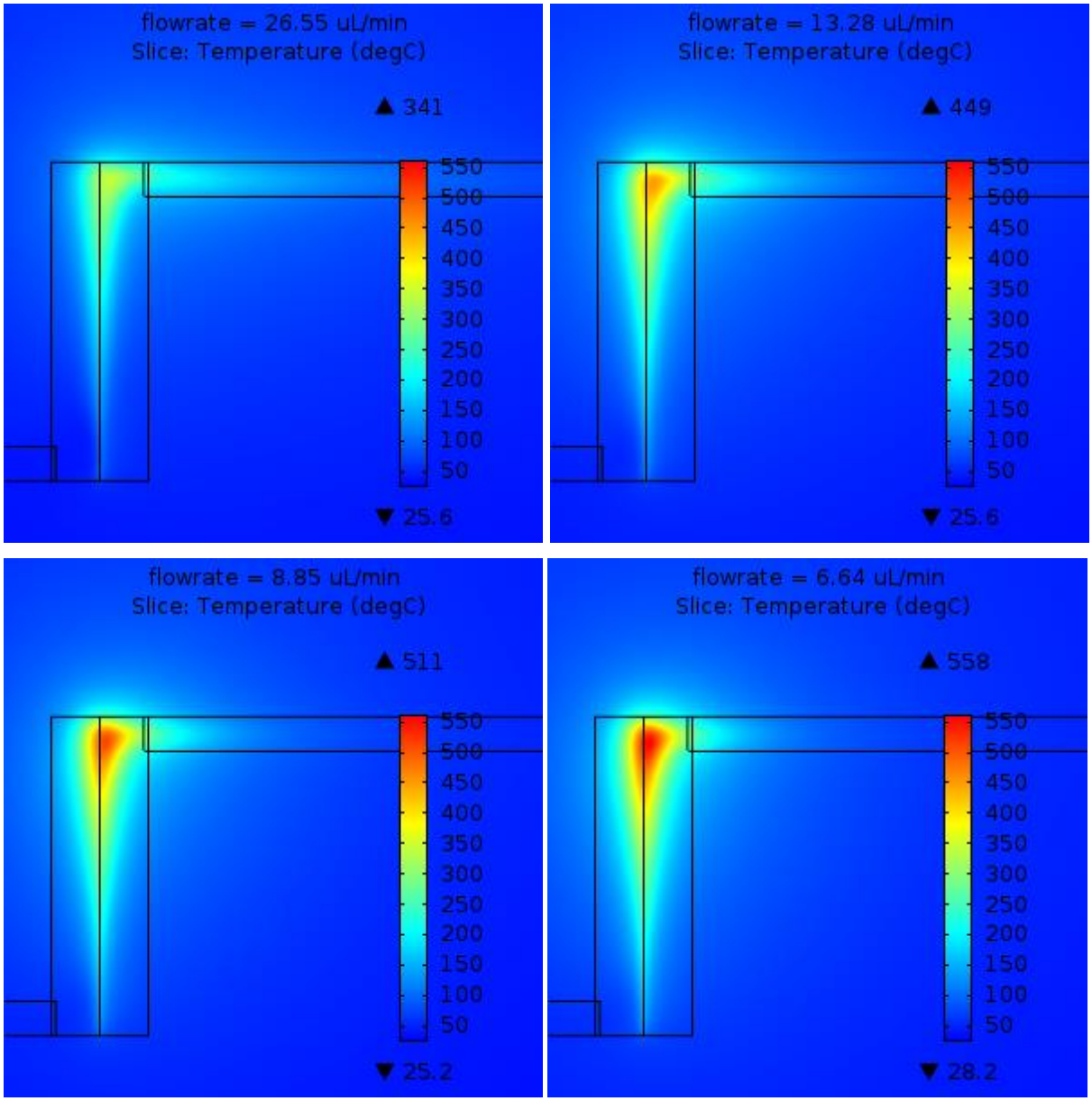


Figure 7.11: Temperature field in the device at different flow rates (synchronised temperature scales). Visualised on an XZ plane at Y = 0.

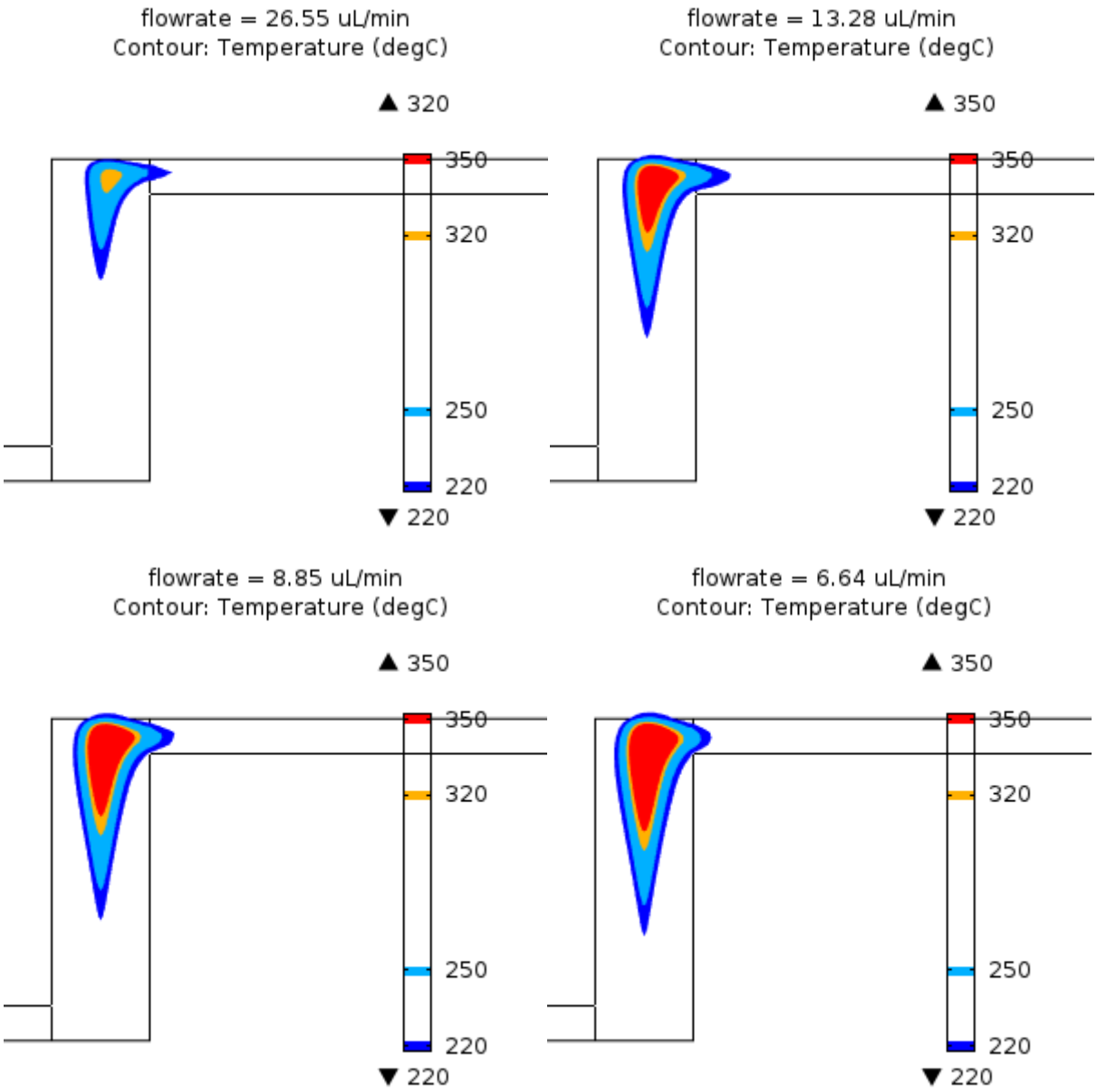


Figure 7.12: Temperature field contours at different flow rates. The contour levels are chosen based on the nucleation and decomposition temperature ranges (Table 7.5).

7.3.2.3 Temperature (fluid) - Particle tracing

Particle tracing results are presented in order to better understand the temperatures experienced by individual streamlines of the fluid (Figure 7.13 - Figure 7.16). Our model can be considered symmetric along the XZ plane, hence the particle tracing plots only show the positive half (y>0) of the channel.

Briefly put, starting points for massless particles were placed at every 10 µm after the end of the inlet channel (at x = -0.345 mm; y = 0, 10e-6, 20e-6, 30e-6, …; z = 0, 10e-6, 20e-6, 30e-6, …), resulting in 336 streamlines leading up and out of the reaction chamber. The particle traces were assigned colour

expressions which indicate the temperature at that point in degrees Celsius. Note that COMSOL's particle tracing plot was used here rather than the streamline plot because its results also show the time.

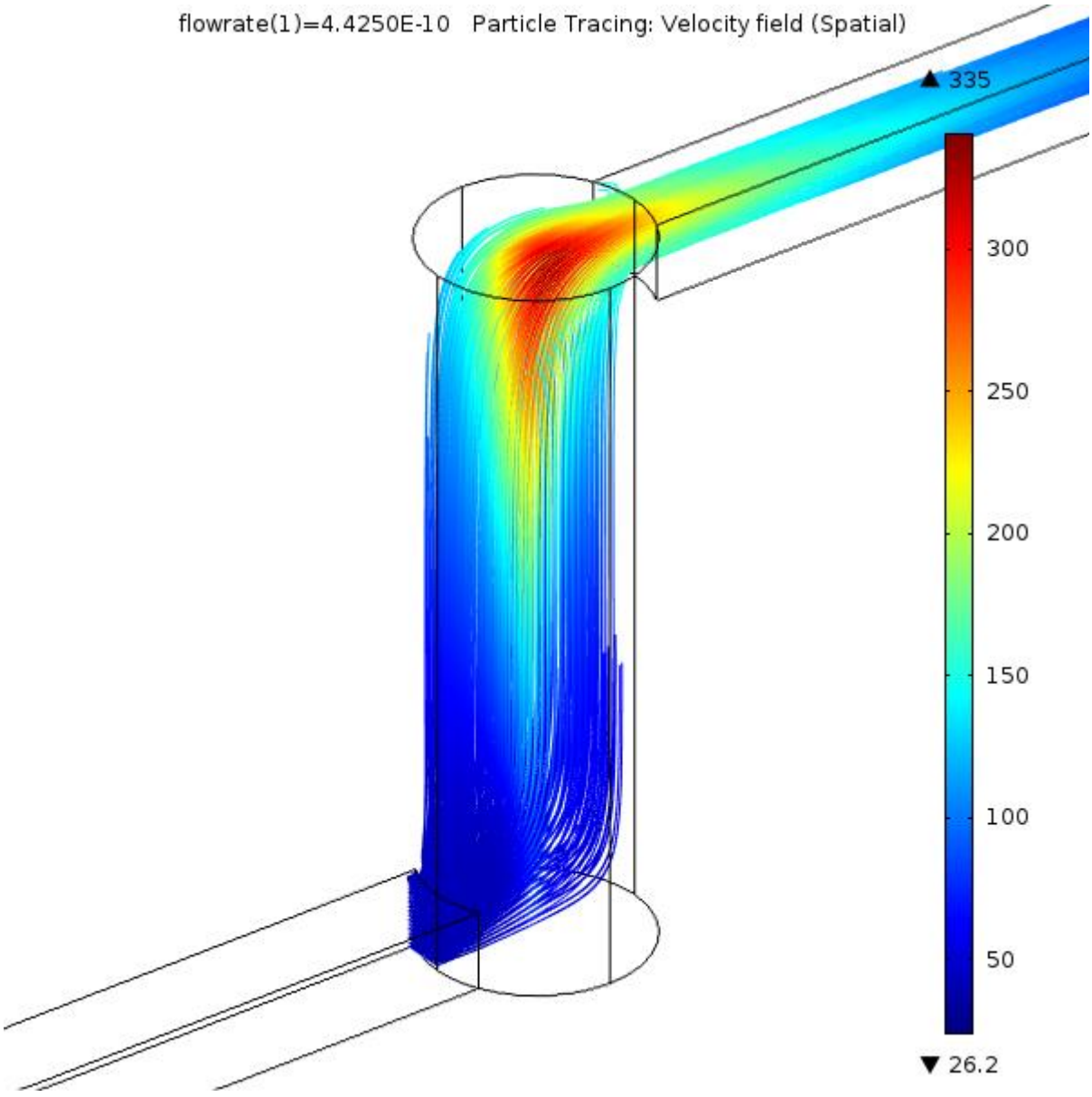


Figure 7.13: Particle tracing in one half (y>0) of the channel (flow rate = 4.4250e-10 mm^3/s). The colour of the traces represents the temperature in degrees Celsius.

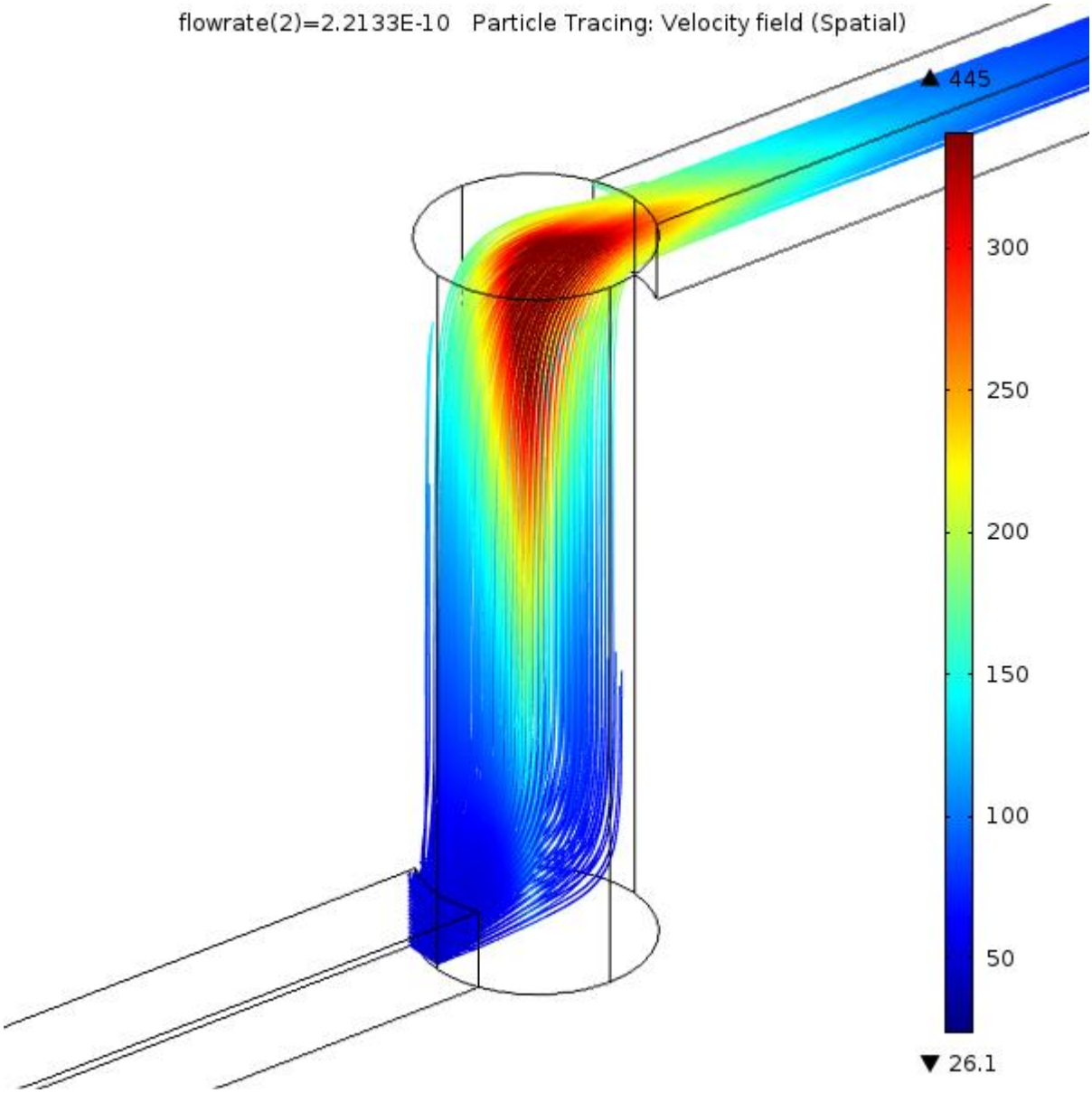


Figure 7.14: Particle tracing in one half (y>0) of the channel (flow rate = 2.2133e-10 mm^3/s). The colour of the traces represents the temperature in degrees Celsius.

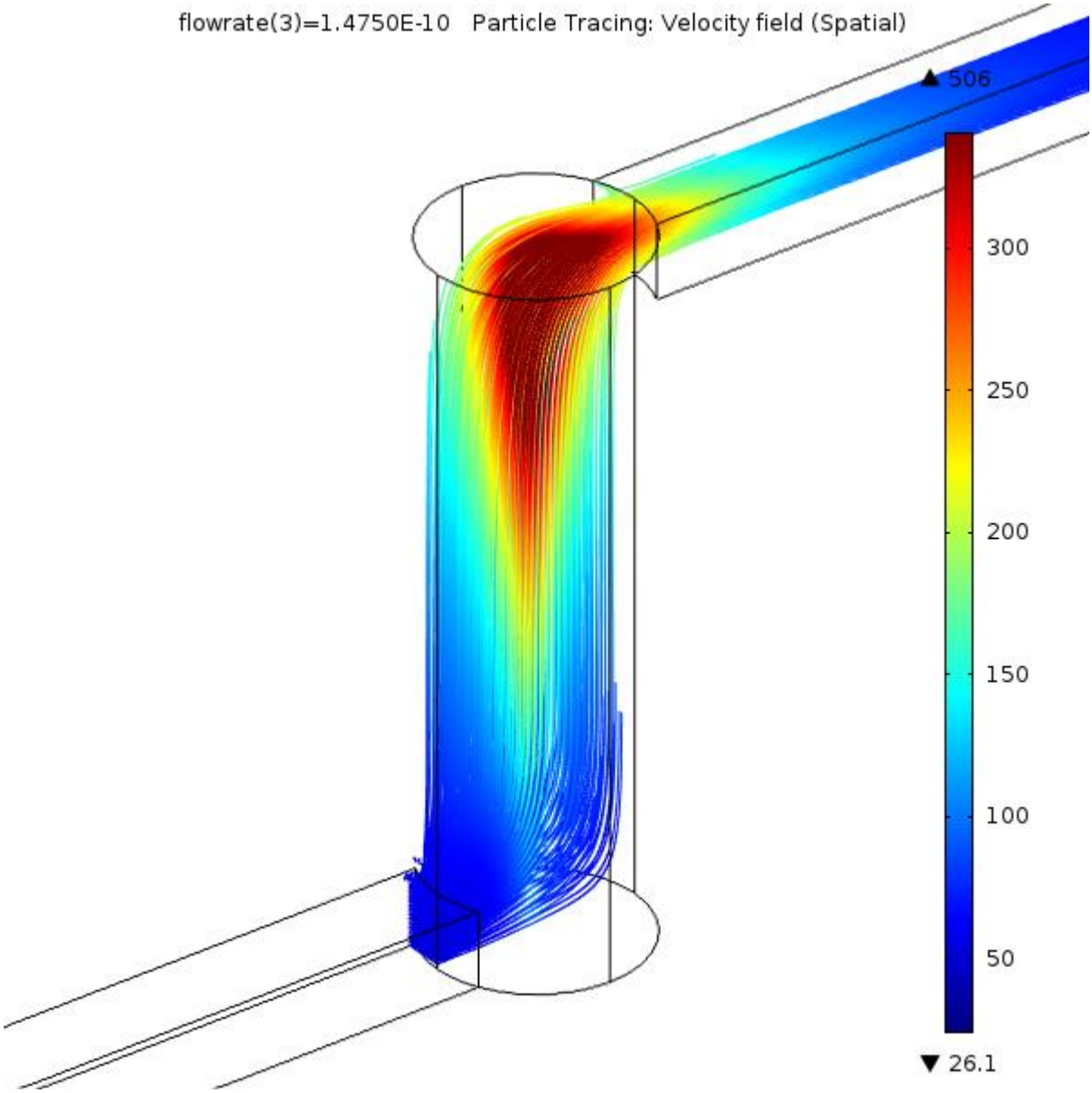


Figure 7.15: Particle tracing in one half (y>0) of the channel (flow rate = 1.4750e-10 mm^3/s). The colour of the traces represents the temperature in degrees Celsius.

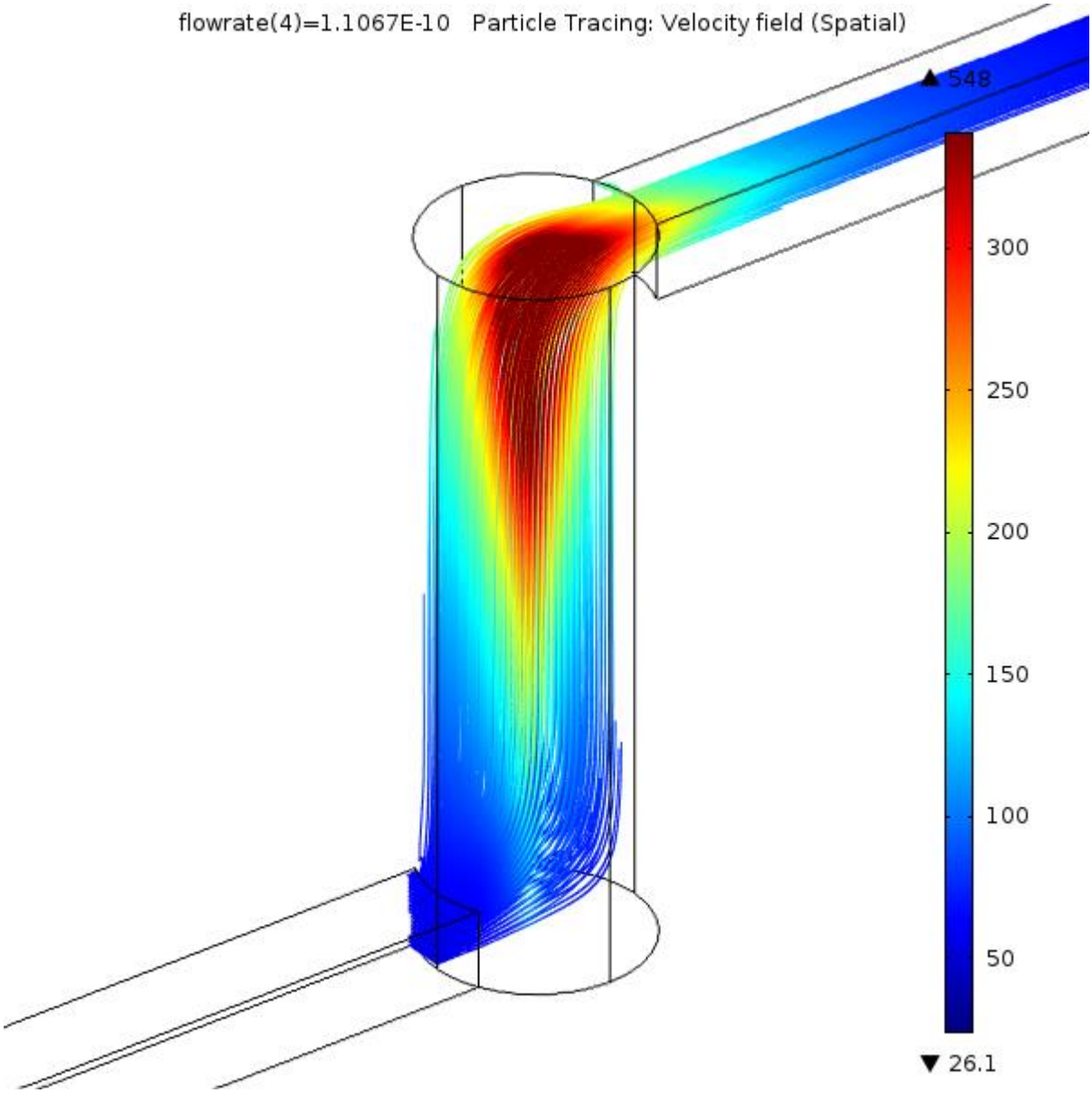


Figure 7.16: Particle tracing in one half (y>0) of the channel (flow rate = 1.1067e-10 mm^3/s). The colour of the traces represents the temperature in degrees Celsius.

7.3.2.4 Temperature (solid) – surface

Figure 7.17 shows the temperatures experienced by the inner surfaces of the acrylic channel. Figure 7.18 shows the same, but contourised based on the list of temperatures shown in Table 7.6, compiled based on Malhotra et al (Malhotra, et al., 1982).

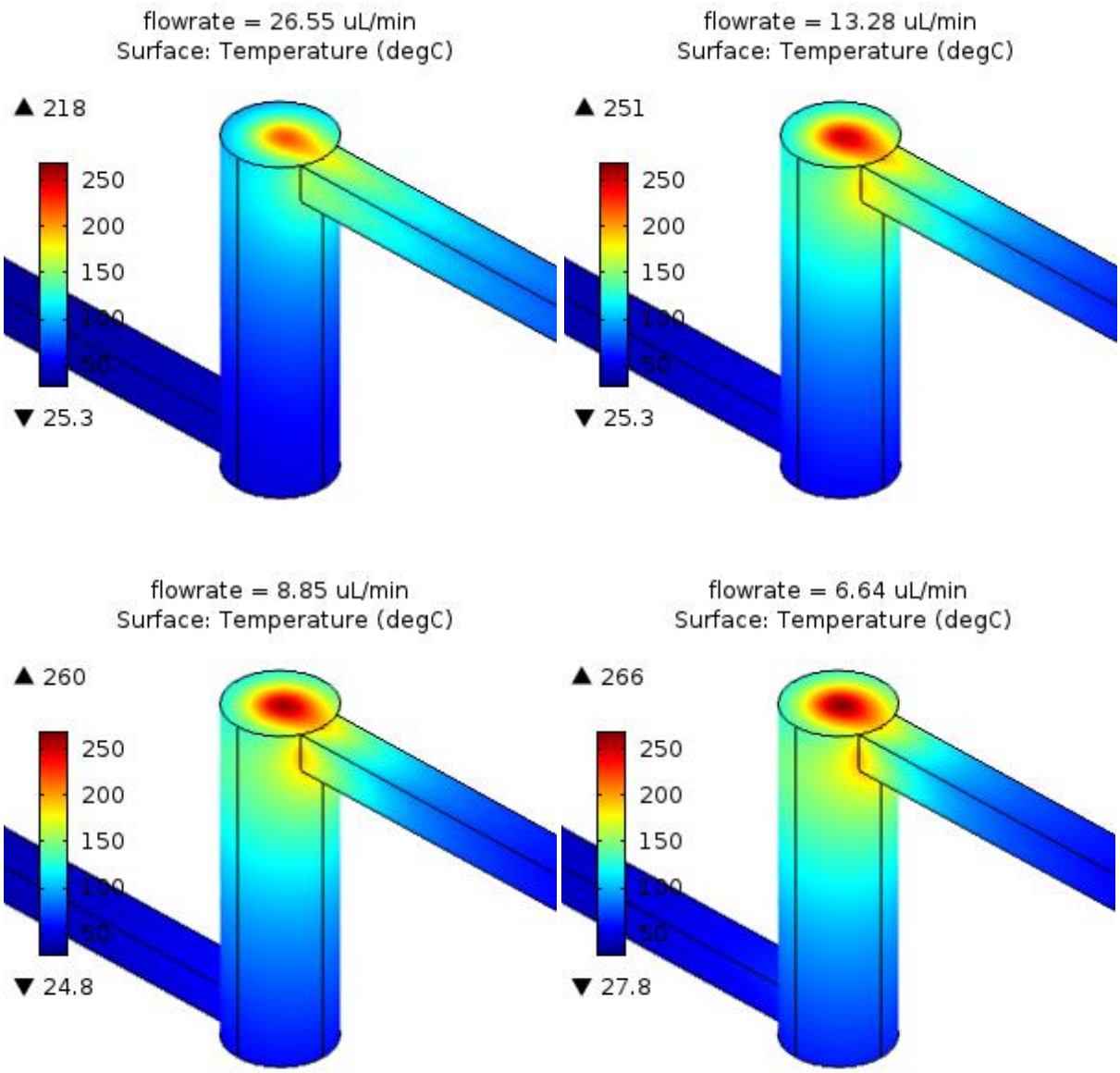


Figure 7.17: Temperature on the inner surfaces of the channel at different flowrates. (synchronised scales)

Table 7.6: Significant temperatures for acrylic plastic

90° C	Acrylic glass transition temperature
170° C	Acrylic melting point
230° C	Acrylic decomposition range (~10% weight loss)
300° C	Acrylic decomposition temperature (~50% weight loss)

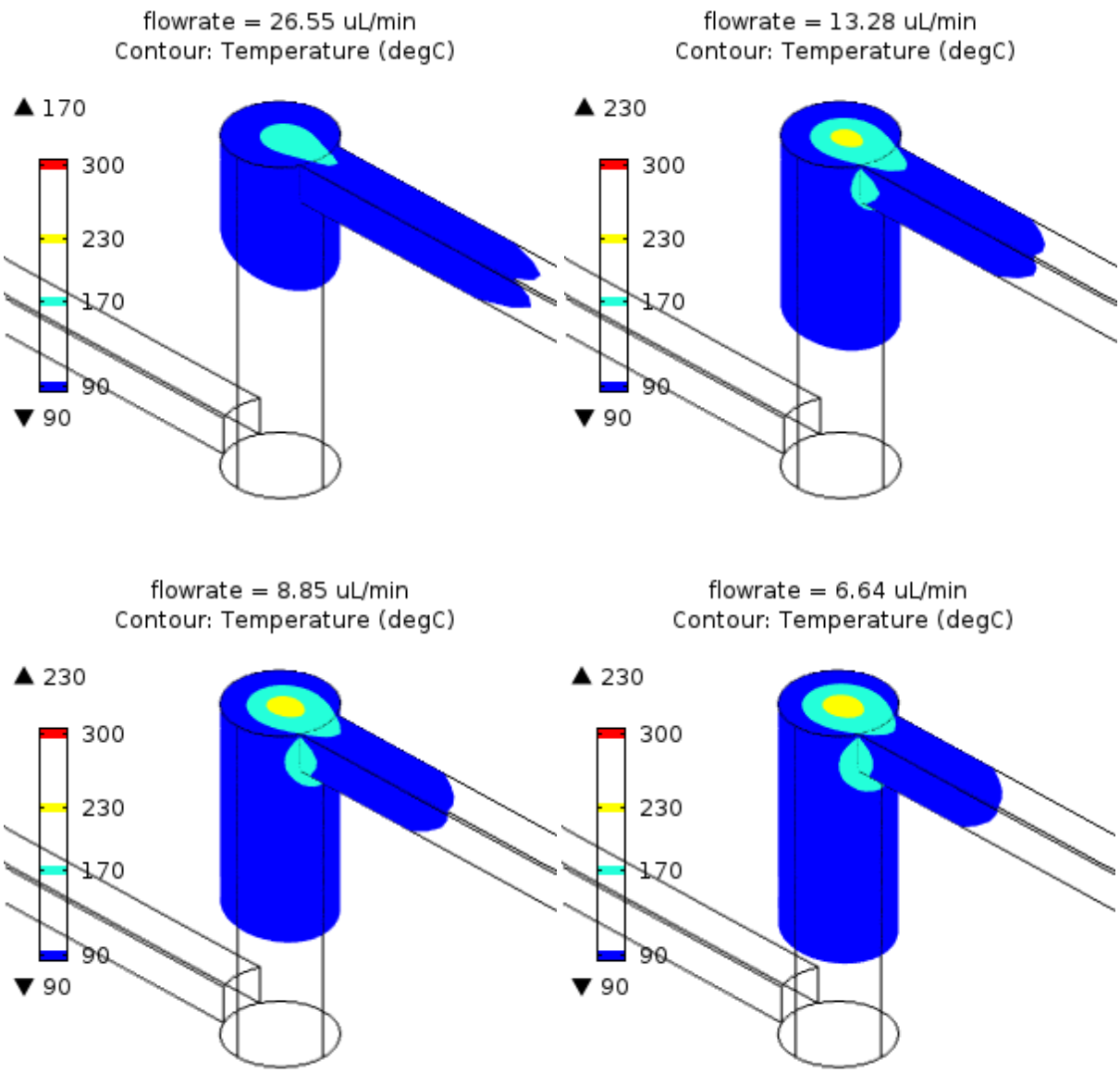


Figure 7.18: Temperature contours on the inner surfaces of the channel. The contour levels are based on Table 7.6, and represent the acrylic glass transition temperature (70 °C), acrylic melting point (170 °C),

7.3.2.5 Stress – slice

Figure 7.19 shows the von Mises stress in the acrylic around the reaction chamber. Figure 7.20 shows the same results but with synchronised scales. A 3D view with synchronised scales is presented in Figure 7.21, which reveals that the highest level of stress is experienced at the top two corners at the mouth of the outlet.

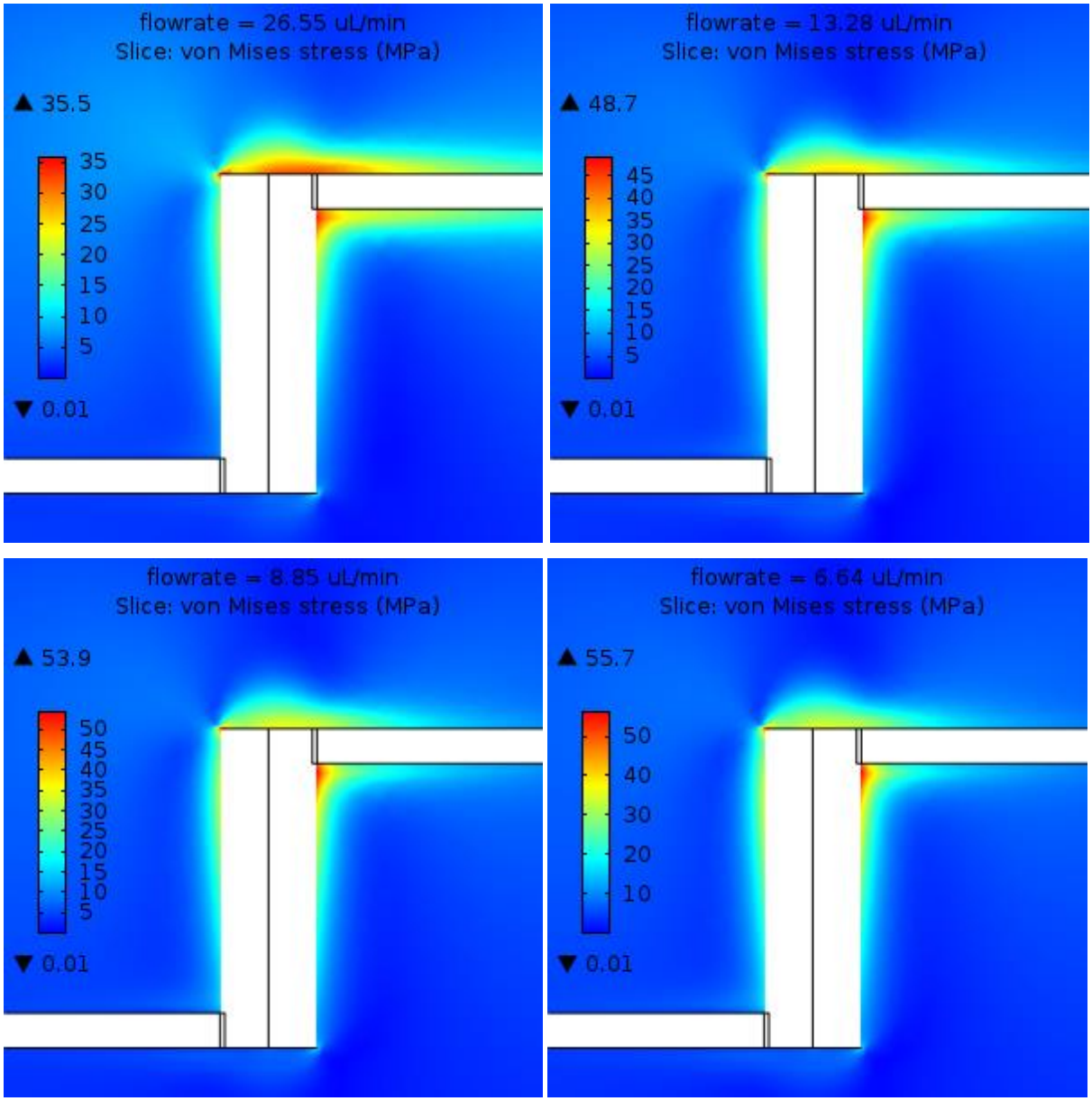


Figure 7.19: von Mises stress in the acrylic around the reaction chamber. Visualised on an XZ plane at Y = 0.

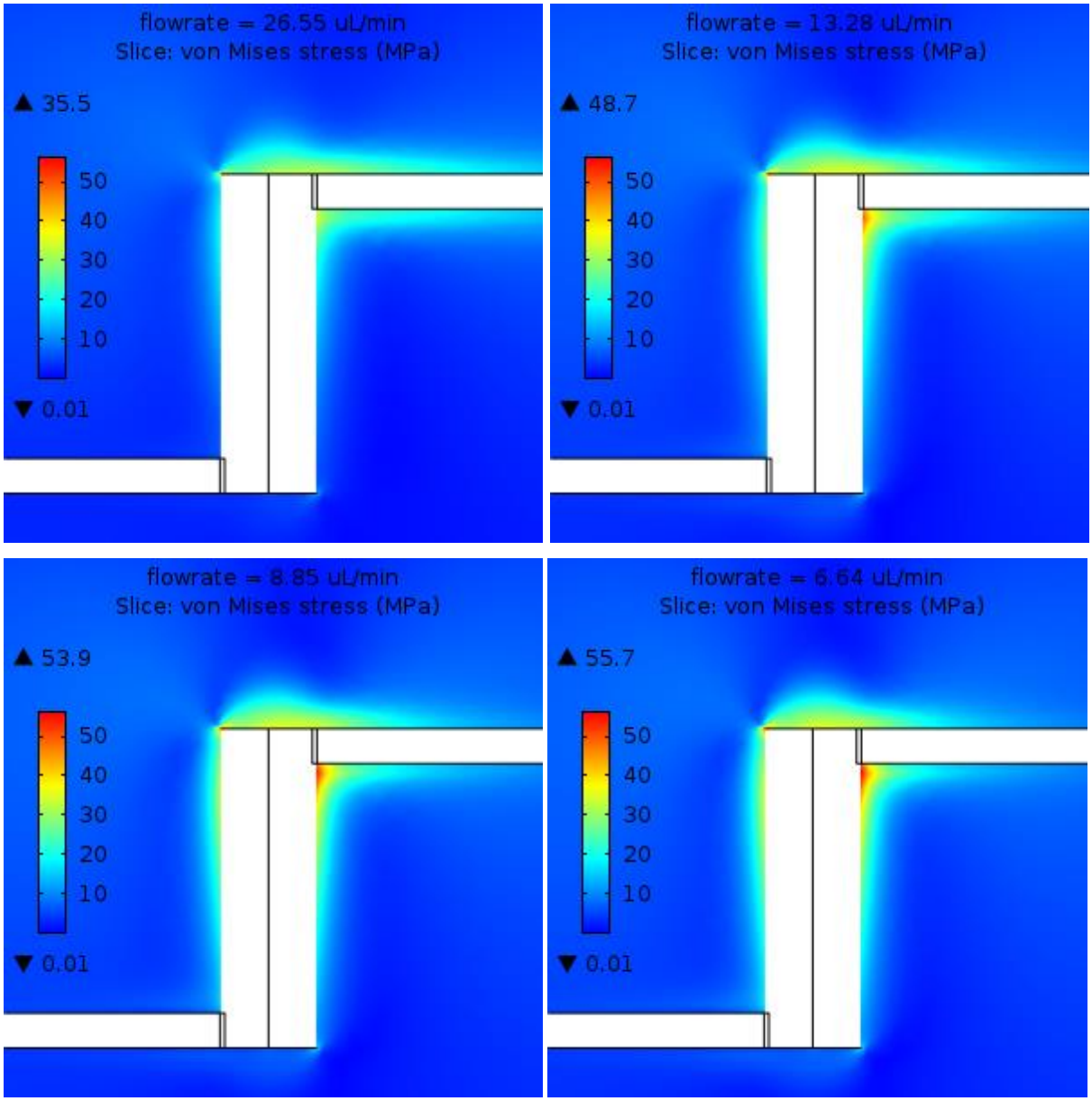


Figure 7.20: von Mises stress in the acrylic around the reaction chamber (synchronised scales). Visualised on an XZ plane at Y = 0.

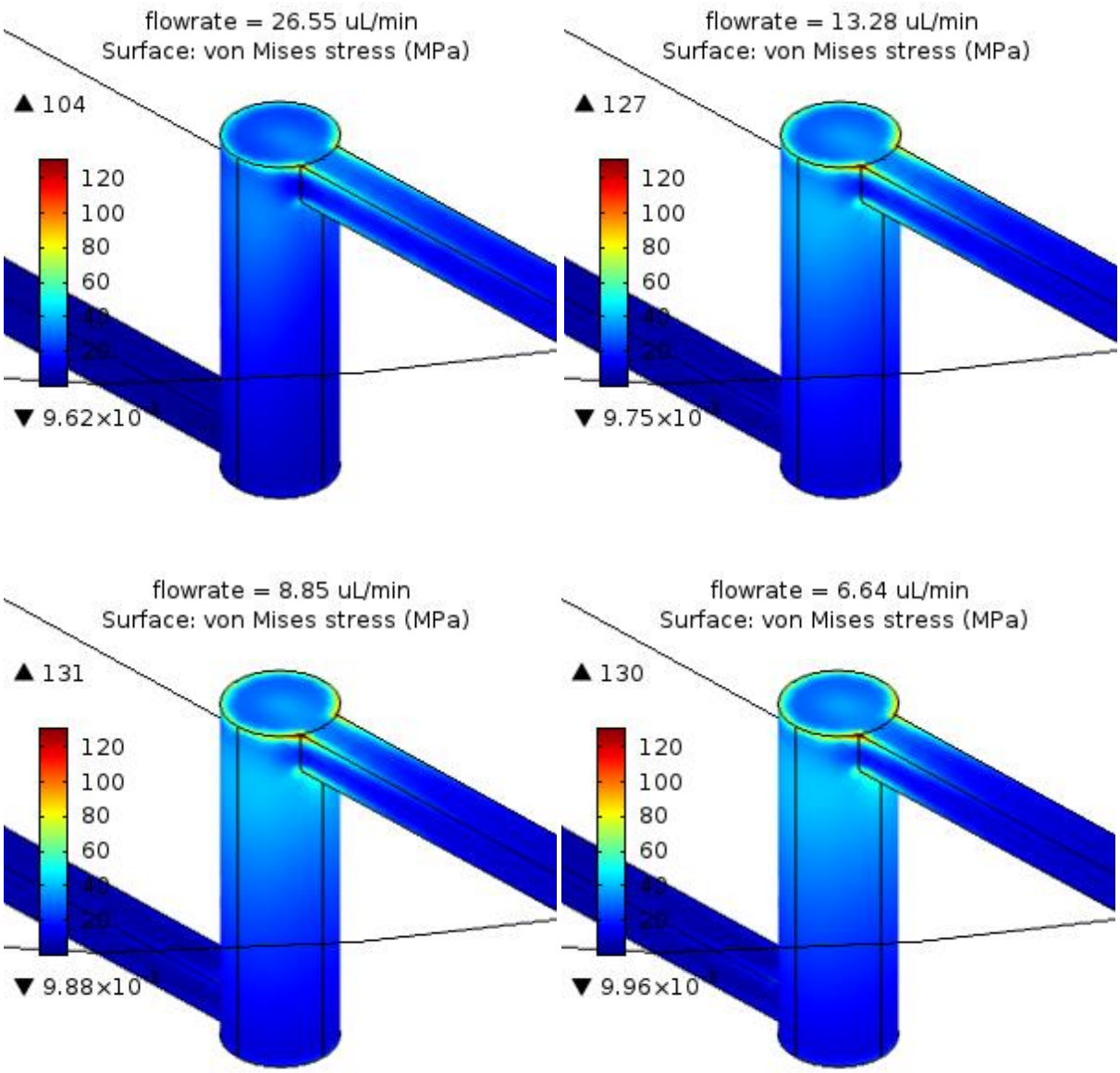


Figure 7.21: 3D view of the von Mises stress on the channel surfaces (synchronised scales)

7.3.3 Study 3: LF and HT Time-dependent

7.3.3.1 Temperature rise

Figure 7.22 shows the surface temperature rise in the semi-elliptical area (section 7.1.3).

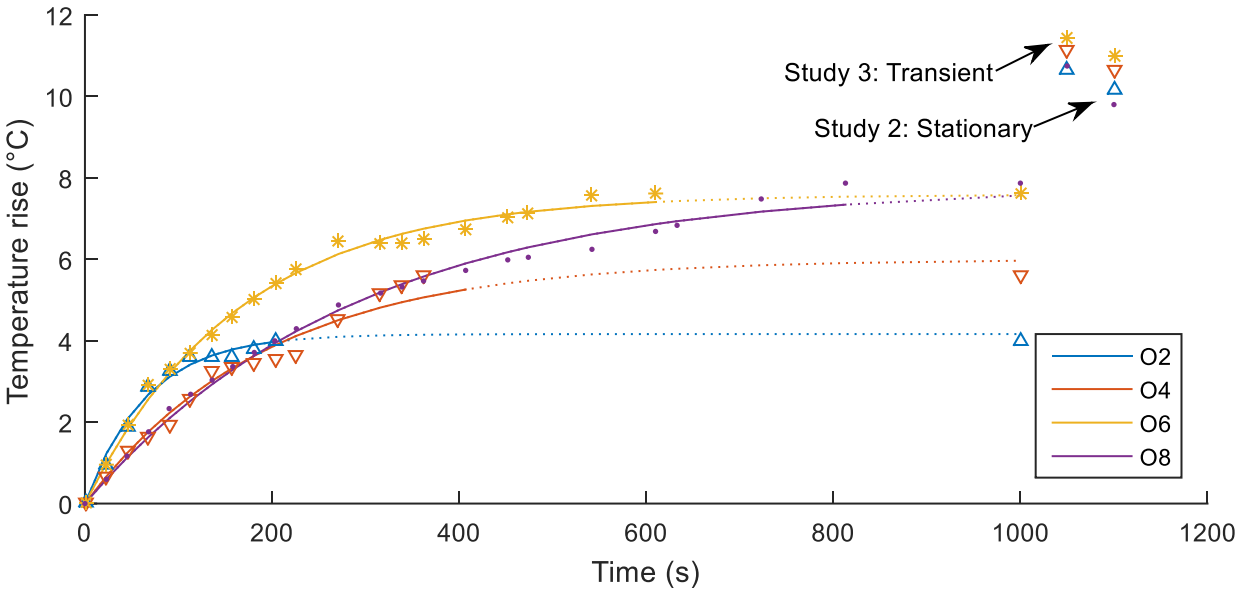


Figure 7.22: Temperature rise in the measured temperatures shown by the curves. The maximum temperatures from the simulated studies are shown higher up.

7.4 Discussion

7.4.1 Limitations of the model

The model does not consider the following aspects:

1. The liquid is modelled as a single phase, incompressible fluid. Although no bubbles were observed during the actual experiment, there is the possibility of highly localised evaporation and condensation of the solvent before exiting the reaction chamber.
2. Heat of decomposition of the iron oleate and oleic acid is not considered. However, their contribution to the overall heat capacity of the solution is relatively small (<13%).
3. One of the by-products of iron oleate decomposition in a typical batch reaction is CO_2. Its effect on the thermophysical properties of the solution is not considered.
4. The phase change and decomposition of the acrylic chip is not modelled.

7.4.2 Fluid flow

The unheated flow (Figure 7.7) shows a typical parabolic profile of a simple laminar flow. When heated (Figure 7.9), the only remarkable result is the change in the velocity due to localised density changes. Any possible localised phase change is beyond the scope of this study.

7.4.3 Solution temperature

The temperature experienced by the solution is one of the most important aspects of the experiment as it determines the morphology of the nanoparticles produced. The presented temperature results are split into three sections:

1. Temperature of the system in an XZ slice (section 7.3.2.2).
2. Temperature of individual fluid streamlines (section 7.3.2.3).

The temperature slices are good for showing the highest temperatures achieved in the system (Figure 7.10), and with synchronised scales they highlight the difference in temperatures between the four flow rates. The contours (Figure 7.12) mark the regions where nucleation and growth can be expected. In all of these cases however, the slice is the hottest one in the channel, i.e., the temperatures in all other slices are lower.

The results show that the minimum decomposition temperature is reached at some points even at the fastest flowrate, however they only give us a static view of the temperature field within the channels. For nanoparticle synthesis, the thermal history, i.e. the temperatures experienced by a body of fluid is also important as it determines the nucleation and growth periods.

To obtain this, particle traces were created (shown in Figure 7.13 - Figure 7.16). The particle tracing data, including the position, time, and temperature, was imported in MATLAB for further analysis.

Percentage breakdown

The traces were divided into two broad groups. Traces with a maximum temperature above the minimum nucleation temperature (220° C) but below the minimum decomposition temperature (320° C) were grouped as “nucleation-only” traces. Traces that exceeded the minimum decomposition temperature (320° C) were grouped as “growth” traces. No nucleation is assumed to have occurred in the remaining traces. A simple percentage breakdown of these three groups for each flowrate is presented in Table 7.7 and plotted in Figure 7.24.

The percentage breakdown in Figure 7.24 shows the percentage of unheated fluid approaching an equilibrium, while the percentage of growth traces could possibly rise further. At the lowest flow rate of 6.65 µL/min, 29.17% of the fluid flows by without nucleation and only 34.82% of the fluid exceeds the minimum growth temperature. These numbers are a big improvement over the faster flow rates, however the extremely high temperatures faced by some of the streamlines can have undesired effects.

Growth and Nucleation periods

The time spent by each trace in the growth or nucleation temperature ranges was calculated and analysed. The nucleation period is the time spent by each trace rising from 220° C to 320° C. In nucleation-only traces it is simply the time spent above 220° C. The growth period is the time spent by each trace between 320° C and 350° C, above which other processes like decomposition of oleate groups and phase change of iron oxide are expected to occur. These lower and upper bounds for growth temperatures are based on "desired" temperatures from the literature rather than a hard limit, but few papers report temperatures outside this range. Our iron oleate also shows its final decomposition at ~320 °C. The results are presented in Table 7.8 and plotted in Figure 7.25.

The mean growth period shows an increase from 13.9 ms to 105.1 ms, with an increase in standard deviation from 13.9 ms to 194.8 ms. The largest increase is seen going from a flow rate of 26.55 µL/min to 13.28 µL/min. The mean nucleation period shows a larger increase from 157.7 ms to 907.1 ms, with the standard deviation rising from 63.3 ms to 441.1 ms. In this case, a more uniform rise in standard deviation is seen. This corresponds well to the experimental results: in both the O and N solutions, the largest change in particle sizes is also seen going from 26.55 µL/min to 13.28 µL/min.

Heating Rate

Finally, the linear heating rate was calculated for each trace that reached or exceeded 320 °C (listed in Table 7.9 and plotted in Figure 7.26). The ramp rate was calculated by dividing the temperature difference by the time difference. In traces where the maximum temperature ranged from 320 °C to 350 °C, the maximum temperature attained was chosen as the upper bound. If the trace exceeded 350 °C, that point was considered the maximum temperature and the upper limit of the time period.

As expected, the average heating rate decreases with decreasing flow rates, with relatively small changes in standard deviation. The mean heating rates in the experiments run from 16,560 °C/min to 5,083 °C/min. This is three orders of magnitude higher compared to the typical ramp rate of 3 °C/min used in a typical batch process.

These results show a fundamental limitation of the current setup. The size difference between the laser beam cross-section and the diameter of the reaction chamber limits the percentage of the fluid

that absorb energy. The gaussian beam intensity and parabolic laminar flow profiles also play a role in increasing non-uniformity of the final temperature distribution.

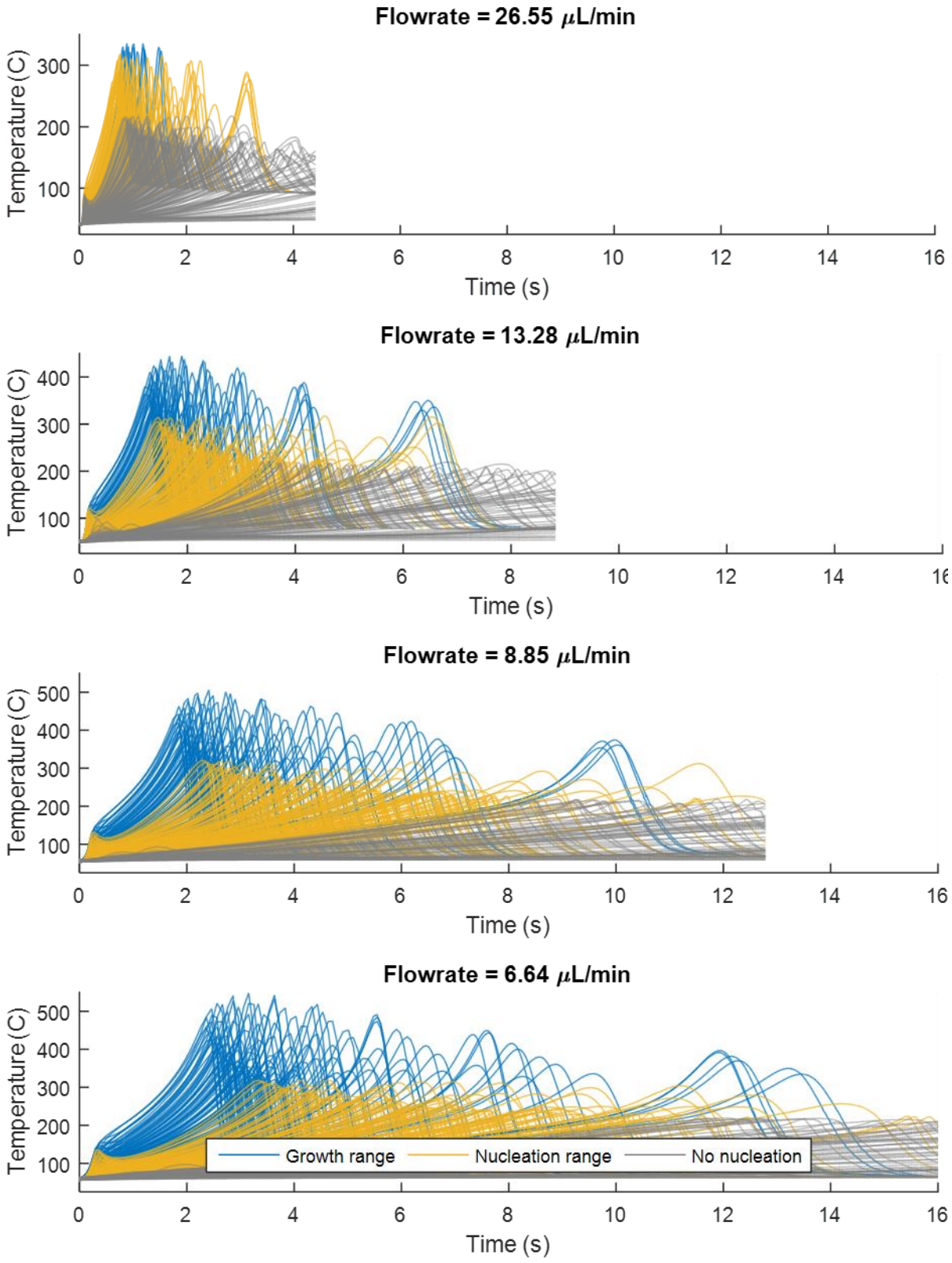


Figure 7.23: Temperature vs time plots of particle traces at the different flowrates. All curves are terminated when they reach x = 2e-3 m (i.e. the particle tracing is stopped when they leave the reaction chamber).

Table 7.7: Number and percentage of traces in each temperature range

Flowrate (µL/min)	Number of traces			Percentage of traces (%)		
	Growth	Nucleation-only	No nucleation	Growth	Nucleation-only	No nucleation
26.55	13	91	232	3.77	27.08	69.15
13.28	79	128	129	23.51	38.10	38.39
8.85	103	135	98	30.65	40.18	29.17
6.64	117	121	98	34.82	36.01	29.17

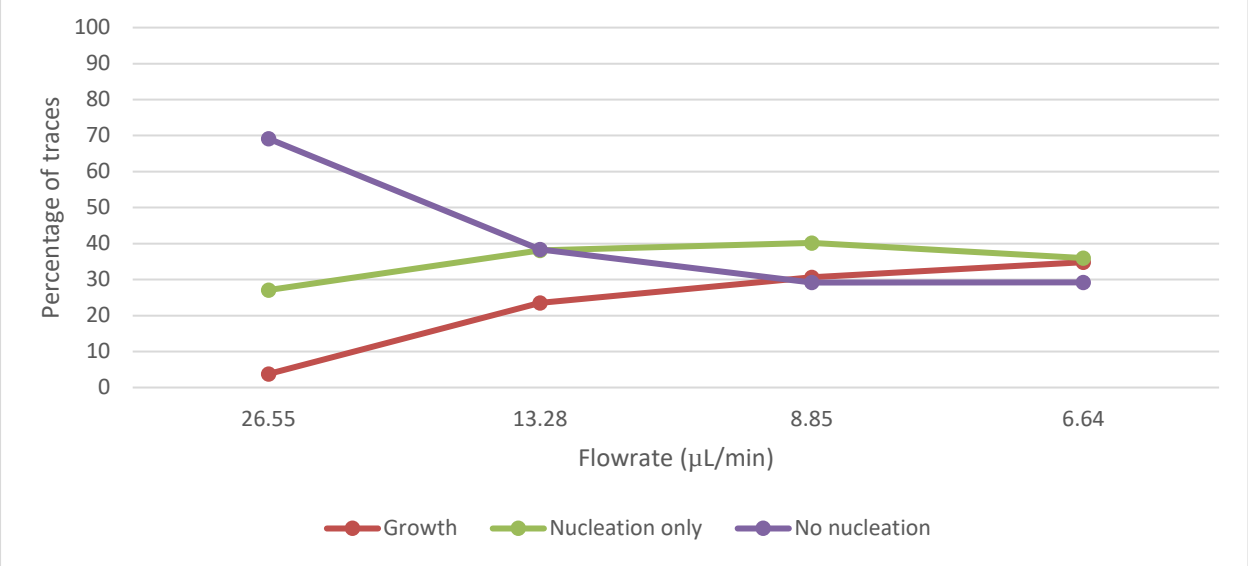


Figure 7.24: Percentage breakdown of traces in each temperature range.

Table 7.8: Mean durations and standard deviation of time periods spent by the traces in growth and nucleation temperature ranges

Flowrate (µL/min)	Growth period			Nucleation period		
	Samples	Mean (s)	Std dev. (s)	Samples	Mean (s)	Std dev. (s)
26.55	13	0.0139	0.0139	104	0.1577	0.0633
13.28	79	0.0581	0.0734	207	0.3460	0.1772
8.85	103	0.0603	0.1346	238	0.6090	0.3069
6.64	117	0.1051	0.1948	238	0.9071	0.4411

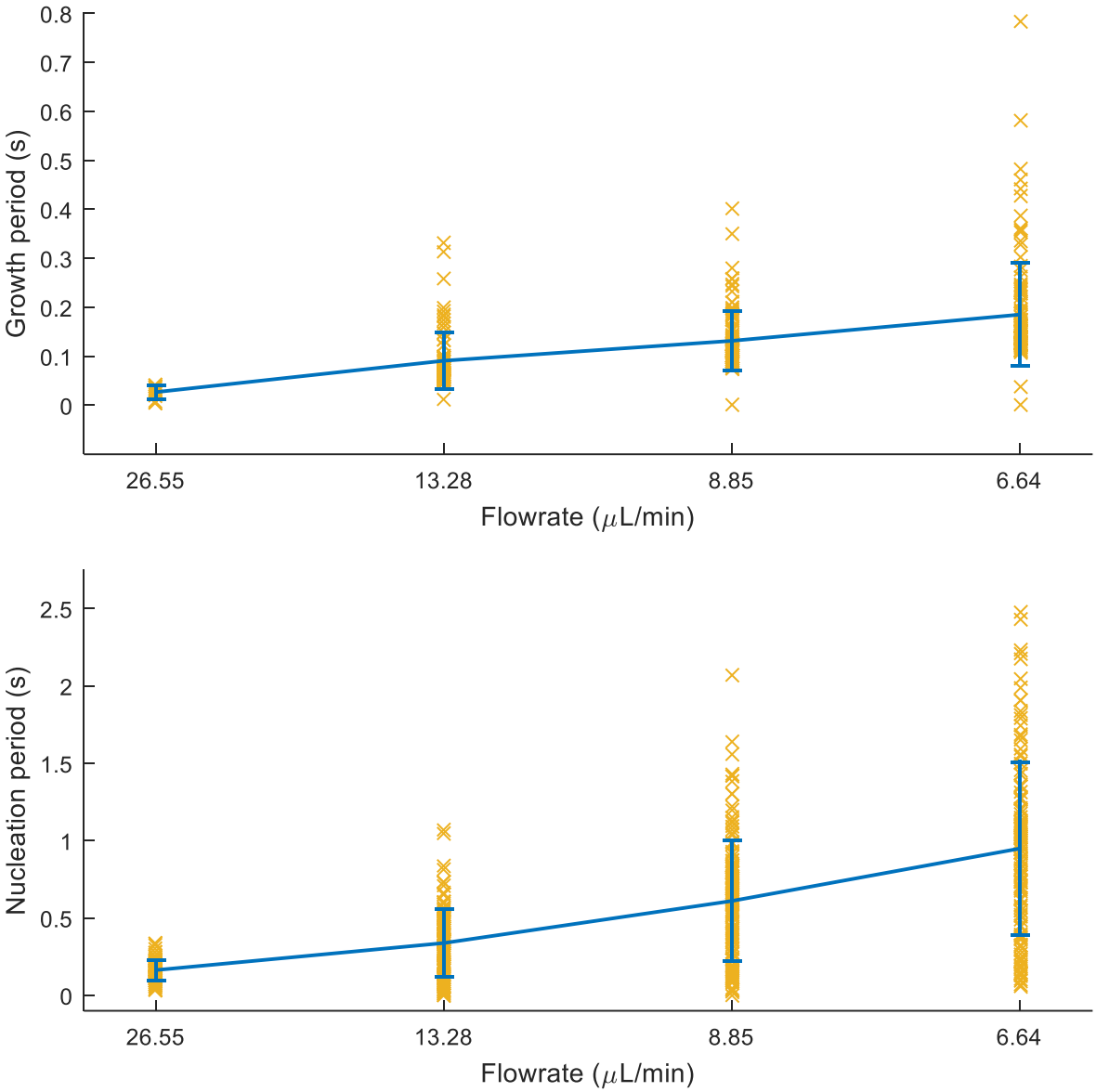


Figure 7.25: Nucleation and growth periods calculated from particle tracing temperature data at different flowrates. Plots show periods of individual traces marked with a yellow x, and the mean periods and standard deviation error bars.

Table 7.9: Mean and standard deviation of heating rates of growth traces at different flow rates

Flowrate (µL/min)	Heating Rate				
	Samples	Mean (°C/s)	Std dev. (°C/s)	Mean (°C/min)	Std dev. (°C/min)
26.55	13	276.00	54.54	16560.00	3272.40
13.28	79	160.07	60.17	9604.20	3610.20
8.85	103	110.55	44.20	6633.00	2652.00
6.64	117	84.72	34.48	5083.20	2068.80

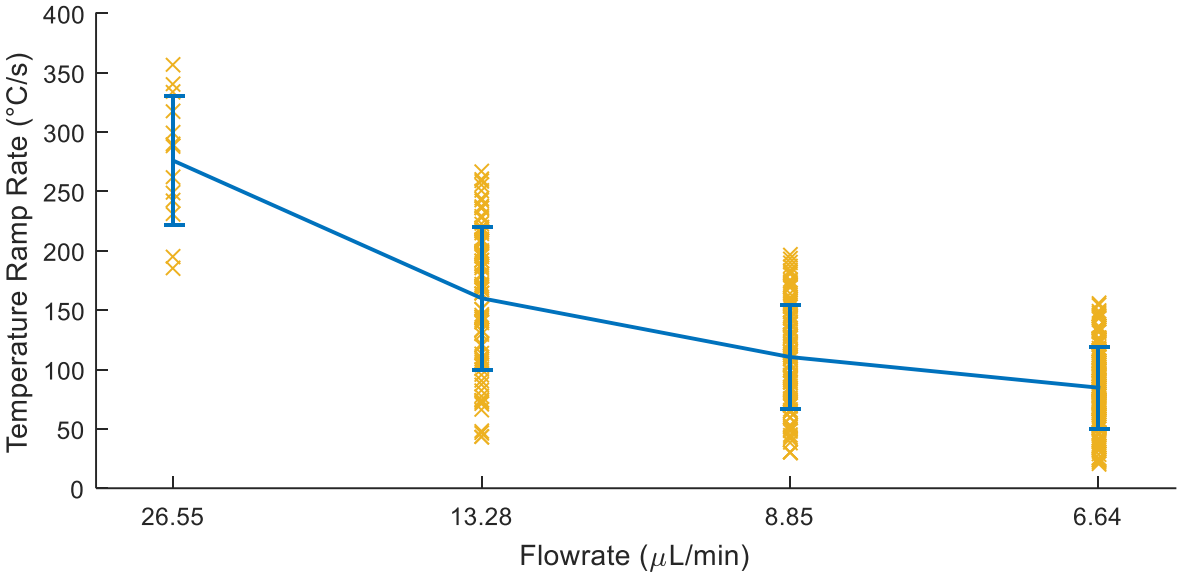


Figure 7.26: Heating rates (yellow x) at the different flow rates, along with the mean and standard deviation error bars.

7.4.4 Surface temperature rise

The acrylic surface temperatures in the study (Figure 7.22) differed from the measured temperature in a few ways:

1. The measured temperature was ~4-8 degrees lower than the simulated temperature rise.
2. The simulated temperatures did not differ as much among the various flow rates.
3. The order: the 8s (6.64 µL/min) run has the highest measured acrylic surface temperature, yet it is the lowest or second lowest in the simulations.

The limitations of the simulation can explain these discrepancies. The heat of decomposition of the iron oleate, oleic acid, and phase change and decomposition of the acrylic all contribute to the

differences between the flow rates, as well as the overall difference between the measured and simulated results.

7.4.5 Reactor temperature and stress

This section looks at the heat and thermal stress experienced by the acrylic chip under steady state operation.

Section 7.3.2.4, shows the surface temperatures of the acrylic directly in contact with the fluid. Shown in Figure 7.17, the highest temperature experienced by the acrylic is 266 °C, at a flow rate of 6.64 μL/min, located near the centre of the top of the reaction chamber. The edges at the entrance of the outlet channel are other major hotspots. Once again there is a large difference between the maximum temperature at a flow rate of 26.55 μL/min and the rest.

The contour map of the same temperature field (Figure 7.18) shows the regions where the acrylic exceeds the glass transition temperature, melting and decomposition points. Only the fastest flow rate of 26.55 μL/min can keep the surface temperatures below the decomposition temperature (and even then, it is quite close at 218 °C). At the three other flow rates, the temperature is well within the decomposition range for PMMA.

Figure 7.19 and Figure 7.20 show the von Mises stress due to thermal expansion in an XZ plane (Y=0). Figure 7.21 shows a 3D view of the stress field on the inner surface of the acrylic channel. Note the increasing stress along the cylindrical walls of the reaction chamber, when going from the fastest to the slowest flow rate. The locations with high stress concentrations predict the failure points of the device quite accurately, considering the damage seen in the chips (section 6.3.3), where most of the fractures originate from the top perimeter of the reaction chamber, and above and below the entrance of the outlet channel.

The stress at the hottest spots at the top of the reaction chamber is not particularly high, hence the damage seen there is more likely to be caused by decomposition of the acrylic.

Note that this model does not take into consideration the phase of the acrylic. At many points the acrylic surface has exceeded its melting point, which means the stress would be slightly relieved through liquidation. In all but the fastest flowrate, a small portion of the top of the chamber exceeds the minimum decomposition temperature of PMMA, which could result in changes in the structural properties of the material. However, this basic analysis is sufficient for determining the safe operating conditions for this device.

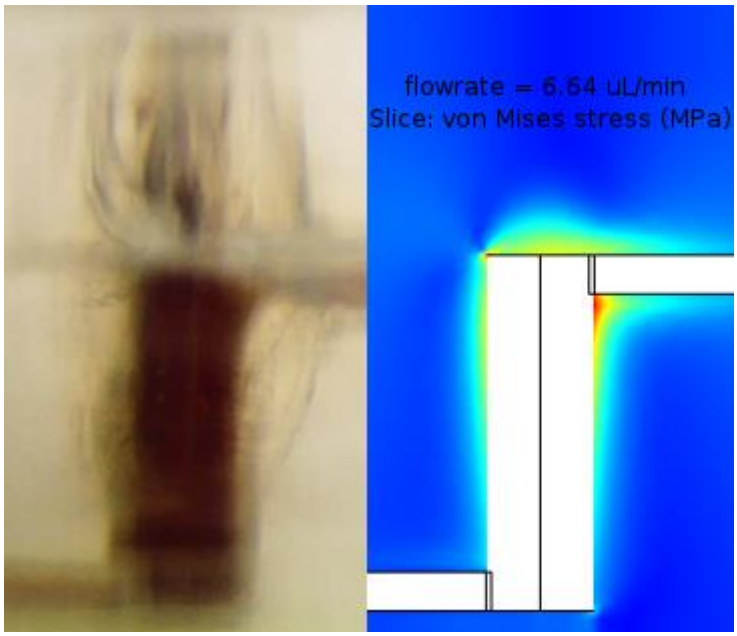


Figure 7.27:Reactor damage seen after the experiments (left) compared with the simulation results (right). (Full simulation results can be seen in Figure 7.19)

7.5 Summary

The microfluidic laser synthesis process by its nature is bound to have sharp temperature gradients within the channel, both spatially and temporally. The simulation helps to paint a complete picture of the synthesis process by illustrating the flow and temperature profiles within the channel. Analysis of the temperature profiles of multiple streamlines within the channel provides a better understanding of the temperatures experienced by that body of fluid, and by extension, the nucleation and growth temperatures and periods.

A very basic validation of the model was done by comparing the rise in average temperatures of the acrylic surface during the heating-up stage of the synthesis process. The simulated temperatures were slightly higher (4-8 °C) than the measured temperatures. This discrepancy can be explained by the fact that the decomposition of the iron oleate and the melting and decomposition of the acrylic were not considered in the simulation.

The solid mechanics physics too does not consider the melting and decomposition of the acrylic. However, the locations of stress concentrations match the locations of fractures observed in the chip after prolonged use. The model can be used to indicate where failures might occur in the acrylic chip.

The streamline analysis shows that further improvements in yield, and thus reduction of partial decomposition by-products, cannot be achieved using this design by adjusting the laser power or flow rate, as the limitations stem from the percentage of fluid that remains unheated. Possible improvements are mentioned in section 9.1.

Overall, the use of acrylic chips was possible for brief testing and characterisation, however it is not suitable for prolonged continuous flow synthesis in its current state. A more heat resistant material like glass or quartz may be useful here. However, acrylic has one of the lowest thermal conductivities in commonly available and suitable materials, and as such helps keep the heat within the chamber. If replaced by glass, a more powerful laser will be required to maintain the same temperature.

A droplet-based system is likely a better answer for future work, as acrylic can still be used if the inlet and outlet connections are properly made so that the droplets do not collapse.

8 Microfluidic synthesis of CdSe quantum dots by laser heating

8.1 Methods and materials

8.1.1 Fabrication

The fabrication method used to produce chips for this batch was identical to previous methods, with a few key differences:

a. Temperature: The brand of acrylic previously used could no longer be found in stores, so another was chosen (Asia Poly A-Cast clear). It was found that the glass transition of this product begins at a higher temperature than the previous one (~120 °C vs ~95 °C). The furnace temperature was set to 125 °C, while ramp rate and heating time were unchanged (3 °C/min, 90 min). The furnace was allowed to cool below 50 °C before removing the jig.
b. Annealing: To save time, the material was sometimes ordered as laser cut pieces. Laser cut edges are known to have higher localised stress (see Figure 8.1) compared to mechanically machined edges. These were annealed at 80 °C for 3 hours and allowed to cool slowly in the closed furnace for several hours. Annealing was done to avoid the possibility of stress cracking when cleaning the acrylic pieces with isopropanol/ethanol before bonding.
c. Alignment holes (diameter: 3.1 mm) were used in some of the later chips to align all the layers together while bonding. Steel dowel pins with a diameter of 3 mm and a length of 7 mm were used to keep the three layers aligned together. During fabrication the three layers were stacked and two 3 mm holes were drilled through all three layers. The alignment holes in the bonding jig were not used in this case.

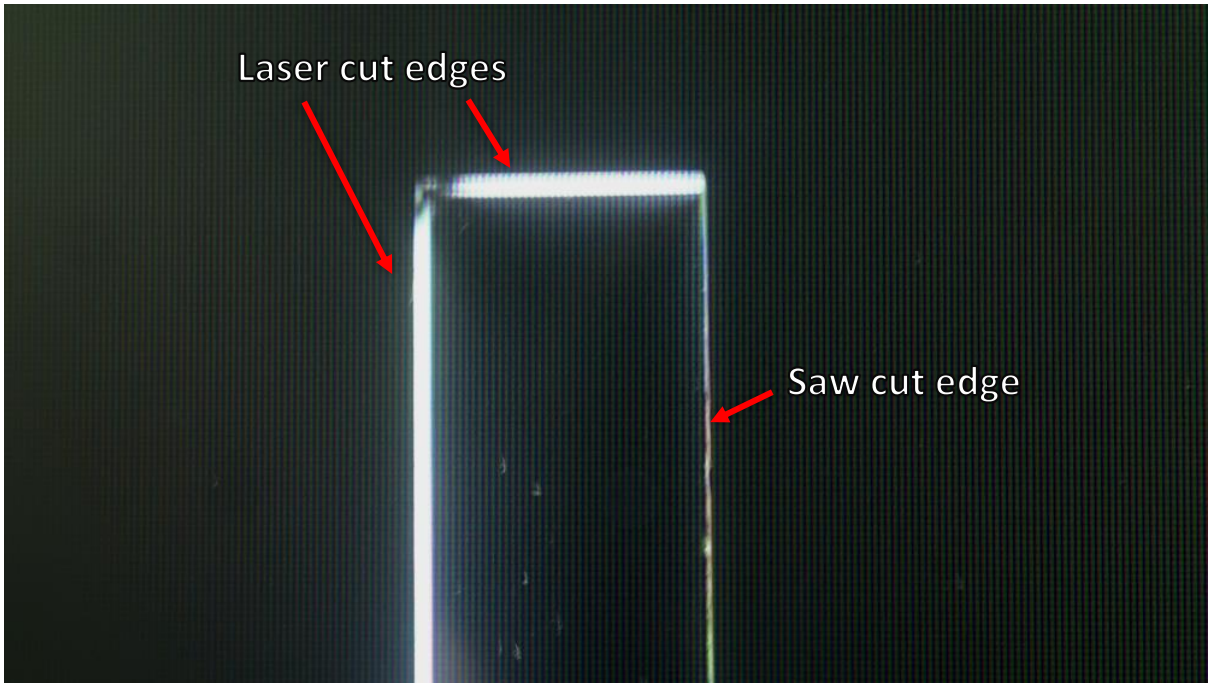


Figure 8.1: Photo of an acrylic sample between two cross-polarised films showing the higher stress on the laser cut edges compared to the saw cut edge.

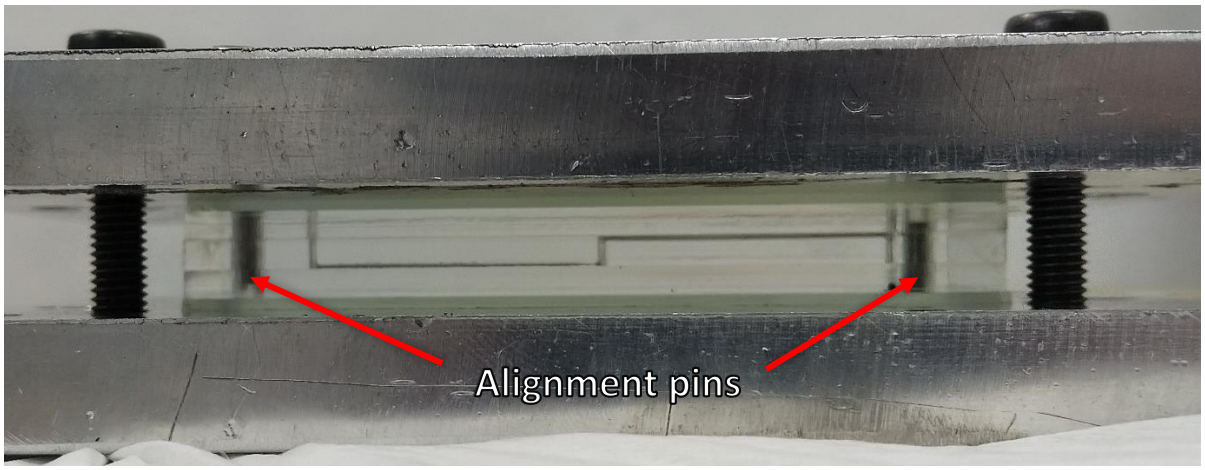


Figure 8.2 Acrylic layers clamped in the bonding jig. The three layers are kept in place using two dowel pins and sandwiched between two glass slides.

One small detail that led to several failed thermal bonding attempts: When the acrylic pieces were washed with a new brand of dish soap, they failed to bond or only bonded partially. Whether this was due to surface modification or deposition of emollients is unclear, but this problem was overcome by washing the layers with isopropanol or alcohol.

8.1.2 Changes to the experimental setup

After preparing the new reaction mixture (cadmium and selenium precursors), its absorbance was measured. The absorbance of the solution at 650 nm (the laser used to produce iron oxide nanoparticles) was negligible, but significant absorption was seen below 450 nm. A 405 nm laser (EleksMaker EL-01-500) with an output power of 500 mW was purchased and installed. While the absorbance is higher at lower (UV) wavelengths, it is easier and safer to work a 405 nm beam as it is visible. Due to the higher output power, the entire setup was now enclosed within a metal cabinet which was kept locked when not in use.

An LCD display and 2 switches were connected to the Arduino board for laser power control. The laser power was controlled using an 8-bit PWM signal (ranging from 0 to 255). The laser output power was measured over a wide range of PWM signals and shows a fairly linear relationship (Figure 8.5). The Arduino controlling the laser was programmed such that the laser power could be set while the door is open, but the laser is only turned on at full power when the door is closed. An interlock was installed

which limits the laser to the lowest power (1/255 PWM = ~2 mW) when the cabinet door is opened. This setup is shown in Figure 8.3 and Figure 8.4.

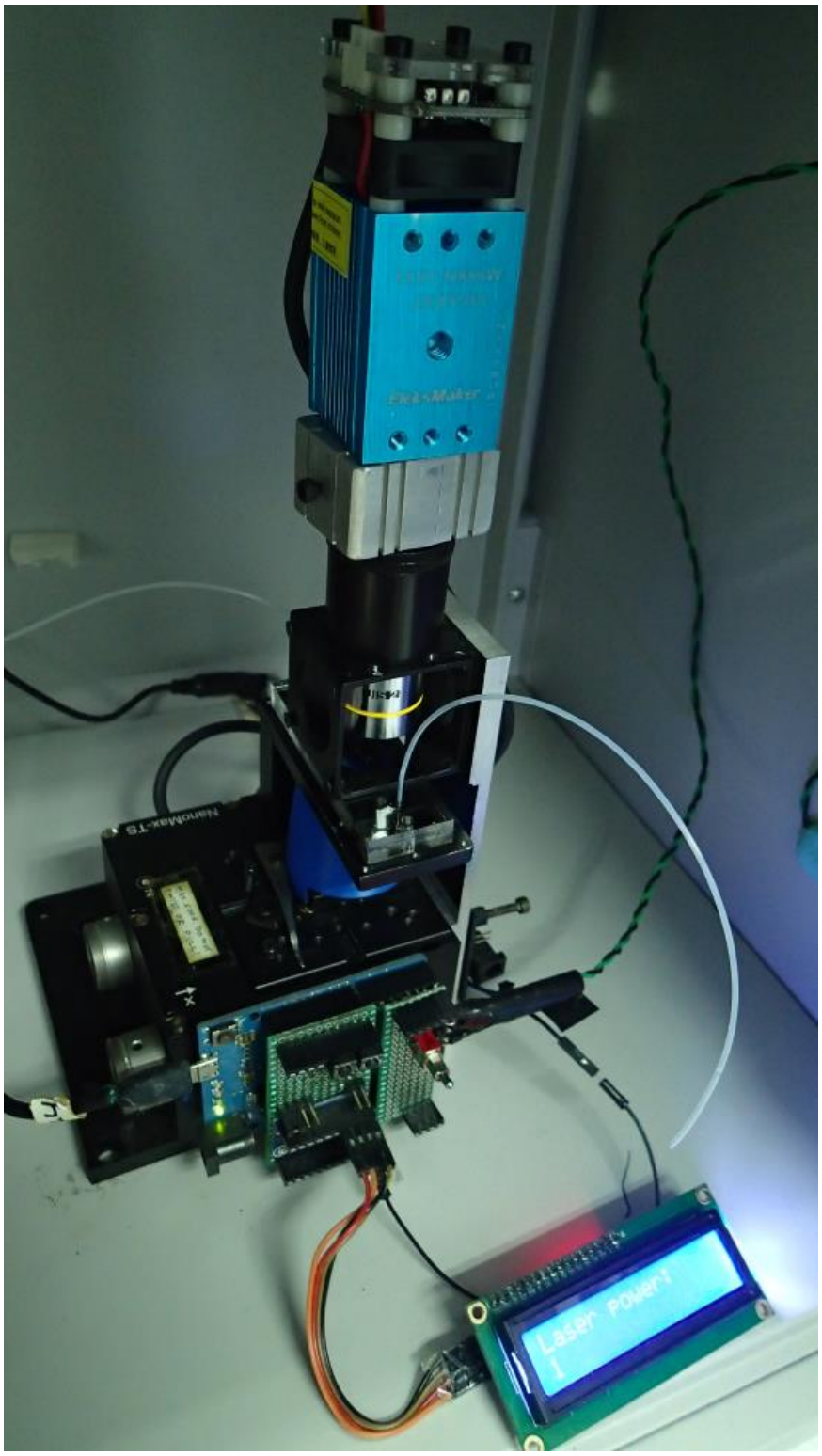


Figure 8.3: The modified setup used for microfluidic CdSe synthesis.

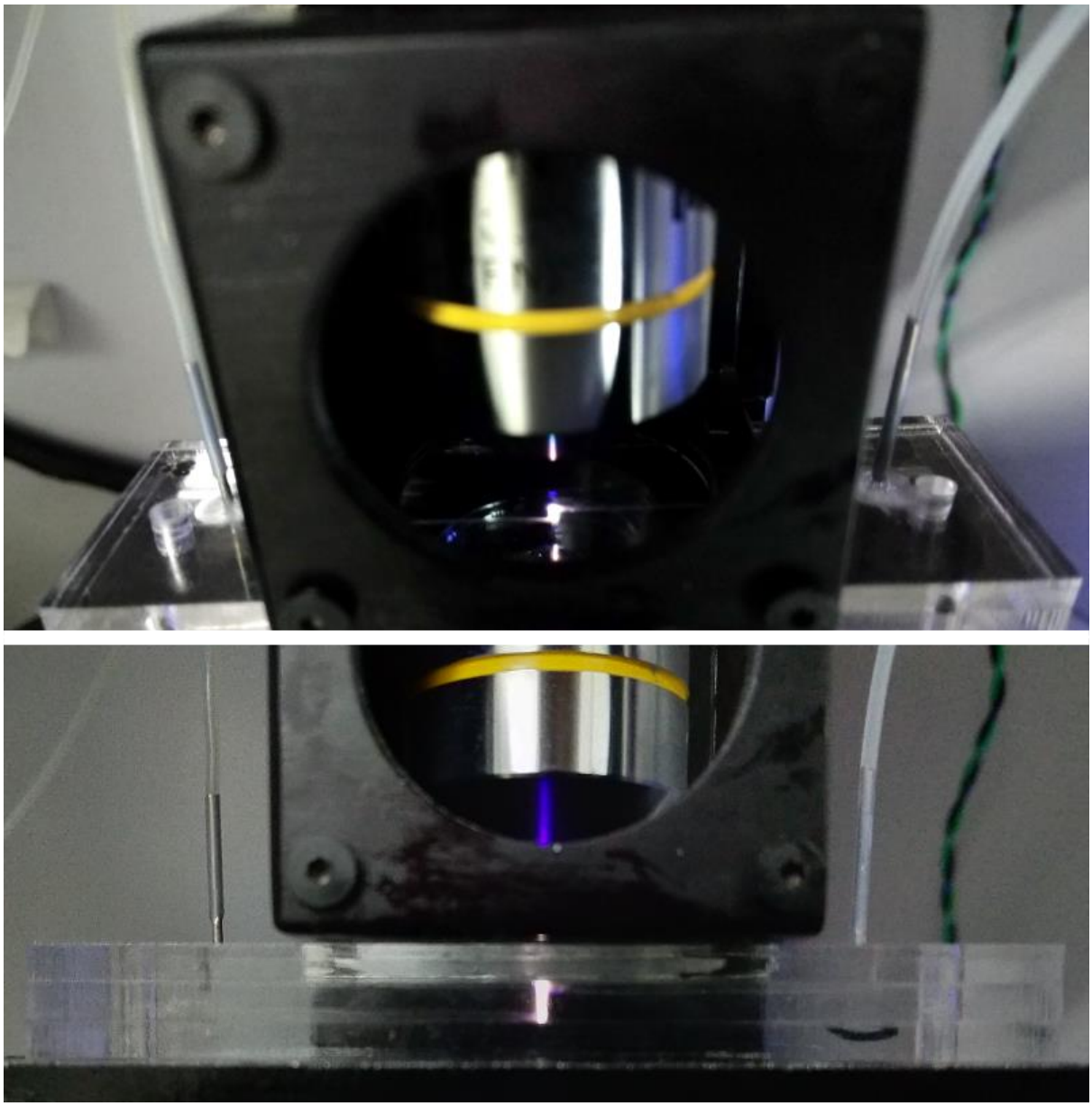


Figure 8.4: (top) Elevated view and (bottom) side view of the experimental setup during alignment (the laser power is set to the minimum).

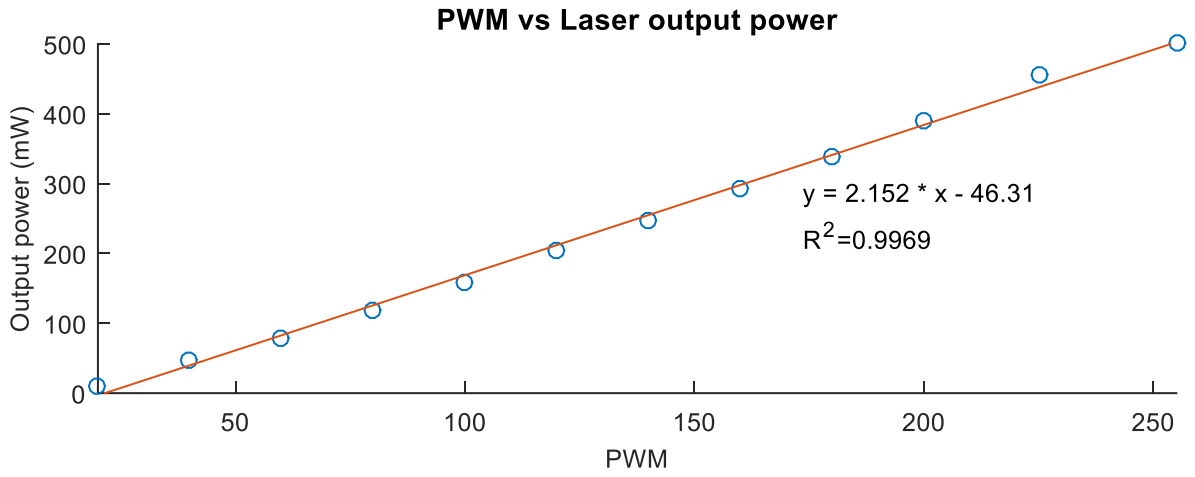


Figure 8.5: Measured laser output power vs PWM input signal, showing a fairly linear relationship between PWM value and output power.

8.2 Experiments

8.2.1 Precursor synthesis

Cadmium oxide (CdO, >99.95%), Selenium dioxide (SeO_2, >99.95%), oleic acid (>90%), 1-octadecene (ODE, technical grade), hexanes(>99%) and toluene (>98%) were acquired from Sigma-Aldrich. Ethanol (>99%, R&M), methanol and isopropanol (>99%, Sigma-Aldrich) were used for purification.

The synthesis route is based on previous work by Moghaddam et al (Mirhosseini Moghaddam, et al., 2013). All liquids were degassed before use. In a typical synthesis, a solution of cadmium oleate was prepared by mixing 64 mg CdO and 1000 mg oleic acid in 15 mL ODE and heating the mixture up to 200 °C under constant stirring and a clear, slightly yellow solution was obtained. A selenium solution was prepared by heating 55 mg of SeO_2 in 15 mL ODE at 170 °C until dissolved and a clear yellow solution was obtained. Several hours after cooling down to room temperature, the selenium dioxide starts to precipitate. Similarly, concentrated cadmium oleate starts gelling after a few days. Gentle heating up to ~70 °C allow the precipitates to dissolve and clears up the solutions before further use.

For some synthesis runs, the concentration of Cd was varied by reducing the amount of ODE used in the cadmium solution. This was done to increase the absorbance of the solution by increasing the concentration. While the concentration of the Se solution could hardly be increased, it is possible to prepared cadmium oleate without any solvent at all. The reaction mixtures were prepared by mixing measured volumes of each of the solutions together, but the molar ratio of Cd to Se was kept constant at 1 in all cases.

The results presented are from 3 of the mixtures that were prepared. More details may be found in Table 8.1.

Table 8.1: Precursor mixtures used for CdSe quantum dot synthesis

Name	**Mix111**	**Mix342**	**Mix461**	**Mix431**	**Mix571**
Cd conc (mmol/mL)	0.016	0.0307	0.0307	0.016	0.0307
Se conc (mmol/mL)	0.016	0.0307	0.0307	0.016	0.0307
Cd:Se molar ratio	1	1	1	1	1
Absorbance (405 nm)	0.951	1.092	1.811	0.940	1.993
Notes	- As per reference (Mirhosseini Moghaddam, et al., 2013) - Only used for bulk synthesis.	- 1 mL ODE used for the CdOA solution.	- No ODE used for the CdOA solution. - CdOA solution was prepared in ambient air. - Only used for bulk synthesis.	- As per reference (Mirhosseini Moghaddam, et al., 2013)	- No ODE used for the CdOA solution. - Se solution was filtered while still warm.

8.2.2 Quantum dot synthesis

For microfluidic synthesis, 1 mL of the mixture was drawn into a 1 mL syringe (Terumo) through a syringe filter. The filter was then removed, and the syringe was placed in the syringe pump and connected to the microfluidic chip inlet. The flow rate and laser power were varied based on simulation results (calculated based on the absorbance of each mixture at 405 nm), and are shown in Table 8.2. After passing through the chip, the solution was collected in a 1.5 mL glass vial. Purification most of the samples was performed by the addition of a small amount of hexane (~0.25 mL) for dilution, followed by ~1 mL of ethanol for precipitation.

After the addition of ethanol, the solution was then centrifuged for 10 minutes at 4500 rpm. The supernatant was pipetted out and the precipitant was then re-dispersed in hexane. Toluene was also

used for some earlier test samples, but due to its higher absorbance and fluorescence, hexane was used for the samples reported here.

A few batch synthesis runs were also conducted for comparison. The details of the samples produced are given in Table 8.3.

Table 8.2: Samples generated from each precursor mixture via microfluidic synthesis. For the samples with x at the end, the chip was found to be damaged after these samples. Hence their results may not be as expected. The samples are labelled using a combination of flow rate and PWM.

Mixture	**3.4.2**	**4.3.1**	**5.7.1**
Flow rate (uL/min) – Power (PWM)	17-184 19-188 20-191 21-194 23-198 24-200	15-180 15-225 15-255x 20-180 20-190 20-200x	24-120 37-137x 65-255 70-255 75-255x

Table 8.3: Samples generated from each precursor mixture via batch synthesis. All times stated are the time at which the sample was taken after reaching that temperature.

Mixture	**1.1.1**	**4.6.1**	**5.7.1**
Temperature-Time@temperature	240C30s	240C5m	190C1m 195C1m 210C0m 220C0m 240C0m 240C5m

8.3 Characterisation

The main characterisation methods used for the samples were UV-VIS (Perkin Elmer 365), PL (photoluminescence) and PLE (photoluminescence excitation) spectrophotometry. PL/PLE measurements were taken using a Hitachi FL-7000. ATR-FTIR measurements were taken on a Perkin Elmer Spectrum 400.

For UV-VIS, PL/PLE measurements of the unpurified solutions, ~30 µL of the solution was diluted in 2.5 mL of ODE and measure against an ODE blank. The purified samples were measured without dilution. For solvent and absolute absorbance measurements, the undiluted solvent/solution was measured against an air blank (empty cuvette). For ATR-FTIR measurements, a small droplet of the sample (~2 µL) was dropped onto the diamond window, and any volatile solvent was allowed to evaporate for a few minutes before starting the measurement.

The product volume was not enough to produce a signal for the XRD detector.

8.4 Results

The purified samples can be seen in Figure 8.6, Figure 8.7, Figure 8.8, and Figure 8.9. It must be noted that for most of the samples from Mix342 and Mix431, the peak emission is violet region (<450 nm) and most camera sensors have lower sensitivity in this region. The images shown here not quite indicative of the actual colour as seen by the human eye.

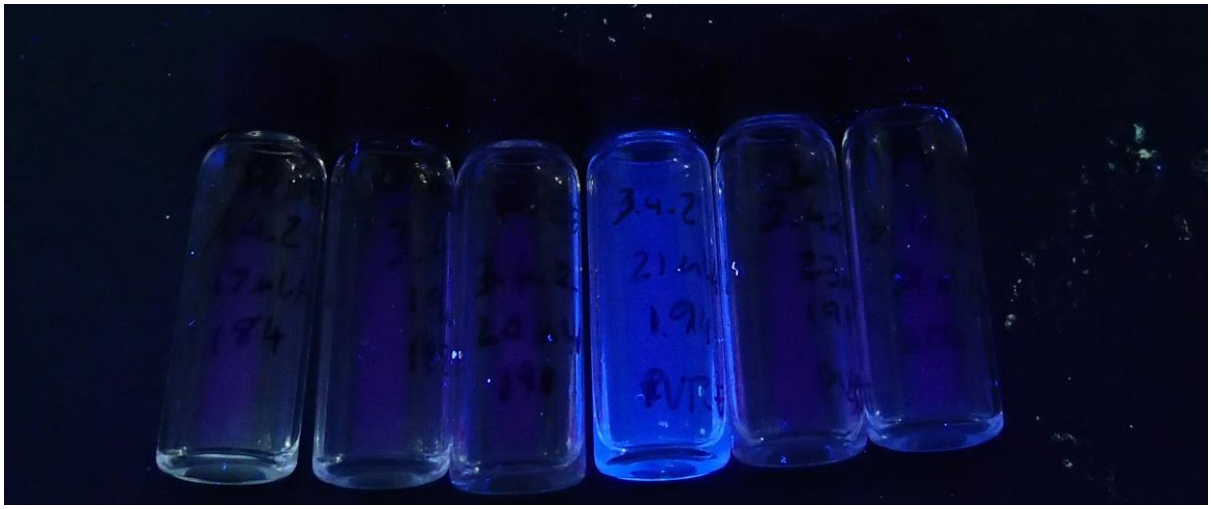


Figure 8.6: Photograph of purified samples made from Mix342 under UV illumination (365 nm). From left to right: 17-184, 19-188, 21-191, 21-194, 23-198, 24-200. While the sample 21-194 appears much brighter, it is mostly due to a higher amount being produced.

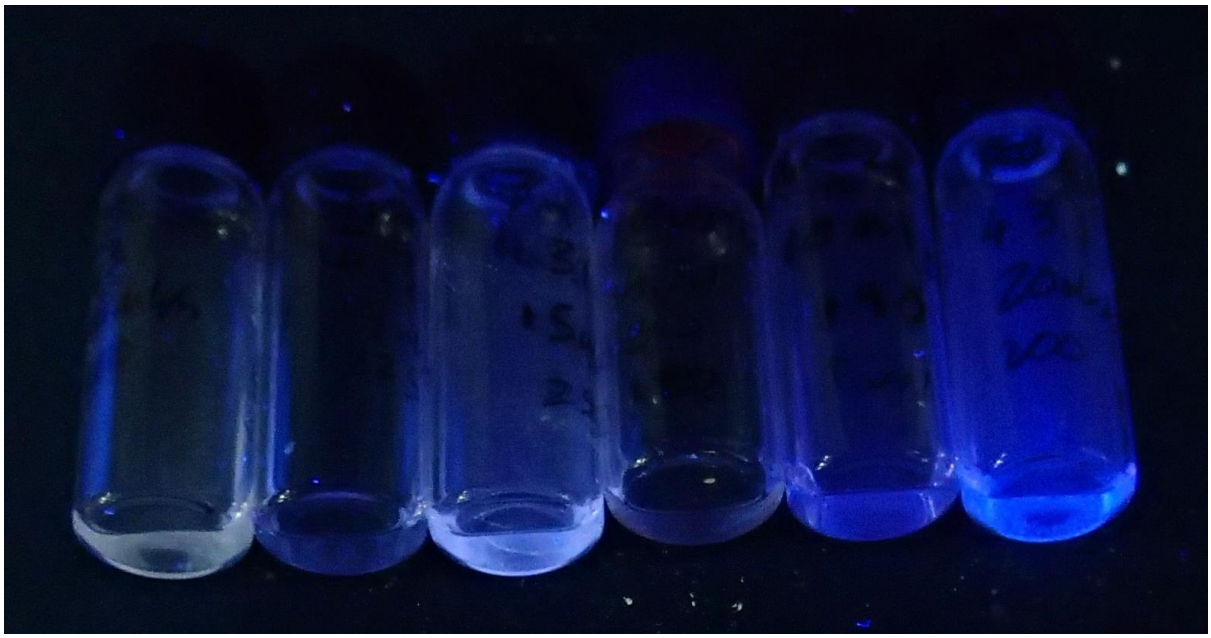


Figure 8.7: Photograph of purified samples made from Mix431 under UV illumination (365 nm). From left to right: 15-180, 15-225, 15-255, 20-180, 20-190, 20-200



Figure 8.8: Photographs of purified samples made from Mix571 under UV illumination (365 nm). From left to right: 20-180, 37-134x, 65-255, 70-255, 75-255x.

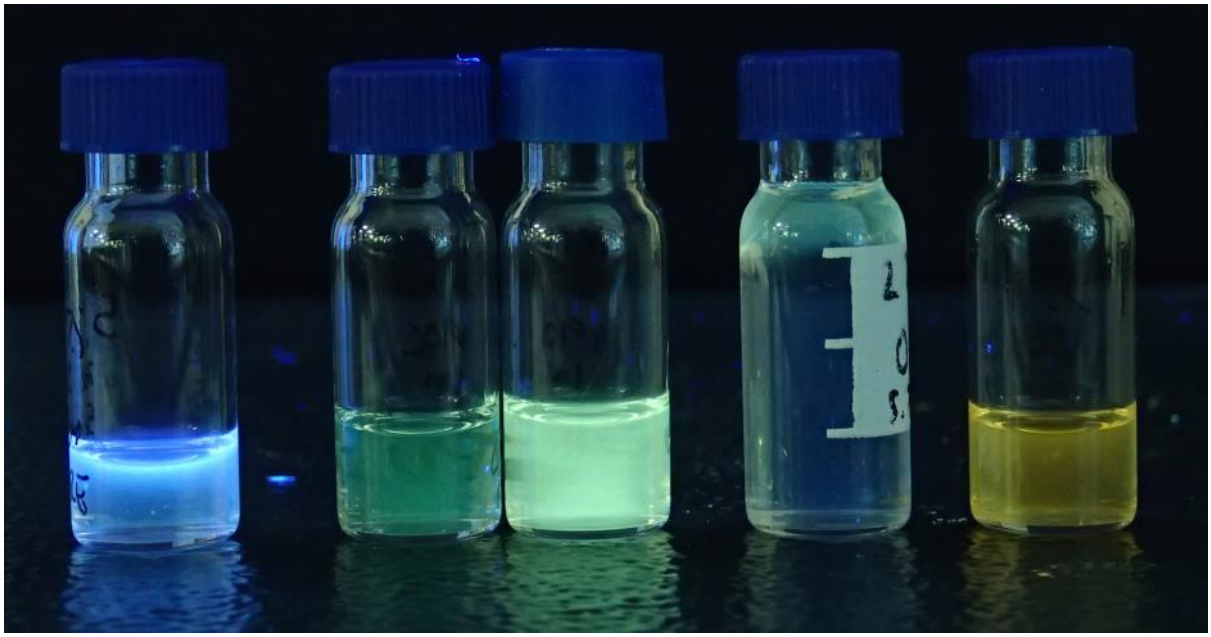


Figure 8.9: Photograph of purified samples generated from batch synthesis using Mix571 under UV illumination (365 nm). From left to right: 70c5d, 190C1m (purified with methanol), 190C1m (purified with ethanol), 220C0m, 240C5m.

8.4.1 FTIR

FTIR analysis was used to confirm the successful removal of ODE and CdOA from the purified product. An example is shown in Figure 8.10, showing the supernatant after purification of sample s70_255 contains the remaining ODE (the supernatant was dropped onto the FTIR window and allowed to evaporate, leaving behind the heavier components). A pair of weak peaks in the s70_255_pure spectrum at 804 cm^{-1} and 471 cm^{-1} are possibly due to Cd-Se vibrations, however the signal was not as clear for most samples, hence no conclusions are drawn on the phase of the product. The wash and mix spectra (s70_255_wash and Mix 571) are nearly completely overlapping, showing that the separation works well. Since the CdOA reacts with the Se in the mixture even at room temperature to form clusters, its signature is not found in any of the samples.

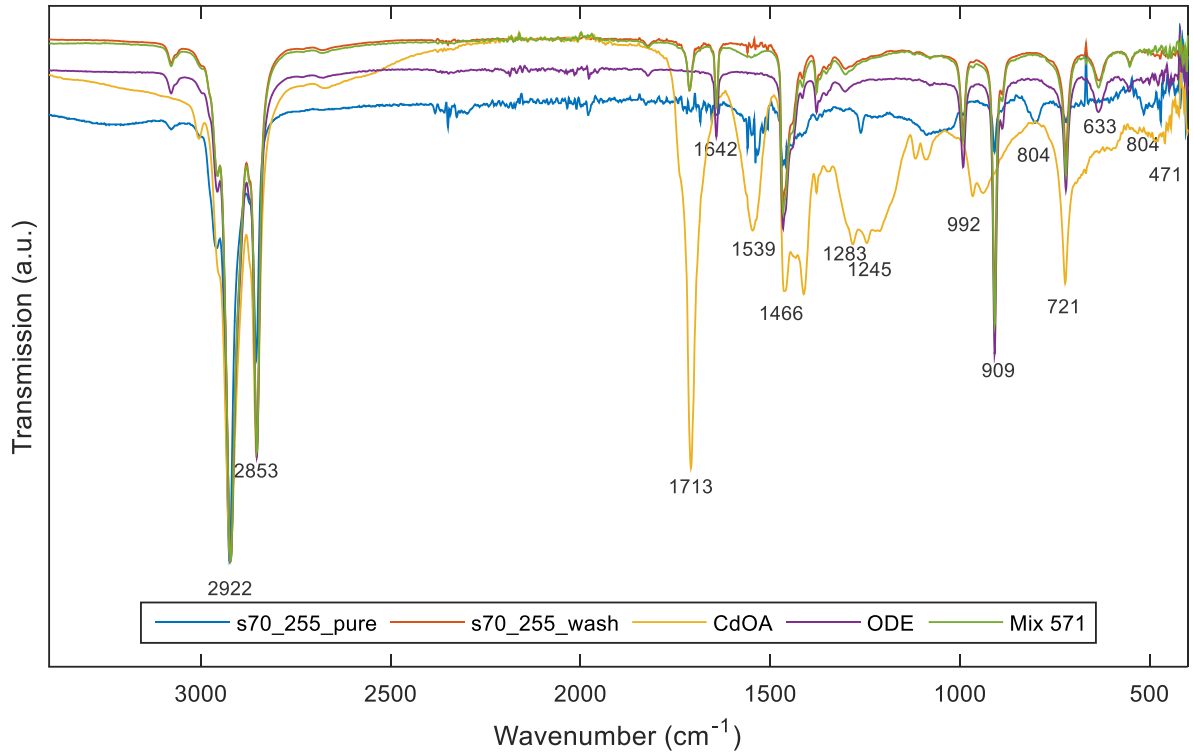


Figure 8.10: FTIR spectra of pure s70_255 and the supernatant after purification.

8.4.2 UV-VIS

The absorbance spectra of the three batch synthesis products are shown in Figure 8.11.

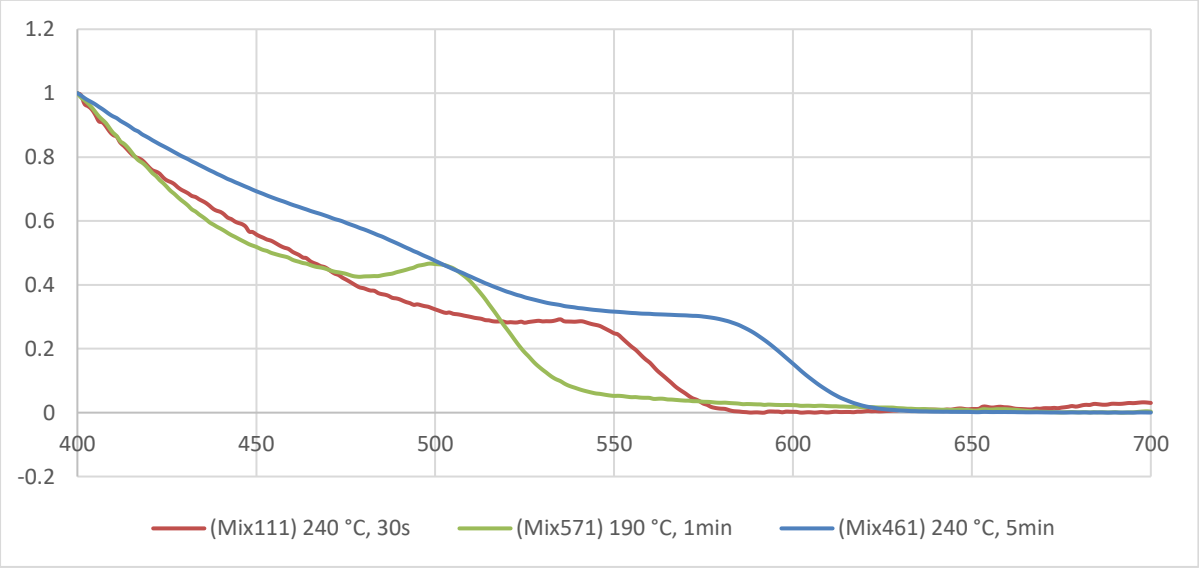


Figure 8.11: Absorbance of purified CdSe quantum dot solutions from batch synthesis runs using three different precursors.

Due to the small volumes produced, most of the samples produced by microfluidic synthesis had very weak UV-VIS absorbance peaks, except for those made using Mix571. UV-VIS absorbance spectra measured from those samples are presented together with their photoluminescence spectra in Figure 8.17.

8.4.3 Photoluminescence

Photoluminescence (PL) and photoluminescence excitation (PLE) spectra were measured using a Hitachi F-7000 fluorescence spectrophotometer at a scanning rate of 240 nm/min using 2.5 nm slits for both excitation and emission. All photoluminescence spectra measured were excited at 365 nm unless specified otherwise.

All the purified products were dispersed in hexane, while the un-purified products and precursor mixes were in the original solvent (1-octadecene). The photoluminescence spectra of the pure solvents are shown in the appendix (section 11.5).

Due to the limitations of the setup, we know our nanoparticle samples will have a wider range of sizes than a typical batch synthesis run. This would result in a wider absorbance and emission band as well However, CdSe clusters are known to emit in a wide range while absorbing in a limited region. This difference can be used to identify the components of the synthesised product.

The PL plots in this section were made using MATLAB, and the visible light spectrum included on the x axis was generated using Spectral and XYZ Color Functions by Jeff Mather (Mather, 2020).

8.4.3.1 *Purified products from batch synthesis*

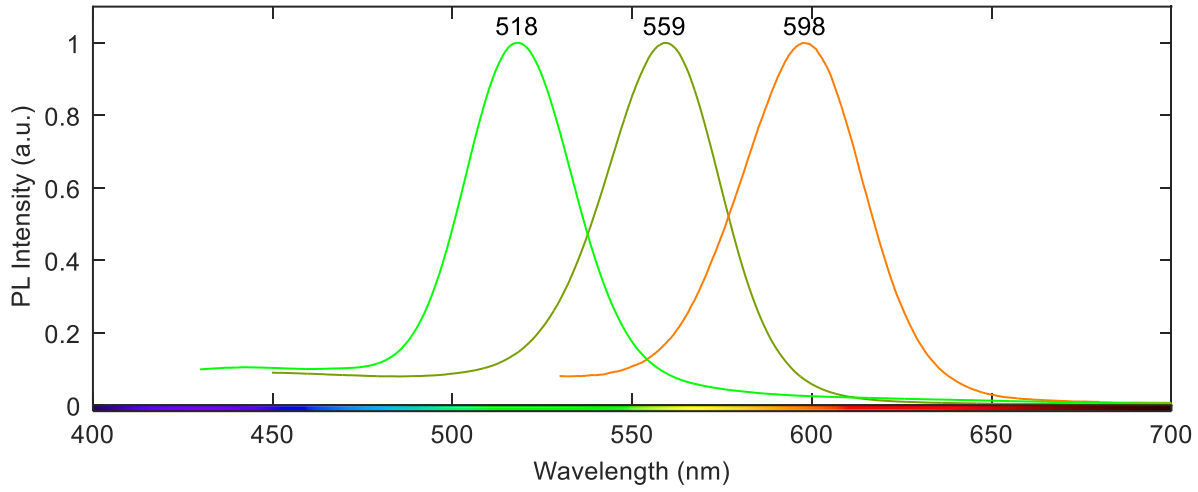


Figure 8.12: PL spectra (normalised) of purified CdSe quantum dot solutions produced via batch synthesis. From left to right, the samples are (Mix571) 190 °C 1 min, (Mix111) 240 °C 30 s, and (Mix461) 240 °C 5 min.

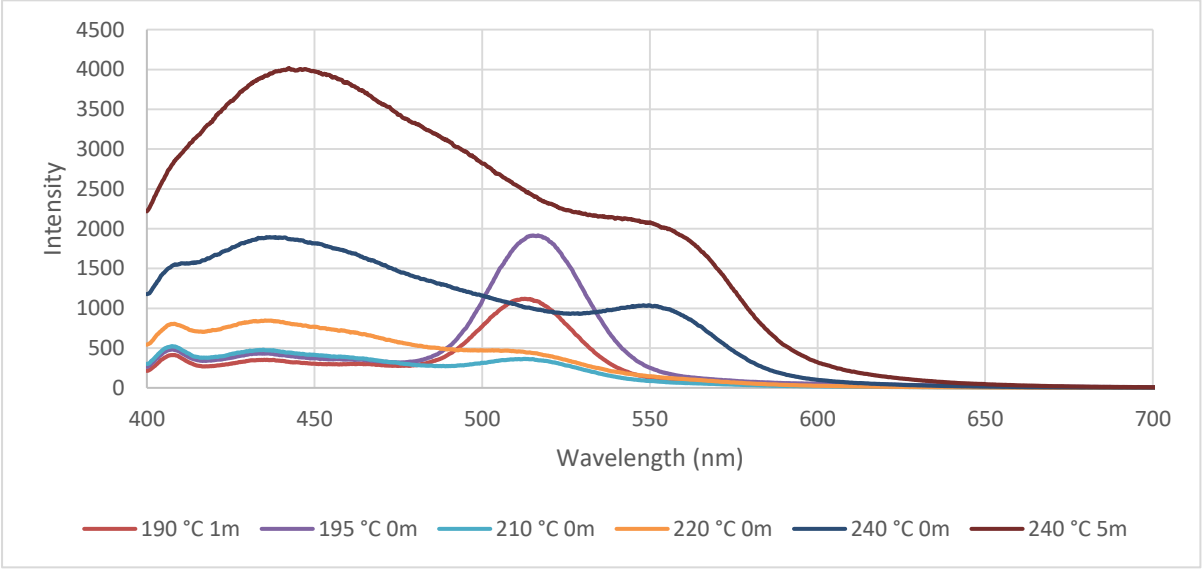


Figure 8.13: PL spectra (normalised) of aliquots taken at various temperatures during a batch synthesis run using Mix571.

8.4.3.2 *Purified products from microfluidic synthesis*

Figure 11.26 shows the spectra of Mix342 and the purified samples produced from it. The peaks at 406 can be attributed to the solvent (ODE in the precursor, and hexane in the purified samples). The sample s17_184 shows its highest peak at 462 nm, which a small hump at ~565 nm. The fluorescence spectrum of this sample is rather broad, with a FWHM of ~130 nm. s19_188 shows a similar but weaker

peak at 460 nm. A peak at 437 nm is seen in s21_194, while s23_198 and s24_200 both show peaks at ~427 nm.

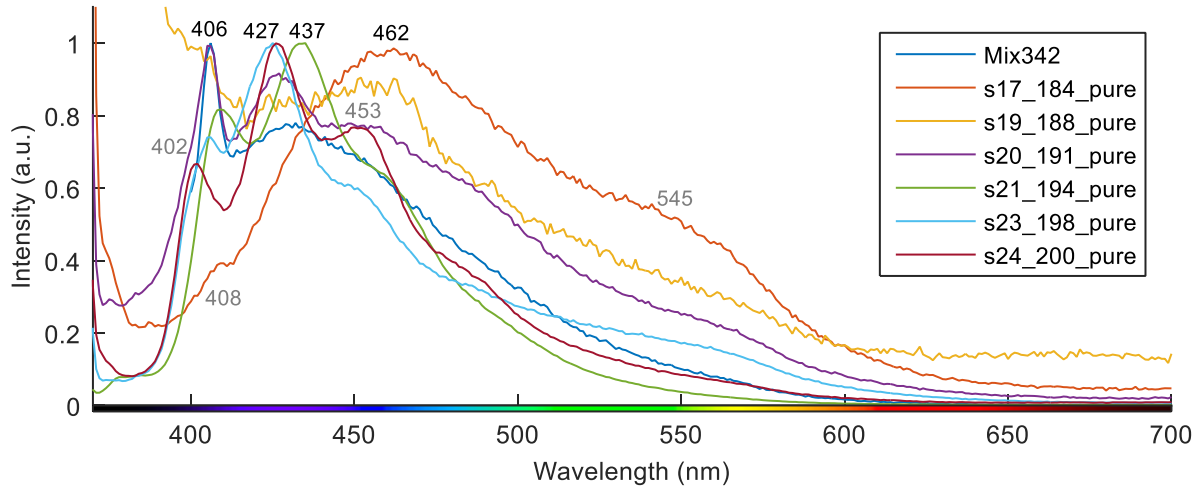


Figure 8.14: Normalised fluorescence spectra of Mix342 and the purified samples produced from it via microfluidic synthesis.

Figure 8.15 shows normalised fluorescence spectra of samples produced from Mix431. It can be seen that the positions of the peaks and their relative intensities are remarkably similar to those seen for Mix342 in Figure 8.14. Although the flow rate and laser powers used for these samples are higher, this is compensated for somewhat by the lower absorbance of the sample.

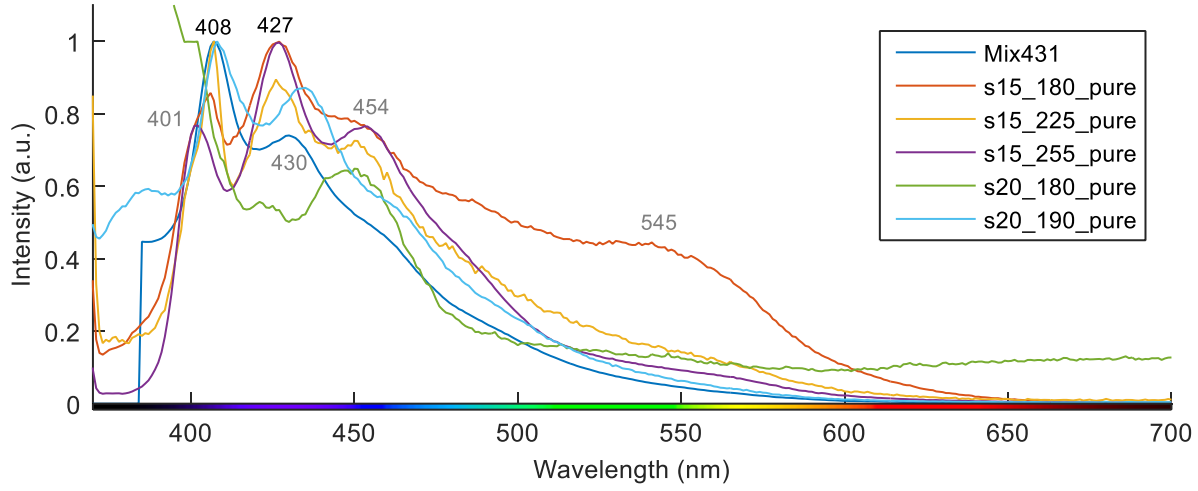


Figure 8.15: Normalised fluorescence spectra of Mix431 and the purified samples produced from it via microfluidic synthesis.

Finally, Figure 8.16 shows the normalised fluorescence spectra of Mix571 and the samples produced using this mixture. Sample s75_255x shows peaks similar to seen in Mix342's s24_200 (Figure 8.14) and Mix431's s15_255x (Figure 8.15). However, the samples produced at lower flow rates show a major reduction in secondary peaks and a red shift in peak with decreasing flow rates. The sample s37_134 is an exception here, as the chip was damaged partway during the synthesis run.

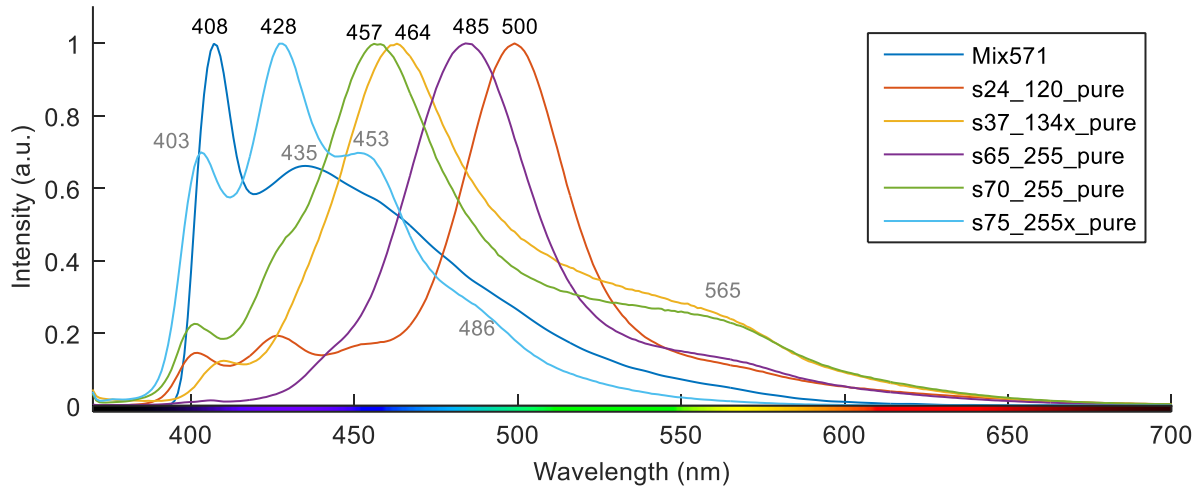


Figure 8.16: Normalised fluorescence spectra of Mix571 and the purified samples produced from it via microfluidic synthesis.

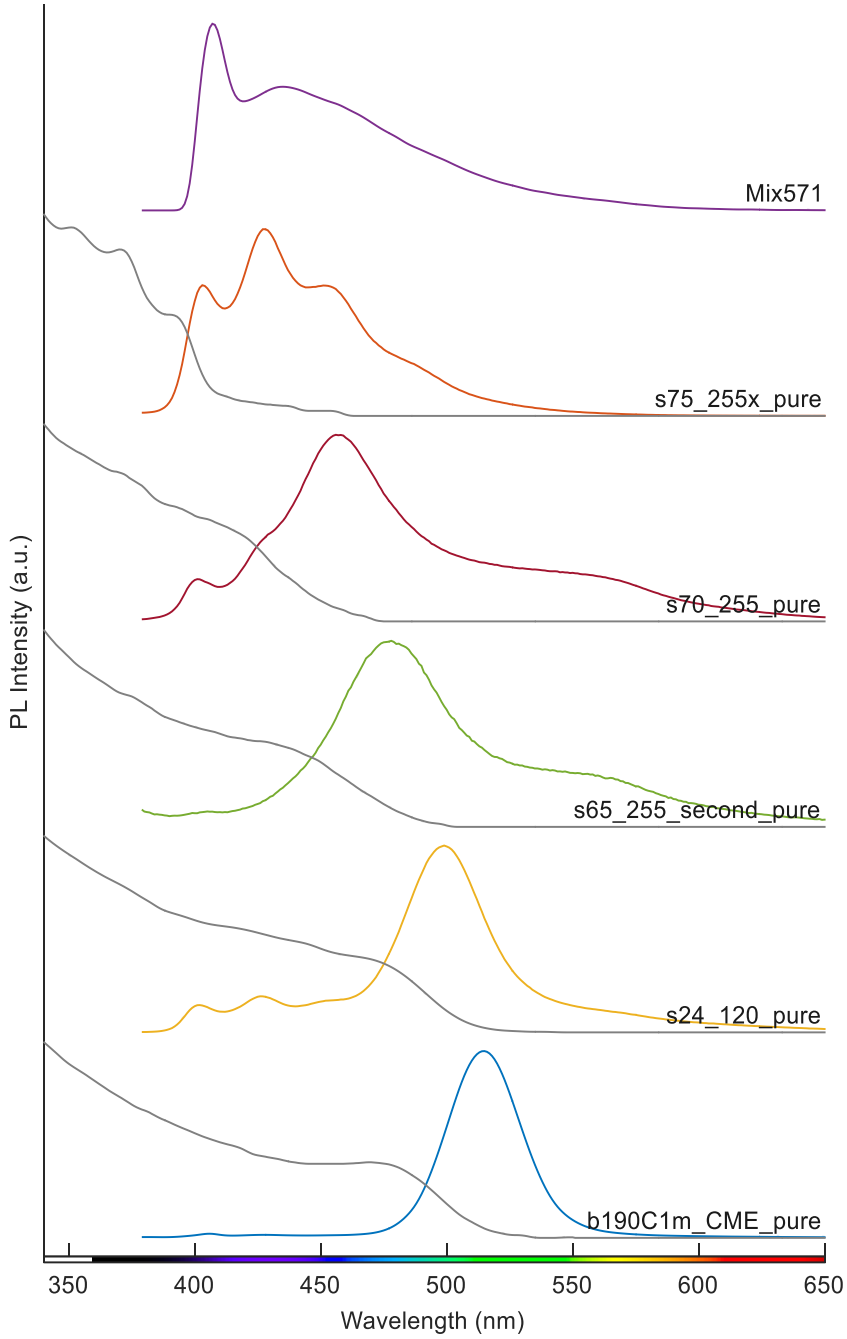


Figure 8.17: Photoluminescence spectra (coloured) and UV-VIS absorbance spectra (grey) of Mix571, and samples produced from it. Sample b190C1m_CME_pure was produced via a batch synthesis run, while the other samples were produced via microfluidic synthesis. All spectra are normalised.

Figure 8.17 shows the PL and UV-VIS absorbance spectra of samples made from Mix571. The batch synthesis product, sample b190C1m_CME_pure shows the sharpest PL peak and the most prominent band absorbance peak in the UV-VIS spectra. Comparing these two spectra, the best result from the microfluidic synthesis (s24_120_pure) comes quite close to the batch synthesis product.

Following is a detailed look at the PL and PLE spectra of each sample. The spectra of samples made from Mix342 and Mix461 can be found in the appendix as they are largely similar.

Mix342

Sample s17_184_pure (Figure 11.27) shows weak band absorption peaks in its PLE spectra, but it also missing the sharp PL and PLE peaks seen in other samples.

In sample s19_184_pure (Figure 11.28), we can clearly see band absorption peaks at a relative distance of 40-50 nm from the emission wavelength. A broader absorption peak also appears at emission wavelengths above 447 nm. This peak also appears to maintain a stokes shift of ~75-85 nm relative to the emission wavelength. The typical absorption peaks associated with CdSe clusters are relatively much weak. Although this sample has a low yield, it appears to contain CdSe quantum dots with a broad size distribution.

Sample s20_191_pure (Figure 11.29) shows a series of band edge absorption peaks throughout the PL spectrum up to the excitation spectrum at 500 nm, above which it gets very weak. This band absorption peak appears to increase continuously and does not seem to follow the discrete increases associated with MSCs. However, the major contributor to the fluorescence appear to be the absorption peaks at 329 nm and 372 nm.

Sample s21_194x, _pure due to the chip burning out, did not reach similarly high temperatures as the other samples, and that is reflected in the PLE spectra (Figure 11.30). The majority of the photoluminescence is due to absorption at 359 nm, 373 nm, and 396 nm. At lower wavelengths the 315 nm absorption peak also contributes. It appears this sample is comprised mainly of MSCs with a broad emission spectrum.

Similar to s20_191_pure, the sample s23_198_pure (Figure 11.31) shows a band edge absorption peak throughout the PL spectra. In this case, the 323 nm absorption peak is relatively weaker, and the 353 nm and 373 nm peaks show a strong absorbance throughout the PL spectrum.

Mix431

Figure 11.32 shows the PL and PLE spectra of Mix431 aged at room temperature for 50 days. Compared to the fresh mixture, the 406 nm PL peak is weaker, the 432 nm and 455 nm peaks are stronger. This indicates the formation of CdSe clusters within the solution at room temperature.

In the PLE spectra for sample s15_180_pure (Figure 11.33), the 330 nm, 353 nm, and 372 nm absorption peaks contribute to the majority of the emission throughout the PL spectrum. A band edge absorption peak can be seen through the PLE spectra with a stokes shift of ~40-50 nm. Similarly, in sample s15_255_pure (Figure 11.34), the same band edge absorption peaks may be seen, but they are much stronger, possibly due to the higher laser power.

In sample s15_255x_pure (Figure 11.35), once again due to the chip burning out, we see a very weak and relatively broad band edge absorption peaks at 425 nm, 438 nm and 446 nm.

Sample s20_180_pure (Figure 11.36) shows dual band edge absorption peaks throughout the spectrum, one at a typical stokes shift of 40-50 nm, and the second at ~90 nm from the emission wavelength. It is unclear what this implies. It must be noted that this sample had a very low yield, and as a result the spectra are very weak.

Sample s20_190_pure shows a series of very weak band absorption peaks.

Sample s20_200_pure (Figure 11.38) shows negligible band absorption. The majority of the fluorescence is wide band emission from absorption at 355 nm, 373 nm, and 394 nm.

Mix571

The samples from this mixture show the best results out of the three. Sample 24_120_pure (Figure 8.18) has a prominent PL peak at 499 nm that dwarfs cluster emission peaks at 402 nm and 426 nm. Measuring the PLE around the 499 nm peak shows a clear band absorption peak that red shifts with the emission wavelength, and displays a narrow stokes shift of 15-26 nm. The contribution of the 355 nm, 373 nm and 394 nm absorption peaks is also lower at higher wavelengths. At higher emission wavelength of 570 nm, no specific band edge peak is seen in the PLE spectra.

Similarly, in sample s37_134x_pure (Figure 8.19), the PLE around the main peak at 462 nm shows a lower contribution from the MSC absorption peaks, and a clear band edge peak may be seen at higher wavelengths with a stokes shift of ~45 – 50 nm.

In sample s65_255_pure (Figure 8.20), the main PL peak emits at 484 nm. The PLE spectrum at 481 nm shows a clear band edge absorption feature with a peak at 465 nm, and no band edge absorption at the emission wavelength of 565 nm. After purifying this sample a second time (Figure 11.39), the main PL peak showed a slight blue-shift to 481 nm, suggesting some of the larger particles were lost.

In sample s70_255_pure (Figure 8.21), the MSC peaks (338 nm, 354 nm, 373 nm, 393 nm) remain strong throughout the PLE spectra, however the main PL peak at 456 nm does appear to have some contribution from band edge absorption.

The chip burned out during the synthesis of sample s75_255x (Figure 8.22), and the MSC peaks are the only contributors to the PL spectrum.

The remainder of Mix571 was kept in an oven at 70 °C for 5 days, resulting in the production of MSCs as seen in Figure 11.40. The 375 nm and 395 nm absorption peaks result in wide band emission while the 440-450 nm peaks contribute to the weak PL at higher frequencies.

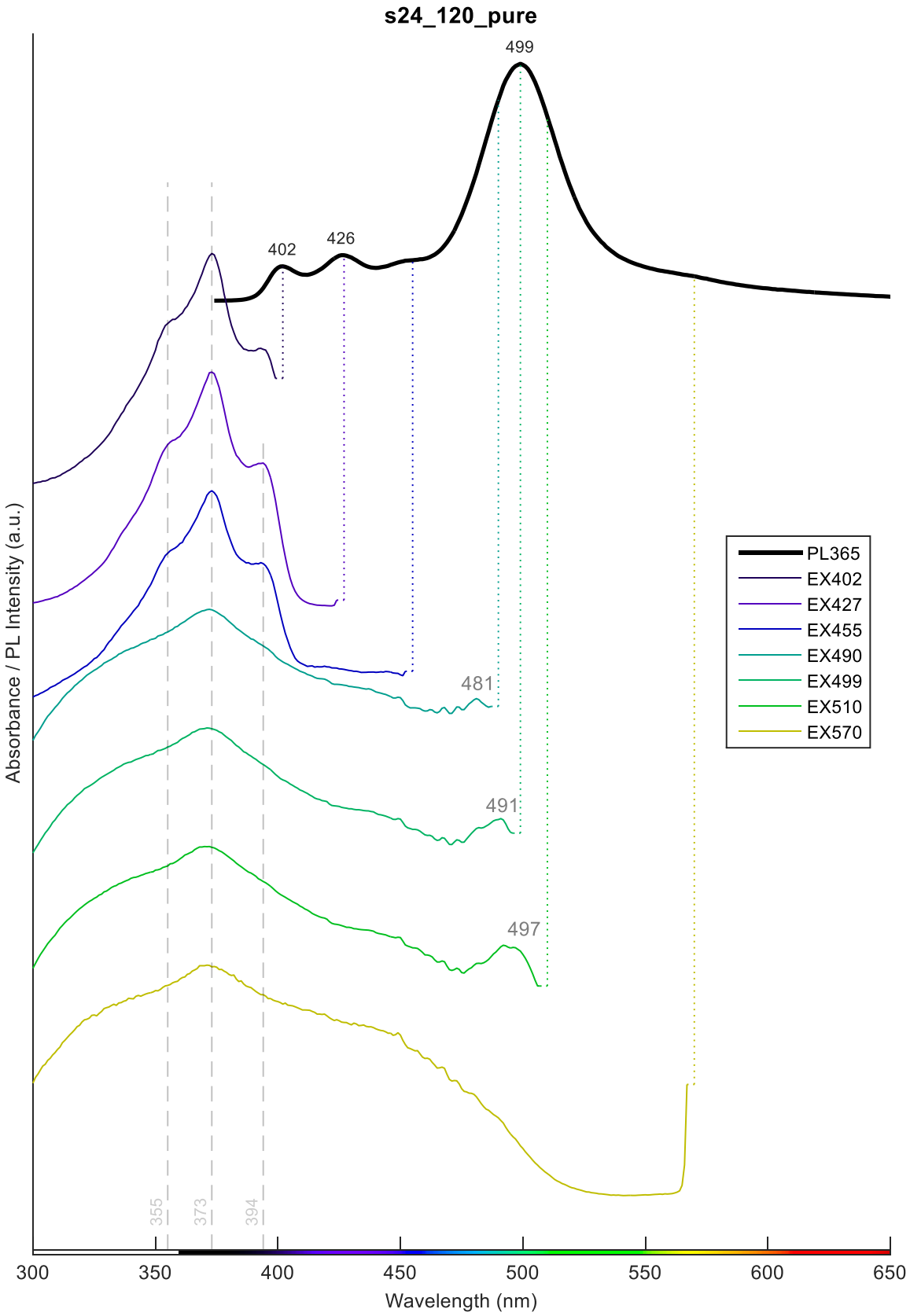


Figure 8.18: Normalised fluorescence (PL365) and PLE spectra of sample s24_120_pure (made from Mix571) measured at various emission wavelengths. The absorption features at 355, 373, and 394 nm are the main contributors to the PL peaks seen below 460 nm. At higher wavelengths the contribution of these peaks is reduced and the PLE spectra around them broadens.

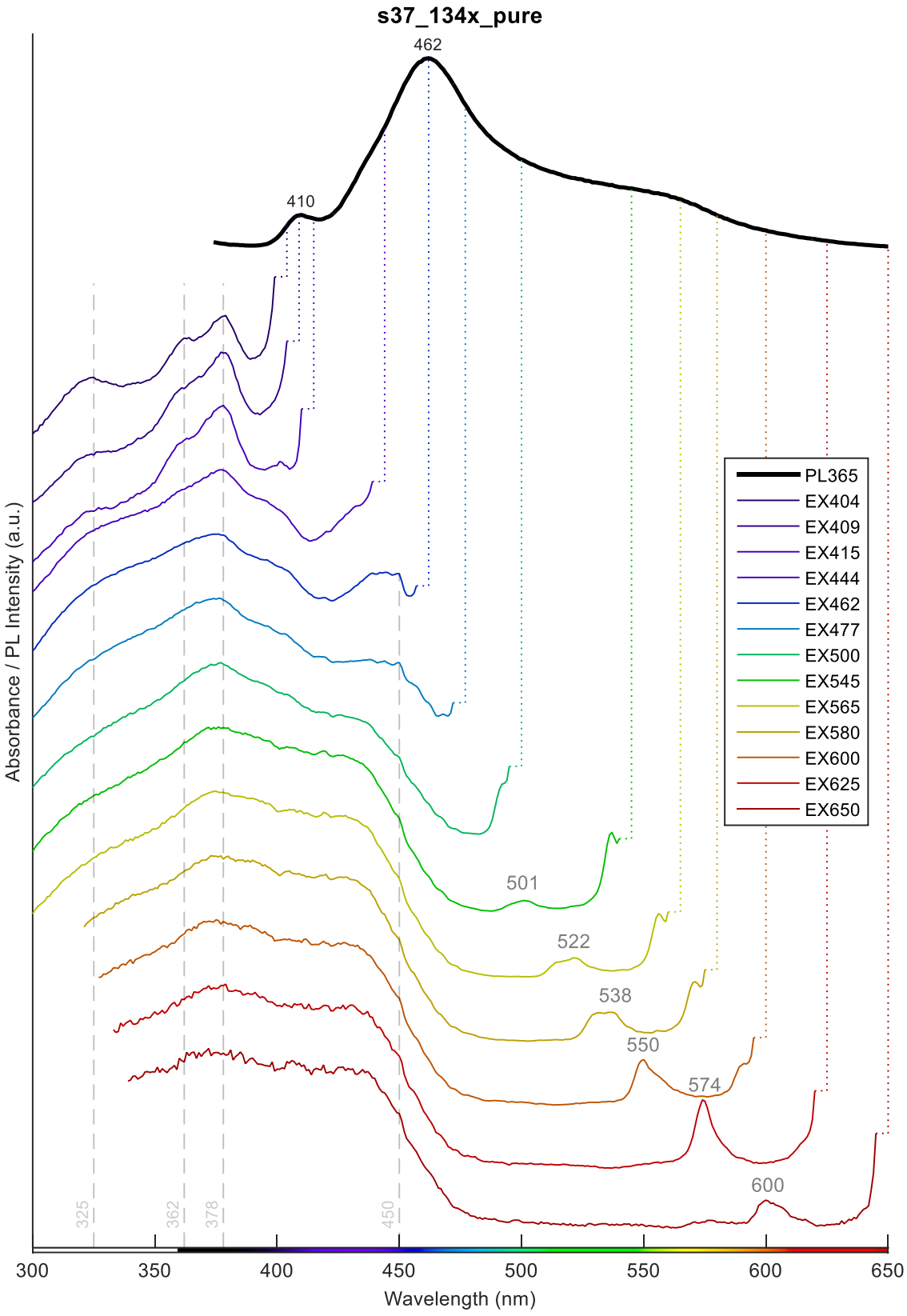


Figure 8.19 Normalised fluorescence (PL365) and PLE spectra of sample s37_134_pure (made from Mix571) measured at various emission wavelengths. The absorption features at 355, 373, and 394 nm are the main contributors to 410 nm PL peak. The 462 nm PL peak sees some absorption features between 433 – 450 nm, which decreases in intensity but does not exhibit a red shift when the emission wavelength is increased to 477 nm.

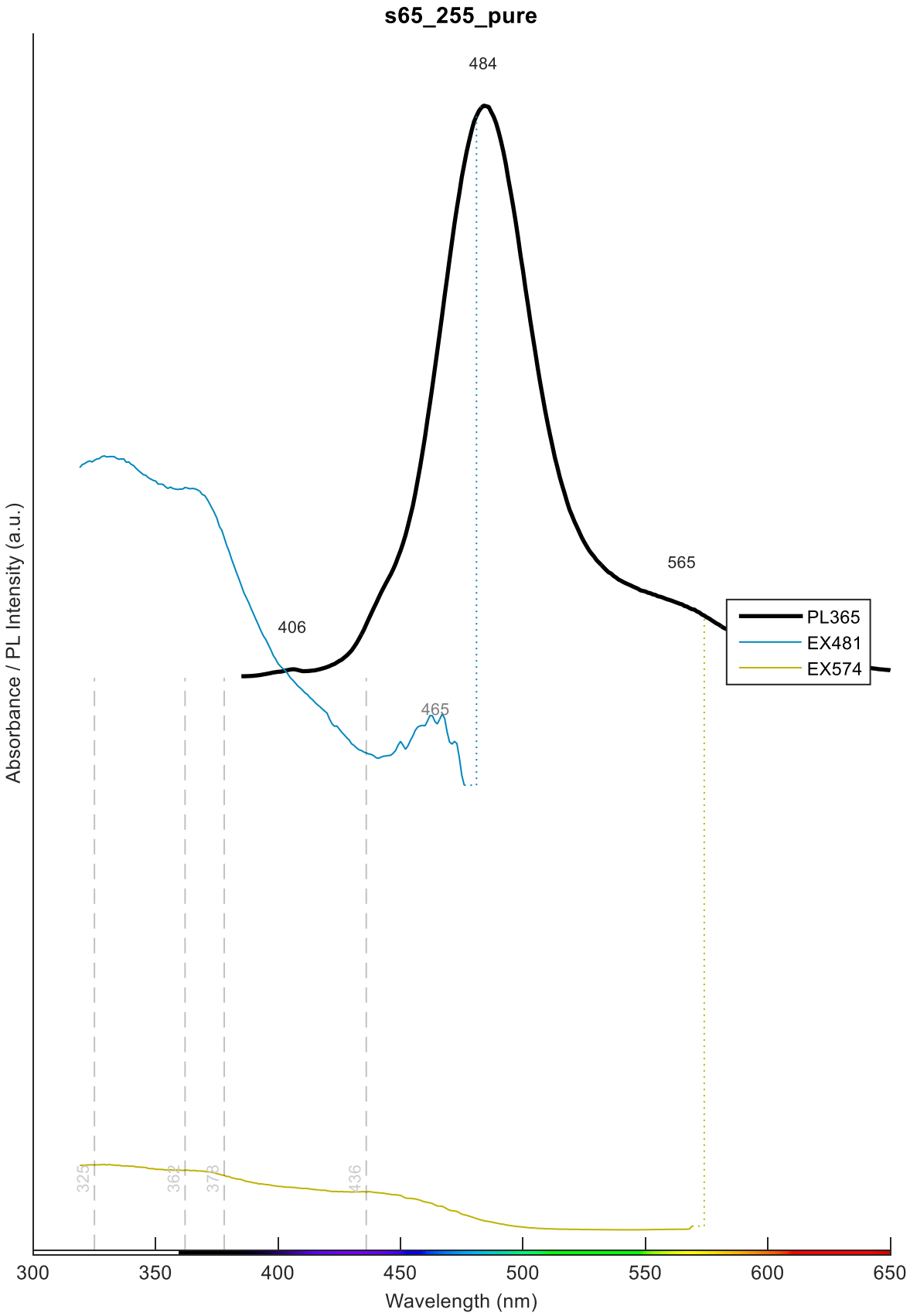


Figure 8.20: Normalised fluorescence (PL365) and PLE spectra of sample s65_255_pure (made from Mix571) measured at various emission wavelengths.

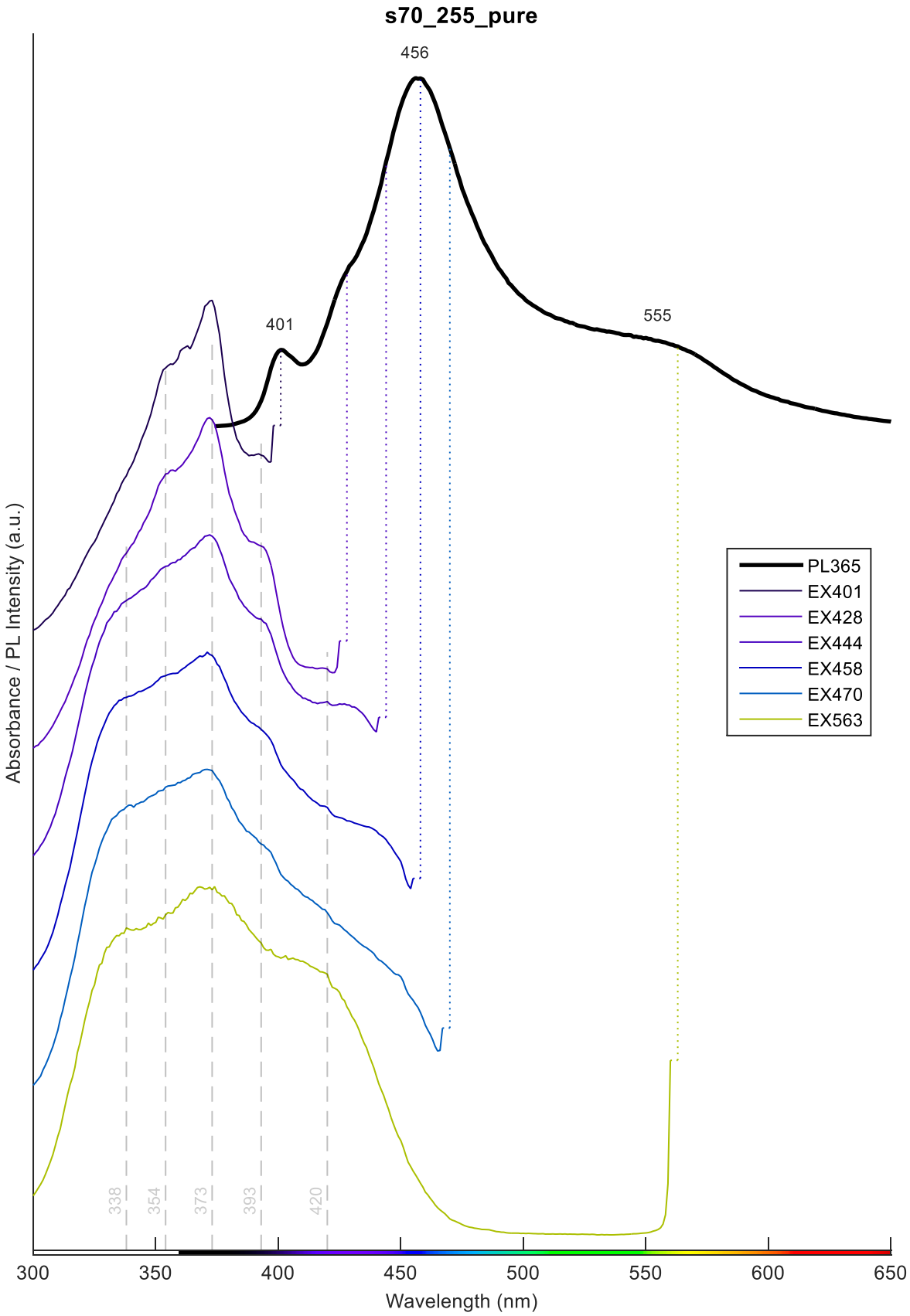


Figure 8.21: Normalised fluorescence (PL365) and PLE spectra of sample 70_255 (made from Mix571) measured at various emission wavelengths. Red shifting can be seen in the weak band edge absorption hump going from EX458 to EX470.

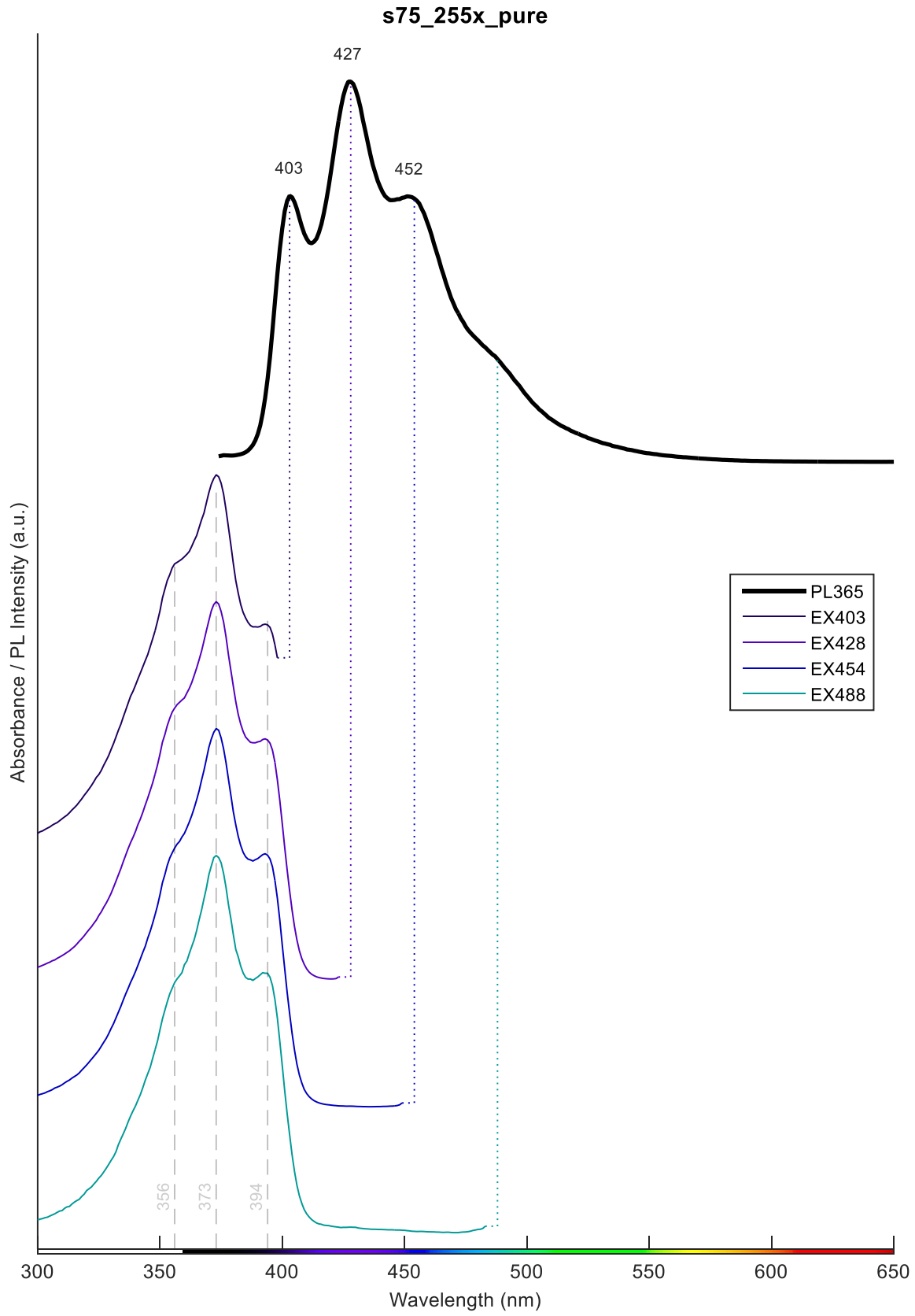


Figure 8.22: : Normalised fluorescence (PL365) and PLE spectra of sample s75_255 _pure (made from Mix571) measured at various emission wavelengths. There is no observable change in the ratio of the excitation absorption peaks seen at 356, 373, and 394 nm at any of the emission wavelengths measured.

8.5 Discussion

Since our samples have a wide range of particle sizes, the PL spectra has been analysed in detail to determine whether the samples contain quantum dots, MSCs or both. The PLE spectra were measured with emission wavelengths set near each of the PL peaks observed. This allows us to see which absorbance peaks contributed to the fluorescence at that peak. Since we know the quantum dot absorbance spectra have a band edge peak which follows the fluorescence peak, we should be able to determine the presence of quantum dots in the sample if this peak is observed in the PLE spectra. For example: If there is a PL peak at 470 nm with a FWHM of 60 nm, and upon measuring the PLE at an emission wavelength of 470 nm, an absorbance peak at 420 nm is found. This absorbance feature may be from quantum dots or from MSCs, and at this point we may not be able to tell. Now, the PLE spectra on the right shoulder of the 470 nm PL peak is measured, i.e. at a slightly red-shifted emission wavelength (around 480 nm). If there are quantum dots contributing to this PL peak, we can expect the absorbance peak to exhibit a red-shift as well. If the PL peak is solely due to MSCs, there will not be a continuous change in absorbance, if any.

8.5.1 Batch synthesis

Batch synthesis was performed using the precursors 1.1.1, 5.7.1, and 4.6.1. Solution 1.1.1 worked as expected, with a colour change being observed at 240 °C. The reaction was stopped 30 seconds after reaching this temperature. The purified product fluoresced at 563 nm, with a FWHM of 36 nm. The PL spectra from this sample and the other batch synthesis samples may be seen in Figure 11.26.

The CdOA solution used in Mix571 was thought to be oxidised, hence a bulk synthesis run was performed to check for suitability. A colour change was observed at relatively low temperatures (~185 °C). A sample aliquot taken after 1 minute at 190 °C contained particles strongly fluorescing at 518 nm, with a FWHM of 39 nm. Continuing the heating, the particles appear to dissolve above 210 °C and above, and at 240 °C resulted in polydisperse particles with a very broad PL spectrum (Figure 8.13). The use of methanol as a precipitating solvent was reported to cause a reduction in quantum yield. In addition to the ethanol based purification, the 190 °C sample was also purified using methanol, and the reduced fluorescence is obvious (Figure 8.9)

Mix461 also showed a colour change at a lower than expected temperature at 210 °C, but unlike with Mix571, continued heating at 240 °C resulted in usable particles with a fluorescence peak at 600 nm with a FWHM of 41 nm. The absorbance spectra of these three samples are as expected from the literature (Figure 8.11).

8.5.2 Cluster formation in reaction mixtures at low temperatures

The fluorescence spectra of new and aged (for 50 days at room temperature) Mix431 are shown in Figure 8.11. A significant increase in the PL peaks at 432 nm and 455 nm is seen, with the 432 nm peak being the strongest. The PLE peaks at 377 nm and 398 nm are the major contributors to the PL up to an emission wavelength of 467 nm. Above this, a broad absorption peak at 434-450 nm dominates the PLE spectra. All of these absorption peaks are associated with MSCs and have been observed in other samples as well.

Mix571 was kept in an oven at 70 °C for 5 days to investigate the formation of MSCs at low temperatures (Figure 11.40). Similar to the aged Mix431, strong absorption peaks are seen in the PLE spectra at 375 nm and 395 nm up to an emission wavelength of 500 nm. The 440-450 nm broad absorption peak is also seen at higher emission wavelengths. In this case however, the 456 nm PL peak is the strongest, indicating the formation of larger MSCs than at room temperature. However, the concentration of both Cd and Se in Mix431 is half of that in Mix571.

The absorbance peak values seen in both cases are consistent with reported values for CdSe clusters (see Section 2.2.1).

8.5.3 Microfluidic synthesis

For samples synthesised from Mix342 and Mix431, the majority of the fluorescence peaks are still in the violet region (400 – 450 nm), with a few samples showing peaks in the blue regions (450 – 480 nm). Some of the samples also show a secondary broad hump at 545-565 nm. A broad fluorescence peak in this region is often associated with trap emission. However, due to the limitations of the current design, we may expect a wider size distribution than normal. If this is the case, we can also expect a few larger particles to emit at higher wavelengths. Hence, PLE measurements were taken around each of the observed PL peaks in the purified samples.

Mix342

For purified samples made from Mix342, the majority of PL peaks seen (Figure 8.14) are known to be a result of CdSe clusters, from literature and from our analysis of aged precursor solutions. However for the samples produced at the two slowest flowrates, s17_184 (17 µL/min) and s19_188 (19 µL/min), broad peaks are observed at 462 nm and 545 nm. PLE analysis of s17_184 (Figure 11.27) shows that a

broad absorbance peak centred at 372 nm is a consistent contributor throughout the entire PL spectrum, confirming the presence of clusters. A relatively small band absorption peak can be seen following the red-shifting of the emission wavelength, and is most evident in the PLE spectrum EX600, with a stokes shift of ~45 nm.

For sample 19_188 (Figure 11.28), the band edge absorbance peaks are much more evident, and the amount of MSCs in this sample appears to be very low, as is the overall yield. Interestingly there appear to be two band edge peaks, the second stronger peak appearing at emission wavelengths above 430 nm with a much larger stokes shift of ~90 nm, but there isn't enough sample volume to investigate further.

The other samples made from Mix342 show similar results (Figure 11.29 to Figure 11.31), with a small amount of quantum dots contributing to the fluorescence throughout the spectrum. However, in all of these, the absorbance of the clusters is much greater than that of the quantum dots.

Mix431

The samples from Mix431 show PL spectra similar to those of the previous batch despite the lower flow rates. Since this mixture had a lower absorbance, it was expected to reach similar temperatures according to the simulation, and that does appear to be the case, given the similar PL spectra. The quantum dots seen in sample s15_255 (Figure 11.34) show the sharpest band absorption peaks so far. Sample s20_180 (Figure 11.36) shows similar peaks in the PLE spectra as in Mix 3.4.1's s_19_188 (Figure 11.28).

Some of these samples were only partially heated due to the chip forming cracks during the synthesis. Sample s20_200x (Figure 11.38) is one such case where only MSCs were formed with no significant band edge peak to be seen.

Mix571

The particles produced using this mixture are the largest so far produced.

The sample s75_255x (Figure 8.22) is another case where the chip was damaged during synthesis and the solution was not properly heated. Similar to previous cases, only MSCs are found in this sample. At a slower flow rate of 70 µL/min, the sample s70_255 (Figure 8.21) shows a small band absorption peak contributing to the main peak at 456 nm, however the cluster absorption is still the largest contributor to the PL spectrum.

In the PL/PLE spectra for sample s65_255 (Figure 8.20 and Figure 11.39), two major observations can be made. First, the main PL peak at 478 – 481 nm is significantly stronger than the peak at 405 nm and 435 nm, and secondly, the band edge absorption peak at the emission wavelengths between 452 nm and 472 nm are larger than the peaks associated with cluster absorption. This confirms that the 478-481 nm peak is indeed due to quantum dot formation. Emission at higher wavelengths appears to be largely due to cluster absorption.

The spectra of s37_134x (Figure 8.19) shows similar results, with a prominent band edge absorption peak in the PLE spectra associated with the main PL peak at 462 nm. In this case, larger quantum dots also appear to be present, contributing to emission at higher wavelengths. Due to chip damage, however, the sample does not follow the overall trend.

Finally, with sample s24_120 (Figure 8.18), it can be seen that the weak PL peaks at 402 nm and 426 nm are due to cluster absorption peaks at 355 nm, 373 nm, and 394 nm. These clusters still contribute to the PL at higher wavelengths, but the presence of the band absorption peak at the major PL peak at 499 nm is evident. There do not seem to be any quantum dots contributing to the emission at higher wavelengths in this case.

The batch synthesis performed using Mix571 shows it resulted in quantum dots at a lower temperature of 190 °C. This, coupled with the fact that it had a significantly higher absorbance than the other mixtures (resulting in more of the laser's energy being converted to heat) are likely reasons why the microfluidic synthesis using this mixture was much more successful.

8.5.4 Size selective precipitation

Size selective precipitation of the reaction products is possible by the gradual addition of the non-solvent and has been demonstrated in the earliest work in this area (Murray, et al., 1993). This would allow us to separate the larger quantum dots from the smaller MSCs. It was not done here due to time constraints and the fact that we wanted to analyse the entire product as the synthesis approach is the novelty of the work.

8.5.5 Effects of atmospheric oxygen and filtration on cadmium oleate synthesis

The cadmium oleate solutions used in mixtures 3.4.2 and 4.3.1 were prepared with 1 mL and 15 mL of ODE respectively. For the solutions used in mixtures 4.5.1 and 5.7.1, no ODE was used at all, and both mixtures show significantly higher absorbance at 405 nm. The ODE acts as a barrier to the oxygen in ambient air, negating the need for an inert atmosphere. While the oxidation does have an effect on

the precursor formed, as demonstrated, it is still possible to use it to produce quantum dots. However, the nucleation and growth temperatures were found to be different compared to the standard procedure. In the case of Mix571, the Se solution was filtered while warm after it was synthesised. When allowed to cool, this purified solution showed different settling behaviour compared to the other Se solutions. Cloudy precipitates were found suspended in the solvent in this case, while in other solutions, the SeO_2 precipitated as white flakes at the bottom of the vial. When using this mixture for batch synthesis, highly fluorescent particles were obtained at a much lower temperature of 190 °C, compared to 240 °C, the temperature that this synthesis is usually performed at. Similarly, Mix461 showed a colour change at 210 °C. If good quality quantum dots can be produced at lower temperatures, this may be an effect worth investigating.

8.6 Conclusion

The experimental setup initially put together to produce iron oxide nanoparticles was adapted to allow heating using a 405 nm violet laser. This was done because the CdSe reaction mixtures have a very low absorbance at 650 nm (the wavelength of the old laser). An LCD display and buttons to control the laser power were added to allow synthesis at slower flow rates without overheating the chip.

Batch synthesis was performed using three different mixtures. The first mixture (Mix111) followed the same procedure as in the literature, and results were as expected, with quantum dots showing strong fluorescence at 559 nm (FWHM: 36 nm). The second mixture (Mix461) was prepared at a higher concentration. Additionally, the cadmium oleate was prepared without any solvent (ODE), which may have resulted in oxidation of the oleate groups. This sample showed a colour change at a lower temperature of 210 °C, however, quantum dots produced at 240 °C appeared to be as expected, showing fluorescence at 600 nm (FWHM: 41 nm). Finally, Mix571 was heated up to 240 °C with aliquots being withdrawn at various points. his mixture was similar to Mix461 with the exception of the Se solution being filtered (this did affect the precipitation behaviour of the Se solution). This mixture saw a colour change at an even lower temperature (~184 °C). An aliquot drawn 1 minute after reaching 190 °C contained quantum dots that strongly fluoresced at 518 nm (FWHM: 39 nm). At higher temperatures, the product exhibited wide band fluorescence.

Microfluidic synthesis using Mix342 and Mix431 resulted largely in CdSe MSCs with a relatively small amount of quantum dots. However, using Mix571, some of the products consisted mainly of quantum dots. Of these, the best results were: sample s24_120 with a fluorescence peak at 499 nm (FWHM: 39 nm), sample s65_255 at 485 nm (FWHM: 44 nm), and sample s37_134x at 462 nm (FWHM: 59 nm).

These results are fairly close to those published by Moghaddam et al (25-30 nm) (Mirhosseini Moghaddam, et al., 2013).

Considering the limitations of the setup, and the fact that we expected a broad range of sizes, these results are quite good and the possibility of a narrower size distribution with an improved approach seems high. These possible improvements are discussed in the future works section.

9 Conclusions

The work presented in this thesis aims to bring together the advantages of microfluidics and laser synthesis to the production of iron oxide nanoparticles via thermal decomposition synthesis. There has been only one paper on the thermal decomposition synthesis of iron oxide nanoparticles by laser heating, and none so far that use a continuous wave laser for nanoparticle synthesis. Rather than large-scale production, which can easily be implemented through parallelisation, the aim of this work is to develop a flexible nanoparticle synthesis system, capable of quickly producing a required amount of nanoparticles on-demand. Another possible application is the study of nanocrystal and cluster growth kinetics. The use of a laser for localised heating allows for quick changes in temperature and enables the use of acrylic as the material for the microfluidic chip. In the future this can also be used to implement custom heating profiles with rapid temperature changes (analysis of the simulation results shows calculated average heating rates as high as 16,560 °C/min or 276 °C/s).

Batch synthesis of iron oxide nanoparticle was performed using both FeOOH and iron oleate as iron sources. The FeOOH synthesis route was deemed unsuitable for microfluidic synthesis due to repeatability and sedimentation issues. The particles synthesised using iron oleate were also found to have a narrower size distribution. The use of store-bought olive oil as a surfactant/solvent was also tested for both iron sources. While a combination of FeOOH and olive oil produced nanoparticles with a wide size distribution, the decomposition of iron oleate in olive resulted in highly polydisperse nanoparticles with a variety of shapes.

Preliminary microfluidic synthesis studies focused on stationary laser synthesis in aluminium and acrylic wells. The solution was poured into these wells and heated for different durations with the laser. In the aluminium well, near complete decomposition was achieved, however the solution was likely overheated, resulting in large particles with a variety of shapes. The acrylic wells were shallower, and while magnetic particles were observed, the yield was much lower and not always recoverable. A preliminary attempt was made at continuous flow synthesis using a simple straight channel. This resulted in nucleation with minimal, if any, nanoparticle growth. The shortcomings of this approach led to the development of the vertical flow chip design, wherein the solution flows upwards while under the laser, resulting in a heating period of several seconds instead of the few milliseconds in the straight channel.

While preliminary synthesis work provided mixed results, the vertical flow synthesis approach reliably produced iron oxide nanoparticles with particle sizes being controlled by the flow rate. Particles

produced from the N solution (with sodium oleate as the surfactant) with an average residence period of 2 s, showed the best results in this experiment with a mean diameter of 84.7±46.8 nm. The particle size distributions are significantly wider than those obtained in batch synthesis. This is due to the parabolic flow profile, as well as the size difference between the reaction chamber diameter and the laser beam, which results in uneven, incomplete heating and thus, uneven decomposition. The residual by-products from this uneven decomposition have been an issue in the characterisation of all samples, but especially so when using the O solution (using oleic acid as the surfactant), which have the highest concentration of oleic acid. The particles obtained in this case are also several times larger than those from the batch synthesis, with mean diameters as high as 250 nm vs 8.3 nm in the batch synthesis run. This is likely due to the increased availability of monomers from cooler regions of lower growth.

A COMSOL simulation was performed to develop a better understanding of the flow and temperature profiles within the channel. Results from this chapter include velocity profiles, temperature profiles in the fluid and acrylic, and stress concentrations developed in the acrylic body due to thermal expansion. The model is limited in complexity in a few areas: highly localised boiling/turbulence is not modelled and is unclear if it should be expected at all (it was not observed during the experiments). The decomposition of the iron oleate and the acrylic has also not been modelled. The flow and temperature results were used to generate multiple streamlines to give us a better understanding of the temperatures experienced by each individual stream of the solution. From this data, the average heating rate, nucleation and growth periods could be calculated. It also gives us an idea of the percentage of the solution that flows by without undergoing complete decomposition. This analysis suggests that at even the slowest flow rate, ~29% of the iron oleate solution does not even undergo nucleation, and only ~35% exceeds 320 °C, the minimum growth temperature observed in batch synthesis. A large percentage (~36%) undergoes nucleation, but no significant growth. The monomers from this part of the solution either form small particles or contribute to the growth of larger particles within nearby growth regions. This explains the large average particle size as well as the smaller particles seen in our experimental work.

The CdSe samples produced showed some of the best results obtained so far in this study. CdSe quantum dots were produced with fluorescence peaks between 464 nm – 499 nm with FWHM values as low as 39 nm could be produced, even with the limitations of the setup. In samples with a low amount of quantum dots, more CdSe clusters were found which emit over a broader range.

The work presented in this thesis successfully fulfils the objectives set out in the beginning:

1. A homogenous precursor solution (FeOleate in ODE) suitable for use in microfluidic reactors was chosen (Chapter 3). Other combinations (FeOOH in ODE, FeOOH in olive oil, and FeOleate in olive oil) were also tested, but had poor reproducibility and/or poor results.
2. A setup was developed (Section 5.1) and improved upon (Section 8.1.2) for the safe and controlled laser irradiation of the solution.
3. Design and fabrication of a microfluidic chip for thermal decomposition synthesis (Chapter 4). A novel microfluidic chip has been designed and fabricated to allow longer residence periods of the solution under the laser.
4. The synthesis conducted in the aluminium well (Chapter 5) was a proof of concept and opened the way for more work in later sections. Iron oxide nanoparticles and cadmium selenide quantum dots were synthesised by thermal decomposition in a microfluidic chip. (Chapter 6 and 8). While many of the results from Chapter 5 could not be recovered, the products obtained in Chapter 6 and 8 were successfully characterised. Most work in the literature use more expensive pulsed lasers, however this work shows that inexpensive continuous flow lasers may also be employed for nanoparticle synthesis with a controlled flow rate.
5. Model of the relationship between experimental parameters and the flow and temperature distributions (Chapter 7). The simulation conducted helps illustrate the temperature variations within the channel and helps explain the size distribution of the products in Chapter 6. The simulation was also used to help choose appropriate starting points for flow rate and laser power for CdSe quantum dot synthesis in the microfluidic chip.

While these objectives have been met, there is always room for improvement. Some of those possibilities are presented in the next section.

9.1 Future work

Due to safety, budgetary and time constraints, the setup used in the studies so far has been limited in certain ways. Possible improvements to the chip design, fabrication and synthesis approach are briefly described in this section.

9.1.1 Droplet-based or segmented flow

Droplet based flow, together with a collimated laser beam can greatly reduce the variation in residence periods, and thus narrow down the size distribution. The use of droplet-based flow may also open up possibilities for continuous synthesis in acrylic chips as the carrier fluid is not directly heated.

Kumar (Kumar, 2013) synthesised iron oxide nanoparticle in a droplet-based capillary reactor; droplets of the reaction solution (iron acetylacetonate and oleylamine in benzyl ether) were created in the carrier fluid (octadecene).

In the experiments in chapter 6, segmented flow using air bubbles was attempted, however it resulted in bubbling of the solution at the air-liquid interface which generated even more bubbles. For future work, segmented flow can be tried with heavier immiscible fluids.

The use of PFPE as a carrier fluid may also be considered, as demonstrated in the literature (Chan, 2006) (Nightingale, et al., 2011) (Nightingale, et al., 2013).

9.1.2 Alternate materials

Alternate materials for chip fabrication, such as glass, silicon, quartz, etc. were deemed too dangerous or too costly for prototype work can be used for continuous synthesis without requiring regular replacements. The diameter of the reaction chamber can also be matched to the laser beam without worrying about the material melting or decomposing.

9.1.3 Changes to the laser used

A more powerful laser with a collimated beam may be considered if a more heat resistant material is used for the chip. The acrylic chip can only be used because the beam is currently focused to the centre of the reaction zone, keeping the heat away from the acrylic surfaces. The use of a collimated beam also requires additional safety considerations.

9.1.4 Post-synthesis addition of surfactants

The results from the iron oleate B solution are also promising as they resulted in some of the lowest particle sizes and narrowest size distributions. However, as they use no surfactants, they suffer from quick agglomeration and sedimentation. The simplest design modification for future work can be the addition of a channel and mixer to add room temperature oleic acid immediately after the reaction chamber in order to stabilise the freshly grown nanoparticles in the B solution. This may reduce the possible polymerisation of oleic acid seen in the O samples. This approach would only stabilise the particles after synthesis, i.e. it does not allow size and shape control using the surfactants.

9.1.5 Changes to the setup

Future work must focus on reducing the dead volume (unheated solution) in the reaction chamber. This can be achieved by reducing the diameter of the reaction chamber or increasing the diameter of the laser beam. The first option is possible using a smaller drill bit and adequate cooling. In the second option, a collimated beam can be used for more uniform heating. The use of a flat-top beam shaper can further improve the beam uniformity compared to a typical gaussian beam. This will, however, require an increase in laser output power which raises the laser safety requirements and may need major changes to the setup. In both cases, the walls of the channel will experience higher temperatures, making acrylic an unsuitable material for the chips.

9.1.6 Other improvements

On-chip separation of nanoparticles from the reaction solution is also a possibility to consider if agglomeration continues to be an issue, or if partial decomposition is being studied. This is made slightly easier in the case of iron oxide due to its magnetic nature.

Other possible improvements include:

- Separation of nucleation and growth sites using two different lasers, or a combination of laser and conventional heating, may be useful to study nanoparticle growth mechanisms.
- Integrated sensing and feedback for live characterisation and control of particle growth, including absorbance and PL measurement of the solution in situ as it is being heated.
- Using the laser to heat a suspended droplet using precise doses of energy, which may allow for precise study of nanoparticle growth kinetics.

10 References

Abou Hassan, A., Neveu, S., Dupuis, V. & Cabuil, V., 2012. Synthesis of cobalt ferrite nanoparticles in continuous-flow microreactors. *RSC Advances,* Volume 2, pp. 11263-11266.

Abou Hassan, A., Sandre, O., Cabuila, V. & Tabeling, P., 2008. Synthesis of iron oxide nanoparticles in a microfluidic device: preliminary results in a coaxial flow millichannel. *Chemical Communications,* pp. 1783-1785.

AbuTalib, N. H. et al., 2021. Shape controlled iron oxide nanoparticles: inducing branching and controlling particle crystallinity. *CrystEngComm,* Volume 23, pp. 550-561.

Alphandery, E., Francois, G. & Chebbi, I., 2012. Preparation of chains of magnetosomes, isolated from Magnetospirillum magneticum strain AMB-1 magnetotactic bacteria, yielding efficient treatment of tumors using magnetic hyperthermia. *International Journal of Pharmaceutics,* Volume 434, pp. 444-452.

Armijo, L. M. et al., 2012. Iron Oxide Nanocrystals for Magnetic Hyperthermia Applications. *Nanomaterials,* Volume 2, pp. 134-146.

Augustyn, C., Allston, T., Hailstone, R. K. & Reed, K. J., 2014. One-Vessel synthesis of iron oxide nanoparticles prepared in non-polar solvent. *RSC Advances,* Volume 4, pp. 5228-5235.

Baufay, L., Dispa, D. & Laude, L., 1982. Laser induced formation of CdTexSe1-x semiconducting compounds. *Journal of Crystal Growth,* 59(1-2), pp. 143-147.

Bau, J. A. et al., 2014. Nickel/Iron Oxide Nanocrystals with a Nonequilibrium Phase: Controlling Size, Shape, and Composition. *Chemical of Materials,* 26(16), pp. 4796-4804.

Bear, J. C. et al., 2014. A low cost synthesis method for functionalised iron oxide nanoparticles for magnetic hyperthermia from readily available materials. *Faraday Discuss,* Volume 175, pp. 83-95.

Bhalerao, G., Sinha, A., Srivastava, H. & Srivastava, A. K., 2009. Synthesis and studies of growth kinetics of monodispersed iron oxide nanoparticles using ferrocene as novel precursor. *Appl Phys A,* Volume 95, pp. 373-380.

Blanchard, M., Lazzeri, M., Mauri, F. & Balan, E., 2008. First-principles calculation of the infrared spectrum of hematite. *American Mineralogist,* 93(7), pp. 1019-1027.

Bronstein, L. et al., 2011. Nanoparticles by Decomposition of Long Chain Iron Carboxylates:From Spheres to Stars and Cubes. *Langmuir,* Volume 27, pp. 3044-3050.

Bronstein, L. M. et al., 2011. Nanoparticles by Decomposition of Long Chain Iron Carboxylates: From Spheres to Stars and Cubes. *Langmuir,* Volume 27, pp. 3044-3050.

Bronstein, L. M. et al., 2007. Influence of Iron Oleate Complex Structure on Iron Oxide Nanoparticle Formation. *Chemical Materials,* Volume 19, pp. 3624-3632.

Bronstein, L. M. et al., 2007. Influence of Iron Oleate Complex Structure on Iron Oxide Nanoparticle Formation. *Chem. Mater.,* Volume 19, pp. 3624-3632.

Bullen, C. et al., 2010. High Activity Phosphine-Free Selenium Precursor Solution for Semiconductor Nanocrystal Growth. *Chem. Mater.,* 22(14), pp. 4135-4143.

Calero-DdelC, V. L., Gonzalez, A. M. & Rinaldi, C., 2010. A Statistical Analysis to Control the Growth of Cobalt Ferrite Nanoparticles Synthesized by the Thermodecomposition Method. *Journal of Manufacturing Science and Engineering,* Volume 132.

Chalasani, R. & Vasudevan, S., 2011. Form, Content, and Magnetism in Iron Oxide Nanocrystals. *J. Phys. Chem. C,* Volume 115, pp. 18088 - 18093.

Chamritski, I. & Burns, G., 2005. Infrared- and Raman-Active Phonons of Magnetite, Maghemite, and Hematite: A Computer Simulation and Spectroscopic Study. *J. Phys. Chem. B,* Volume 108, pp. 4965-4968.

Chan, E.-Y., 2006. *(Thesis) Synthesis and Manipulation of Semiconductor Nanocrystals in Microfluidic Reactors,* s.l.: University of California, Berkeley.

Chan, E., Alivisatos, A. P. & Mathies, R. A., 2003. CONTROLLED GROWTH OF SEMICONDUCTOR NANOCRYSTALS IN MICROFLUIDIC REACTORS. *7th lnternational Conference on Miniaturized Chemical and Biochemlcal Analysts Systems.*

Chen, C.-J.et al., 2009. Preparation of Monodisperse Iron Oxide Nanoparticles via the Synthesis and Decomposition of Iron Fatty Acid Complexes. *Nanoscale Res Lett,* Volume 4, pp. 1343-1350.

Chen, C. et al., 2009. Preparation of Monodisperse Iron Oxide Nanoparticles via the Synthesis and Decompostion of Iron Fatty Acid Complexes. *Nanoscale Res Lett.,* 4(11), pp. 1343-1350.

Cheng, R. et al., 2020. Magnetothermal microfluidic-directed synthesis of quantum dots. *J. Mater. Chem. C,* Volume 8, pp. 6358-6363.

Chen, H. et al., 2014. Highly crystallized iron oxide nanoparticles as effective and biodegradable mediators for photothermal cancer therapy.. *Journal of Materials Chemistry B,* 2(7), p. 757.

Chen, Z., 2012. Size and Shape Controllable Synthesis of Monodisperse Iron Oxide Nanoparticles by Thermal Decomposition of Iron Oleate Complex. *Synthesis and Reactivity in Inorganic, Metal-Organin and Nano-Metal Chemistry,* Volume 42, pp. 1040-1046.

Chen, Z., 2014. Synthesis of monodisperse organic- and water-soluble iron oxide nanoparticles using Fe(OH)3 as precursor. *Journal of Experimental Nanoscience,* 9(4), pp. 406-414.

Chernyshova, I., Hochella, M. J. & Madden, A., 2007. Size-dependent structural transformations of hematite nanoparticles. 1. Phase transition. *Physical Chemistry Chemical Physics,* Volume 9, pp. 1736-1750.

Chiu, W. S. et al., 2007. One pot synthesis of monodisperse Fe3O4 nanocrystals by pyrolysis reaction of organometallic compound. *Materials Chemistry and Physics,* Volume 106, pp. 231-235.

COMSOL Inc., n.d. *Joule Heating of a Microactuator - Application ID: 8493.* [Online] Available at: https://www.comsol.com/model/joule-heating-of-a-microactuator-8493

Dai, C. et al., 2017. The Study of a Novel Nanoparticle Enhanced Wormlike Micellar System. *Nanoscale Research Letters,* p. 12:431.

Demin, A. et al., 2016. 3-Aminopropylsilane-modified iron oxide nanoparticles for contrast-enhanced magnetic resonance imaging of liver lesions induced by Opisthorchis felineus. *International Journal of Nanomedicine,* 2016(11), pp. 4451-4463.

Dhaene, E. et al., 2019. The Trouble with ODE: Polymerization during Nanocrystal Synthesis. *Nano Lett.,* Volume 19, pp. 7411-7417.

Ding, X., Bao, L., Jiang, J. & Gu, H., 2014. Colloidal synthesis of ultrathin gamma-Fe2O3 nanoplates. *RSC Advances,* Volume 4, p. 9314.

Dorniani, D. et al., 2013. Sustained release of prindopril erbumine from its chitosan-coated magnetic nanoparticles for biomedical applications. *Int. J Mol. Sci.,* 14(12), pp. 23639-23653.

Dreiss, C. A. & Feng, Y., 2017. *Wormlike Micelles: Advances in Systems, Characterisation and Applications.* s.l.:s.n.

Dreyer, A. et al., 2016. Organically linked iron oxide nanoparticle supercrystals with exceptional isotropic mechanical properties. *Nature Materials,* Volume 15.

Edel, J. et al., 2003. Controlled synthesis of compound semiconductor nanoparticles using microfluidic reactors. *12th International Conference on Solid State Sensors, Actuators and Microsystems.*

Erdem, E. et al., 2011. *Chemically robust, rapidly printed polyurethane microreactor for synthesis of monodisperse magnetic iron oxide nanoparticles.* Seattle, s.n.

Frenz, L. et al., 2008. Droplet-Based Microreactors for the Synthesis of Magnetic Iron Oxide Nanoparticles. *Angewandte Chemie International Edition,* 47(36), pp. 6817-6820.

Galli, M. et al., 2017. Superparamagnetic iron oxide nanoparticles functionalized by peptide nucleic acids. *RSC Advances,* Volume 7, pp. 15500-15512.

Gaur, U. L. S.-f., Wunderlich, B. & Wunderlich, B., 1982. Heat Capacity and Other Thermodynamic Properties of Linear Macromolecules VI. Acrylic Polymers. *J. Phys. Chem. Ref. Data,* 11(4).

Gavrila-Florescu, L. et al., 2017. Synthesis of Fe-based core@ZnO shell nanopowders by laser pyrolysis for biomedical applications. *Applied Physics A.*

Grimes, C. et al., 2000. Laser pyrolysis fabrication of ferromagnetic gamma-Fe4N and FeC nanoparticles. *Journal of Applied Physics,* 87(9).

Guidelli, E. J. et al., 2018. Mechanistic Insights and Controlled Synthesis of Radioluminescent ZnSe Quantum Dots Using a Microfluidic Reactor. *Chem. Mater.,* 30(23), pp. 8562-8570.

Harley, B., 2011. *Characterization of a PDMS Microfluidic Reactor for Synthesizing Quantum Dots,* San Luis Obispo: California Polytechnic State University.

Hasna, K. et al., 2013. Synthesis of chemically pure, luminescent Eu3+ doped HAp nanoparticles: a promising fluorescent probe for in vivo imaging applications. *Phys. Chem. Chem. Phys.,* Volume 15, p. 8106.

Hassinen, A. et al., 2012. Short-Chain Alcohols Strip X-type Ligands and Quench the Luminescence of PbSe and CdSe Quantum Dots, Acetonitrile Does Not. *J. Am. Chem. Soc.,* 134(51), pp. 20705-20712.

Henley, S., Mollah, S., Giusca, C. & Silva, S., 2009. Laser-induced self-assembly of iron oxide nanostructures with controllable dimensionality. *Journal of Applied Physics,* Volume 106.

Horoz, S. et al., 2012. CdSe quantum dots synthesized by laser ablation in water and their photovoltaic applications. *Applied Physics Letters,* Volume 101.

Hsieh, T.-E.et al., 2018. Unraveling the Structure of Magic-Size (CdSe)13 Cluster Pairs. *Chem. Mater.,* 30(15), pp. 5468-5477.

Hyeon, T. et al., 2001. Synthesis of highly crystalline and monodisperse maghemite nanocrystallites without a size-selection process. *Journal of the American Chemical Society,* Volume 123, pp. 12798-12801.

Ievlev, A. V. et al., 2014. Intermittency, quasiperiodicity and chaos in probe-induced ferroelectric domain switching. *Nature Physics,* Volume 10, pp. 59-66.

Ishikawa, T., Yan Cai, W. & Kandori, K., 1992. Characterization of the thermal decomposition products of δ-FeOOH by Fourier-transform infrared spectroscopy and N2 adsorption. *J. Chem. Soc. Faraday Trans.,* 88(8), pp. 1173-1177.

Ito, A., Shinkai, M., Honda, H. & Kobayashi, T., 2005. Medical Application of Functionalized Magnetic Nanoparticles. *Journal of Bioscience and Bioengineering,* 100(1), pp. 1-11.

Jeong, D.-W.et al., 2016. Fine Tuning of Colloidal CdSe Quantum Dot Photovoltaic Properties by Microfluidic Reactors. *Electrochimica Acta,* Volume 222, pp. 1668-1676.

Jubb, A. & Allen, H., 2010. Vibrational Spectroscopic Characterization of Hematite, Magnetite, and Magnenite Thin Films Produced by Vapor Deposition. *ACS Applied Minerals and Interfaces,* 2(10), pp. 2804-2812.

Kangning, R., Jianhua, Z. & Hongkai, W., 2013. Materials for Microfluidic Chip Fabrication. *Accounts of Chemical Research,* 46(11), pp. 2396-2406.

Kedarnath, G. et al., 2006. 2-(N,N-Dimethylamino)ethylselenolates of cadmium(II): Syntheses, structure of [Cd3(OAc)2(SeCH2CH2NMe2)4] and their use as single source precursors for the preparation of CdSe nanoparticles. *Polyhedron,* 25(12), pp. 2389-2391.

Kim, B. H. et al., 2011. Large-scale Synthesis of Uniform and Extremely Small-sized Iron Oxide Nanoparticles for High-Resolution T1 Magnetic Resonance Imaging Contrast Agents. *Journal of the Americal Chemical Society,* Volume 133, pp. 12624-12631.

Kim, B. et al., 2013. Sizing by Weighing: Characterizing Sizes of Ultrasmall-Sized Iron Oxide Nanocrystals Using MALDI-TOF Mass Spectrometry. *J. Am. Chem. Soc.,* 135(7), pp. 2407-2410.

Kovalenko, M. V. et al., 2007. Fatty Acid Salts as Stabilizers in Size- and Shape-Controlled Nanocrystal Synthesis: the Case of Iron Oxide. *Journal of the American Chemical Society,* pp. 6352-6353.

Krishnadasan, S., Yashina, A., deMello, A. & deMello, J., 2010. Microfluidic Reactors for Nanomaterial Synthesis. In: J. Schouten, ed. *Advances in Chemical Engineering (Volume 38).* s.l.:Elsevier, p. 195.

Krishna, K., Li, Y., Li, S. & Kumar, C., 2013. Lab-on-a-chip synthesis of inorganic nanomaterials and quantum dots for biomedical applications. *Advanced Drug Delivery Reviews,* Volume 65, pp. 1470-1495.

Kudera, S. et al., 2007. Sequential Growth of Magic-Size CdSe Nanocrystals. *Adv. Mater.,* Volume 19, pp. 548-552.

Kumar, K., 2013. *(Thesis) Microfluidic Synthesis of Superparamagnetic Iron Oxide Nanocrystals for Magnetic Resonance Imaging,* s.l.: Imperial College London.

Kumar, K. et al., 2012. Direct synthesis of dextran-coated superparamagnetic iron oxide nanoparticles in capillary-based droplet reactor. *J. Mater. Chem.,* Volume 22, p. 4704.

Kwak, C. H. et al., 2018. Droplet-Based Microfluidic Reactor for Synthesis of Size-Controlled CdSe Quantum Dots. *Journal of Nanoscience and Nanotechnology,* 18(2), p. 1339–1342.

Kwon, S. & Hyeon, T., 2011. Formation Mechanisms of Uniform Nanocrystals via Hot-Injection and Heat-Up Methods. *small,* 7(19), pp. 2685-2702.

Kwon, S. et al., 2007. Kinetics of Monodisperse Iron Oxide Nanocrystal Formation by "Heating-Up" Process. *J. Am. Chem. Soc.,* Volume 129, pp. 12571-12584.

Labidi, N. S. & Iddou, A., 2007. Adsorption of Oleic Acid on Quartz/Water Interface. *J. Saudi Chem. Soc.,* 11(2), pp. 221-234.

LaMer, V. & Dinegar, R., 1950. Theory, Production, and Mechanism of Formation of Monodispersed Hydrosols. *J. Am. Chem. Soc.,* 72(11), pp. 4847-4854.

Lassenberger, A. et al., 2017. Monodisperse Iron Oxide Nanoparticles by Thermal Decomposition: Elucidating Particle Formation by Second-Resolved in Situ Small-Angle X-ray Scattering. *Chemistry of Materials,* Volume 29, pp. 4511-4522.

Laurent, S. et al., 2008. Magnetic Iron Oxide Nanoparticles: Synthesis, Stabilization, Vectorization, Physicochemical Characterisations and Biological Applications. *Chemical Reviews,* Volume 108, pp. 2064-2110.

Lee, J. N., Park, C. & Whitesides, G. M., 2003. Solvent Compatibility of Poly(dimethylsiloxane)-Based Microfluidic Devices. *Analytical Chemistry,* Volume 75, pp. 6544-6554.

Li, L. et al., 2020. Fragmentation of Magic-Size Cluster Precursor Compounds into Ultrasmall CdS Quantum Dots with Enhanced Particle Yield at Low Temperatures. *Angew. Chem. Int. Ed.,* Volume 59, p. 12013–12021.

Li, L. et al., 2019. Identifying Clusters and/or Small-Size Quantum Dots in Colloidal CdSe Ensembles with Optical Spectroscopy. *J. Phys. Chem. Lett.,* 10(20), pp. 6399-6408.

Limosani, F., Carcione, R. & Antolinia, F., 2020. Formation of CdSe quantum dots from single source precursor obtained by thermal and laser treatment. *J. Vac. Sci. Technol. B,* Volume 38.

Lin, Y.-W., Hsieh, M.-M., Liu, C.-P. & Chang, H.-T., 2005. Photoassisted Synthesis of CdSe and Core-Shell CdSe/CdS Quantum Dots. *Langmuir,* Volume 21, pp. 728-734.

Lin, Z., 1996. Branched Worm-like Micelles and Their Networks. *Langmuir,* Volume 12, pp. 1729-1737.

Li, Y., Church, J. & Woodhead, A., 2012. Infrared and Raman spectroscopic studies on iron oxide magnetic nano-particles and their surface modifications. *Journal of Magnetism and Magnetic Materials,* Volume 324, pp. 1543-1550.

Lobato, N., Mansur, M. & Ferreira, A., 2017. Characterization and Chemical Stability of Hydrophilic and Hydropobic Magnetic Nanoparticles. *Materials Rsearch,* 20(3), pp. 736-746.

Luan, W., Yang, H., Fan, N. & Tu, S.-T., 2008. Synthesis of Efficiently Green Luminescent CdSe/ZnS Nanocrystals Via Microfluidic Reaction. *Nanoscale Research,* 3(4), pp. 134-139.

Luan, W., Yang, H., Tu, S. & Wang, Z., 2007. Open-to-air synthesis of monodisperse CdSe nanocrystals via microfluidic reaction andits kinetics. *Nanotechnology,* 18(17).

Lu, A.-H., Salabas, E. L. & Schuth, F., 2007. Magnetic Nanoparticles: Synthesis, Protection, Functionalization, and Application. *Angewandte Chemie International Edition,* Volume 46, pp. 1222-1244.

Luo, X. et al., 2018. Laser-ablated vortex fluidic-mediated synthesis of superparamagnetic magnetite nanoparticles in water under flow. *ACS Omega,* Volume 3, pp. 11172-11178.

Lu, Y. & Miller, J. D., 2002. Carboxyl Stretching Vibrations of Spontaneously Adsorbed and LB-Transferred Calcium Carboxylates as Determined by FTIR Internal Reflection Spectroscopy. *Journal of Colloid and Interface Science,* Issue 256, pp. 41-52.

Lynch, J. et al., 2011. Gas-Bubble Effects on the Formation of Colloidal Iron Oxide Nanocrystals. *J. Am. Chem. Soc.,* 133(32), pp. 12664-12674.

Malhotra, S. L., Minh, L. & Blanchard, L. P., 1982. Thermal Decomposition and Glass Transition Temperature of Poly(methyl Methacrylate) and Poly(isobutyl Methacrylate). *Journal of Macromolecular Science: Part A - Chemistry: Pure and Applied Chemistry,* 19(4), pp. 579-600.

Malumbres, A. et al., 2013. Continuous production of iron-based nanocrystals by laser pyrolysis. Effect of operating variables on size, composition and magnetic response. *Nanotechnology,* Volume 24.

Marcu, A. et al., 2013. Magnetic iron oxide nanoparticles as drug delivery system in breast cancer. *Applied Surface Science,* Volume 281, pp. 60-65.

Mather, J., 2020. Spectral and XYZ Color Functions. *MATLAB Central File Exchange.*

Mirhosseini Moghaddam, M. et al., 2013. Continuous-Flow Synthesis of CdSe Quantum Dots: A Size-Tunable and Scalable Approach. *Chem. Eur. J.,* Volume 19, pp. 11629-11636.

Misuk, V. et al., 2015. Segmented Flow-Based Multistep Synthesis of Cadmium Selenide Quantum Dots with Narrow Particle Size Distribution. *Chem. Eng. Technol.,* 38(7), pp. 1150-1153.

Moghaddam, M. et al., 2013. Continuous-flow synthesis of CdSe quantum dots: A size-tunable and scalable approach. *Chem. Eur. J.,* 19(35).

Mornet, S. et al., 2006. Magnetic nanoparticle design for medical applications. *Progress in Solid State Chemistry,* Volume 34, pp. 237-247.

Murray, C. B., Norris, D. J. & Bawendi, M. G., 1993. Synthesis and Characterization of Nearly Monodisperse CdE (E=S,Se,Te) Semiconductor Nanocrystallites. *J. Am. Chem. Soc.,* Volume 115, pp. 8706-8715.

Nakamura, H. et al., 2004. Application of a microfluidic reaction system for CdSe nanocrystal preparation: their growth kinetics and photoluminescence analysis. *Lab on a Chip,* 4(3).

Namduri, H. & Nasrazadani, S., 2007. Quantitative analysis of iron oxide using Fourier transform infrared spectrophotometry. *Corrosion Science,* Volume 50, pp. 2493-2497.

Nasrazadani, S. & Raman, A., 1993. The application of infrared spectroscopy to the study of rust systems—II. Study of cation deficiency in magnetite (Fe3O4) produced during its transformation to maghemite (γ-Fe2O3) and hematite (α-Fe2O3). *Corrosion Science,* 34(8), pp. 1355-1365.

Nightingale, A. M. et al., 2013. Large-scale synthesis of nanocrystals in a multichanneldroplet reactor. *Journal of Materials Chemistry A,* 1(12), pp. 4067-4076.

Nightingale, A. M. et al., 2011. A stable droplet reactor for high temperature nanocrystal synthesis. *Lab on a chip,* Issue 7.

Odio, O. et al., 2014. Sorption of Gold by Naked and Thiol-Capped Magnetite Nanoparticles: An XPS Approach. *J. Phys. Chem. C,* 5(2276-2791), p. 115.

Ogilvie, I. et al., 2010. *Solvent processing of PMMA and COC chips for bonding devices with optical quality surfaces.* Groningen, s.n.

Okamoto, T. et al., 2018. Synthesis of Bare Iron Nanoparticles from Ferrocene Hexane Solution by Femtosecond Laser Pulses. *ChemPhysChem.*

Osman, M. & Suter, U., 2002. Surface Treatment of Calcite with Fatty Acids: Structure and Properties of the Organic Monolayer. *Chem. Mater.,* 14(10), pp. 4408-4415.

Palchoudhury, S. et al., 2012. Chontrolled synthesis of iron oxide nanoplates and nanoflowers. *Chemical Communications,* Volume 48, pp. 10499-10501.

Park, J. et al., 2004. Ultra-large-scale syntheses of monodisperse nanocrystals. *Nature Materials.*

Park, J. et al., 2005. One-Nanometer-Scale Size-Controlled Synthesis of Monodisperse Magnetic Iron Oxide Nanoparticles. *Angewandte Chemie International Edition,* 44(19), pp. 2872-2877.

Patel, D. et al., 2008. Poly(D,L-lactide-co-glycolide) coated superparamagnetic iron oxide nanoparticles - Synthesis, characterization and in vivo study as MRI contrast agent. *Colloids and Surfaces A: Physicochemical Engineering Aspects,* pp. 91-94.

Patsula, V. et al., 2014. Monodisperse superparamagnetic nanoparticles by thermolysis of Fe(III) oleate and mandelate complexes. *Colloid and Polymer Science,* Volume 292, pp. 2097-2110.

Pei, W., Kakibe, S., Ohta, I. & Takahashi, M., 2005. Controlled Monodisperse Fe Nanoparticles Synthesised by Chemical Method. *IEEE Transactions on Magnetics,* 41(10).

Peng, X., Wickham, J. & Alivisatos, A., 1998. Kinetics of II-VI and III-V colloidal semiconductor nanocrystal growth: "Focusing" of size distributions. *J. Am. Chem. Soc.,* Volume 120, pp. 5343-5344.

Ptatschek, V. et al., 1998. Quantized Aggregation Phenomena in II-VI-Semiconductor Colloids. *Bunsengesellschaft Für Physikalische Chemie,* 102(1), pp. 85-95.

Qu, L., Yu, W. W. & Peng, X., 2004. In Situ Observation of the Nucleation and Growth of CdSe Nanocrystals. *Nano Letters,* 4(3), pp. 465-469.

Raghavan, S. R., 2009. Distinct Character of Surfactant Gels: A Smooth Progression from Micelles to Fibrillar Networks. *Langmuir,* 25(15), pp. 8382-8385.

Rahimi, S. et al., 2014. Iron oxide/hydroxide (a, g-FeOOH) nanoparticles as high potential adsorbents for lead removal from polluted aquatic media. *J. Ind. Eng. Chem..*

Rendon, J. L. & Serna, C. J., 1981. IR Spectra of Powder Hematite: Effects of Particle Size and Shape. *Clay Minerals,* Volume 16, pp. 375-381.

Ren, W. et al., 2014. Whole ceramic-like microreactors from inorganic polymers for high temperature and/or high pressure chemical synthesis. *Lab on a Chip,* 14(4), pp. 779-786.

Richard, C. et al., 2020. On-demand Milifluidic Synthesis of Quantum Dots in Digital Droplet Reactors. *Ind. Eng. Chem. Res.,* 59(9), pp. 3730-3735.

Robinson, I. et al., 2009. Synthesis of Co Nanoparticles by Pulsed Laser Irradiation of Cobalt Carbonyl in Organic Solution. *Journal of Physical Chemistry,* Volume 113, pp. 9497-9501.

Roonasi, P. & Holmgren, A., 2009. A Fourier transform infrared (FTIR) and thermogravimetric analysis (TGA) study of oleate adsorbed on magnetite nano-particle surface. *Applied Surface Science,* 255(11), pp. 5891-5895.

Rosson, T. E. et al., 2012. Bright White Light Emission from Ultrasmall Cadmium Selenide Nanocrystals. *J. Am. Chem. Soc.,* Volume 134, pp. 8006-8009.

Ruth, A. A. & Young, J. A., 2006. Generation of CdSe and CdTe nanoparticles by laser ablation in liquids. *Colloids and Surfaces A: Physiochem. Eng. Aspects,* Volume 279, pp. 121-127.

Salazar-Alvarez, G., Muhammed, M. & Zagorodni, A. A., 2006. Novel flow injection synthesis of iron oxide nanoparticles with narrow size distribution. *Chemical Engineering Science,* Issue 61, pp. 4625-4633.

Shakeri, B. & Meulenberg, R. W., 2015. A Closer Look into the Traditional Purification Process of CdSe Semiconductor Quantum Dots. *Langmuir,* 31(49), pp. 13433-13440.

Shao, H. et al., 2010. Magnetic Nanoparticles for biomedical NMR-based diagnostics. *Beilstein Journal of Nanotechnology,* Volume 1, pp. 142-152.

Sheng-Nan, S. et al., 2014. Magnetic iron oxide nanoparticles: Synthesis and surface coating techniques for biomedical applications. *Chin. Phys. B,* 23(3).

Shen, Y., Gee, M. Y. & Greytak, A. B., 2017. Purification technologies for colloidal nanocrystals. *Chem. Commun.,* Volume 53, pp. 827-841.

Shestopalov, I., Tice, J. D. & Ismagilov, R. F., 2004. Multi-step synthesis of nanoparticles performed on a millisecond time scale in a microfluidic droplet-based system. *Lab Chip,* Volume 4, pp. 316-321.

Si, H. et al., 2008. Controlled synthesis of different types of iron oxides nanocrystal in paraffin oil. *Journal of Colloid and Interface Science,* Volume 327, pp. 466-471.

Silva, C., Silva, L., Edwards, H. & de Oliveira, L., 2006. Diffuse reflection FTIR spectral database of dyes and pigments. *Anal Bioanal Chem,* Volume 386, pp. 2183-2191.

Siy, J. T., Brausera, E. M. & Bartl, M. H., 2011. Low-temperature synthesis of CdSe nanocrystal quantum dots. *Chem. Commun., 2011,* Volume 47, pp. 364-366 .

Song, N.-N.et al., 2013. Non-monotonic size change of monodisperse Fe3O4 nanoparticles in the scale-up synthesis. *Nanoscale,* Volume 5, pp. 2804-2810.

Sun, S. & Zeng, H., 2002. Size-controlled Synthesis of Magnetite Nanoparticles. *Journal of the American Chemical Society,* Volume 124, pp. 8204-8205.

Swinehart, D., 1962. The Beer-Lambert Law. *Journal of Chemical Education,* 39(7), pp. 333-335.

Tangeysh, B. et al., 2013. Gold Nanoparticle Synthesis Using Spatially and Temporally Shaped Femtosecond Laser Pulses: Post-Irradiation Auto-Reduction of Aqueous [AuCl4]−. *J. Phys. Chem. C,* Volume 117, pp. 18719-18727.

Teng, X. & Yang, H., 2004. Effects of surfactants and synthetic conditions on the sizes and self-assembly of monodisperse iron oxide nanoparticles. *Journal of Materials Chemistry,* Volume 14, pp. 774-779.

Tian, Z.-H.et al., 2018. Morphology Control of CdSe Nanoparticles via Two-Step Segmented Microreactors. *Cryst. Growth Des.,* 18(7), pp. 3953-3958.

Tian, Z.-H., Xu, J.-H., Wang, Y.-J. & Luo, G.-S., 2016. Microfluidic synthesis of monodispersed CdSe quantum dots nanocrystals by using mixed fatty amines as ligands. *Chem. Eng. J.,* Volume 285, pp. 20-26.

Tsao, C.-W. & DeVoe, D., 2009. Bonding of thermoplastic polymer microfluidics. *Microfluid Nanofluid,* Volume 6, pp. 1-16.

Unni, M. U. A. et al., 2017. Thermal Decomposition Synthesis of Iron Oxide Nanoparticles with Diminished Magnetic Dead Layer by Controlled Addition of Oxygen. *ACS Nano,* 11(2), pp. 2284-2303.

Wang, H. et al., 2004. Continuous synthesis of CdSe-ZnS composite nanoparticles in a microfluidic reactor. *Chem. Commun.,* pp. 48-49.

Wang, H. et al., 2005. Highly Luminescent CdSe/ZnS nanocrystals synthesized using a single-molecular ZnS source in a microfluidic reactor. *Adv. Func. Mater.,* 15(4).

Wang, H. et al., 2004. Synthesis of CdSe magic-sized nanocluster and its effect on nanocrystal preparation in a microfluidic reactor. *J. Mater. Res..,* 19(11).

Wang, J., Zhao, H., Zhu, Y. & Song, Y., 2017. Shape-Controlled Synthesis of CdSe Nanocrystals via a Programmed Microfluidic Process. *J. Phys. Chem. C,* 121(6), pp. 3567-3572.

Wetterskog, E. et al., 2014. Precise control over shape and size of iron oxide nanocrystals suitable for assembly into ordered particle arrays. *Science and Technology of Advanced Materials,* Volume 15.

Willis, A., Turro, N. & O'Brien, S., 2005. Spectroscopic Characterisation of the Surface of Iron Oxide Nanocrystals. *Chem. Mater.,* 17(24), pp. 5970-5975.

Woo, K. et al., 2004. Easy Synthesis and Magnetic Properties of Iron Oxide Nanoparticles. *Chemical Materials,* Volume 16, pp. 2814-2818.

Wu, W. et al., 2015. Recent progress on magnetic iron oxide nanoparticles: synthesis, surface functional strategies and biomedical applications. *Sci. Technol. Adv. Mater.,* Volume 16.

Xu, Z. et al., 2010. Organic phase synthesis of monodisperse iron oxide nanocrystals using iron chloride as precursor. *Nanoscale,* Volume 2, pp. 1027-1032.

Yaws, C. L., 2010. *Yaws' Thermophysical Properties of Chemicals and Hydrocarbons (Electronic Edition). Knovel..* s.l.:s.n.

Yaws, C. L., 2010. *Yaws' Transport Properties of Chemicals and Hydrocarbons (Electronic Edition). Knovel..* s.l.:s.n.

Yen, B. et al., 2005. A microfabricated gas-liquid segmented flow reactor for high-temperature synthesis: The case for CdSe quantum dots. *Microreactor fluidics,* Volume 117, pp. 5583-5587.

Yu, W. & Peng, X., 2002. Formation of High-Quality CdS and other I-VI Semiconductor Nanocrystals in Noncoordinating Solvents: Tunable Reactivity of Monomers. *Angew. Chem. Int. Ed.,* Volume 13, p. 41.

Yu, W. W., Falkner, J. C., Yavuz, C. T. & Colvin, V. L., 2004. Synthesis of monodisperse iron oxide nanocrystals by thermal decomposition of iron carboxylate salts. *Chemical Communications,* pp. 2306-2307.

Zamiri, R. et al., 2013. The effect of laser repetition rate on the LASiS synthesis of biocompatible silver nanoparticles in aqueous starch solution. *International Journal of Nanomedicine,* Volume 8, pp. 233-244.

Zhang, D., Gokce, B. & Barcikowski, S., 2017. Laser Synthesis and Processing of Colloids: Fundamentals and Applications. *Chemical Reviews,* Volume 117, pp. 3990-4103.

Zhang, J. et al., 2018. Individual Pathways in the Formation of Magic-Size Clusters and Conventional Quantum Dots. *J. Phys. Chem. Lett.,* 9(13), pp. 3660-3666.

Zholudov, Y. T., Sajti, C. L., Slipchenko, N. N. & Chichkov, B. N., 2015. Generation of fluorescent CdSe nanocrystals by short-pulse laser fragmentation. *J Nanopart Res,* Volume 17:490.

Zhu, X., Liu, G., Guo, Y. & Tian, Y., 2007. Study of PMMA thermal bonding. *Microsyst. Technol.,* Volume 13, pp. 403-407.

11 Appendix

11.1 FTIR analysis of iron oleate and iron oxides

IR spectra are formed by molecular vibrations caused by the energy of the absorbed light. The frequency of the vibration depends on the bond length and strength, which can be theoretically modelled as a vibrating spring system using Hooke's Law. This works well for simple molecules like linear hydrocarbons but grows in complexity when 3D molecules with multiple bonds are involved. The vibration frequency is also affected by surrounding conditions that affect the freedom of movement of the bond. While this may hamper IR analysis and identification, it may also offer useful clues about the material's interactions with other molecules around it.

Molecular vibrations are classified into two broad categories: stretching and bending. These vibrations can be symmetric or asymmetric, and bending vibrations can move out of the plane of reference, resulting in various fundamental vibration modes unique to a molecule. These vibrations can also combine in various ways leading to higher order symmetry and asymmetry; these details are based on Group Theory which is beyond the scope of this thesis.

11.1.1 Iron oleate

Carboxylate groups adsorbed onto the surface of metals show two characteristic bands at 1510-1650 cm^{-1} (asymmetrical) and 1280-1400 cm^{-1} (symmetrical) (Lu & Miller, 2002) (Bronstein, et al., 2007). The distance between the asymmetrical and symmetrical bands is known to be affected by the coordination state. Additionally, in the presence of multiple coordination modes, the asymmetrical band is known to split into a doublet; for example, as described by Lu and Miller (Lu & Miller, 2002), the 1550 cm^{-1} band in adsorbed calcium oleate splits into 2 bands, one at 1540 cm^{-1} and one at 1575 cm^{-1}. Multiple coordination modes are likely to appear at high concentrations of carboxylic acid relative to the surface area available for adsorption.

The band at 1711 cm^{-1} is typically assigned to the carbonyl bond (the C=O bond within the carboxylate group). While this band is quite strong in free oleic acid, it is much weaker in iron oleate as the carbonyl bond ceases to exist when the carboxylate group binds to the iron oxide. Bronstein et al (Bronstein, et al., 2007) were able to remove this excess oleic acid by washing the iron oleate with ethanol (Figure 11.1), which also had the added effect of changing the coordination mode to a single mode and resulted in the doublet converging to a single band at 1527 cm^{-1}.

The FTIR curve presented by Bronstein et al (Bronstein, et al., 2007) extended from 4000 to 1000 cm^{-1} and did not address peaks below 1414 cm^{-1}, as they are mostly within the molecular "fingerprinting region".

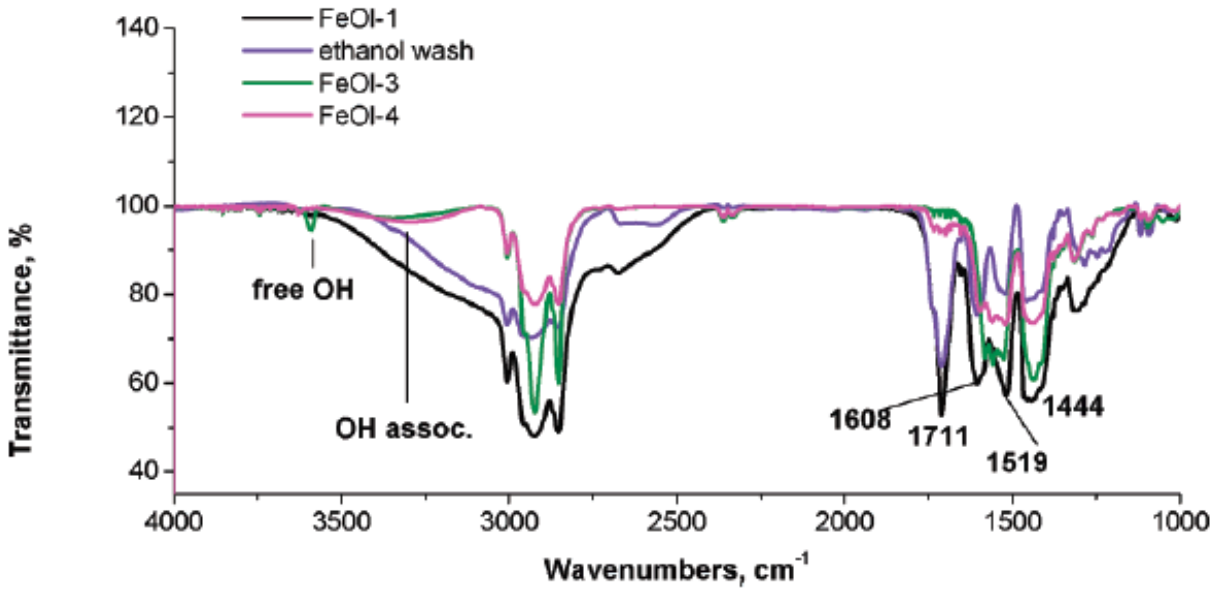


Figure 11.1: FTIR curves of iron oleate samples dried at 30 °C (FeOl-1), washed with ethanol and then dried at 30 °C (FeOl-3) and 70 °C (FeOl-4). Source: (Bronstein, et al., 2007)

11.1.2 Iron oxides

The FTIR spectra of common iron oxides typically show peaks within the 700-400 cm^{-1} region (and beyond, but that is out of range for typical FTIR instruments). Namduri and Nasrazadani (Namduri & Nasrazadani, 2007) measured the FTIR spectra of commercial iron oxide powders: magnetite (Fe_3O_4), maghemite (γ-Fe_2O_3) and hematite (α-Fe_2O_3). While hematite and maghemite show distinct peaks, magnetite samples can show broad bands in the same region. The IR peaks of iron oxides in this region are known to shift depending on temperature of formation and particle size and shape (Rendon & Serna, 1981) (Nasrazadani & Raman, 1993), all of which influence the lattice structure of the final product.

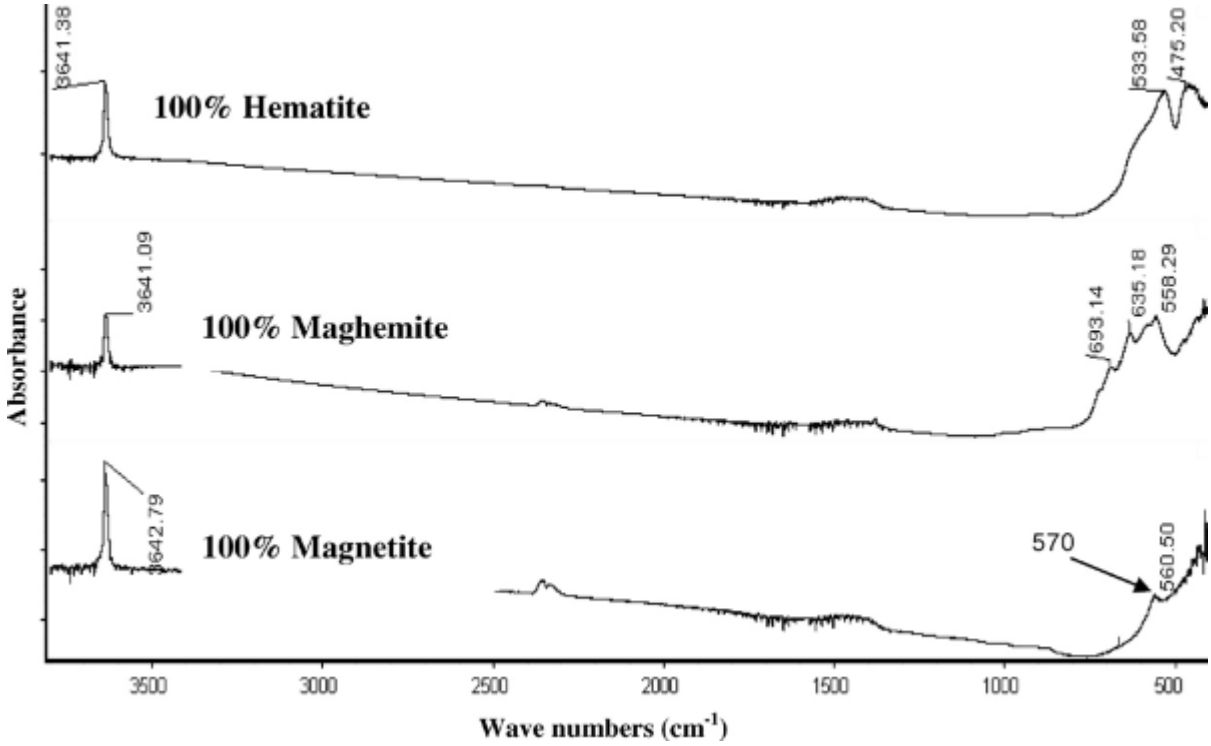


Figure 11.2: FTIR spectra of commercial powders of 100% hematite, maghemite and magnetite. The peak at 3642 cm^{-1} is from the CaO added for calibration. Source: (Namduri & Nasrazadani, 2007)

For comparison, a study by Li et al (Li, et al., 2012) (Figure 11.3) shows the transformation of magnetite nanoparticles to hematite, with maghemite as an intermediate. Here, the 572 cm^{-1} peak is distinct and much stronger compared to the commercial powder spectrum (Figure 11.2).

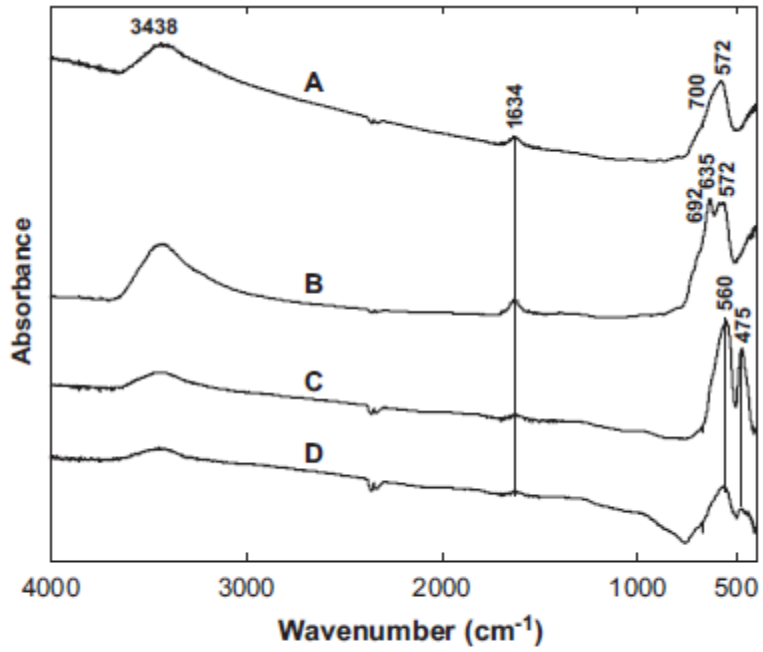


Fig. 5. FTIR spectra of Fe_3O_4 MNP after annealing at different temperatures: (A) 25 °C (vacuum dried); (B) 109 °C; (C) 500 °C; (D) 935 °C.

Figure 11.3: FTIR spectra of magnetite nanoparticles annealed at different temperatures. The conversion from magnetite (A) to maghemite (B) to hematite (C and D) can be clearly seen. Source: (Li, et al., 2012)

Magnetite

The magnetite spectra shown by Namduri and Narazadani (Figure 11.2) shows the 570 cm^{-1} peak almost covered up by the broader peak below 400 cm^{-1}. They have mentioned that the samples were commercially obtained powders, but they are likely not nanoparticles. A wide range of wavenumbers have been reported between 535 – 589 cm^{-1} (Demin, et al., 2016) (Dorniani, et al., 2013) (Odio, et al., 2014) (Lobato, et al., 2017) (Galli, et al., 2017) (Chernyshova, et al., 2007) (Chamritski & Burns, 2005) (Li, et al., 2012) for the second peak of magnetite nanoparticles. The first peak has also been shown to vary between 350 – 410 cm^{-1} (with Chamritski and Burns (Chamritski & Burns, 2005) giving a calculated value of 360 cm^{-1}) and varies in intensity relative to the second one. Like hematite, it may also be more sensitive to the particle size distribution, a high polydispersity causing broadening of the peak which would be more noticeable in commercial powders than in carefully prepared nanoparticles.

Maghemite

Maghemite shows a strong peak at 540-570 cm^{-1} and <400 cm^{-1} (Chernyshova, et al., 2007) (Jubb & Allen, 2010) (Li, et al., 2012) and a weak peak at 440-450 cm^{-1}, which may be hard to observe nanoparticles and thin films (Jubb & Allen, 2010). addition, weak sharp peaks can be seen at ~635 cm^{-1} and ~693 cm^{-1}, on the slope of the broad 560 cm^{-1} peak. These smaller peaks are characteristic of maghemite and are not observed in any of the other phases.

Hematite

Hematite shows strong peaks at 436-476 cm^{-1} and 526-534 cm^{-1} (Chernyshova, et al., 2007) (Chamritski & Burns, 2005) (Jubb & Allen, 2010) (Li, et al., 2012). The peak at 526-534 cm^{-1} is a combination of two vibrational modes (Jubb & Allen, 2010) and may show broadening when particle morphology is polydisperse (Blanchard, et al., 2008).

Calculated values

Table 11.1 shows calculated and observed values of the vibrational modes of iron oxides from two different sources. Chamritski and Burns (Chamritski & Burns, 2005) compare calculated values from their simulation to those found in literature, while Jubb and Allen (Jubb & Allen, 2010) compare calculated and observed values from literature to their observed values measured from 45 nm and 230 nm thin films. They also make a distinction between the transverse optical (TO) and longitudinal optical (LO) components of the vibrational modes in their study. The magnitude of the LO component is thought to be connected to an increase in crystallinity of the sample, and in the case of hematite causes broadening of the E_u peak at 436-459 cm^{-1}.

Table 11.1: Calculated and observed vibrational modes of hematite, maghemite and magnetite from the literature. Only values of peaks observable above 400 cm^{-1} are shown. Sources: (Chamritski & Burns, 2005), and (Jubb & Allen, 2010)

Phase	Source	Vibrational Mode	Peak #	Wavenumber	
				Calculated	Observed
Hematite (α-Fe_2O_3)	(Chamritski & Burns, 2005)	E_u	1	368	380-400
		A_{2u}	1	378	380-400
		E_u	2	454	440-470
	(Jubb & Allen, 2010)	A_{2u}	1	299 (TO), 414 (LO)	385
		A_{2u}	3	526 (TO), 662 (LO)	526
		E_u	2	437 (TO), 494 (LO)	436-459
		E_u	3	524 (TO), 662 (LO)	526
Maghemite (γ-Fe_2O_3)	(Chamritski & Burns, 2005)	$T_2(2)$	1	362	319
		$T_2(3)$	2	440	440
		$T_2(4)$	3	523	553
	(Jubb & Allen, 2010)	$T_{1u}(1)$	2	440 (TO), 453 (LO)	439 (230 nm)
		$T_{1u}(2)$	3	550 (TO), 572 (LO)	546 (45 nm), 547 (230 nm)
Magnetite (Fe_3O_4)	(Chamritski & Burns, 2005)	$T_{1u}(3)$	1	360	350
		$T_{1u}(4)$	2	491	560
		T_{1u}	2	558 (TO), 576 (LO)	560

Figure 11.4 shows the ranges of the peaks mentioned in Table 11.1 that have been found in the literature. Peak 1 is mostly out of the range of our instrument, but if the peak is seen at ~400-420 cm^{-1}, it may point to the presence of magnetite, however if just the slope is visible in the region, it may be from any of the three phases.

Peak 2 of hematite is one of its most distinct identifiers at ~475 cm^{-1}. Although maghemite has a peak in the same region, it is generally weak in the case of nanoparticles, and the only contribution of maghemite and magnetite in this region would be a slope.

Peaks 4 and 5 of maghemite are distinct and can be used for identification of the phase, while its other peaks may blend in with those from other phases.

In a mixed phase sample, the presence/quantity of magnetite may be difficult to determine because it doesn't have a prominent peak comparted to the other two phases.

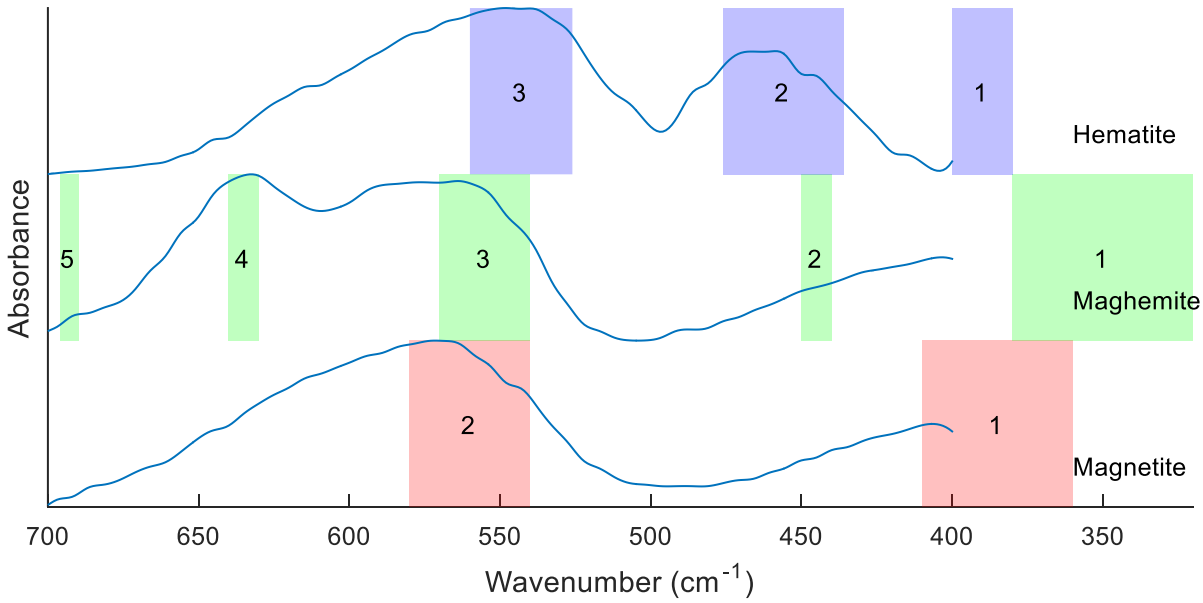


Figure 11.4: FTIR curves of hematite, maghemite and magnetite nanoparticles (from Li et al (Li, et al., 2012)) over laid with the peak range obtained from the literature. The ranges show where the tip of the peak may lie, and not its entire breadth.

11.2 FTIR analysis of solvents

11.2.1.1 ***1-Octadecene***

The FTIR spectrum of 1-octadecene is shown in Figure 11.5. As expected, the major peaks from CH_2 stretching at 2922 and 2853 cm^{-1} are present, along with the weaker peak at 1466 cm^{-1} from CH_2 and CH_3 bending. The medium peak at 909 cm^{-1} is assigned to bending of the $C{=}CH_2$ double bond. The peak at 1642 cm^{-1} is characteristic of the C=C double bond.

Other peaks can be seen in the fingerprinting region (400 – 1500 cm^{-1}). Since 1-octadecene is being used as a non-coordinating solvent, we will not go into greater detail here. The peaks in the fingerprinting region can be used to determine the amount, if any, of 1-octadecene in the final purified product.

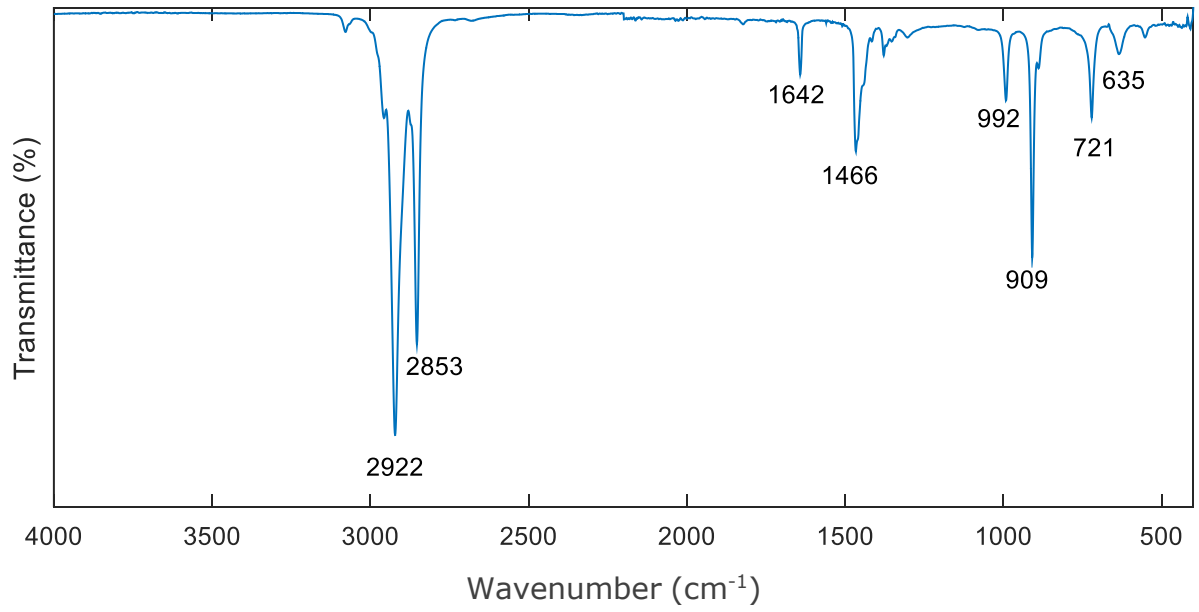


Figure 11.5: FTIR spectrum of 1-Octadecene.

11.2.1.2 ***Oleic acid***

The spectrum of oleic acid is shown in Figure 11.6, with the labelled bands explained in Table 11.2. In this case, we have a more detailed explanation as we expect the oleic acid to coordinate with the iron atoms when producing iron oleate, and later, with the iron oxide nanoparticles.

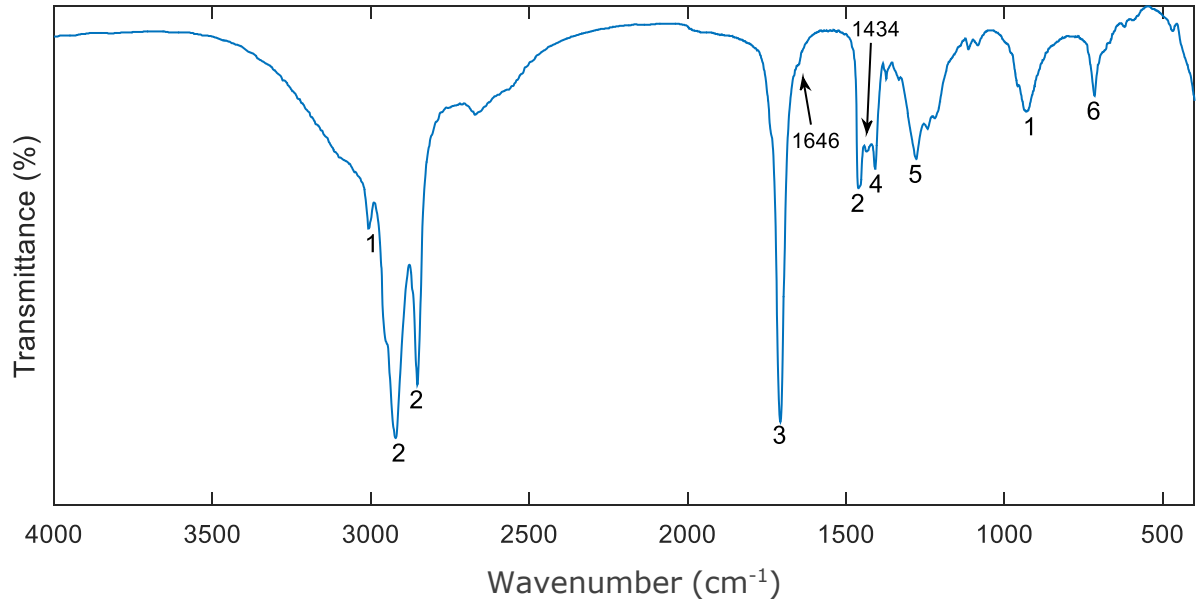


Figure 11.6: FTIR transmission spectrum of liquid oleic acid. Peaks are labelled according to the bond that causes them. More details in Table 11.2. Source: NIST

Table 11.2: Prominent FTIR bands seen in the FTIR spectrum of oleic acid

Peaks	Wavenumber	Shape and Strength	Assignment
1	3006 cm^{-1}	Broad, medium	O-H stretching
	930 cm^{-1}	Sharp, weak	O-H bending
2	2925 cm^{-1}	Sharp, strong	Asymmetric CH, CH_2 and CH3 stretching
	2854 cm^{-1}	Sharp, strong	Symmetric CH, CH_2 and CH3 stretching
	1460 cm^{-1}	Sharp, weak	CH_2, CH_3 bending
3	1706 cm^{-1}	Sharp, strong	C=O (carybonyl) stretching
4	1410 cm^{-1}	Sharp, weak	C-O-H bending
5	1280 cm^{-1}	Sharp, weak	C-O stretching
6	715 cm^{-1}	Sharp, weak	C-H bending

The oleic acid FTIR spectrum is as described by several authors in the literature (Labidi & Iddou, 2007) (Lu & Miller, 2002). The strongest peaks are seen at 2925 cm^{-1}, 2854 cm^{-1} and 1706 cm^{-1}.

1. There is a broad band from ~3500 to ~2600 cm^{-1}, peaking at 3006 cm^{-1}. This region is assigned to stretching of O-H bonds whose absorption frequencies vary due to intermolecular forces, resulting in a broader absorption band rather than a sharp strong band.
2. The peaks at 2925 cm^{-1} and 2854 cm^{-1} are from asymmetric and symmetric stretching vibrations from the CH_2 bonds throughout the molecule; since these bonds form the backbone of the molecule it is not surprising that the peaks are so strong. The stretching vibration peaks from CH and CH_3 bonds are also seen in the same region; in this case they have most likely been covered up by the stronger peaks from the more numerous CH_2 bonds. A weaker peak from bending vibrations of CH_2 groups can also be seen at 1460 cm^{-1}. The smaller peak (~1434 cm^{-1}) between peaks 2 and 4 is likely caused by bending within the single CH_3 group.
3. The peak at 1706 cm^{-1} is commonly associated with the C=O (carbonyl) bond in the carboxylic acid group and is known to be one of the stronger peaks seen in FTIR spectra. The C=C double bond peak at 1648 cm^{-1} is almost completely covered by the carbonyl peak.
4. The bending within the C-O-H group results in the peak at 1410 cm^{-1}.
5. A sharp, weak peak is seen at 1280 cm^{-1} caused by stretching in the C-O bond within the carboxyl functional group.
6. The C-H bonds bending vibrations result in the sharp peak at 715 cm^{-1}.

The oleic acid binds to the iron atoms in iron oleate, or to the surface of the iron oxide nanoparticles, through the carboxylate group COO-, therefore any changes in the FTIR spectrum are expected to be in the peaks associated with the carboxylate group: 3006 cm^{-1}, 1706 cm^{-1}, and 1410 cm^{-1}. The next section deals with the FTIR spectrum of our synthesised iron oleate.

11.3 SEM and STEM images of nanoparticles produced by microfluidic synthesis

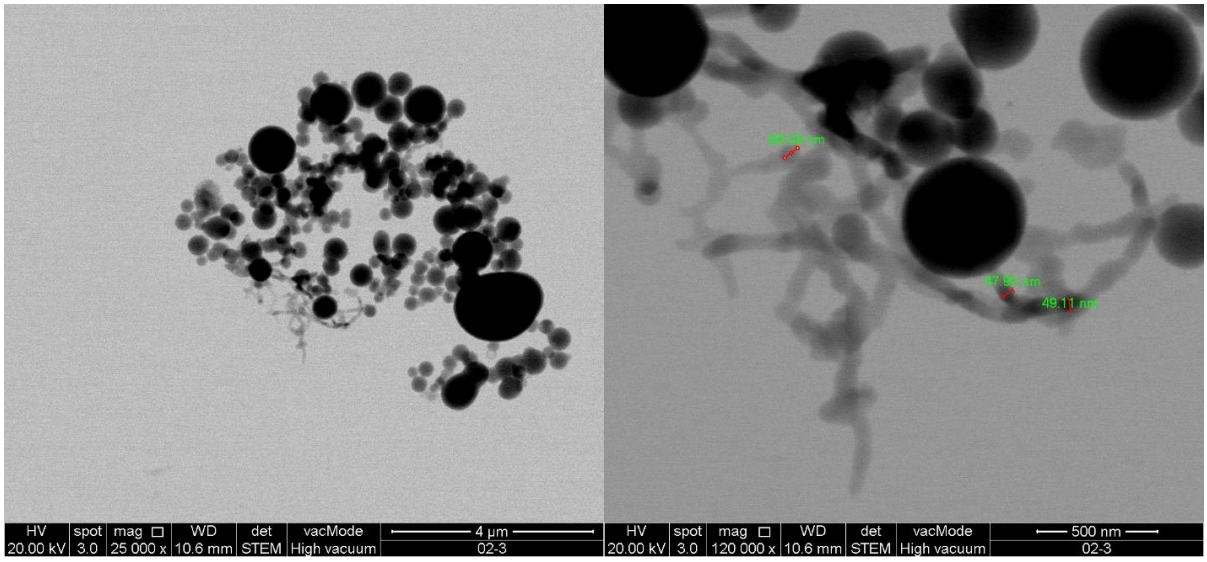


Figure 11.7: STEM images of purified sample O2-3, produced by microfluidic synthesis using the O solution with an average residence period of 2s.

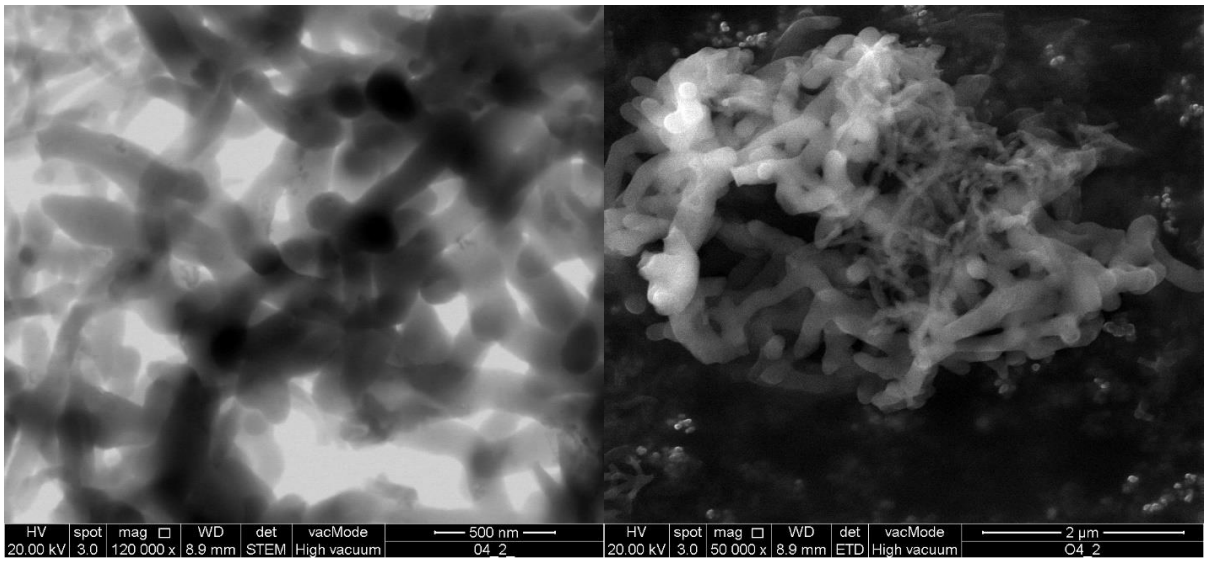


Figure 11.8: STEM and SEM images of sample O4-2 (bottom), produced by microfluidic synthesis using the O solution with an average residence period of 4s.

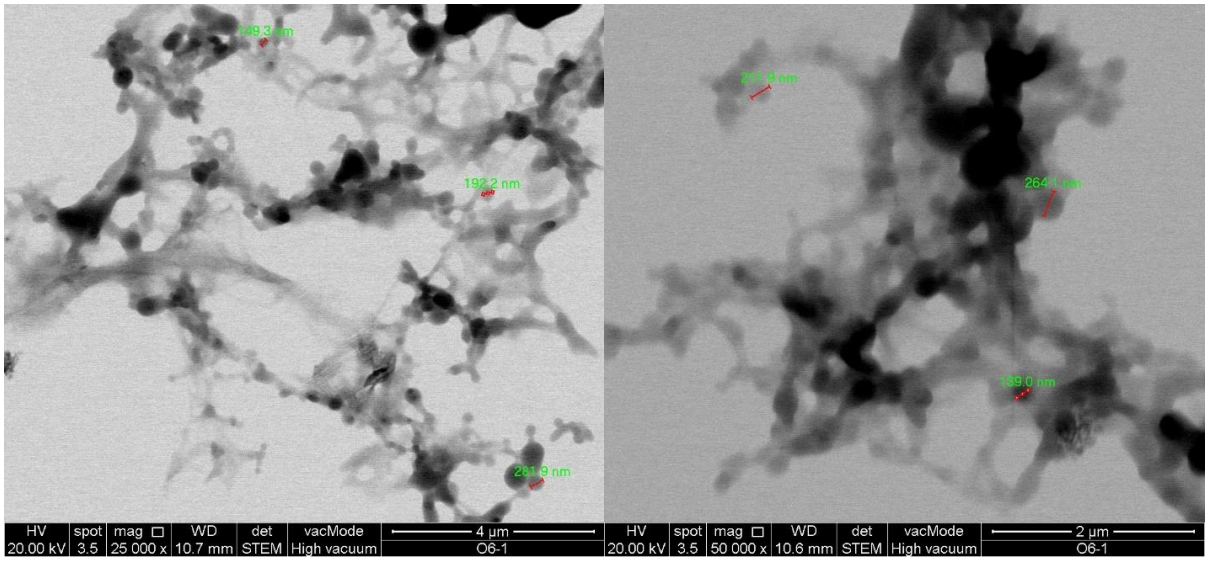


Figure 11.9: STEM images of sample O6-1, produced by microfluidic synthesis using the O solution with an average residence period of 6s. Denser iron oxide particles can be seen embedded in lighter organic networks.

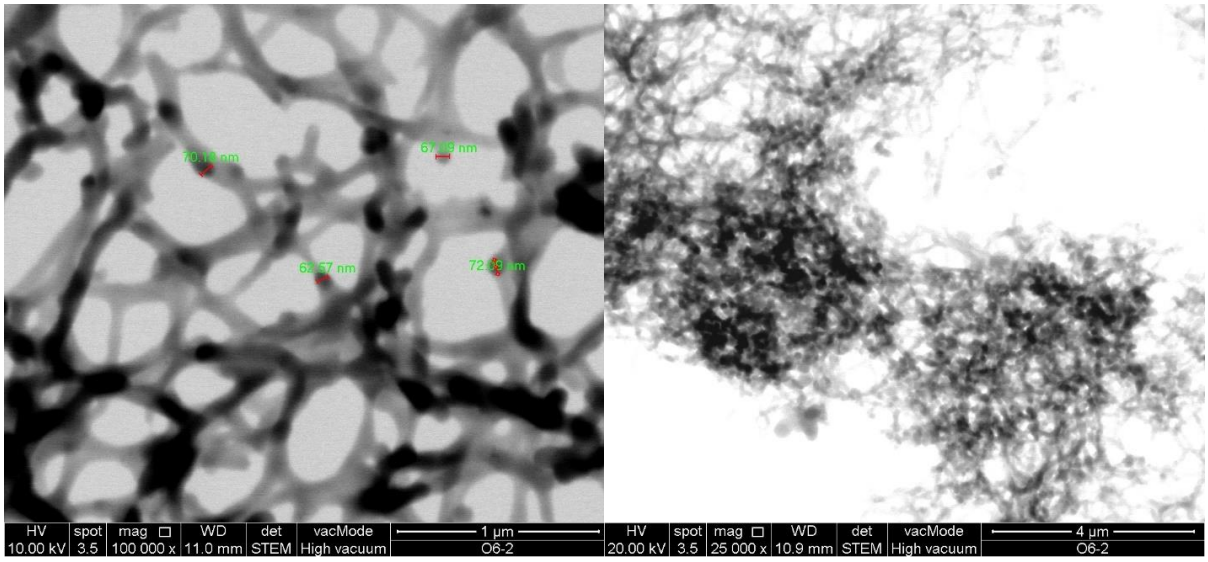


Figure 11.10: STEM images of sample O6-2, produced by microfluidic synthesis using the O solution with an average residence period of 6s.

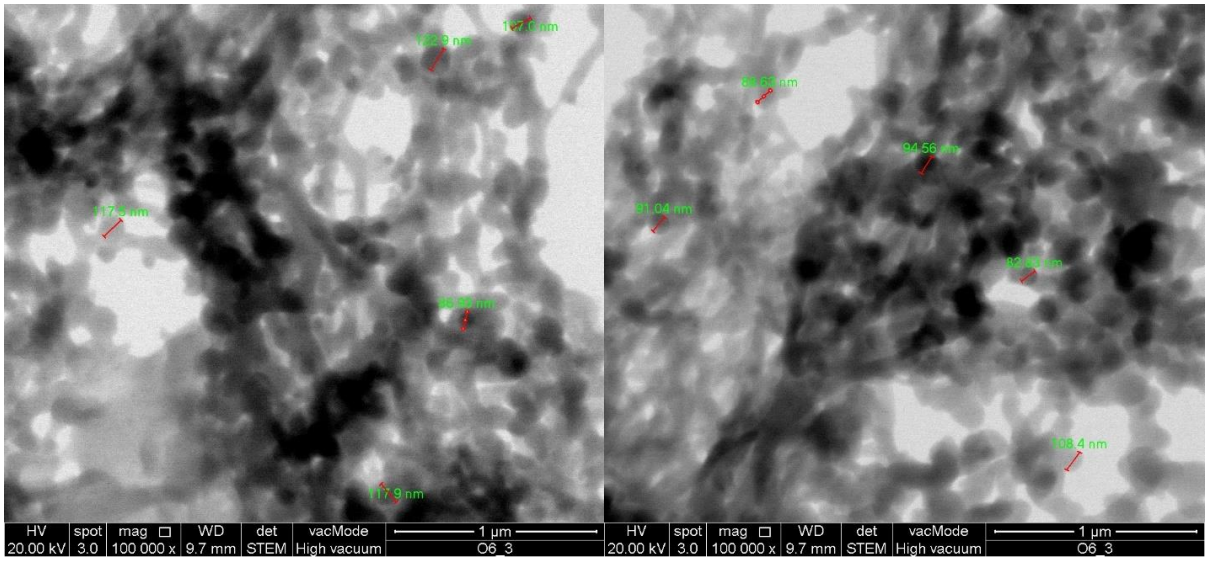


Figure 11.11: STEM images of sample O6-3, produced by microfluidic synthesis using the O solution with an average residence period of 6s.

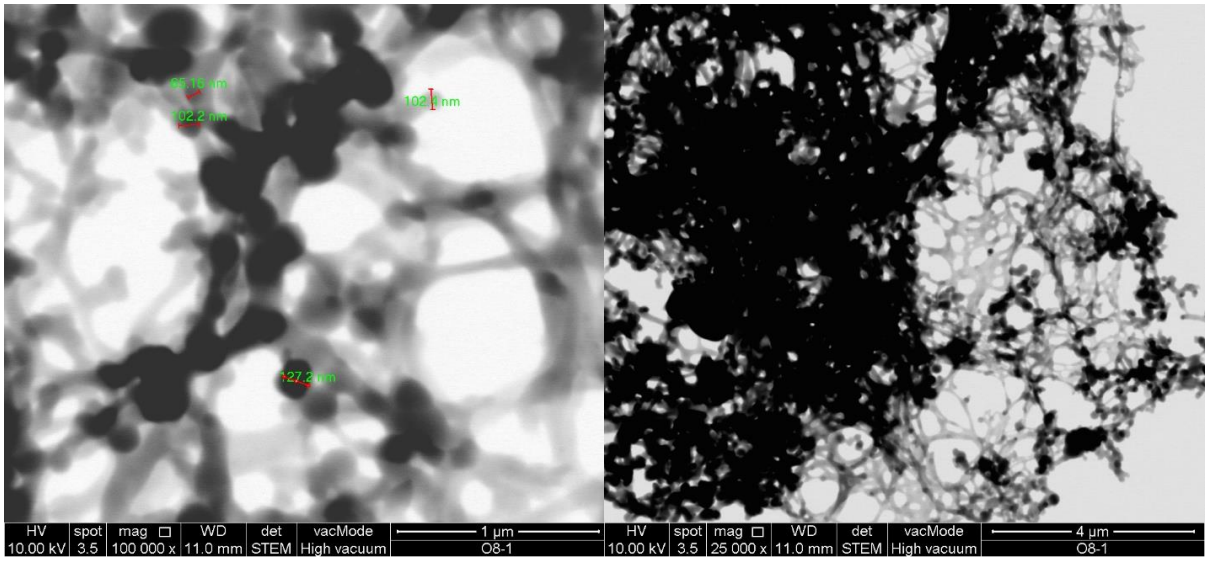


Figure 11.12: STEM images of sample O8-1, produced by microfluidic synthesis using the O solution with an average residence period of 8s.

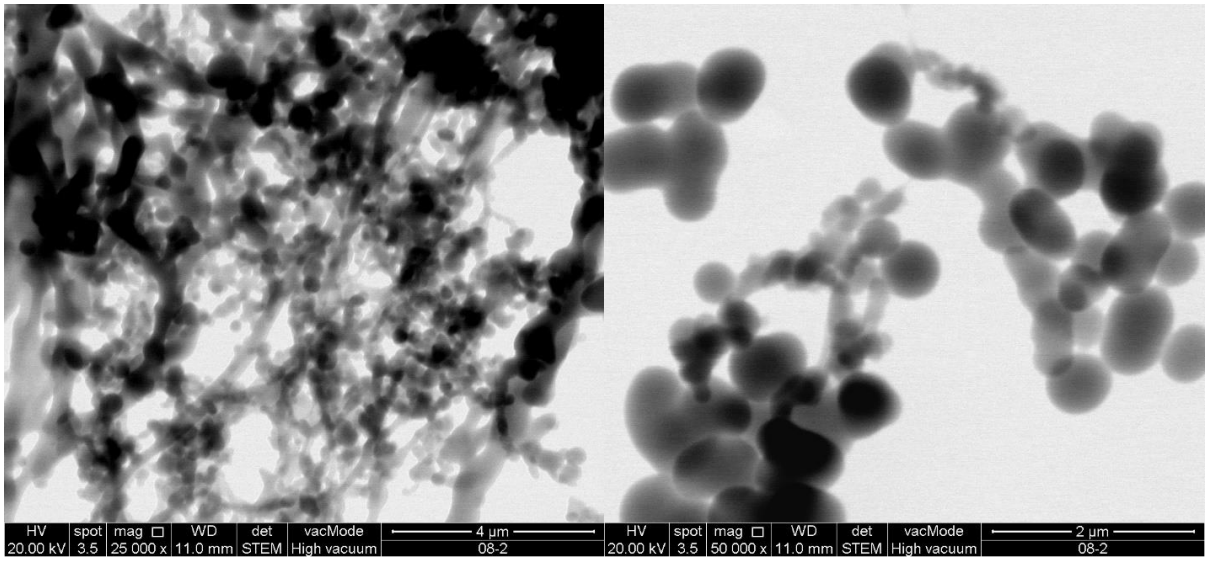


Figure 11.13: STEM images of sample O8-2, produced by microfluidic synthesis using the O solution with an average residence period of 8s.

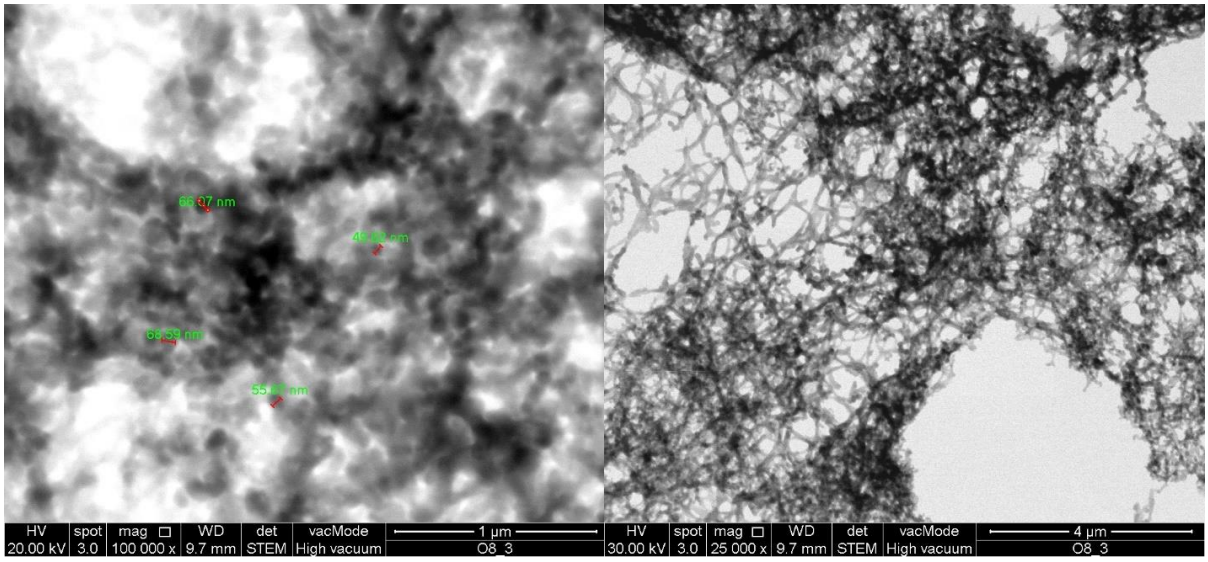


Figure 11.14: STEM images of sample O8-3, produced by microfluidic synthesis using the O solution with an average residence period of 8s.

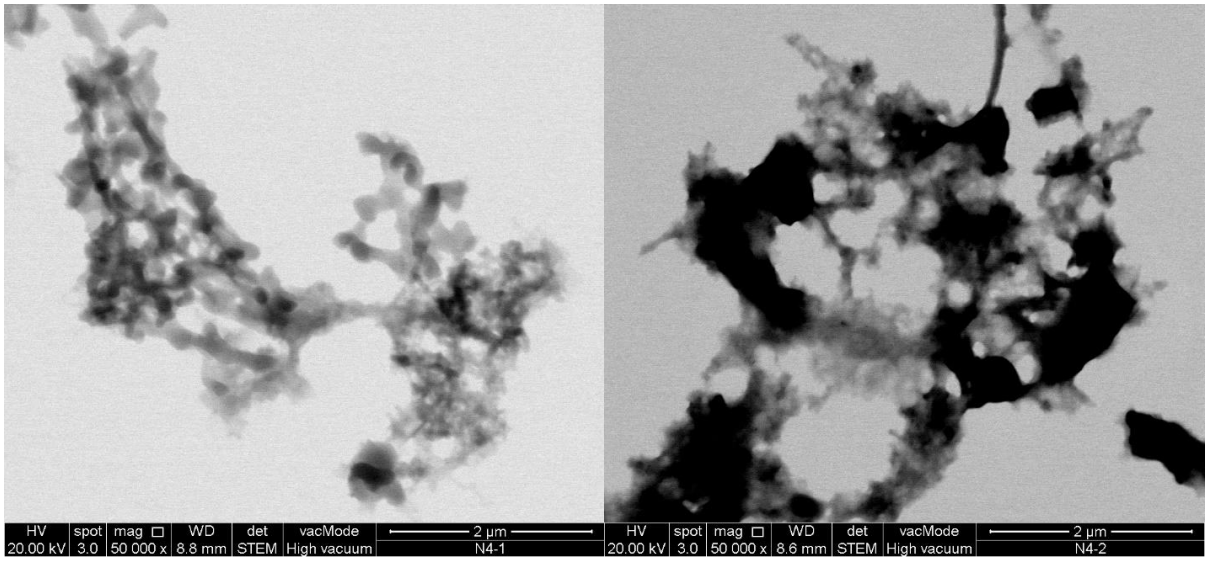


Figure 11.15: STEM images from samples N4-1 and N4-2, produced by microfluidic synthesis using the N solution with an average residence period of 4s.

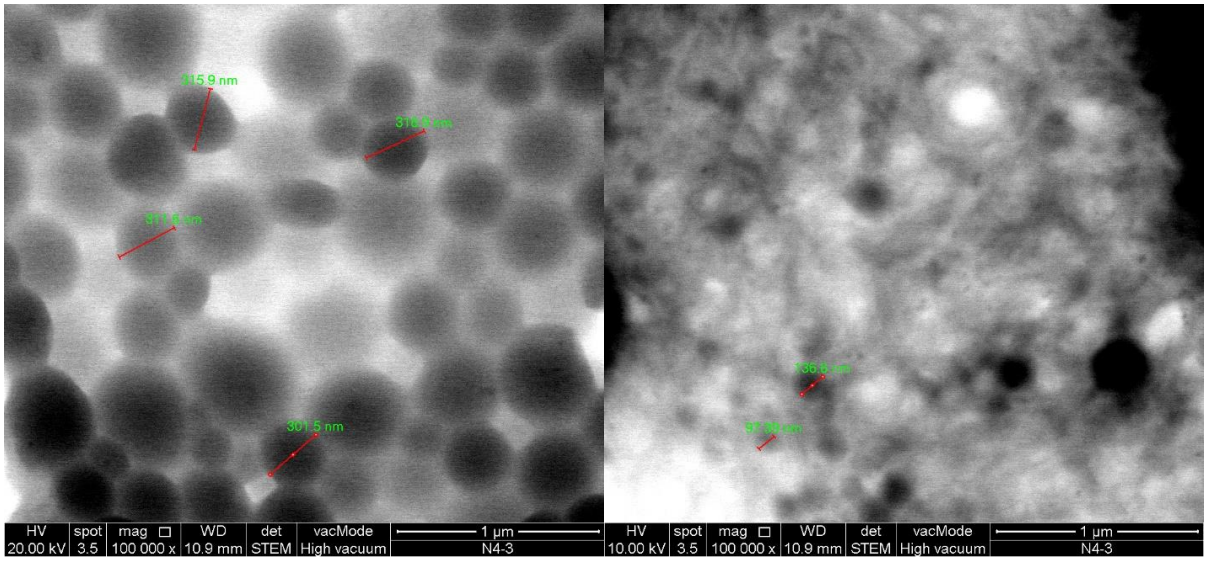


Figure 11.16: STEM images from sample N4-3, produced by microfluidic synthesis using the O solution with an average residence period of 4s.

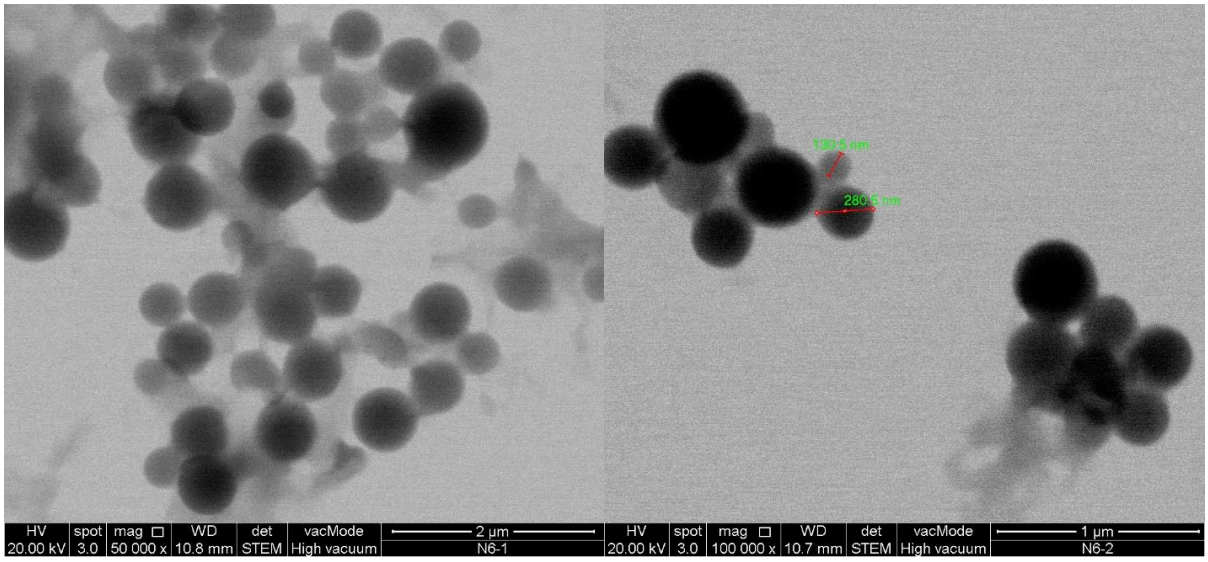


Figure 11.17: STEM images from sample N6-1 and N6-2, produced by microfluidic synthesis using the N solution with an average residence period of 6s.

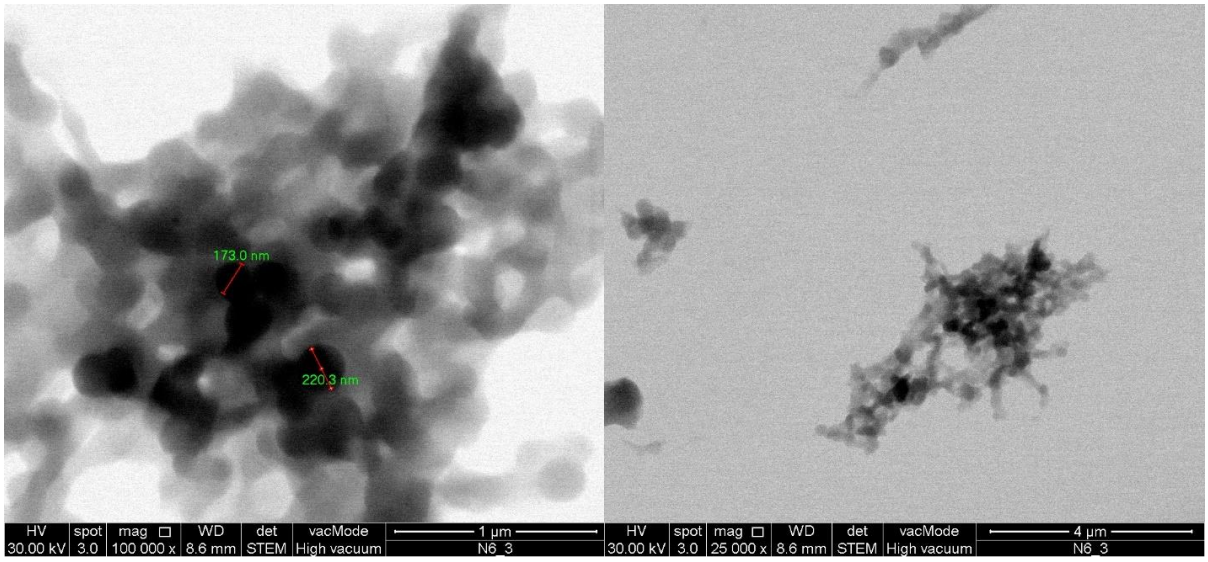


Figure 11.18: STEM images from sample N6-3, produced by microfluidic synthesis using the N solution with an average residence period of 6s.

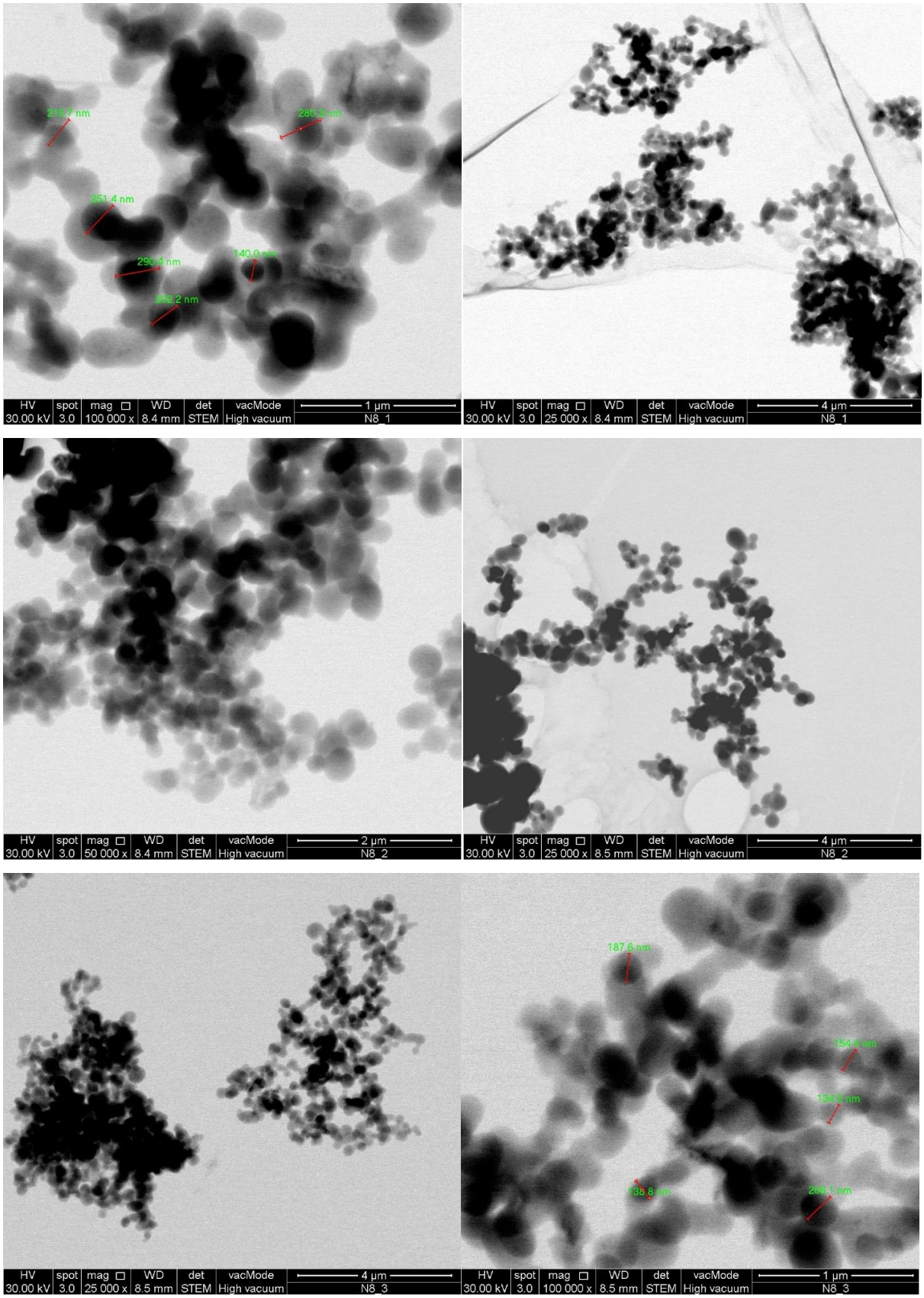


Figure 11.19: STEM images from samples N8-1 (top row), N8-2 (middle row), and N8-3 (bottom row), produced by microfluidic synthesis using the N solution with an average residence period of 8s.

11.4 Material properties used for the simulation

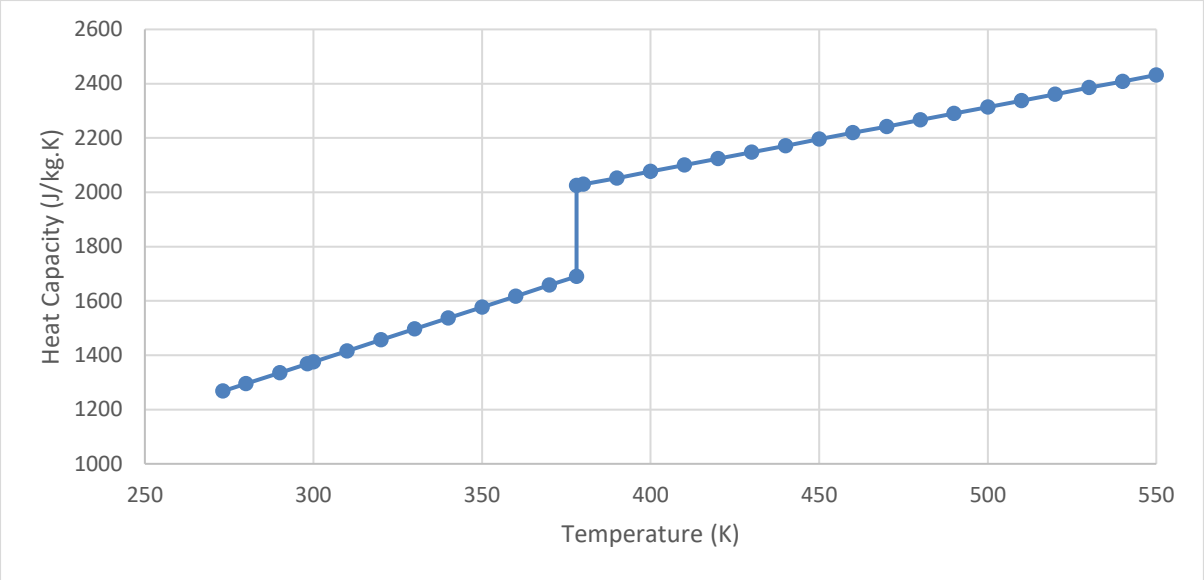


Figure 11.20: Heat Capacity of PMMA. (Gauri et al)

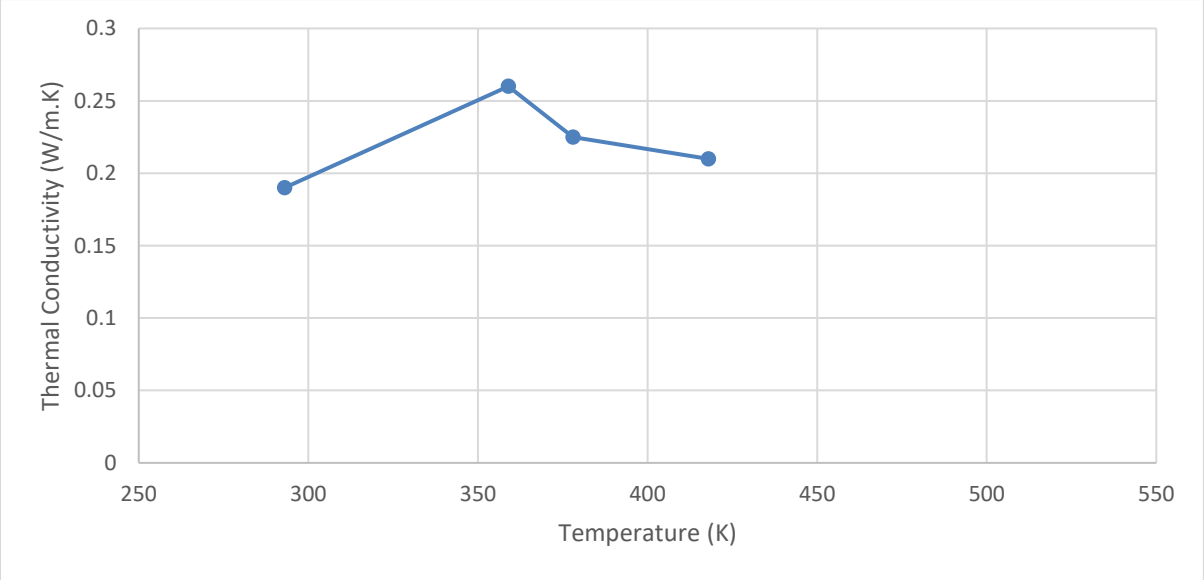


Figure 11.21: Thermal conductivity of PMMA. (dos Santos et al)

Table 11.3: Heat capacity coefficients (J/mol.K) (Yaws, 2010)

Coefficient	Octadecene	Oleic acid	Cobalt (II) oleate
A	247.6425	278.686	1117.601203
B	2.077973	2.5434	-8.138172882
C	-0.004898773	-0.0054355	0.04001785
D	0.00000499978	0.000004924	-7.37436E-5
E	0	0	6.89529E-8
F	0	0	-3.2371E-11
G	0	0	6.0416E-15

Table 11.4: Thermal and physical properties of 1-octadecene (Source: Yaws)

Property	Thermal Conductivity	Viscosity	Density
Source	Yaws (Yaws, 2010)		Yaws (Yaws, 2010)
Equation	$k = A + B.T$	$\eta = 10^{(A+\frac{B}{T}+C.T+D.T^2)}$	$\rho = A.B^{-\left[1-\frac{T}{C}\right]^N}$
Units	**W/m.K**	**cP**	**g/mL**
A	0.202235	-7.029500	0.240500
B	-0.000200	1465.400000	0.247310
C	-	0.011707	748.000000
D	-	-9.099700e-6	-
N	-	-	0.327240
Final Units	**W/m.K**	**Pa.s**	**kg/m³**
Conversion	**-**	$\eta/1000$	$\rho * 1000$

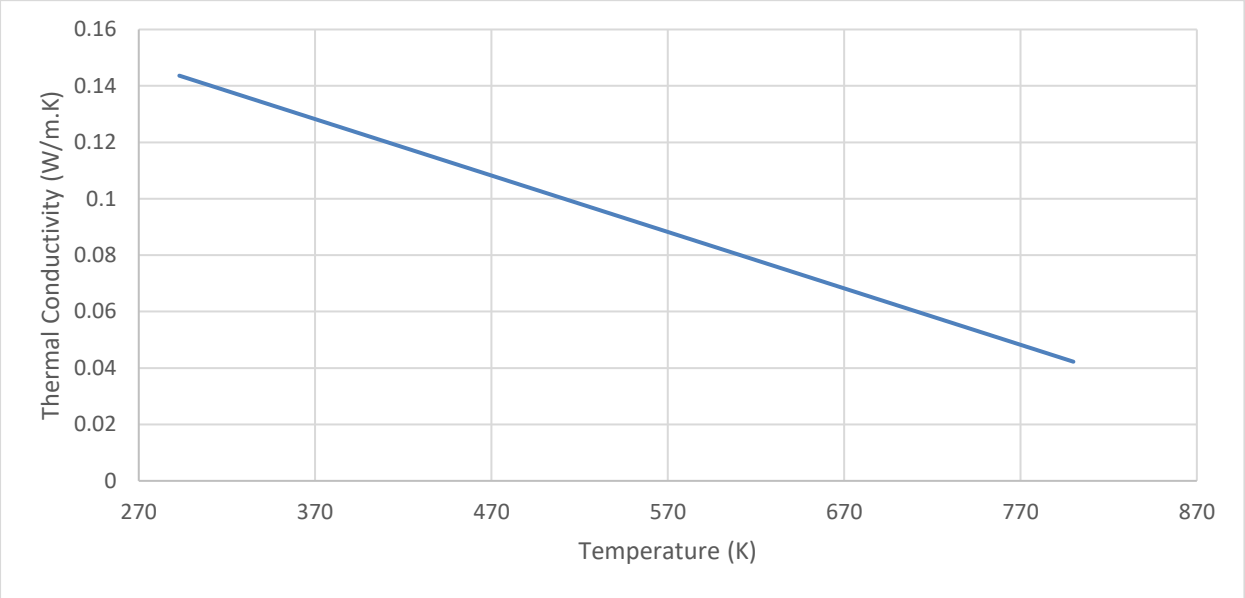


Figure 11.22: Thermal conductivity of 1-octadecene (Yaw)

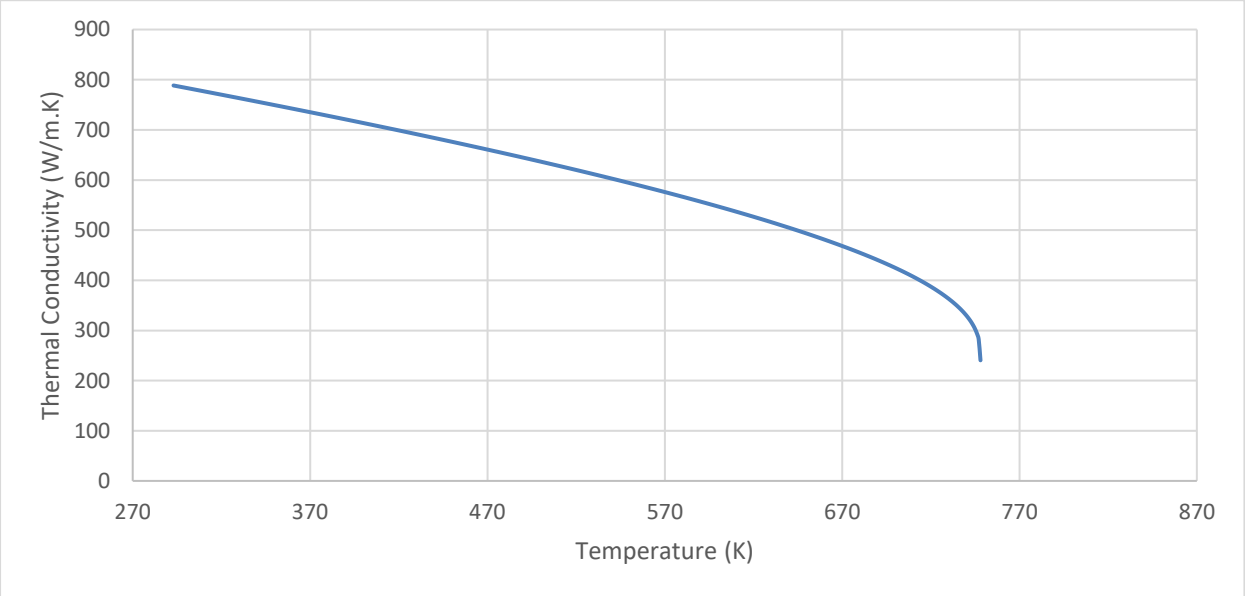


Figure 11.23: Density of 1-octadecene (Yaw)

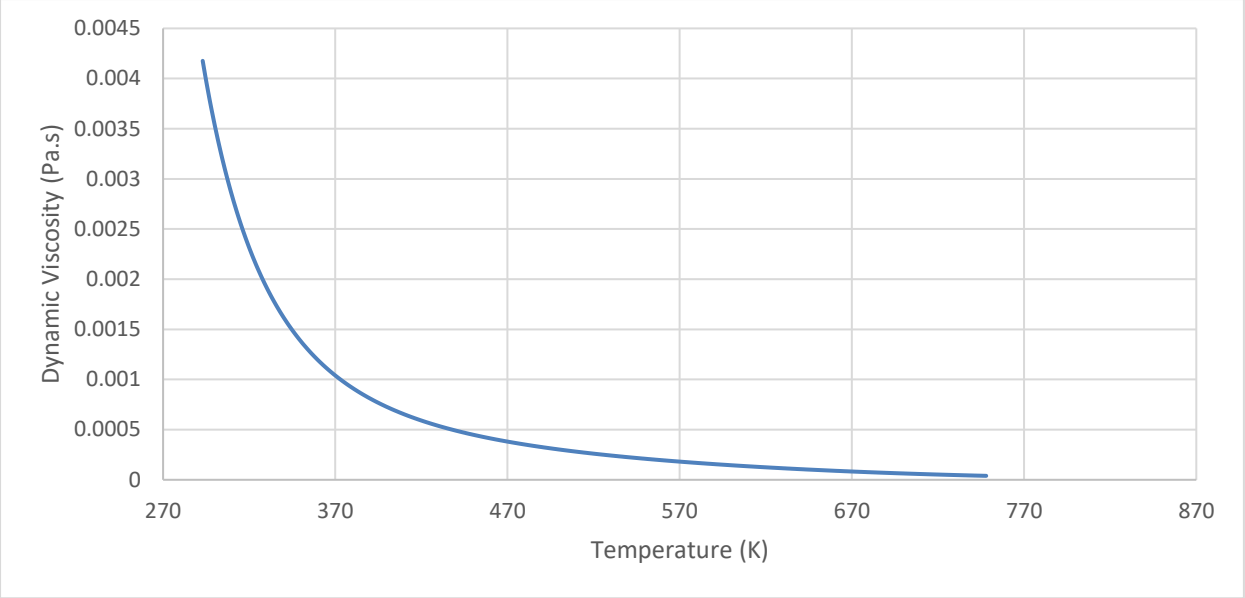


Figure 11.24: Viscosity of 1-octadecene

11.5 UV-VIS spectra of solvents

The UV-VIS absorbance spectra of the solvents used in the synthesis and purification processes are shown in Figure 8.2. The absorbance of pure oleic acid was very high in the UV region, hence a sample diluted in ODE was also measured.

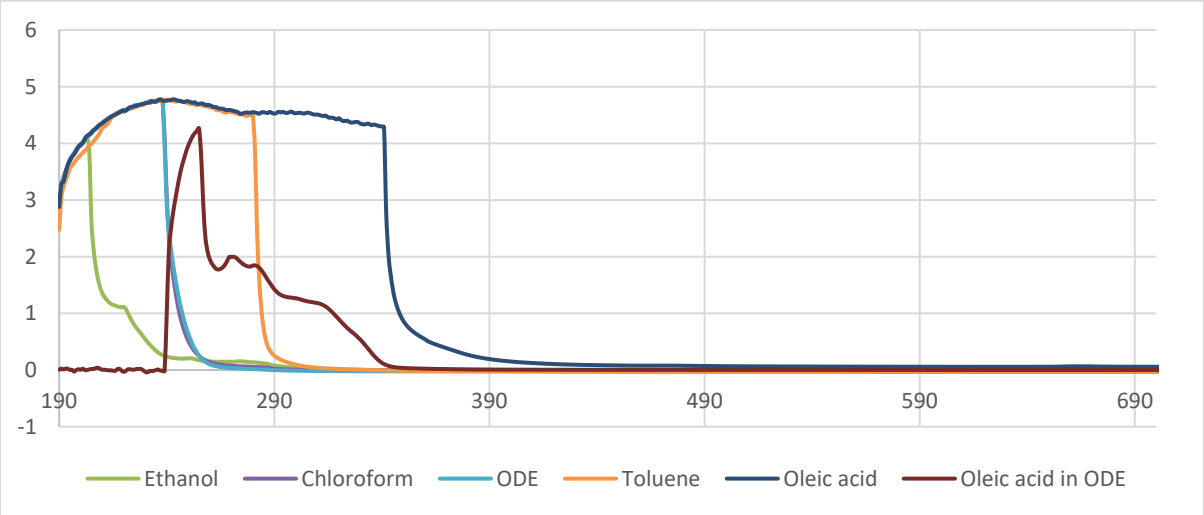


Figure 11.25: UV-VIS absorbance spectra of the solvents used in CdSe synthesis, measured against air.

11.6 Photoluminescence spectra of solvents

Figure 11.26 shows the fluorescence spectra of the various solvents used in the synthesis and purification steps. The measurements were taken using the same settings and have not been normalised. Among these solvents, ODE has lowest fluorescence, making it a suitable solvent for fluorescence measurements. The overall fluorescence exhibited by toluene is also quite low and is also quite suitable for fluorescence measurement. While all the solvents have a fluorescence peak around 406-408 nm, the peak displayed by hexane is a more prominent, however its fluorescence at higher wavelengths is lower and flatter than toluene. The intense fluorescence of chloroform rules it out as a solvent for fluorescence spectroscopy (note: the chloroform used here was regular chloroform, however, there are chloroform formulations available with low fluorescence). ODE was not used as a solvent for the purified product as it is relatively viscous, oily, and more difficult to work with. While toluene is suitable for fluorescence measurements, it has extremely high absorbance at wavelengths below 300 nm making it unsuitable for UV absorbance measurements. There are peaks produced by CdSe clusters in this region which cannot be seen using toluene. This leaves hexane as the solvent of choice for both fluorescence and UV-VIS measurements.

The purified quantum dots are not soluble in ethanol or methanol, but these solvents are included here as they have been used for the purification steps, and some of the washes have also been analysed.

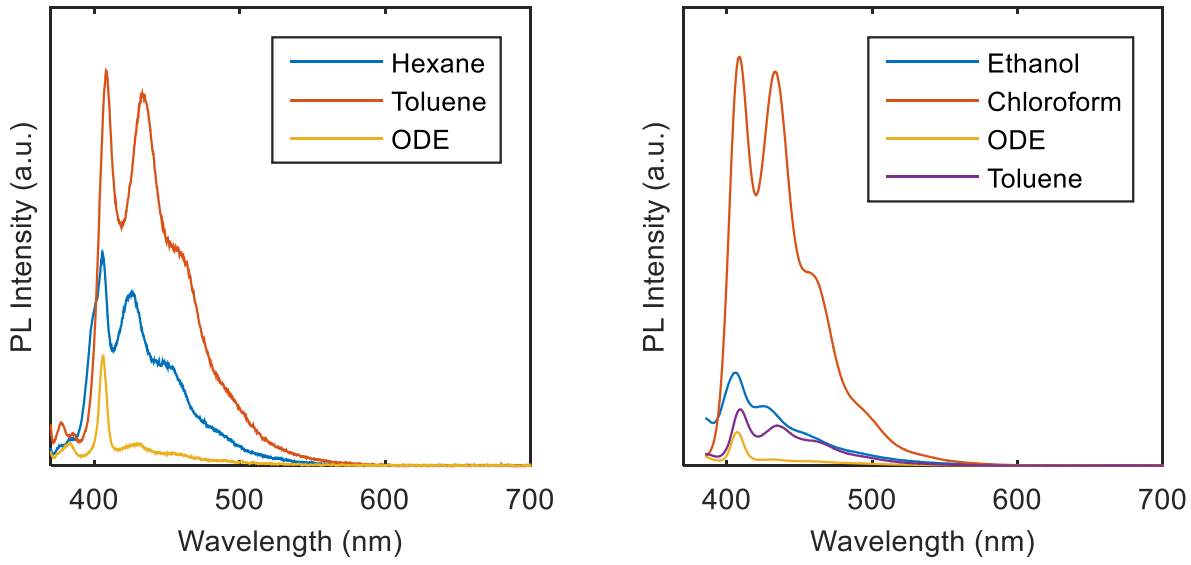


Figure 11.26: Fluorescence spectra of the various solvents used in the CdSe synthesis runs. These spectra in each subplot were measured using the same settings (photomultiplier voltage: (left) 950V, (right) 400V) and have not been normalised.

11.7 PL/PLE spectra of purified quantum dot samples

11.7.1 Samples made using Mix342

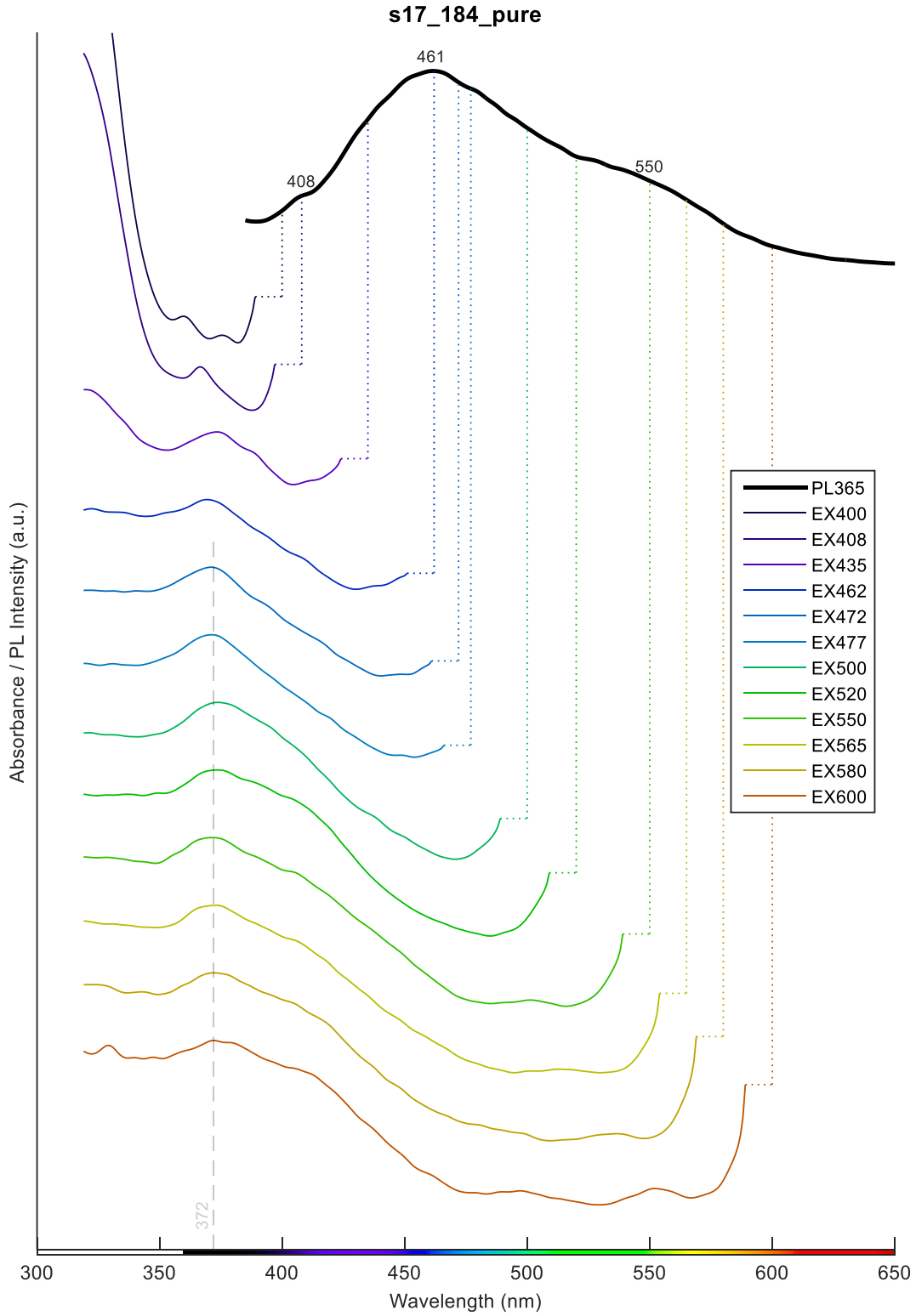


Figure 11.27: Normalised fluorescence (PL365) and PLE spectra of sample s17_184_pure (made from Mix342) measured at various emission wavelengths. No peaks stand out prominently in this case in either the PL or PLE spectra, but very weak band absorption peaks may be seen in the 550, 565, 580 and 600 nm PLE spectra.

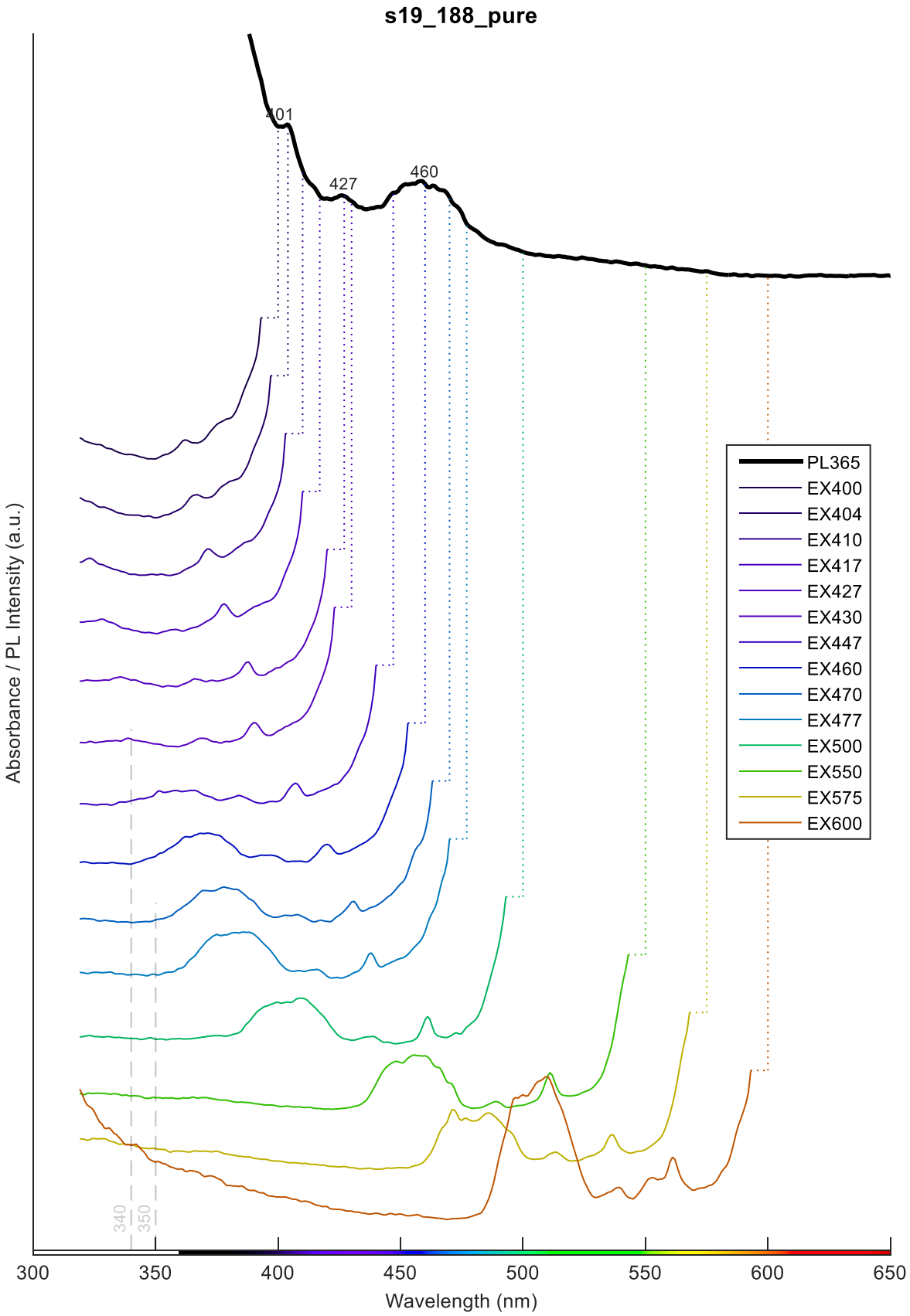


Figure 11.28: Normalised fluorescence (PL365) and PLE spectra of sample s19_188_pure (made from Mix342) measured at various emission wavelengths. This sample is similar to s20_180_pure (Figure 11.36), with significant band edge absorption peaks, but very low yield.

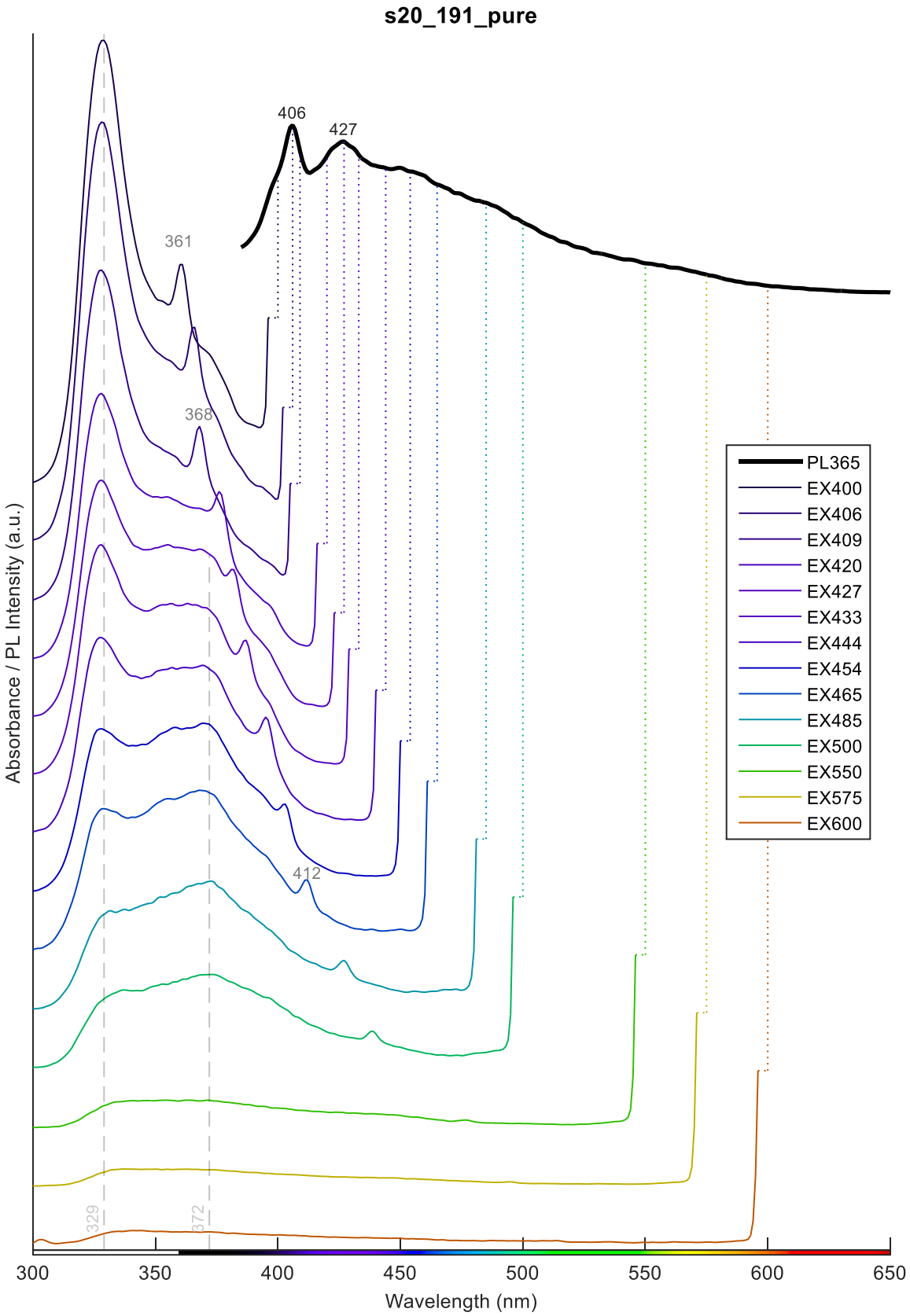


Figure 11.29: Normalised fluorescence (PL365) and PLE spectra of sample s20_191_pure (made from Mix342) measured at various emission wavelengths. While the 329 nm and 372 nm peaks contribute the most to the PLE spectra, a sharp peak can be seen with in most of them with a constant stokes shift of ~40-55 nm.

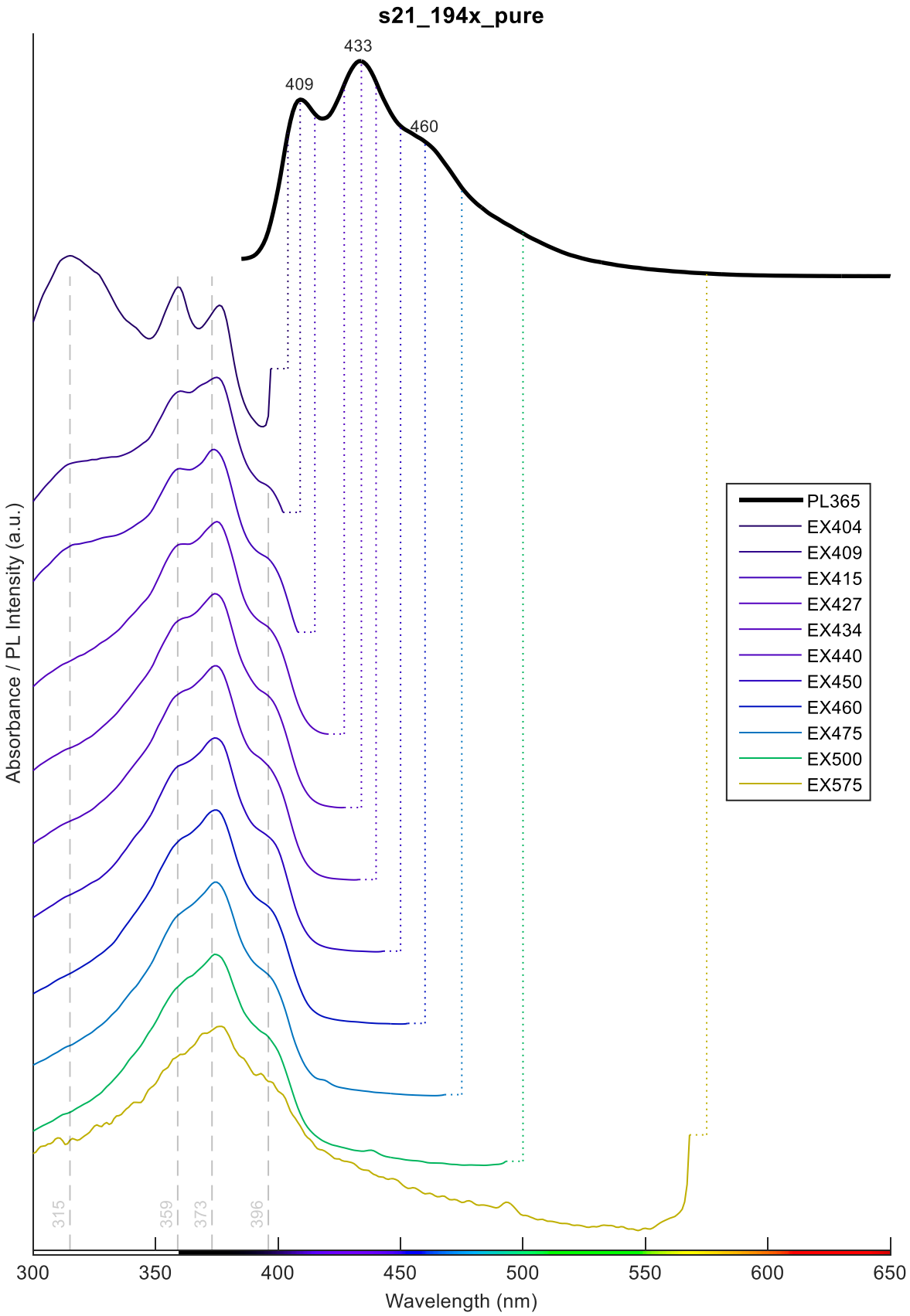


Figure 11.30: Normalised fluorescence (PL365) and PLE spectra of sample s21_194x_pure (made from Mix342) measured at various emission wavelengths. The band edge absorption peaks seen here are negligible. Note: the chip was damaged during the synthesis of this sample.

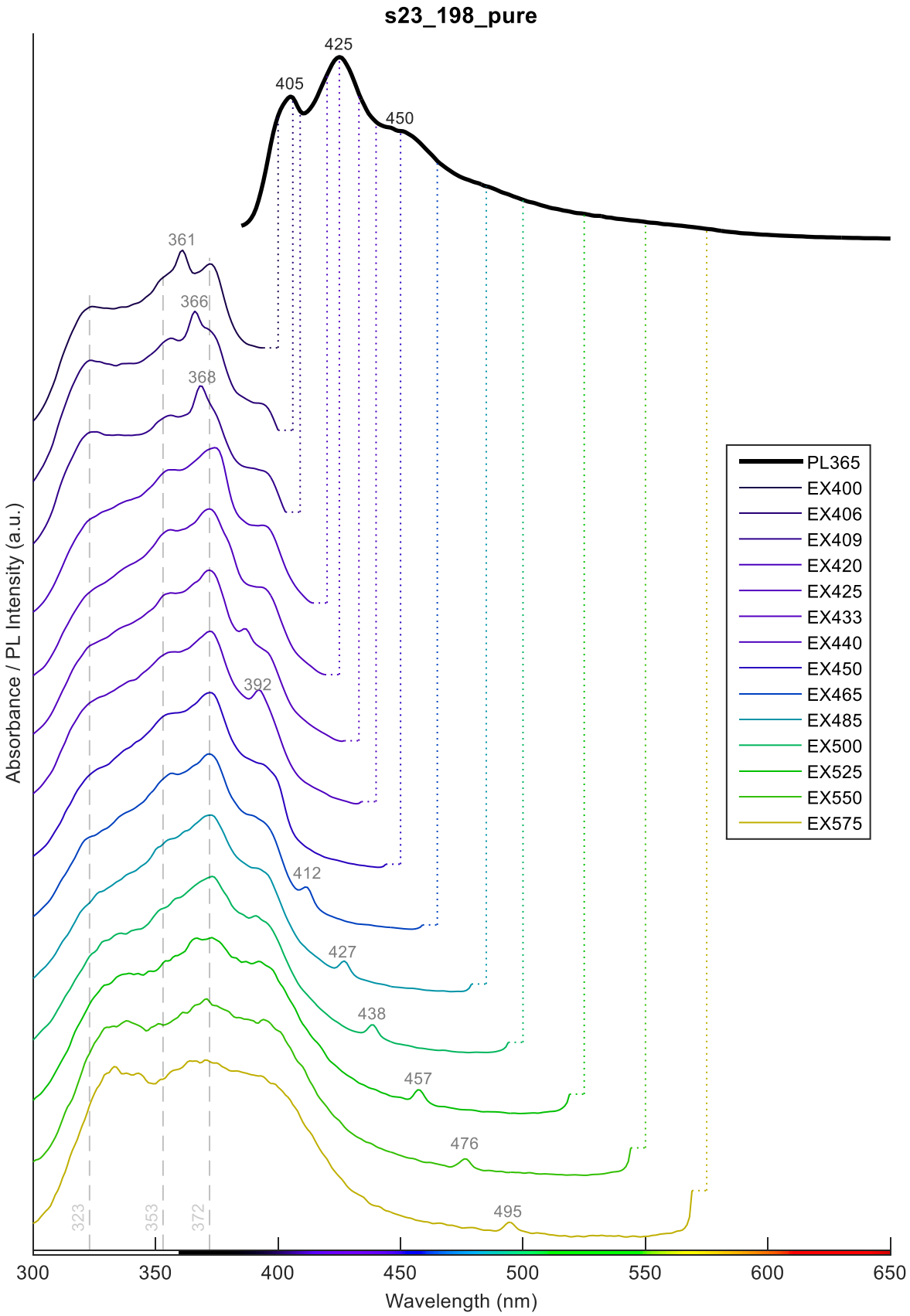


Figure 11.31: Normalised fluorescence (PL365) and PLE spectra of sample s21_194x_pure (made from Mix342) measured at various emission wavelengths. The band edge absorption peaks can clearly be seen throughout the PLE spectra.

11.7.2 Samples made using Mix431

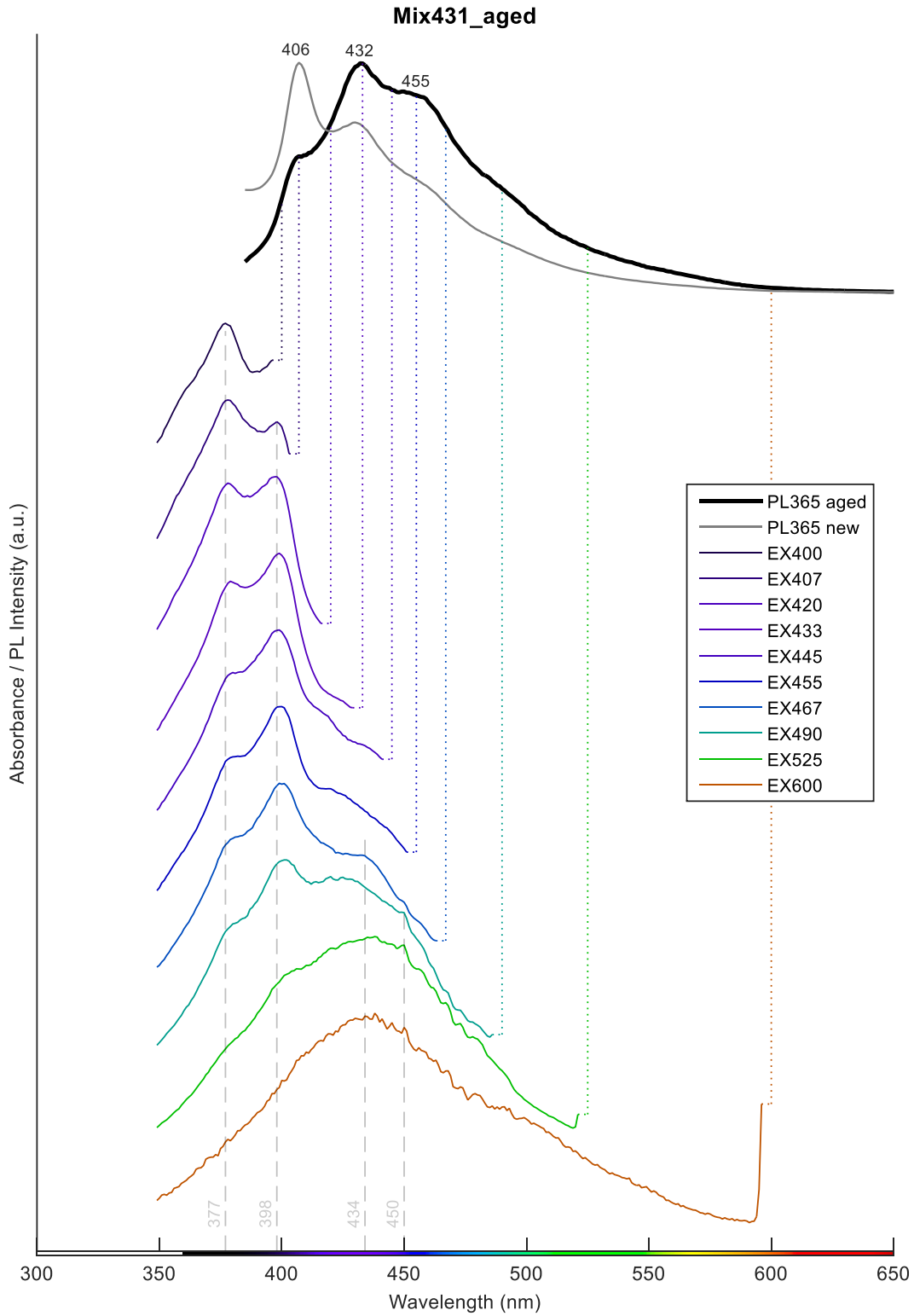


Figure 11.32: Normalised fluorescence (PL365) and PLE spectra of Mix431 aged at room temperature for 50 days, measured at various emission wavelengths. The PL365 spectrum of fresh Mix431 is included for comparison. An increase in the 432 nm and 455 nm PL peaks is seen after aging, while the 406 nm peak is reduced.

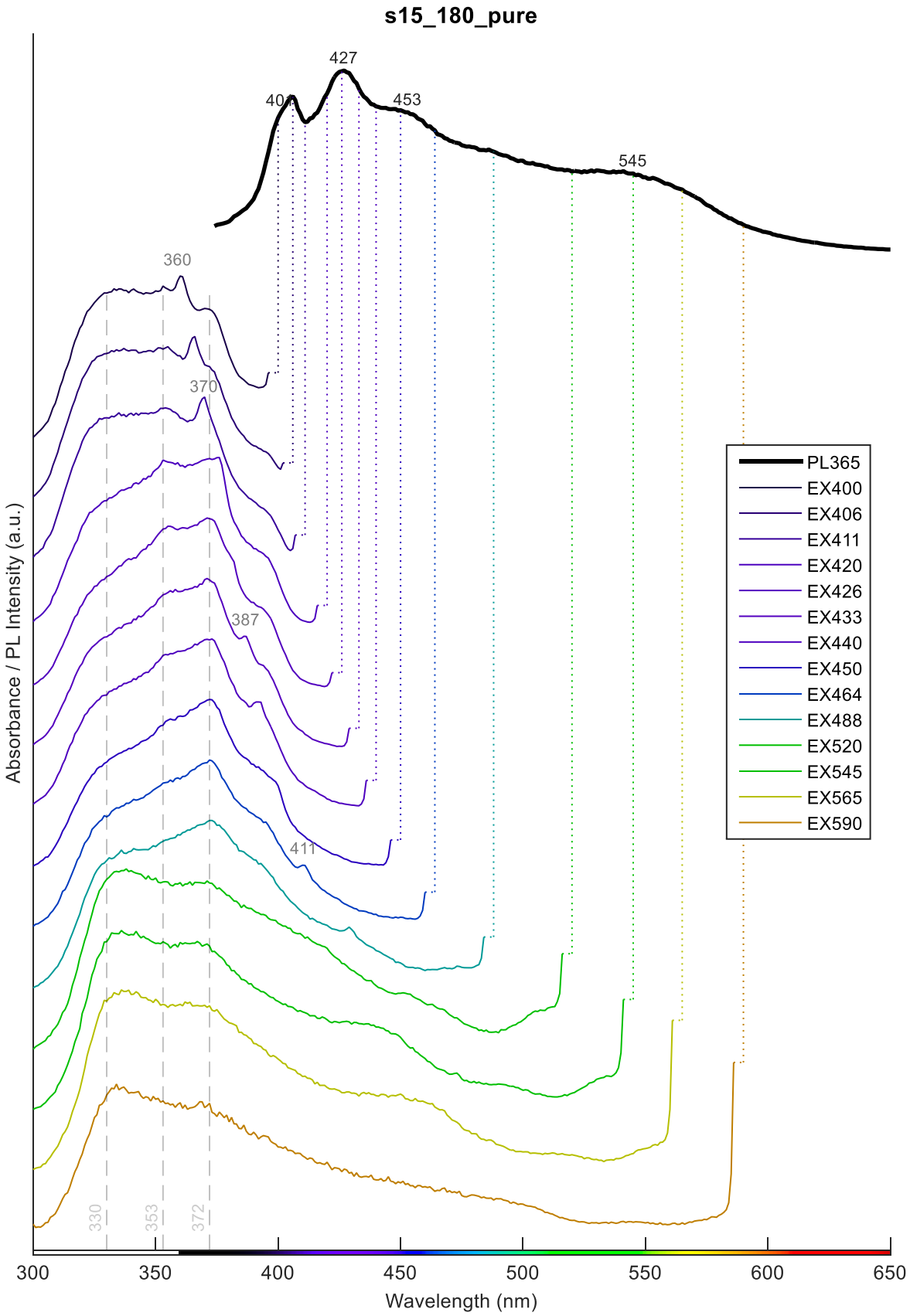


Figure 11.33: Normalised fluorescence (PL365) and PLE spectra of sample s15_180_pure (made from Mix431) measured at various emission wavelengths. A small but well-defined peak can be seen throughout the PLE spectra, with a constant Stokes shift of ~40 – 60 nm.

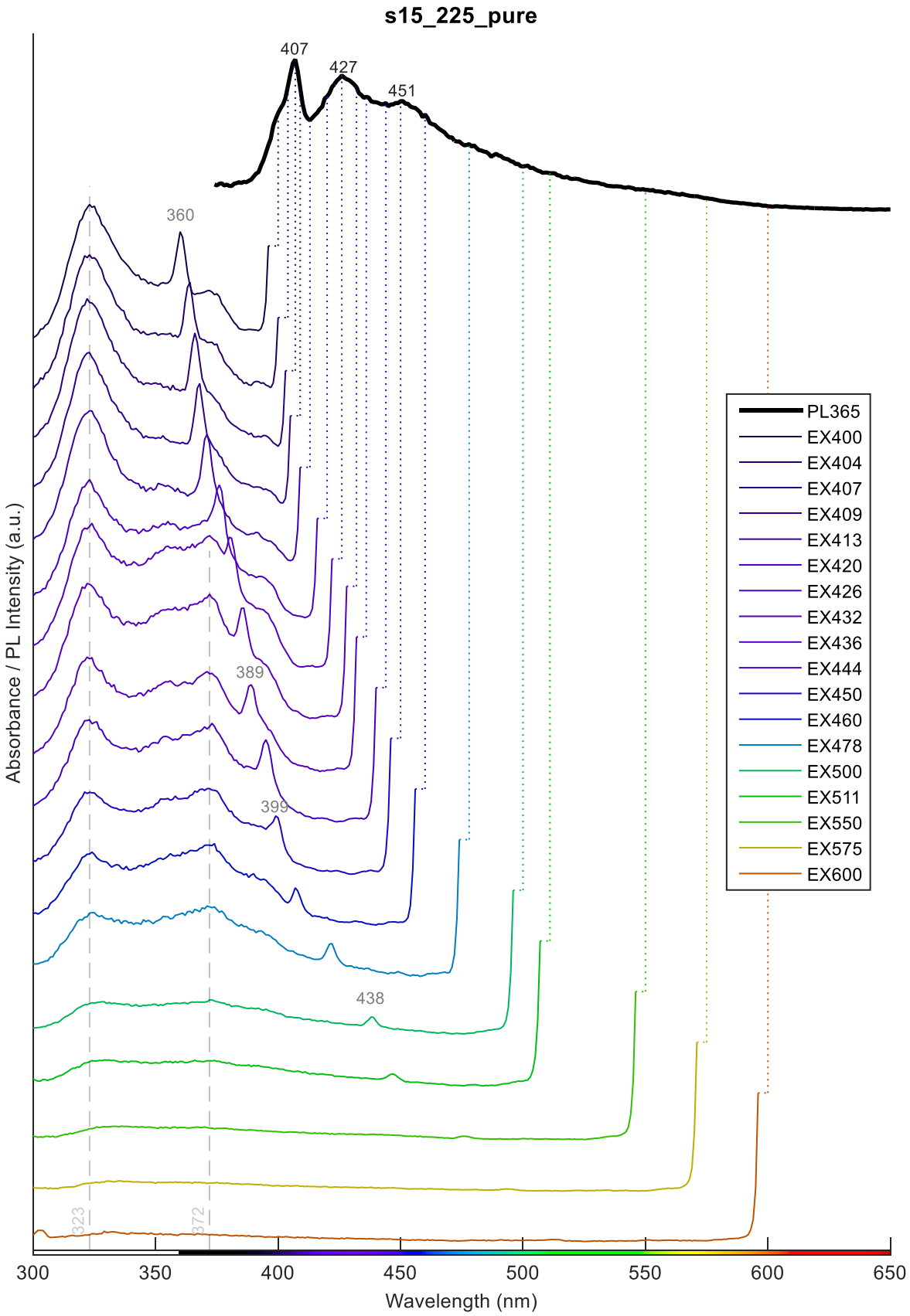


Figure 11.34: Normalised fluorescence (PL365) and PLE spectra of sample s15_225_pure (made from Mix431) measured at various emission wavelengths. A small but well-defined peak can be seen throughout the PLE spectra, with a constant Stokes shift of ~40 – 60 nm

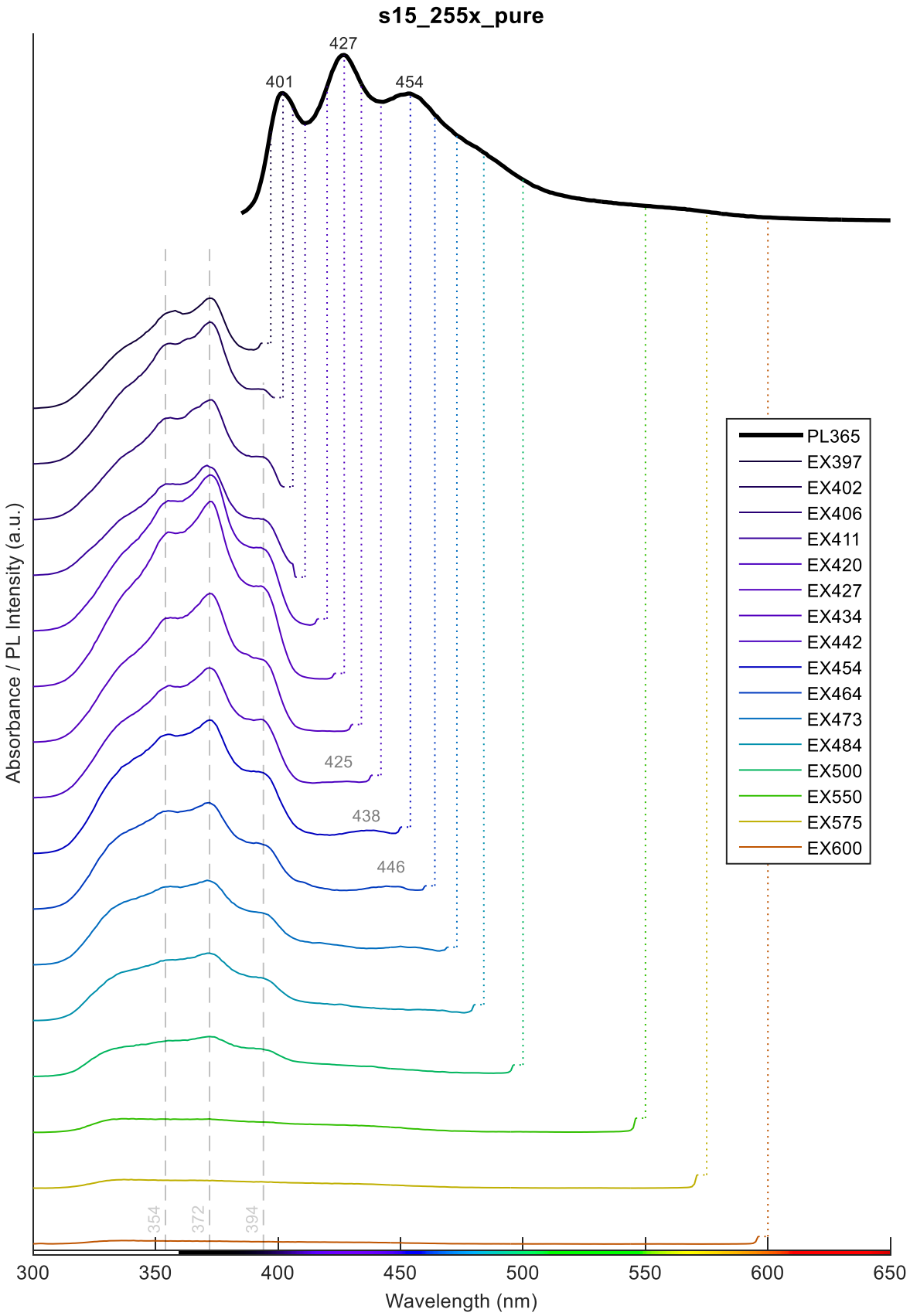


Figure 11.35: Normalised fluorescence (PL365) and PLE spectra of sample s15_250x_pure (made from Mix431) measured at various emission wavelengths. A small band edge absorption peak can be seen in the PLE spectra emitting at 442 nm to 464 nm.

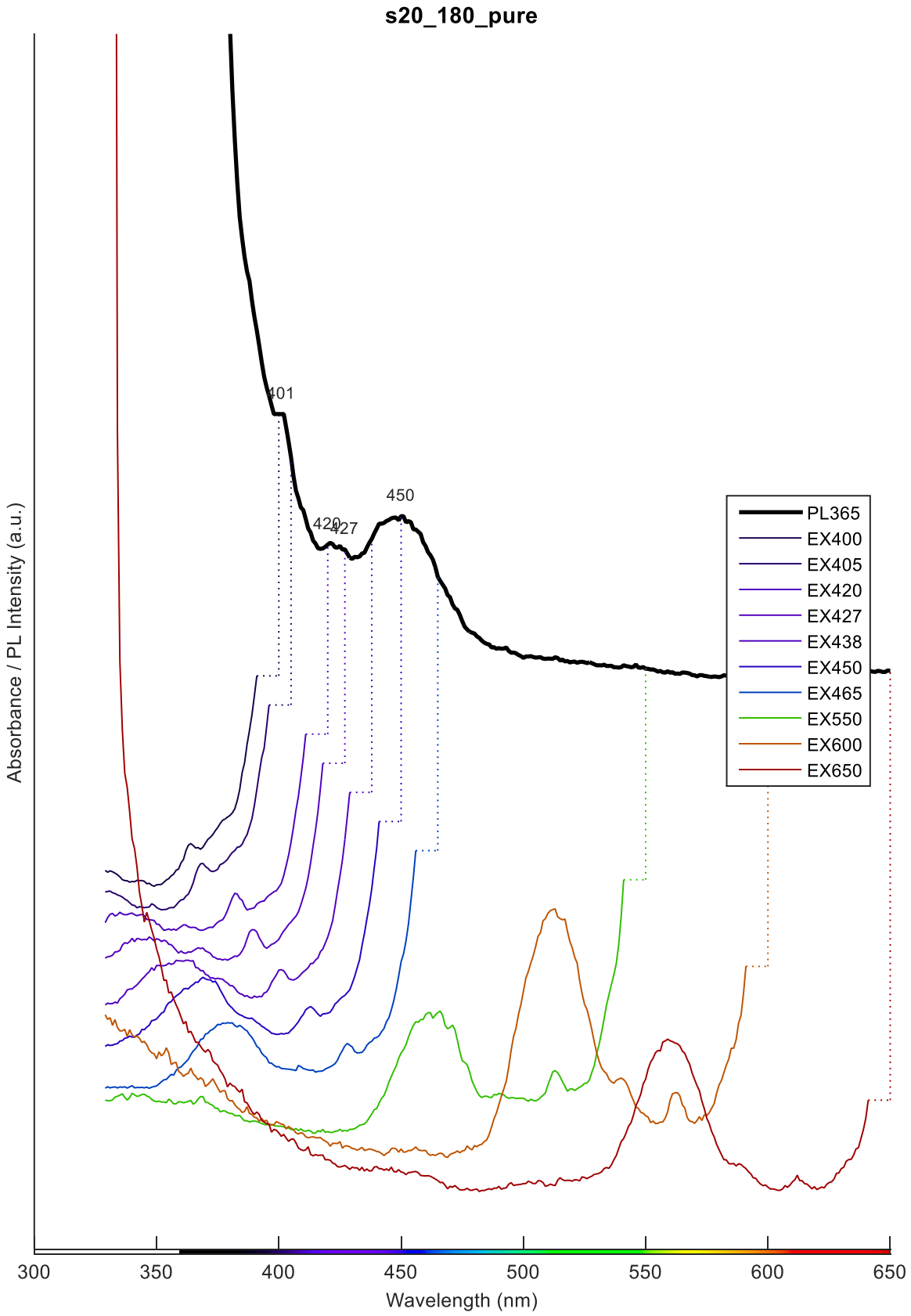


Figure 11.36: Normalised fluorescence (PL365) and PLE spectra of sample s20_180_pure (made from Mix431) measured at various emission wavelengths. While this sample shows significant band edge emission, the overall amount is incredibly low. The peaks are visible due to normalisation, but compared to other samples, this is barely visible.

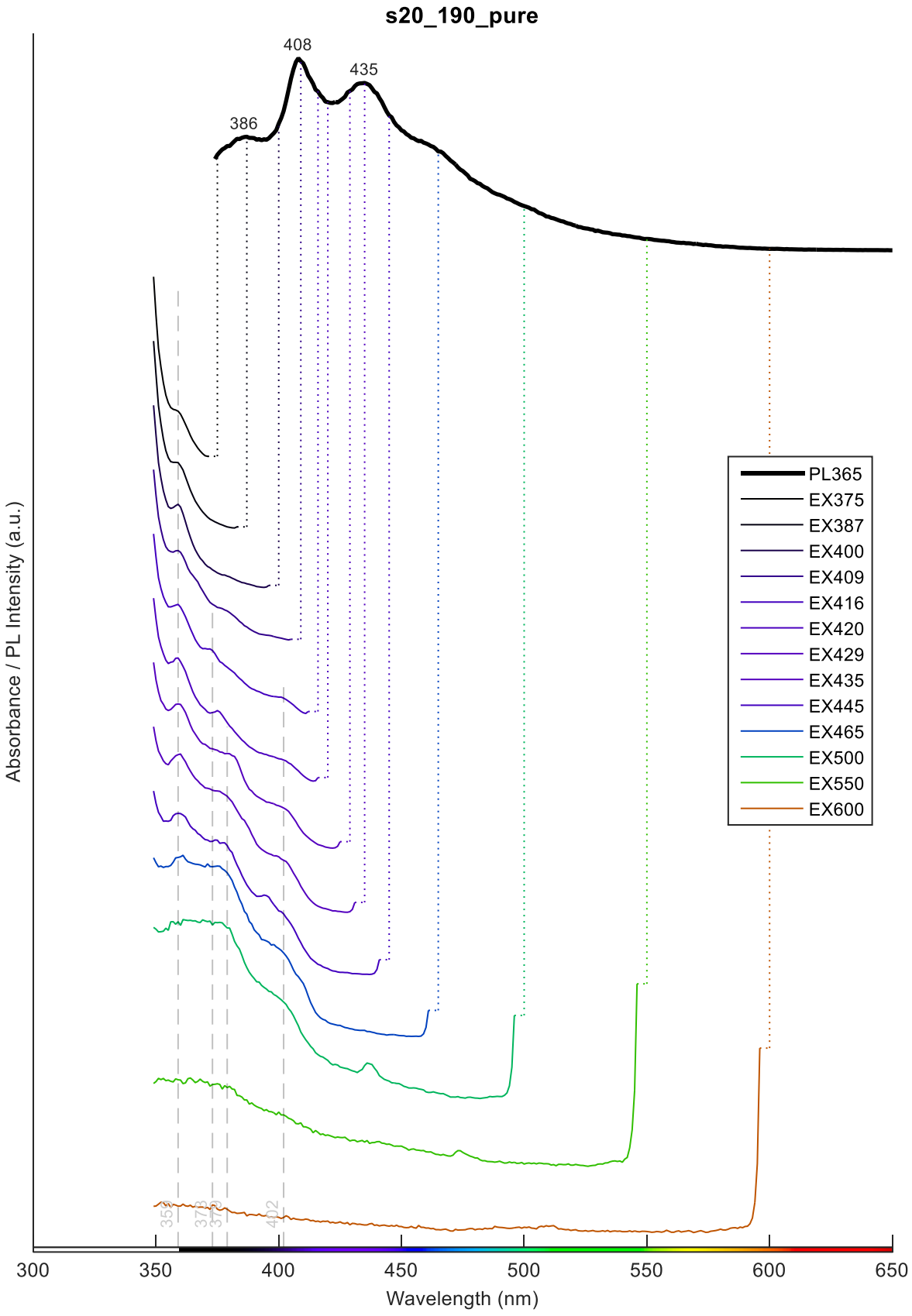


Figure 11.37: Normalised fluorescence (PL365) and PLE spectra of sample s20_190_pure (made from Mix431) measured at various emission wavelengths.

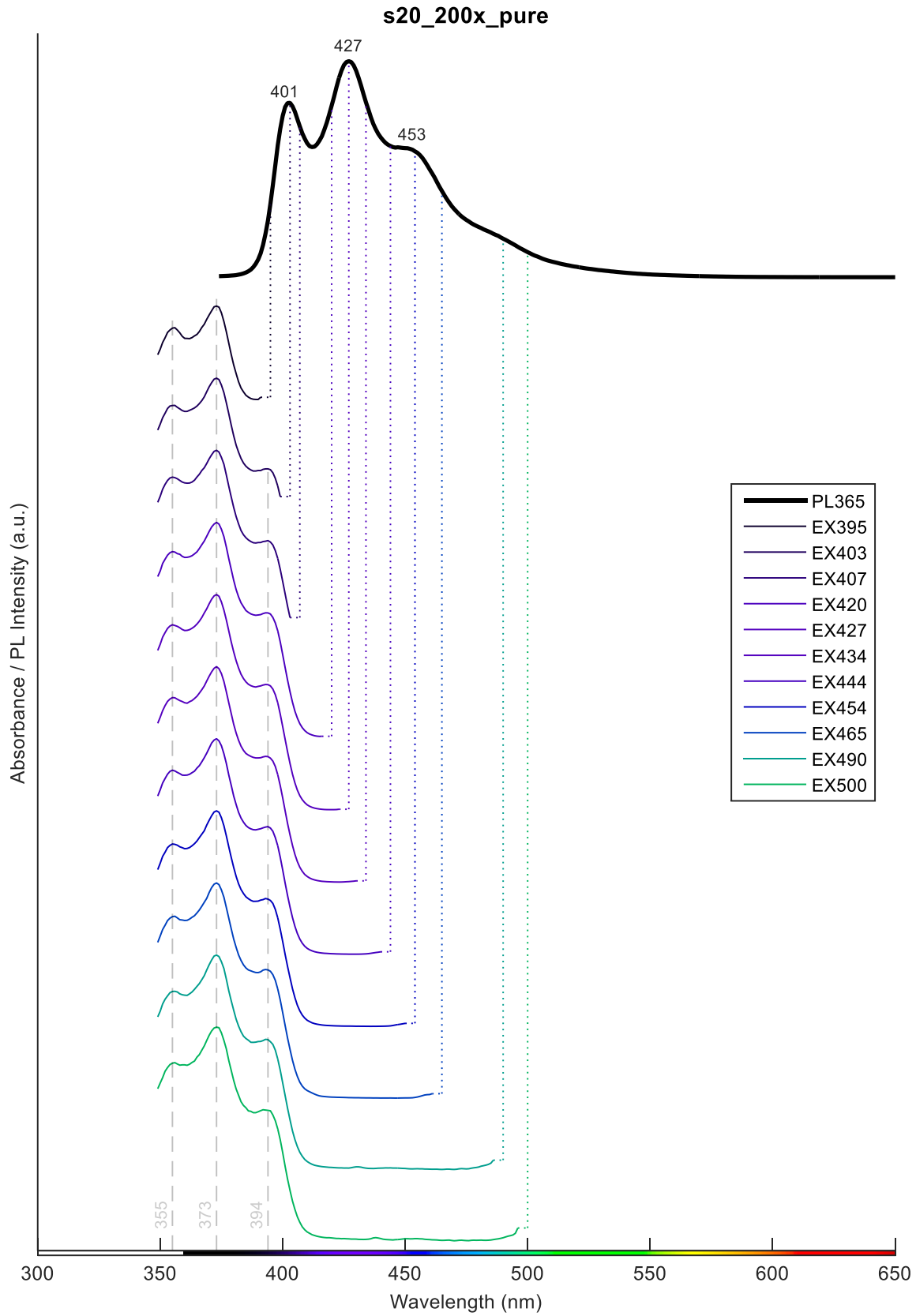


Figure 11.38: Normalised fluorescence (PL365) and PLE spectra of sample s20_190_pure (made from Mix431) measured at various emission wavelengths. Almost all the photoluminescence is due to the absorption features at 355, 373, and 394 nm.

11.7.3 Samples made using Mix571

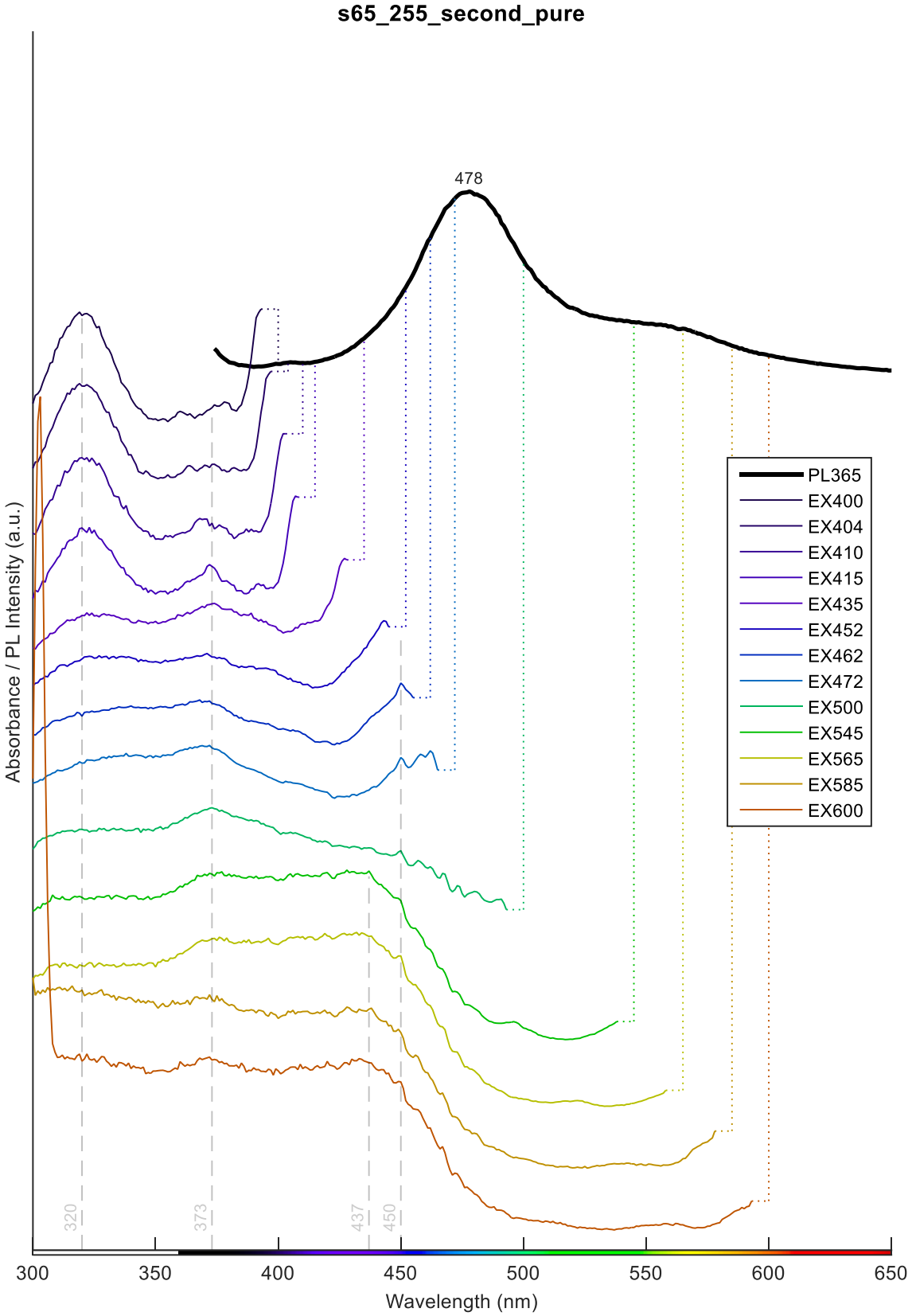


Figure 11.39: Normalised fluorescence (PL365) and PLE spectra of sample s65_255_second_pure (made from Mix571) measured at various emission wavelengths. The second washing of this sample resulted in a small blue shift (-3 nm) of the main peak compared to sample s65_255_pure.

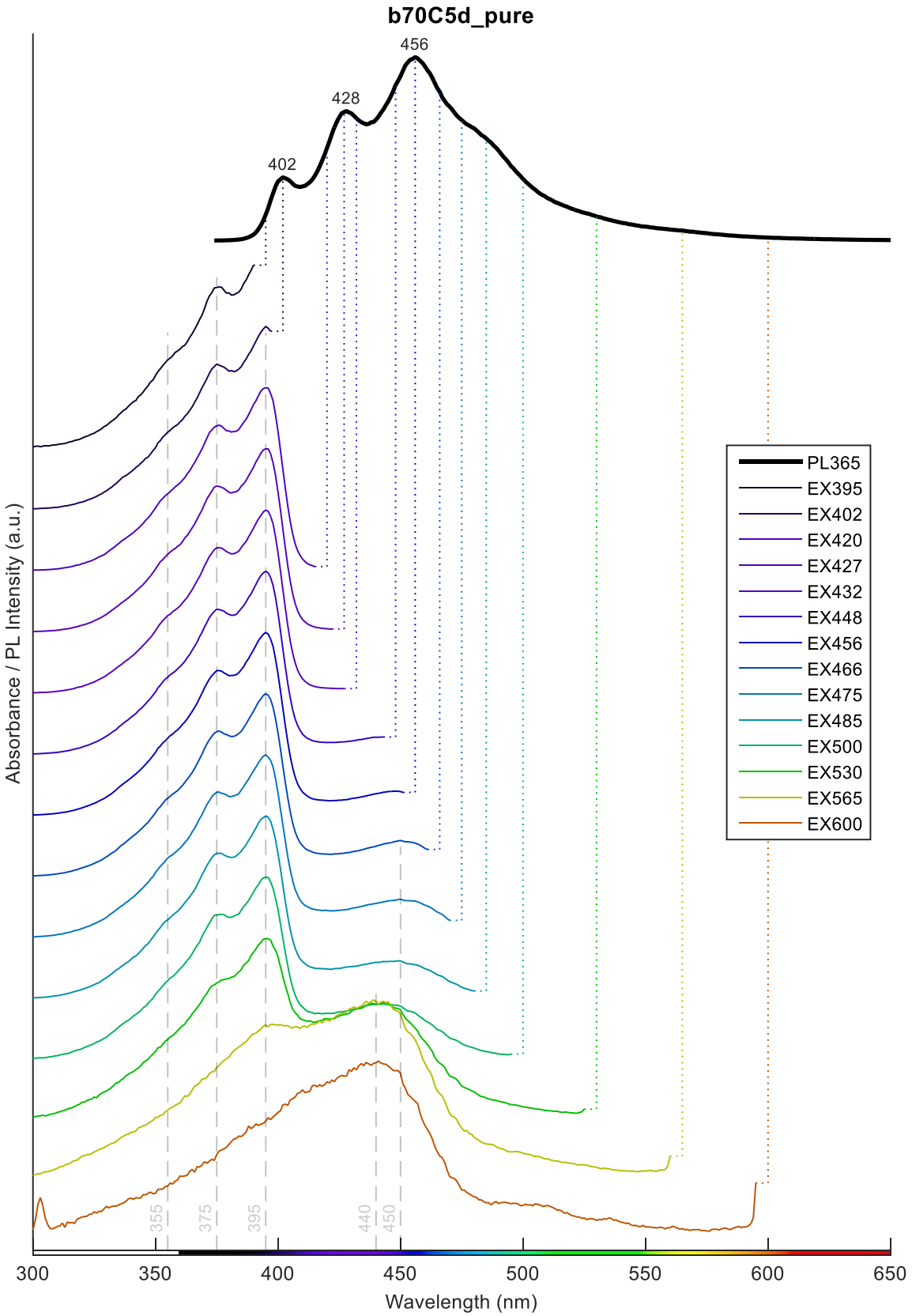


Figure 11.40: Normalised fluorescence (PL365) and PLE spectra of sample b70C5d_pure (made from Mix571) measured at various emission wavelengths. The PLE peaks at 355, 375, and 396 nm are major contributors to the fluorescence intensity up to 500 nm, above which another much broader PLE peak (444 nm) becomes the dominant contributor.